A CO_2 Measurement System for Low-Cost Applications using Chemical Transduction

by

Andrew Douglas Maxwell, B.Eng (Hons)

Dissertation

Submitted in Fulfillment

of the Requirements

for the Degree of

Doctor of Philosophy

at the

The University of Southern Queensland

Faculty of Engineering & Surveying

March 2002

Abstract

It is demonstrated that by using a miniature chemical reaction vessel under adaptive mechatronic control, it is possible to design and construct a low-cost carbon dioxide measurement system. With further development such a system would be potentially suitable for low-cost commercial application, in particular as sacrificial, single-mission instrumentation packages in horticultural cargo monitoring.

Current instrumentation systems for carbon dioxide (CO_2) gas measurement are reviewed and their limitations with respect to low cost commercial applications determined. These utilise technology intended for laboratory measurements. In particular the optical energy absorbance of CO_2 in the infra-red electromagnetic spectrum. These systems require large optical paths (typically 10cm) in order to measure small CO_2 concentrations. This in turn has a large impact on the physical size of the sensing system.

Of the many applications requiring online CO_2 sensing packages (such as medical, petroleum, environmental and water treatment) the horticultural industry is the primary focus for this research. CO_2 sensing systems are primarily used in horticulture to monitor the produce environment and help extend storage time. For these applications CO_2 concentrations are typically low (in the range 0 to 1%) and the paramount need is for low-cost (and possibly disposable) sensing packages.

The basis of the measurement technique is the use of bulk (but small volume) aqueous chemical reaction under mechatronic control. Unlike thin film technologies where very thin membranes are passively exposed to the gaseous sample, here a small volume (approximately 2mL) of simple and very cheap liquid chemical indicator (calcium hydroxide solution) is used to produce an opaque precipitate. CO_2 concentration is then assessed by low-cost optical attenuation measurements of the developing opacity of the solution. The instrumentation package comprises pumps, flowmeter, reaction cell and infra-red optics for the turbidity measurement, plus reagent and waste vessels, pipelines and electronics.

During each measurement cycle, the reaction cell is flushed, with fresh chemical indicator and a sample of gas admitted. The indicator and the sample gas are then vigorously mixed and the change in the indicators optical properties measured at regular intervals. An embedded 8-bit microcontroller performs the necessary analysis to deduce the CO_2 concentration (as percentage by volume) for the sample gas by reference to one or more of five "Time-To-Threshold" calibration models. These models evaluate the trend in turbidity development as precipitate is formed.

First and second prototypes of the measurement system have been constructed and their (low-cost) components and overall performance evaluated, the first a 'proof-of-concept' and the second to investigate methodology shortcomings. As a result the design of a third prototype is outlined. The measurement systems have been shown to work adequately well within expected limitations, resulting in a usable low-cost measurement technique. The current prototypes have a useful range of at least 5% to 100% CO_2 with a discrimination of typically $\pm 6\%$. Deficiencies, particularly performance at low concentrations, are identified and potential enhancements for future prototypes proposed.

Certification of Thesis

I certify that the ideas, experimental work, results, analyses, software and conclusions reported in this dissertation are entirely my own effort, except where otherwise acknowledged. I also certify that the work is original and has not been previously submitted for any other award, except where otherwise acknowledged.

Signature of Candidate	Date

ENDORSEMENT

Signature of Supervisors	Date

Acknowledgments

I would very much like to thank the following people for their assistance and support throughout the duration of my Ph.D. studies.

I would firstly like to thank my supervisors, Associate Professor Nigel Hancock, and Professor John Billingsley, for their help, and advice which have made so many opportunities become available.

I would also like to thank contributors to this dissertation, namely Professor Thanh Tran-Cong for his assistance with the theoretical cell analysis. Many thanks to John Leis, and Ross Varnes, both of whose UNIX and LaTeX wisdom helped me numerous times in the preparation of this manuscript. Thanks to Brendan Horsfield, Dean Beliveau, and the many other co-researchers with whom I studied with for their valuable input and assistance throughout this journey.

Contents

List of Tables

List of Figures

Chapter 1

Introduction

1.1 Carbon Dioxide Gas Measurement

Currently there are three major technologies for measuring the concentration of CO_2 in a gas mixture.

Firstly, most common and traditional systems exploit the optical energy absorbance of CO_2 in the infra-red electromagnetic spectrum. Light of a specific wavelength (typically 4.3μm) is passed through a tube ("cell") containing the sample gas and energy is absorbed in proportion to the amount of CO_2 in the cell volume. This CO_2 concentration is then deduced from the Beer-Lambert Law (Watts (1983, p1176), for example) where the increase in energy absorbance is indicated as the reduced energy level reaching the infra-red detector. These systems typically require large optical paths in order to measure small CO_2 concentrations (<5% of a gas mixture) which has a large impact on the final physical size of the resultant sensing system. A minimum measurement cell length of typically 10cm is required for concentration measurements in the range of 0 to 1%.

Secondly, recent systems have utilised chemical dye and thin film technologies in which complex chemical receptors are embedded in a surface film and exposed to the sample

gas. The change in the optical properties of the dye/film in response to CO_2 is detected and the CO_2 concentration calculated (Mills & Chang, 1993; He & Rechnitz, 1995). However, these systems utilise exotic and expensive chemicals which are not readily available, are difficult to construct, and their performance in the presence of various gaseous contaminants is uncertain.

And finally, general purpose chemical instrumentation may be used, but such equipment is expensive. Gas and liquid chromatography in which individual chemical species are isolated through complex chemical reactions and are measured independently (Hester, 1995, for example). Chromatography systems in particular are physically large (typically one meter cube) and seldom suited for harsh environments, automatic operation, or online applications outside the laboratory.

It is seen that the requirement for small, low cost and possibly disposable CO_2 sensing systems is not met by any of the foregoing. This dissertation explores and examines an alternative methodology to facilitate effective, low cost absolute measurement of CO_2 concentrations suitable for monitoring of ambient gas concentration levels.

Applications for such low-cost systems include measurement packages for medical, petroleum, environmental air and water treatment, and in the food industry, e.g. to measure CO_2 when used as a pH-adjusting agent in cheese production (Losos, 1998), and in association with horticultural storage and transportation.

This research topic arose from a need for suitable carbon dioxide instrumentation for controlled atmosphere (CA) maintenance of foodstuffs, especially fresh, and therefore respiring, horticultural produce. Carbon dioxide sensing systems are used in this area primarily to monitor the produce environment and help extend storage time (Wolfe, 1993). For these applications CO_2 concentrations are typically low (in the range 0 to 1%) with differential measurement capabilities usually being required (e.g. to monitor respiration rate, typically to a discrimination of at least 0.01%). For many of the applications there is also a principal need for low-cost (and possibly disposable) CO_2 sensing.

1.2 Research Overview

This dissertation presents the design of a quantitative mechatronic[1] CO_2 instrumentation system based on "wet chemical analysis", fully automated by means of miniature and low-cost mechatronic and optical components and a microcontroller support system. A block diagram of the fundamentals of the instrument and its subsystems is shown in Figure 1.1.

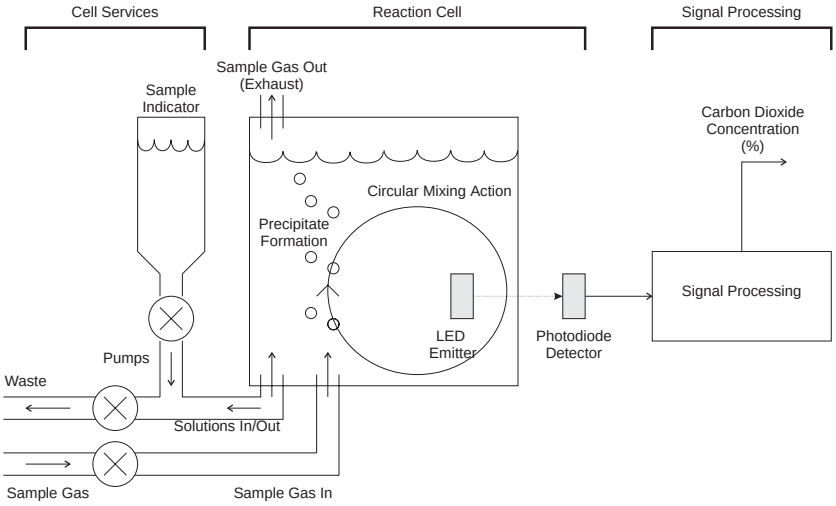

Figure 1.1: A simplified pictorial overview of the fundamental CO_2 sensor system.

The instrument consists of three principal components, namely; chemical reaction "cell" (Figure 1.1 center), cell mechatronics, and a smart sensor controller. The chemical reaction cell provides containment of indicator chemicals used to transduce the gaseous CO_2 concentration into a response suitable for optical turbidity measurement. The cell mechatronics are used to control fluid movement throughout the instrument, including filling, draining and cleaning functions. The smart sensor controller then takes the optical turbidity measurement and applies models to translate the optical turbidity measurement into a concentration value of the CO_2 concentration (%) in the sample gas being supplied to the instrument. The design and analysis of all of these components is presented in the subsequent chapters with two prototypes having been developed;

[1] Mechatronic systems involve a combination of robotics, computer control and specialist electronics.

an initial 'proof-of-concept' prototype, illustrated in Figure 1.2(a), and a larger more flexible experimental test bed, Figure 1.2(b).

1.3 Research Aims and Objectives

The aim of this work was to research the applicability of wet chemical measurement techniques combined with intelligent mechatronics to provide a low-cost instrumentation system suitable for absolute CO_2 measurement.

1.3.1 Specific Research Objectives

The research set out to address the following objectives.

1. Investigate applications requiring low-cost absolute and differential CO_2 sensing and derive suitable performance specifications and design criteria for the sensing systems instrumentation suited to these applications.
2. Investigate existing instrumentation systems and methodologies to determine limitations in their current design, measurement technique and/or performance, and investigate advantages of integration with non-traditional and/or novel technologies.
3. Describe and model novel and non-traditional methods and phenomenon useful for the measurement of CO_2, in particular those involving potentially low cost chemical, and mechatronic interactions.
4. Devise and develop prototype CO_2 sensing systems to meet the devised specifications utilising previously explored methodologies (Objective 3).
5. Derive suitable evaluation procedures and employ these to evaluate the prototyped sensor(s) and demonstrate performance capabilities and limitations.

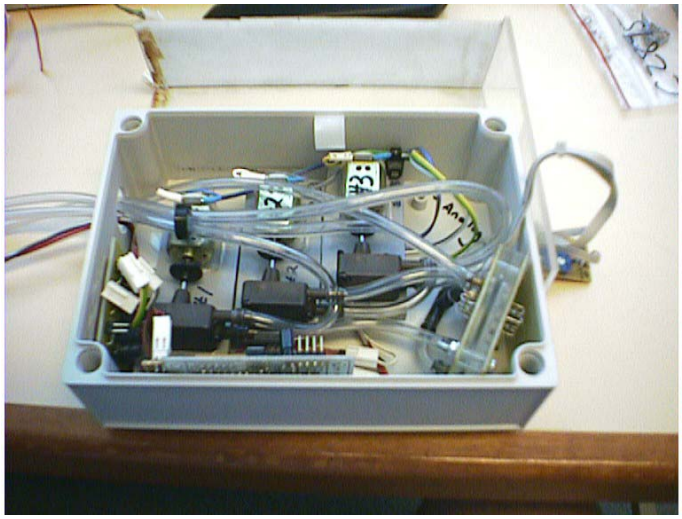

(a) A photograph of the first prototype measurement system developed ('Mk.I').

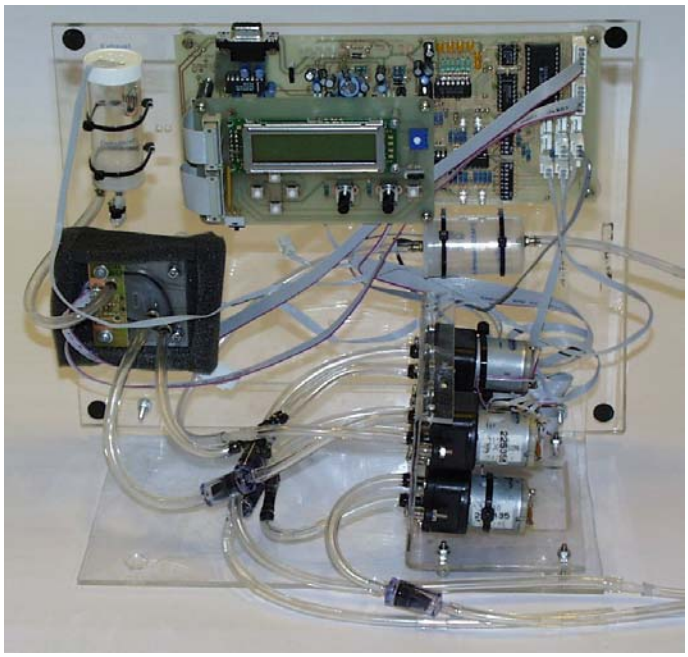

(b) A photograph of the second prototype measurement system developed ('Mk.II').

Figure 1.2: Photographs of the two prototype instrumentation systems developed.

1.4 Dissertation Outline

Following is a brief outline of the subsequent chapters within this dissertation.

Chapter 2 - Carbon Dioxide Measurement Techniques, discusses the relevant fundamental properties of CO_2 and measurable effects which may be used for quantitative measurement. The wide range of potentially useful CO_2 effects and interactions are organised according to the physical transduction involved and how these might be implemented in a measurement system. The chapter presents in detail many of the commonly used techniques for measurement of gaseous CO_2, as well as the current state-of-the-art-sensors and instrumentation systems being used within industry. Selection of the research field which deemed suitable for further exploration is then justified.

Chapter 3 - Concept Establishment, shows how the selected technique (wet chemical analysis) was developed and expanded to form the basis for a measurement system. The chemistry used, preliminary trials showing the usefulness of the technique, and the theoretical basis for the chemical reactions are developed. Basic requirements and design parameters for the instrument based on this technique are listed plus a general analysis of external and internal influences that could potentially affect the instrument's performance.

Chapter 4 - Chemical Containment Cell Design I - Fluid Interactions, presents the design and development of the chemical cells required to contain the chemical indicator used as an indicator for the concentration of CO_2, and the evolution of the cell from its initial form to the final version. Requirements for the design and operation of these cells are developed, and analysis of the cells performance both experimentally and theoretically are presented.

Chapter 5 - Chemical Containment Cell Design II - Turbidity Measurement, presents the fundamental basis of the turbidity measurement, the development of the optics, the method used and the implementation for the turbidity

measurement. Various optical designs and analysis of these are also set out.

Chapter 6 - Fluid Transport & Control, presents the requirement for solution control and transport, and how this was achieved. The components used, their mechanical linkup, and the control mechanisms for these are explained, as well as extra systems devised to overcome some deficiencies in the selected components.

Chapter 7 - System Calibration Model, presents the details of the models used to model the turbidity measurement system from Chapter 5.

Chapter 8 - System Implementation, describes how all the sub-components of the system and software work together to form the final measurement system.

Chapter 9 - Software Development, presets an overview of software developed for this work, from the simulation software to test the system model, to the PC controlling software required to permit smart sensor functions and to control the subcomponents from Chapters 3, 4, and 6. (Listings of code are provided on the CDROM accompanying the dissertation.)

Chapter 10 - System Performance, indicates the performance of both the Mk.I and Mk.II systems with respect to other existing sensing systems. Experimental results are analysed and the quality of the carbon dioxide measurements is deduced.

Chapter 11 - Discussion, reviews the successes and limitations of the Mk.I and Mk.II measurement systems respectively. This leads to the design for a future 'Mk.III' prototype both conceptually and with some specific detail.

Chapter 12 - Conclusion, briefly reviews achievements of the research undertaken with respect to the aims and objectives (Section 1.3).

Appendices are included to aid future work, as follows:

Appendix A - Electrical & Mechanical Design Information, presents details of all relevant hardware systems developed including electronic schematics, printed

circuit board designs, cell mechanical drawings, and specifications for some of the specialist components used.

Appendix B - Modelling of the Time-to-Threshold Calibration Data, presents the specific details of the Mk.I and Mk.II measurement instrument calibration models, previously shown in Chapter 7.

Appendix C - Software Listings, lists all software code developed. Because of the large amount of code produced during this work, source listings could not be included in this printed document however are available on the supplied CDROM.

Appendix D - CO_2 Properties & Measurable Effects, lists many of the fundamental physical, chemical and electromagnetic properties of CO_2 as well as work performed examining the electrochemical properties of $Ca(OH)_2$.

Appendix E - Alternative Cell and Fluid Management Designs, discusses additional cell designs conceived during this work. Also presented are alternative cells, pumps and valves designed to overcome some of the difficulties experienced with the instrumentation prototype mechatronics.

Appendix F - Gas Laboratory, presents the experimental gas laboratory configured as part of this work to permit in testing of the prototypes. This comprises a metering system to combine carbon dioxide and nitrogen gas in accurately known proportions for both calibration and evaluation of the instruments developed. Specifications on the components used, calibration requirements and operational procedures are included.

Appendix G - CDROM Contents, lists the contents of the supplied CDROM which contains all applications, software listings, analysis scripts, hardware and mechanical drawings, plus extra documentation.

1.5 Summary of Original Work

The original work presented in this dissertation consists of the development of generic miniature chemical instrumentation cells coupled to mechatronic control systems, to form an instrumentation system for a gaseous molecule (CO_2); and the analysis of these component's performance using the 'limewater reaction' for the measurement of CO_2 concentration.

Specifically the original contributions reported in this dissertation are:

1. The development of generic miniature chemical reaction cells suitable for use in observation of chemical reactions.
2. Empirical and preliminary theoretical analysis of the fluid dynamics within the developed miniature chemical reaction cells.
3. An investigation into the use of wet chemical analysis for absolute measurement of gaseous CO_2.
4. The development modelling structures and theoretical analysis of the performance of the model used to derive CO_2 concentration information from turbidity measurements.
5. The development of a hardware platforms consisting of microcontroller and mechatronics suitable for the testing of wet chemical based gas instrumentation.
6. The development of low level firmware to create the functionality of the hardware platforms.
7. Implementation and testing of miniature cell control and fluid/gas transport systems suitable for mechatronic sensor design.
8. The development of software to simulate the above models and to perform smart sensor control functions.

Analysis of the fluidic performance of the chemical reaction cells was performed in collaboration with Prof Thanh Tran-Cong (Faculty of Engineering & Surveying, University of Southern Queensland).

1.6 Publications

Publications as at March, 2002:

- A. Maxwell, N. Hancock & J. Billingsley (1997), "Carbon Dioxide Sensing - A Mechatronic Approach," *Proceedings Mechatronics and Machine Vision in Practice 1997,* Toowoomba, Australia, 23–25 September 1997, pp 79–83.
- A. Maxwell & , N. Hancock (2000), "Automated carbon dioxide measurement via miniaturised chemical reaction chambers," presented at International Meeting on Chemical Sensors (IMCS) 2000, Basel, Switzerland, July 2000 (Abstract Book, p490).
- A. Maxwell, N. Hancock & T. Tran-Cong (2000), "Automated carbon dioxide measurement via miniaturised chemical reaction chambers under mechatronic control," presented at *Proceedings Mechatronics and Machine Vision in Practice,* Hervey Bay, Australia, September 2000; and subsequently published in Billingsley, J. (2000), "Mechatronics and Machine Vision", pp 135–142.

In preparation:

- A. Maxwell, N. Hancock, "Automated carbon dioxide measurement via miniaturised chemical reaction chambers," to be submitted to Sensors and Actuators B – Chemical.
- A. Maxwell, N. Hancock, "Low-cost gas measurement using mechatronic techniques," to be submitted to IEEE Sensors Journal.

Chapter 2

Carbon Dioxide Measurement Techniques

2.1 Introduction

This chapter sets out a review of potential techniques for carbon dioxide measurement developed from the perspective of measurement theory. It reviews these techniques ordered by the energy type used for the transduction. The objective is to reveal alternative sensing options, and potentially those suitable for realisation at low cost. Selection of the method to further explore is also presented.

2.2 Measurement Transduction

Presently the concentration of gaseous CO_2 cannot be measured directly in a convenient electrical form suitable for further processing, therefore one or more transduction stages are required. Carbon dioxide has the capacity for chemical reaction, and also responds to energy supplied in various form, such as infra-red electromagnetic radiation. A comprehensive review of these physical and chemical interactions is therefore required.

2.2.1 Theory of Measurement Transduction

A useful symbolic representation of a general measurement transducer is shown in Figure 2.1, where an energy input is modulated by the measurand to produce a final modulated output signal (e.g. Sydenham et al., 1993, p186). The energy input and the modulated output are the same type of energy and the energy types are usually classified as mechanical, thermal, electrical, magnetic, radiant, and chemical (Grandke & Ko, 1989; Stein, 1991).

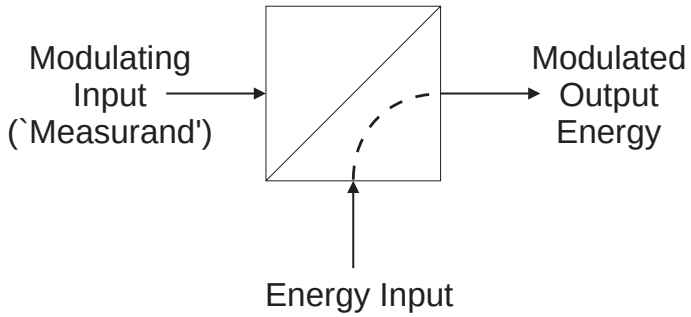

Figure 2.1: The generic representation for a general measurement transducer.

To present a review of possible transductions, a means of organisation was established. The method used here is via the energy input type, i.e. the energy signal to be modulated by the measurand, carbon dioxide. For any given measurand, other possible methods of classification exist such as a simple catalog (e.g. Doebelin, 1990), physical effect, technology material, accuracy, cost, and area of application.

Representation may also take the form shown in Figure 2.2, however this table does not directly reveal differences in energy types between the modulating input, the energy input and modulated output. (In this illustration the modulating input is termed the primary signal, and the energy input and modulated output are termed the secondary signal.)

A useful general representation is the "Sensor Effect Cube" which establishes a general transduction space as shown in Figure 2.3 (Stein, 1991; Van Duyn & Middelhoek, 1991).

Primary Signal \ Secondary Signal	Mechanical	Thermal	Electrical	Magnetic	Radiant	Chemical
Mechanical	(Fluid) Mechanical and Acoustic Effects: eg, Diaphragm, Gravity Balance, Echo Sounder	Friction Effects (eg, Friction Calorimeter) Coolings Effects (eg, Thermal Flow Meters)	Piezoelectricity Piezoresistivity Resistive, Capacitive, and Inductive Effects	Magnetomechanical Effects: eg, Piezomagnetic Effect	Photoelastic Systems (Stress-induced Birefringence) Interferometers Sagnac Effect Doppler Effect	
Thermal	Thermal Expansion (Bimetalic Strip, Liquid-in-Glass and Gas Thermometers, Resonant Frequency) Radiometer Effect (Light Mill)		Seebeck Effect Thermoresistance Pyroelectricity Thermal (Johnsen) Noise		Thermooptical Effects (eg, in Liquid Crystals) Radiant Emission	Reaction Activation eg, Thermal Dissociation
Electrical	Electrokinetic and Electromechanical Effects: eg, Piezoelectricity Electrometer Ampere's Law	Joule (Resistive) Heating Peltier Effect	Charge Collectors Langmuir Probe	Biot-Savart's Law	Electrooptical Effects: eg, Kerr Effect Pockels Effect Electroluminescence	Electrolysis Electromigration
Magnetic	Magnetomechanical Effects: eg, Magnetostriction Magnetometer	Thermomagnetic Effects: eg, Righi-Leduc Effect Galvanomagnetic Effects eg, Ettingshausen Effect	Thermomagnetic Effects: eg, Ettingshausen-Nernst Effect Galvanomagnetic Effects: eg, Hall Effect, Magnetoresistance		Magnetooptical Effects: eg, Faraday Effect Cotton-Mouton Effect	
Radiant	Radiation Pressure	Bolometer Thermopile	Photoelectric Effects: eg, Photovoltaic Effect Photoconductive Effect		Photorefractive Effects Optical Bistability	Photosynthesis, -dissociation
Chemical	Hygrometer Electrodeposition Cell Photoacoustic Effect	Calorimeter Thermal Conductivity Cell	Potentiometry, Conductimetry, Amperometry Flame Ionization Volta Effect Gas Sensitive Field Effect	Nuclear Magnetic Resonance	(Emission and Absorption) Spectroscopy Chemiluminescence	

Figure 2.2: Physical and chemical transduction principles potentially useful in measurement systems (reproduced from Grandke & Ko, 1989, Table 1-2).

Any input, modulation, output transduction can hence be described by a 'cell' in the 3D space, as illustrated. Not all cells are 'occupied': some effects and transductions are not possible either due to incompatible effects, or limitations in current technology. McGhee et al. (1998) have added a fourth dimension to the cube to represent contamination or noise effects of the desired measurement information. However, this extension was not used in the sensor concept development because of the extra complexity involved. Considerations about the external influences were made as shown in Section 3.6.

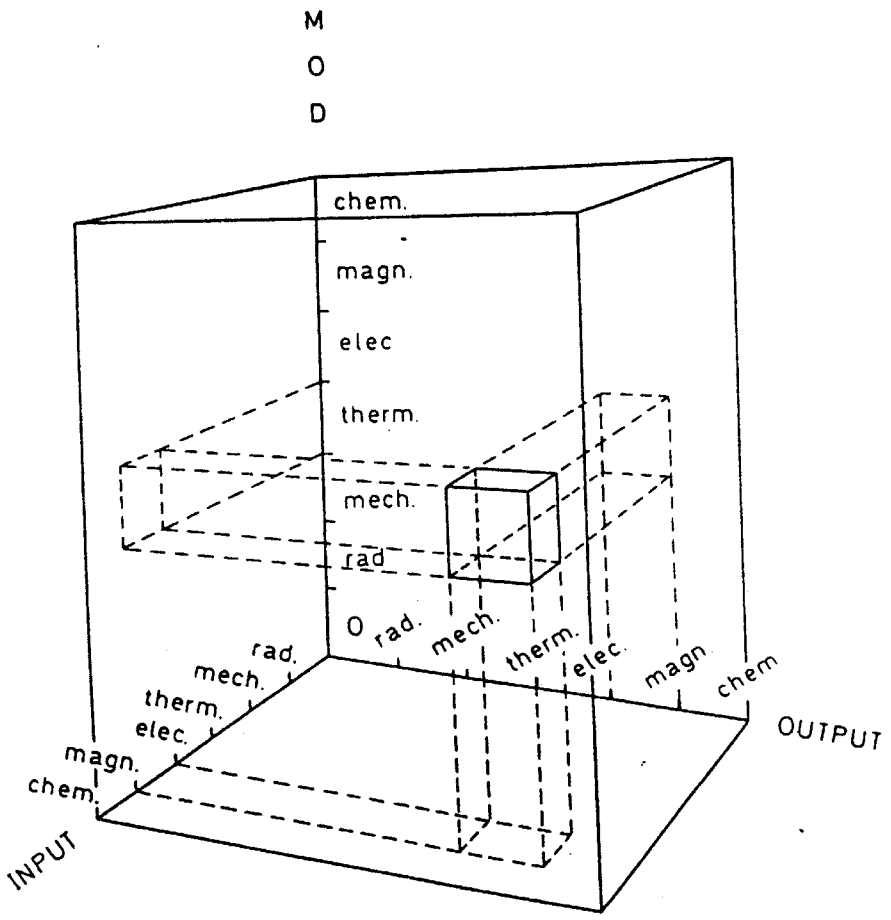

Figure 2.3: An example of physical and chemical transduction principles based on the sensor effect cube (reproduced from Van Duyn & Middelhoek, 1991).

2.2.2 Multiple Stage Transductions

Due to the modular nature of the transduction concept, it is possible to join several transductions together to form a final instrument where the output from each transduction becomes the input for the immediately following stage as shown in Figure 2.4.

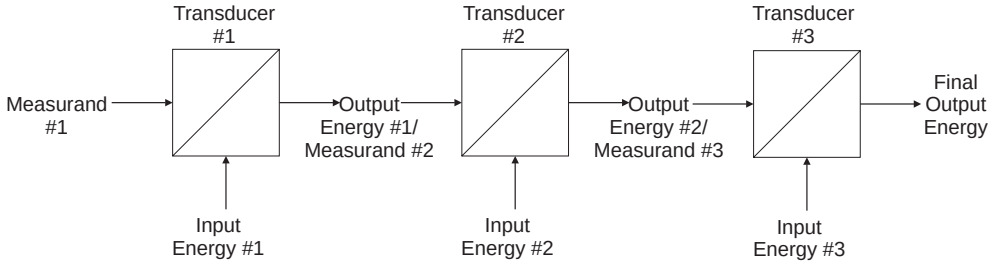

Figure 2.4: An example of a multi-stage transducer.

Typically most sensor designs use this approach, which poses several limitations on the method chosen to appropriately order a review of measurement techniques. Almost all of the methods used to detect CO_2 are multistage such that many variations of the same method are possible. A choice has to be made as to which transduction stage would be used for the ordering, if not the overall composite transduction.

If the overall composite transduction is considered, this does not allow sufficient description of the technology being used. For example, as most sensors typically have an electrical output, almost all sensors for sensing CO_2 would have a chemical measurand, and electrical input and output energies. Likewise, if individual stages of the transduction flow are considered, a decision as to which one needs to be made.

Of all the possible methods (presented in the following sections), two distinct groups were identified being:

- "physical effect" transductions, where an immediately observable effect was able to be measured without further transduction (single stage transductions); and
- "reactive" transductions, where an initial chemical transduction was required to

form a chemical indicator for a further transduction to a more easily measurable effect (multi-stage transductions).

Specifically, the "physical effect" transductions comprised those of the "radiative" energy regime with all other measurable effects being of a "reactive" nature. Should the methods be ordered by this type, most of the effects would be classified as "chemical" transductions, and not allow sufficient scope to present the methodologies. Therefore the following categorisation will present the transduction effects ignoring the initial chemical transduction for all "reactive" transductions, and organising by the immediately next transduction in the energy signal flow.

Also many of these measurable effects can exist under multiple categories due to variations in the later transduction stages, and final output energies used for the particular sensor types. Where this occurs, a note to their additional categorisation is made.

2.2.3 Notation

In the sections following, the notation:

$$CO_2 \rightarrow \Delta(quantity) \tag{2.1}$$

is used to summarise the technique with the meaning:

"gaseous CO_2 causes a change in the quantity indicated"

Shown in Section 2.3 through to Section 2.10 is a description of available measurement techniques for CO_2 organised by the input energy type.

2.3 Mechanical Transductions

Mechanical transduction of CO_2 has the general form illustrated in Figure 2.5 where an initial chemical transduction is required.

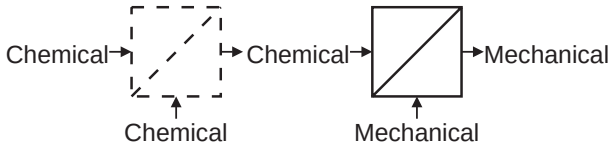

Figure 2.5: Energy flow representation of the potential mechanical transduction of CO_2.

The forms of mechanical energy producing useful transductions effects are:

- acoustic (i.e. vibrational); and
- potential energy (as sensed in a mechanical balance, resulting in a mass measurement).

These two forms are considered respectively in Section 2.3.1 and 2.3.2 following.

2.3.1 Surface Acoustic Wave Sensors (SAW)

$$CO_2 \rightarrow \Delta(vibration) \tag{2.2}$$

These devices utilise acoustic waves travelling through a substrate coating which absorbs the gas species of interest. With this absorption, the mass of the substrate changes, therefore affecting the velocity that the wave travels through the substrate. When placed into an oscillating circuit these devices can vary the oscillation frequency which is functionally related to the gas concentration being measured. Common SAW configurations include interdigital (White & Turner, 1997), delay line and bulk quartz resonators (Langdon, 1987), the last of which are most common in chemical sensing applications. These sensors are capable of being used under low current consumption

conditions ideal for remote sensing applications, and can be easily coupled with sensing and signal conditioning electronics. They can however suffer from low gas selectivity (Nylander, 1987), and temperature/humidity stability problems. This technique has been commonly used for other gases such as hydrogen (Langdon, 1987), hydrogen sulphide and NO_2 (Moseley, 1997, p235), explosive volatiles (Kress-Rogers, 1993, p652), and have also been shown to be useful for CO_2 measurement (e.g. Li & Thompson, 1994; Lueptow & Phillips, 1994; Block et al., 1992).

2.3.2 Chemical Absorption

$$CO_2 \rightarrow \Delta(mass) \tag{2.3}$$

This method relies on the chemical absorption of CO_2 by compounds which then affects the dry weight of the material. Simple weight measurement methods can be used to determine the mass of CO_2 absorbed and hence the concentration. Compounds such as solid soda lime (sodium hydroxide and calcium hydroxide), and barium hydroxide exhibit this characteristic (e.g. Ayres, 1968, p208). In each case the indicating compound is fully reacted requiring fresh materials for each chemical measurement.

2.4 Thermal Transduction

Thermal transduction of CO_2 has the general form illustrated in Figure 2.6 where an initial chemical transduction is required.

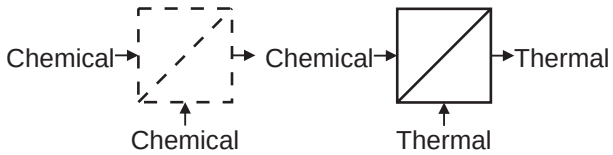

Figure 2.6: Energy flow representation of the potential thermal transduction of CO_2.

The primary form of thermal energy producing useful transductions effects are catalytic

gas sensors, and is considered in Section 2.4.1 following.

2.4.1 Thermal Conductivity - Catalytic Gas Sensors

$$CO_2 \rightarrow \Delta(temperature) \tag{2.4}$$

This method exposes the gas to a heated catalyst (heated usually by the platinum wire used for sensing - below) which produces a temperature increase. This temperature change is then measured either through temperature sensors or by conductive means through a (usually) thin platinum wire. As such this method could also be further transduced by an electrical transduction. This method is usually used for explosive or flammable gases such as methane (Debéda et al., 1997), and hydrogen (Moseley, 1997, p235), and is typically used for carbon monoxide (Bartolomeo, 1995). The useful detection resolution is typically in the hundreds of PPM[1]. (Harrous et al., 1994*a*; Harrous et al., 1994*b*). This effect is sometimes catogorised using the 'electrical-conductive' energy regime (Section 2.5.2) where the conductivity or resistivity of the sensing wire is measured.

2.5 Electrical Transduction

Electrical transduction of CO_2 has the general form illustrated in Figure 2.7 where an initial chemical transduction is required.

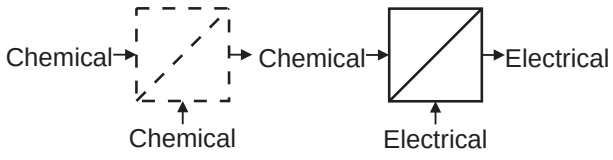

Figure 2.7: Energy flow representation of the potential electrical transduction of CO_2.

The forms of electrical energy producing useful transductions effects are:

[1]Parts Per Million

- electrochemical (i.e. producing a voltage potential);
- impedance (i.e. varying conductivity, resistance, or capacitance); and
- Chemical Field Effect Transistors (i.e. based on semiconductor effects).

These forms are considered respectively in Section 2.5.1, 2.5.2 and 2.5.3 following.

2.5.1 Electrochemical Gas Sensors

$$CO_2 \rightarrow \Delta(\textit{voltage or current potential}) \tag{2.5}$$

Electrochemical gas sensors, (also known as potentiometric), as the name suggests use a chemical cell capable of producing a voltage or current potential related to the concentration of the gas species being measured. The effect usually uses an aqueous reaction cell which is electrochemically receptive to the gas species being measured. A voltage potential is then created with respect to this measurement cell and a reference cell, with the resultant voltage being a function of the gas species concentration. Typically these type of sensors are considered ion-selective electrodes. Aqueous electrochemical cells for CO_2 have also been presented (Moseley, 1997, p224) (Tsionsky & Lev, 1995) using the above principle with the most well known being the Severinghaus CO_2 electrode (Severinghaus & Bradley, 1958).

A variation of the strictly aqueous electrochemical cell is the solid electrolyte gas sensor. Solid electrolyte gas sensors are a solid packaged form of the aqueous electrochemical cells shown above and are typically used in the automotive industry for monitoring of emission levels. Numerous gases are able to be detected using these sensors including CO_2 (Moseley, 1997, p227). Another variation uses an immobilised NASICON ('N_a superionic conductor' constructed from $Na_3Zr_2Si_2PO_{12}$(Son et al., 2001)) layer which was also suitable for CO_2 sensing (White & Turner, 1997, p17).

There are numerous subtypes usually categorised by the type of metal used for the

element, and also whether they are based on solid electrolytes, catalytic combustion or semiconducting oxides. However all are generally functionally equivalent. There are also different types of substrate used including thin films (Debéda et al., 1997). At the time of writing many of these devices suffered from a broad sensitivity therefore requiring careful configuration to achieve CO_2 only sensing. Applications suitable for CO_2 measurement have been demonstrated (Ishihara et al., 1991; Tsionsky & Lev, 1995; Ishiji et al., 1993; Miura et al., 1992; Patel et al., 1994), and differential potentiometric sensors (Meyerhoff et al., 1988).

Amperometric measurement is a variation of the electrochemical method (Section 2.5.1) where instead of a voltage potential, a current is produced. Amperometric CO_2 instrumentation has been demonstrated by Ishiji et al. (1993).

2.5.2 Impedance Gas Sensors

$$CO_2 \rightarrow \Delta(conductivity, resistivity, capacitance) \tag{2.6}$$

Impedance gas sensors presented in this subsection behave much like as gas sensitive resistors. There are many variations of this method that measure a change in the conductivity, resistivity or capacitance of some electrical or electronic component chemically altered to be receptive to the gas species of interest.

The most common type of sensor is (as previously discussed in Section 2.4.1) catalytic type sensors. Instead of a direct temperature being measured, the resistance or conductance of a platinum wire is measured.

Another impedance based method is the use of semiconducting oxide gas sensors where the sensing element is usually comprised of a metal oxide material mounted into a heating surface. Reactions with gases vary the electrical properties of a semiconducting element. At high temperatures (hundreds of degrees) this reaction is reversible, hence the use of the heating mechanism. These changes can then be measured using simple

electrical techniques (Nylander, 1987, p134). However these sensors have a very broad response and are affected by many other gas species (Kress-Rogers, 1993, p615).

There is also a variation of this method that utilises Metal Oxide Semiconductor (MOS) transistors. These devices act like capacitors, and any external influences (caused by the chemical modulation) that affect the conductance between the source and drain terminals can be measured and an effective sensor constructed. These devices are primarily used for the detection of hydrogen and ammonia (Moseley, 1997, p234), however examples have also been reported for carbon monoxide (Bartolomeo, 1995), nitrous oxide (White & Turner, 1997, p15), methane (Debéda et al., 1997) as well as for carbon dioxide (Moseley, 1997, p226).

Open capacitive type sensors have also been developed. These use special combinations of metals to detect small chances in the permittivity of the space enclosed within the capacitor, and trials have shown that CO_2 can be measured by these sensors using $BaTiO_2$ oxides (Ishihara et al., 1991).

2.5.3 Chemical Field Effect Transistors (ChemFETs)

$$CO_2 \rightarrow \Delta(current\ flow) \tag{2.7}$$

ChemFETS are devices very similar to metal oxide semiconductors shown above. In the MOSFET, a small current flows through the semiconductor surface from the source to the drain. A thin oxide layer is deposited into the surface and serves as the gate electrode. An electrical potential applied to the gate electrode generates a charge carrier inversion layer which carries the current to control the current flow through the rest of the FET. By using different electrochemically sensitive chemicals sensors for various ions can be produced. CO_2 gas sensors have been demonstrated utilising this principle (Nylander, 1987, p139).

2.6 Magnetic Transduction

Magnetic transduction of CO_2 has the general form illustrated in Figure 2.8.

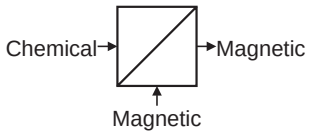

Figure 2.8: Energy flow representation of the potential magnetic transduction of CO_2.

$$CO_2 \rightarrow \Delta(magnetic) \tag{2.8}$$

As CO_2 is not a polar molecule (Table D.1), it exhibits no response to magnetic fields. Direct magnetic effects (such as paramagnetic sensors, sometimes used for oxygen) cannot be used. Naturally however, an extra transduction stage could be added (Figure 2.9) so that magnetic modulation could be used.

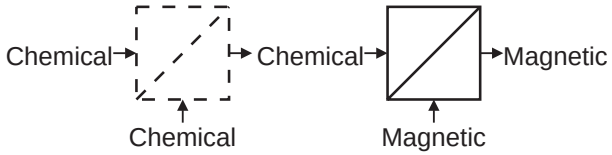

Figure 2.9: Energy flow representation of the potential chemical and then magnetic transduction of CO_2.

2.7 Chemical Transduction

Chemical transduction of CO_2 has the general form illustrated in Figure 2.10.

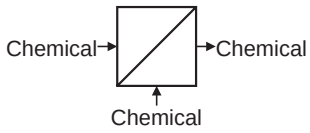

Figure 2.10: Energy flow representation of the potential chemical transduction of CO_2.

$$CO_2 \rightarrow \Delta(detectable\ chemical) \tag{2.9}$$

Because chemical transduction results in a chemical output, this transduction is very common. As a result, this transduction is typically used as an indicator of CO_2 concentration. A problem however exists in that further transduction is usually required to yield a more suitable effect for logging or further processing. For this reason, this transduction appears as the initial transduction stage in most of the methods presented in this chapter, with the exceptions involving measurement of direct physical properties of CO_2 (Section 2.9).

2.8 Biological Transductions

Biological transduction of CO_2 has the general form illustrated in Figure 2.11.

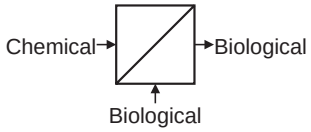

Figure 2.11: Energy flow representation of the potential biological transduction of CO_2.

2.8.1 Microbial Carbon Dioxide Sensor

$$CO_2 \rightarrow \Delta(chemical\ production) \tag{2.10}$$

Microbial sensors suitable for CO_2 measurement have also been demonstrated. These sensors use groups of bacteria, responsive to the concentration of CO_2 being presented to them, and vary either a chemical, or optical property of themselves or their immediate surroundings.

One such sensor uses a particular bacteria (S-17) which could only grow with carbonate

as the carbon source. These cells were firstly immobilised and placed onto a gas permeable membrane on an oxygen sensor forming a gel (By using 5% $CaCl_2$ solution). CO_2 was supplied through the acidification of HCO_3 and the resultant $NaHCO_3$ concentration could be related to the CO_2 concentrations (Karube, 1992, p1734). Obviously, further transduction of this chemical product would then be required to achieve an more easily analysed signal.

Enzyme electrodes (Janata et al., 1998) and organic semiconductors (Nylander, 1987) are also used.

2.9 Radiant Transduction

Radiant energy transduction of CO_2 has the general form illustrated in Figure 2.12. For this transduction method, no initial chemical transduction is required.

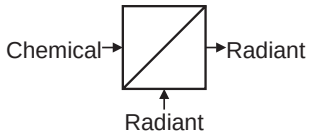

Figure 2.12: Energy flow representation of the potential radiative transduction of CO_2.

In these sensing systems the radiant energy is electromagnetic with wavelengths in the visible and infra-red regions. Radiant mechanical energy, e.g. ultrasonic energy, would be classified as 'mechanical', Section 2.3.

2.9.1 Infra-Red Gas Analysers (I.R.G.A)

$$CO_2 \rightarrow \Delta(radiant\ absorption) \tag{2.11}$$

This is a non destructive technique (i.e. the gas under test is not absorbed or involved in any chemical reaction) which relies on absorption of radiation at specific wavelengths by the gas molecules being measured. Absorption of radiation follows

the Beer-Lambert Law (Watts (1983, p1176), for example) and for CO_2 occurs principally at a wavelength of 4.3μm (Robinson, 1980, p61) noting that the absorption spectra of CO_2 has several other strong absorption bands from 4 to 4.3μm (Conn & Avery, 1960, p171)(Straughan, 1976, p184). This absorption occurs as a result of the fundamental vibration modes of the molecule, namely symmetrical, asymmetrical, and scissoring/bending (Pinchas & Laulicht, 1971, p16)(Silverstein et al., 1974, p75). This is by far the most common method of CO_2 measurement for atmospheric gas (Dillig, 1994; Helenelund, 1996; Weldon et al., 1993; Uehara, 1991). Significant interference effects are present with this method primarily caused by the high extinction coefficient of water over a majority of the infra-red spectrum region.

Two major subtypes exist depending on the detector type. Thermal detectors (e.g. thermopiles) sense a rise in temperature due to the absorption of photons (radiation), whilst 'quantum sensors' (e.g. photovoltaic cells, photodiodes) convert the photon directly into a change in electrical properties of the detector. Pressure measurements can also be used where variations in absorption vary the temperature in each cell and pressure differences between the two are transduced (Butler, 1979, p175).

Sub systems also exist such as Raman Spectrometers (Watts, 1983, p1186)(Fredericks, 1995) and through the use of acoustic-optic tunable filters (AOTF) devices (Lewis et al., 1993; Heuber et al., 1995; Jackel et al., 1995; Glenar et al., 1994; Tran & Lu, 1995)(Benson, 1993, p130) smaller and more flexible systems can be constructed.

Variations of this technique also exist which may be grouped as follows.

Fingerprint Identification. Each gas which can be measured by these techniques have their own distinctive adsorption characteristic: these characteristics are known as 'finger prints'.

Correlation Spectroscopy. By using two samples of gas measured alternately, one sample as a reference of non-absorbing gas and the other as the measurement sample), the difference in absorption can be determined through the use of mod-

ulation techniques.

High resolution spectral measurements. Through the use of dispersed optical systems, multiple optical frequencies can be scanned in one pass. This also gives the ability to determine the fingerprint of the gas.

The use of interferometric techniques constitutes a further variation of these methods. As with previous infrared spectroscopy techniques, the direct measurement is the amount of optical attenuation over a fixed path length. While this is inherently simple, it does pose a problem with small concentrations as the detector must be extremely sensitive, and therefore expensive. In order to avoid the use of expensive optical detectors the opposite can be done, namely the path length is adjusted until the same 'threshold' attenuation value is observed. In this case, the detector only has to be calibrated for a single attenuation value. By this means greater precision can be achieved for lower concentration gases, as the path length will be the greatest before the preset level of optical attenuation is achieved.

A further modification of this technique is the use of mirrors to achieve multiple path lengths within a small space. Thus in addition to the movable detector, the light path can be modified in multiples of two times the gas chamber length. Control of the mirrors would be via a servo or stepper motor system, or could be modified manually depending on the range of measurements required. This has been shown as a useful principle (Bhatia et al., 1996) but its specific application for measurement of CO_2 has not been confirmed.

This technique could also encompass the use of evanescent wave sensors (Section 2.9.2 following).

2.9.2 Evanescent Wave Sensors

$$CO_2 \rightarrow \Delta(radiant\ absorption) \tag{2.12}$$

These types of devices rely on the use of the evanescent wave energy associated with the outer portion of a 'D' shaped optic fibre (Pride, 1993; Future Fibre Technologies, 2001). This optical energy field exists outside of the cladding of the optic fibre. By placing this type of optical fibre into the measurement environment, the resulting attenuation of the optical signal can be measured (using spectrometric methods, Section 2.9.1), with the optical energy attenuation being proportional to the concentration of the gas being measured.

The optical excitation usually is provided from a LED or similar device having a similar wavelength to that of the maxima absorption of the gas to be measured. By pulsing the light source, and using a rapid sense detector, synchronous detection can be used to lower the noise and artefact readings. Some sensors utilise optic fibres completely stripped of cladding to increase the potential for the light radiation to escape into the measurement medium, thereby increasing the attenuation per unit gas that would otherwise be measured with the above 'D' type cable. Due to the use of spectrometry methods, this method is also capable of CO_2 measurement.

2.10 Modified Radiant Transductions

Modified radiant transduction of CO_2 has the general form illustrated in Figure 2.13. These transductions differ from the previous radiative methods (Section 2.9) in that an initial chemical transduction is used.

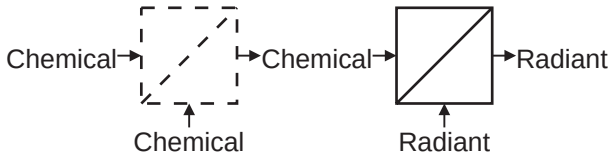

Figure 2.13: Energy flow representation of the potential modified radiative transduction of CO_2.

These sensing techniques may be grouped under four headings, as follows.

2.10.1 Colorimetric Gas Sensors

$$CO_2 \rightarrow \Delta(colour\ intensity) \tag{2.13}$$

This process involves the mixing of the gas to be measured with a chemical reagent/dye which results in a colour change/shift of the chemicals. This colour change can be measured and compared to a standard. Typically the chemical reagent is immobilised in a thin film or similar structure with the variation in colour intensity being detected via inexpensive LED and photodiode optoelectronics. Many have shown the usefulness of colorimetric analysis for CO_2 measurement (Hauser & Liang, 1997; Mills et al., 1992; Mills & Monaf, 1996; McMurray, 1992; Uttamial & Walt, 1995; Weigl & Wolfbeis, 1994; Weigl et al., 1994).

Variations of this method are also available that use 'bulk' chemical reactions, such as Potassium Hydroxide solution (which froths up in the presence of CO_2), barium hydroxide (which can be titrated to methyl orange), and calcium hydroxide (which produces a white precipitate in the presence of CO_2 (Durrant, 1964, p406)(Macbeth, 1945, p10). Ayres (1968, p208) provides an overview of bulk colorimetric techniques.

2.10.2 Fluorescence Gas Sensors

$$CO_2 \rightarrow \Delta(colour) \tag{2.14}$$

This technique is similar to the colorimetric method except that the dye used generates its own radiative energy at a different wavelength to that of the excitation wavelength. Often measurements are made over a range of wavelengths to generate excitation spectra which vary depending on the sample gas concentration.

This method has also been shown useful for CO_2 instrumentation (Choi & Hawkings, 1995*a*; Choi & Hawkings, 1995*b*; He & Rechnitz, 1995; Mills & Chang, 1993; Wolfbeis & Weis, 1988).

2.10.3 Microwave Analysis

$$CO_2 \rightarrow \Delta(absorbed\ microwave\ spectrum) \tag{2.15}$$

These types of sensors measure energy absorbance in the microwave region of the electromagnetic spectrum instead of the visible and infra red region as shown above and typically use large and complex microwave spectrometers as the core of their instrumentation. These types of sensors have been shown to be useful for CO_2 detection after a change to form a labelled ^{17}OCO and ^{18}OCO isotope (Gripp et al., 1995), when ethylene oxide is perturbed by CO_2 (Johri & Pathak, 1989), and for CO_2–H_2O solutions (Peterson et al., 1994).

2.10.4 Surface Plasmon Resonance (SPR)

$$CO_2 \rightarrow \Delta(refractive\ index) \tag{2.16}$$

A surface plasmon resonance (SPR) device detects minute variations in the refractive index of a sensing surface (Kress-Rogers, 1993, p647). This technique uses a sensing film coated with a chemical receptor. Variations in the absorption of this receptor vary the refractive index of the sensing surface. This variation is then measured optically with variations in the refractive index being proportional to variations in the chemical absorber. Typically, moving prisms have been used to 'scan' for the refractive angle however solid-state methods such as fixed prisms with CCD cameras (Frutos, 1998) as well as Acoustically Optically Tuneable Filter (AOTF) devices (Jory et al., 1995). AOTF devices are solid state radio-frequency tuneable devices used to isolate specific wavelengths of light (Heuber et al., 1995; Glenar et al., 1994) and use acoustic waves generated by piezo transducers to affect the polarisation of a light beam based on the frequency of the transducers (Jackel et al., 1995; Tran & Lu, 1995). SPR devices have been shown useful for 100ppm detection of NO_2 (Jory et al., 1995).

2.11 Conclusion - Transductions Chosen

In the great majority of CO_2 measurement/transduction options reputed in the literature (as reviewed above) either high precision components or exotic chemicals were required, resulting in potentially expensive measurement systems. This placed these alternatives outside the aim of the research, namely to investigate low-cost (possibly disposable) CO_2 measurement systems.

Therefore the chosen transduction to investigate further was a method based on the colorimetric analysis method (Section 2.10.1). Instead of using thin films, a larger "bulk" method would be tested but at as small a scale as practically feasible. This offered scope for the use of readily available low-cost components both for fluid handling and the optical measurement of chemical precipitates created in an aqueous solution.

As previously shown, the universal symbolic form of a transducer is that of Figure 2.1. The overall transduction for the chosen colorimetric CO_2 instrumentation is therefore as shown in Figure 2.14 with a transduction equation of:

$$CO_2 \rightarrow \Delta(electrical) \tag{2.17}$$

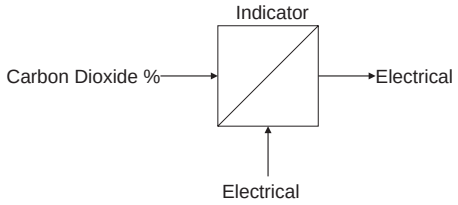

Figure 2.14: The overall form of the transduction necessary for the wet chemical analysis of CO_2.

The input signal will be gaseous CO_2 (as a proportion of the gas stream) with the output being an electrical signal.

More usefully, this overall representation contains three successive transductions as shown in Figure 2.15.

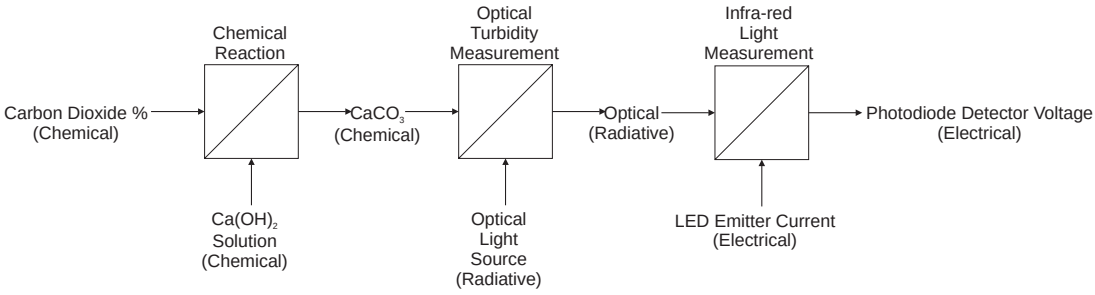

Figure 2.15: Specific transduction necessary for wet chemical analysis of CO_2. As shown, three transduction stages are necessary.

The transduction equation is then:

$$CO_2 \rightarrow \Delta(chemical) \rightarrow \Delta(radiative) \rightarrow \Delta(electrical) \tag{2.18}$$

The incoming CO_2 concentration needs to firstly be transduced with the indicator solution which in turn produces a turbid solution (a white precipitate because $Ca(OH)_2$ is used as the indicator). This turbidity is then detected optically (radiative), which is finally transduced into an electrical signal. The initial chemical transduction is further presented in Chapter 3 with the latter two transductions, radiative and electrical, being presented in Chapter 5.

Chapter 3

Concept Establishment

3.1 Introduction

From the review of possible methods for carbon dioxide gas detection and potential measurement (Chapter 2), one has been chosen as suitable for further exploration. This chapter outlines the selected method, its basic implementation as a measuring instrument, the fundamental theoretical basis for the sensor, and both design and modelling requirements. These latter are further expanded in later chapters.

3.2 Chosen Method

The chosen method involves the use of automated "wet chemistry" and therefore instrumentation to determine the progress of the chemical reactions involved.

3.2.1 Wet Chemical Analysis

"Wet chemical" analysis is the process of combining aqueous reagents with the substance being measured with any resulting change being observed and subsequently analysed.

The basis of the system required the following key components as illustrated in Figure 3.1.

- a reaction vessel ("cell"),
- indicator chemicals (in aqueous solution),
- gas sample,
- gas/indicator solution mixing mechanism,
- chemical change measurement mechanism, and
- cell control mechanism (to permit repetitions).

The indicator and the sample source chemical components are required in order to provide the necessary transduction from the gas sample concentration to an easily measurable mode, in this case the production of a visible precipitate and hence change in the turbidity of the indicator solution. The mixing mechanism is necessary to provide the combination of the chemical reagents. The control system is required to fill, empty and clean the cell in order to maintain the chemical indicator consistency and in-cell conditions throughout the life of the measurement system.

The quality of the measurement system (and repeatability between measurements) is then governed by:

- variations in the molar concentration of the indicator solution;
- sample gas injection flow rate;

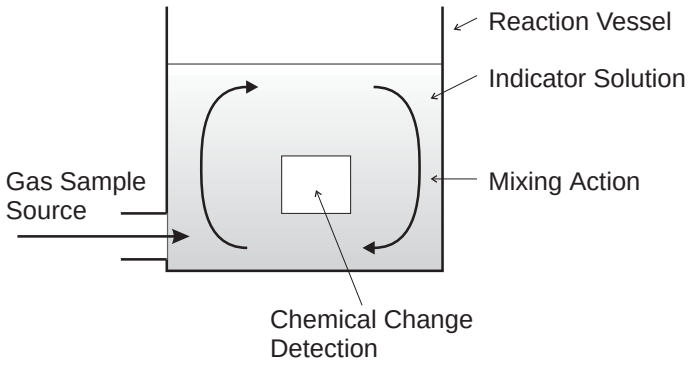

Figure 3.1: Conceptual overview of the components required for "wet chemical" analysis.

- turbidity measurement system performance; and
- cross contamination of the fresh solution from old measurements.

All of these items need to be managed and, where necessary, compensated for by control systems within the overall measurement system.

There are obvious disadvantages to this scheme of sensing. These include the need for chemical solutions, transport of these solutions within the measurement system, and cleaning requirements. However this technique provides great flexibility in the choice and management of the chemical reaction; and permits variations in measurement technique to increase overall measurement system performance ("smart sensing").

It is also possible to miniaturise the whole measurement system. A miniature reaction cell requires correspondingly small values of reagent. Motors, pumps, and the control electronics can also be miniaturised. The total size of the system will then be determined largely by mechanical fabrication limits of these components and the number of replicate measurements required (which determines the total reagent volume). This contrasts with other techniques such as direct IR absorption in which a substantial optical path length is often unavoidable. The potential for miniaturisation opens up further application areas where this measurement system could be applied.

3.2.2 Chosen Chemical Indicator - Basic Chemistry

The chemical indicator chosen was saturated calcium hydroxide solution ($Ca(OH)_2$, "lime water"). This easy-to-handle and non-hazardous solution was prepared by combining solid calcium oxide (CaO) with water (H_2O):

$$CaO_{(s)} + H_2O_{(aq)} \rightleftharpoons Ca(OH)_{2(aq)} \tag{3.1}$$

or by combining solid calcium hydroxide ($Ca(OH)_2$) with water:

$$Ca(OH)_{2(s)} + H_2O_{(aq)} \rightleftharpoons Ca(OH)_{2(aq)} \tag{3.2}$$

Interaction between aqueous $Ca(OH)_2$ and CO_2 yields a white calcium carbonate precipitate ($CaCO_3$) according to the reaction:

$$Ca(OH)_{2(aq)} + CO_{2(g)} \rightleftharpoons CaCO_{3(s)} + H_2O_{(aq)} \tag{3.3}$$

The precipitate produced is finely divided and settles out of suspension only slowly. Hence it is readily detected by optical attenuation measurements of a light path through the cell (subsequent research has revealed that the reaction between $Ca(OH)_2$ and CO_2 is more complicated as shown in Section D.2.1).

3.2.3 Transduction Stages

As set out in Section 2.11, three stages of transduction are required - Figure 2.15. This is reproduced as Figure 3.2 for convenience.

This chapter, in particular the analysis of Section 3.4 following, will deal with the first two transductions, namely chemical reaction and optical turbidity measurement.

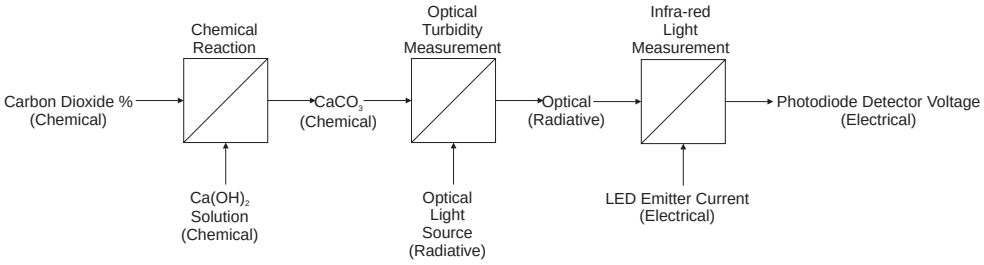

Figure 3.2: Transduction necessary for wet chemical analysis of CO_2 (at each stage the measurement information energy regime is indicated in parenthesis).

3.3 Preliminary Experiments

Several preliminary experiments were conducted to ascertain and verify the useful properties of $Ca(OH)_2$ solution. These tests were designed to determine the usefulness of the optical translucence/turbidity properties of the chosen indicator solution in response to the presence of carbon dioxide.

Two glass test tubes were placed next to each other filled with the calcium hydroxide indicator solution. One tube was reserved as the control tube for objective comparison and the other tube served as the reaction vessel which would have the sample gas injected (Figure 3.3(a)).

This sample gas source was approximately 95% CO_2 supplied by a miniature compressed gas bottle (Figure 3.3(b)) with a custom made gas fitting used to couple the cylinder to the chamber and provide some gas flow control (Figure 3.3(c)).

As the sample gas was bubbled through the reaction vessel the change in properties of the indicator was noted. There were four distinct stages observed as seen in Figure 3.4 and illustrated in Figure 3.5.

These stages were:

1. Precipitate production (Figure 3.4(c));

2. Precipitate production peak (Figure 3.4(d));

3. Precipitate fallout (Figure 3.4(e)); and

4. Precipitate settlement (Figure 3.4(f)).

It was noted; (i) that significant precipitate fallout and settling was only apparent once the solution agitation (bubbling) was removed but (ii) that some precipitate coating was forming on the vertical walls of the test tube in areas of little agitation (Figure 3.4(f)).

It seemed reasonable to assume that the size of the bubbles and the flow rate through the measurement chamber would affect the level of absorbance of the carbon dioxide and hence vary the chemical activity. This was expected because the bubble surface area (for the reaction) was proportional to r^2 (where r is the radius of the bubble) as opposed to the gas volume which is proportional to r^3.

For every carbon dioxide molecule one calcium carbonate molecule will be produced. It was assumed that this was a linear reaction with no saturation or other rate limitations occurring during the generation of precipitate, and from this it was deduced that the level of carbon dioxide directly absorbed would affect the level of precipitation in a manner which is at least approximately linear.

The indicator solution would therefore present a repeatable change from clear and transparent through to very opaque over time for a given continued injection of carbon dioxide gas. This optical change could then be measured by an optical transmitter/receiver pair coupled to the reaction vessel.

Provided that the optical attenuation properties of the precipitate (opacity) remained constant over a wide range of operating conditions, i.e. for differing proportions of carbon dioxide in the gas stream, the measurement technique was considered to be viable.

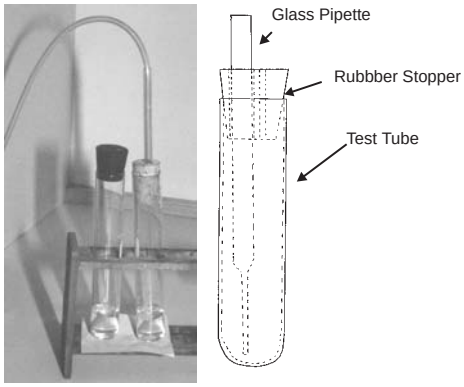

(a) Experimental configuration with the gas sample source seen in (b). A small glass pipette was used to inject the gas stream into the indicator solution.

(b) Miniature gas cylinder used as the approximately 95% CO_2 source.

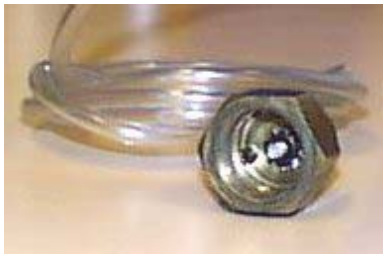

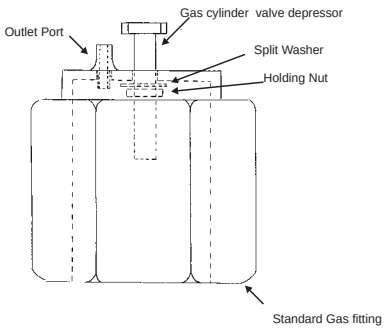

(c) Control Tap and exhaust hose coupling used to couple the gas cylinder to the glass pipette.

Figure 3.3: Experimental configuration for the preliminary $Ca(OH)_2$ experiments.

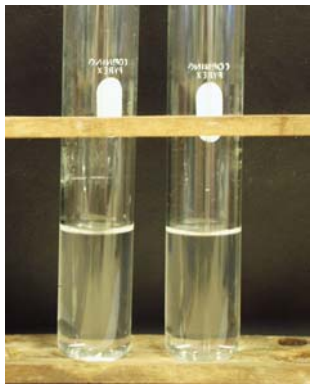

(a) Fresh indicator solution (Approx 1.7 molar). Shown is the reaction chamber (right) and the control tube (left).

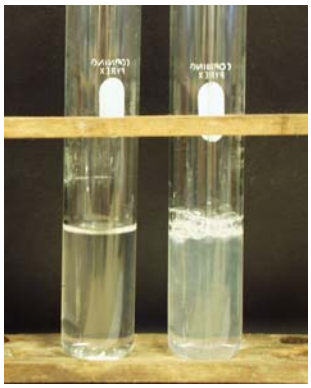

(b) Beginning of the bubbling process. The reaction chamber is starting to show signs of $CaCO_3$ precipitation (after approx 12 seconds).

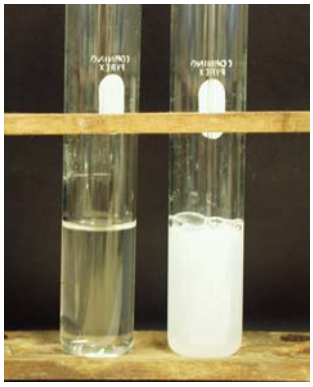

(c) Bubbling process underway. The reaction chamber is continuing to produce $CaCO_3$ precipitation (after approx 20 seconds).

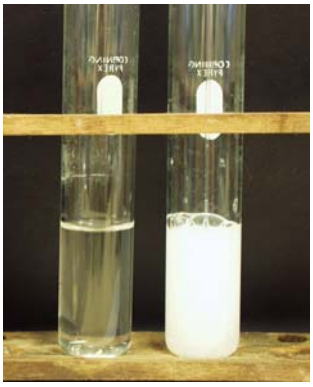

(d) The reaction chamber has reached maximum opacity (after approx 30 seconds), with the $CaCO_3$ remaining in suspension due to the bubble motion.

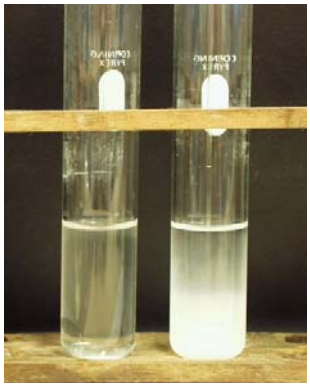

(e) Beginning of the suspension fallout without bubble agitation (after approx 1200 seconds).

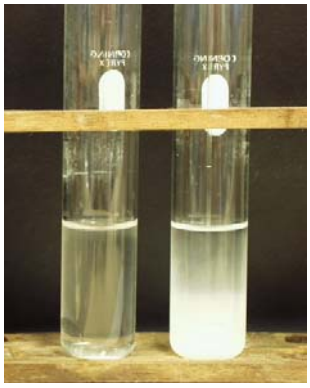

(f) Most of the precipitate has fallen out of suspension without bubble agitation (after approx 2400 seconds).

Figure 3.4: Examples of the effect of carbon dioxide (CO_2) on calcium hydroxide ($Ca(OH)_2$) and the effects of precipitate falling out of suspension.

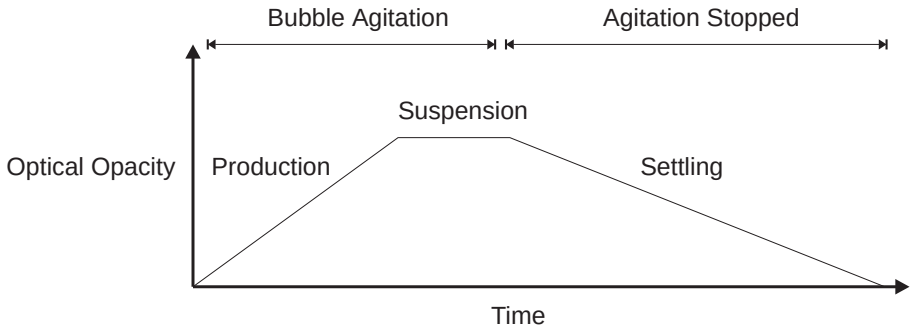

Figure 3.5: Conceptually observed amount of suspended $CaCO_3$ within the test tube assembly (conceptual only).

3.4 Theoretical Basis of the Measurement Method

As previously observed, the fundamental chemical reaction:

$$Ca(OH)_2 + CO_2 \rightleftharpoons CaCO_3 + H_2O \tag{3.4}$$

produced a precipitate ($CaCO_3$). This precipitate had certain observable properties; was white in colour, formed small clumps of coalesced precipitate of typically 0.3mm scale after typically 20 seconds with 100% CO_2. As expected for any precipitate it was denser than the aqueous solution and as such would settle on the bottom of any measurement chamber, as well as coat any surface in the measurement system including vertical surfaces, any optics or other measurement system components.

As indicated in Equation 3.4 this reaction is reversible under certain conditions however for this work this reaction may be considered irreversible, i.e:

$$Ca(OH)_2 + CO_2 \rightarrow CaCO_3 + H_2O \tag{3.5}$$

If the amount of precipitate produced in the reaction may be assumed to be proportional to the amount of carbon dioxide present in the gas stream being bubbled through the calcium hydroxide solution, then:

$$Q_p = k_1 ct \tag{3.6}$$

where:

Q_p = precipitation concentration [kg/m^3];
c = the concentration of CO_2 gas in the incoming gas stream being bubbled through the sample [mol L^{-1}];
t = time from commencement of bubbling [s]; and
k_1 = a scaling constant dependent on:

- reagent molarity;
- rate of gas flow [L/s];
- reaction vessel geometry;
- temperature; and
- the assumption that other components in the gas stream are inert with respect to the limewater reaction, Equation 3.5.

It is further assumed that the optical attenuation through this solution is proportional to the level of precipitate present i.e.:

$$\frac{I_o - I_d}{I_o} = k_2 Q_p \tag{3.7}$$

where:

I_o = the output intensity of the optical source;
I_d = the detected intensity through the solution; and
k_2 = a scaling constant dependent on the optical path.

Hence combining Equations 3.6 and 3.7, the concentration of carbon dioxide c present

in the incoming gas supply is given by:

$$c = \frac{K}{t}(I_o - I_d) \tag{3.8}$$

where:

K = $1/k_1 k_2 I_o$, is defined as the sensitivity coefficient for the final measurement system.

For a constant CO_2 concentration c in the gas stream , differentiation of Equation 3.8 yields:

$$\frac{dI_d}{dt} = -\frac{c}{K} \tag{3.9}$$

which is constant (as expected from the foregoing linear assumption in each transduction stage). This is illustrated in Figure 3.6.

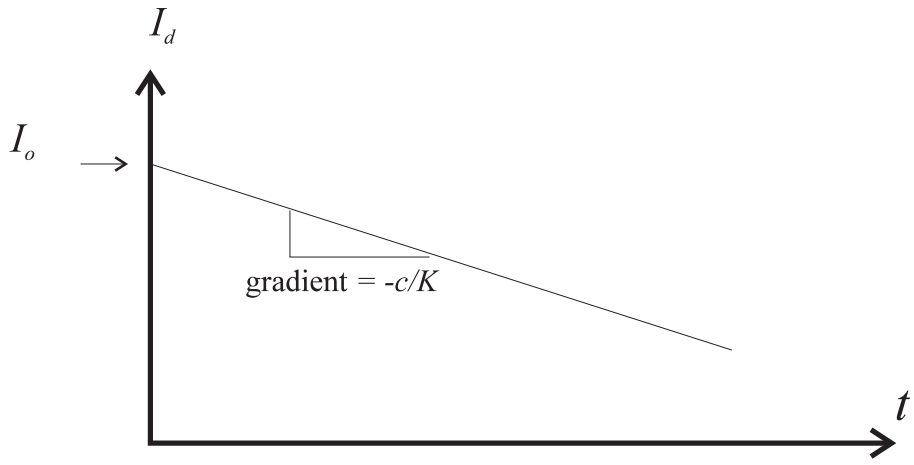

Figure 3.6: Characteristics of I_d over time t. Shown is the dependency on the CO_2 concentration and the sensitivity coefficient K for the final measurement system.

3.4.1 Implications of Non-Linear Transduction Relationships

Both of the assumptions of transduction proportionality, Equation 3.6 and 3.7, are questionable, particularly as regards:

- limewater reaction chemistry; and
- opacity of the suspended particulate within the optical measurement zone of the cell.

Hence the sensitivity coefficient K may be dependent on precipitate concentration Q_p, time from commencement t, as well as gas concentration c. However over significantly small ranges of the variables, Equation 3.8 will serve as an adequate representation because there is no reason to suspect that the relationship will be other than continuous, smooth and monotonic. Of course this presumption holds only if:

1. the rate of precipitate settlement remains less than the rate of production (such that opacity continues to increase); and
2. all saturation effects are avoided, i.e.
    - the $Ca(OH)_2$ reagent is non saturated (and there is no availability limitation at the bubble surface where the reaction is presumed to occur);
    - the precipitate suspension does not become completely opaque; and
    - the operational range of the optical detector is not exceeded.

Within these limitations the sensitivity coefficient K will have a unique value for a particular measurement system state $\{Q_p, t, I_d, c\}$. Knowledge of the K value for a succession of such states then permits interpolation such that direct knowledge of the functional form of $K = K(Q_p, t, I_d, c)$ is not required. A calibration scheme ("Time to Threshold", Section 7.2) is adopted to encapsulate the K value information such that the CO_2 gas concentration c may be deduced according to Equation 3.8.

3.5 Measurement System Overview

The final instrumentation package consists of several interlinking components each with specific duties to perform. The package consists of the following components.

- Chemical containment cell. This is the chamber in which the mixing of the sample gas and the indicator chemical will take place.
- Fluid transport and control. These will provide a storage and transportation system for the fluid and gas supplies.
- Turbidity measurement system. And
- Microcontroller, software and modelling (automation system). This will provide the necessary controller base as well as signal processing system and display and readout system.

These components are illustrated in Figure 3.7. Each is introduced in the subsections following.

3.5.1 Chemical Containment Cell

The reaction vessel ("cell") was created to primarily provide containment of the chemical reaction. Other critical functions performed include chemical mixing, the provision of an optical measurement area, the entrapment of gas for exhaust without loss of reagent, as well as allowing the effective removal of precipitate with a minimum quantity of cleaning fluid. This is further discussed in Chapter 4.

3.5.2 Turbidity Measurement

Turbidity measurement and calculation of the carbon dioxide concentration optical attenuation (and hence turbidity) is measured by an optical source/detector pair as

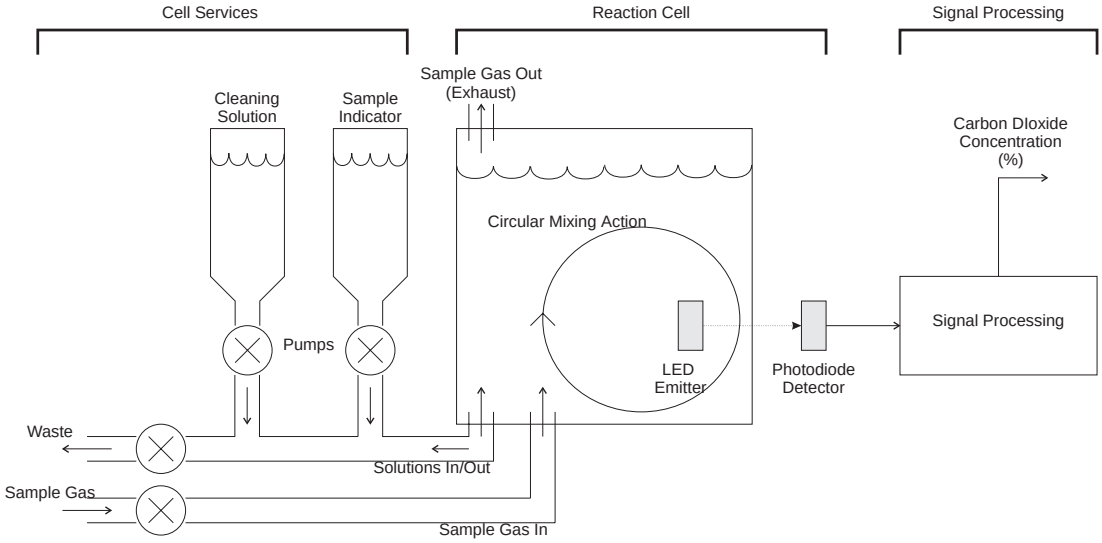

(a) "Open loop".

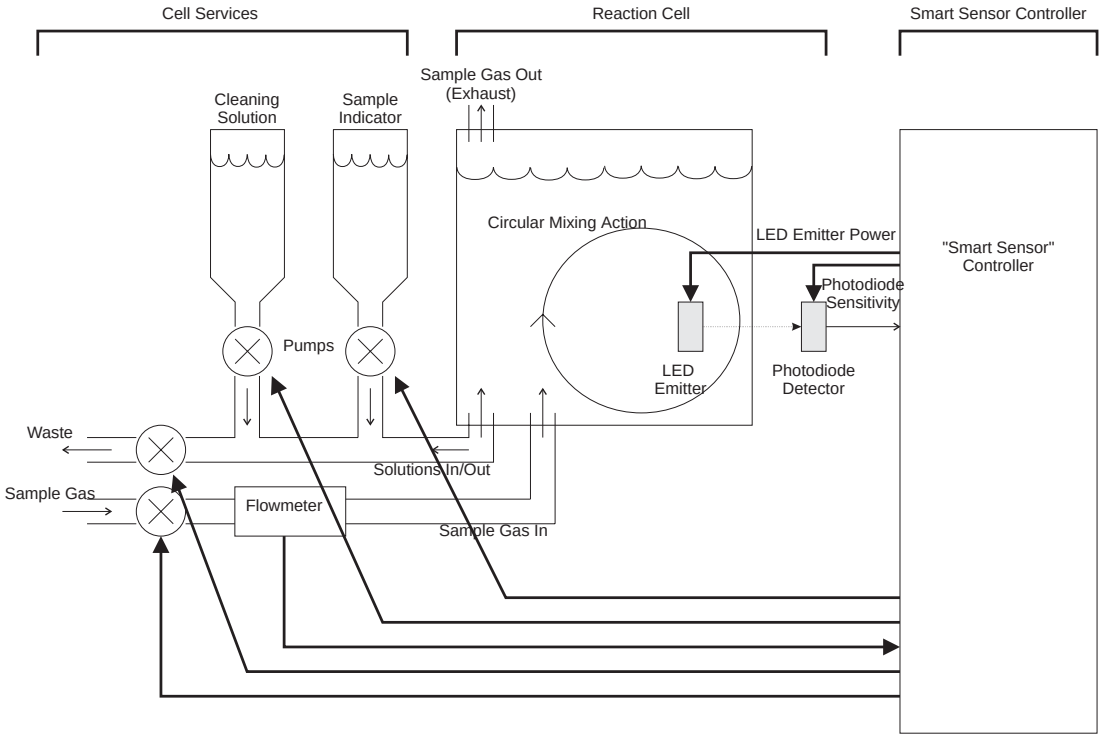

(b) "Closed loop", i.e. with control and adaptive feedback.

Figure 3.7: The CO_2 measurement system block diagram.

the quantity of calcium carbonate precipitate develops in the cell. A model is then used to translate this turbidity information back into a concentration value. Details of the turbidity measurement are presented in Chapter 5.

3.5.3 Fluid Transport and Control

Fluid transport is required to transport the reagent and cleaning solutions to and from the cell. Control of this transport is required to maintain consistent conditions within the cell. These details are covered in Chapter 6.

3.5.4 Microcontroller, Software & Modelling

The measurement instrument utilises an embedded microcontroller to provide control of the measurement system. Operations to be performed include control of the reaction chamber operation, turbidity sensing, and calculation of the carbon dioxide concentration. Details of the control are covered in Chapters 6, 7, 8 and 9.

3.6 Internal & External Variables

As shown in Section 3.2.1, certain parameters will influence the quality of the measurement system. A flowchart showing all significant variables for the measurement system is set out in Figure 3.8 and 3.9, of which only the more fundamental variables were examined as part of this research.

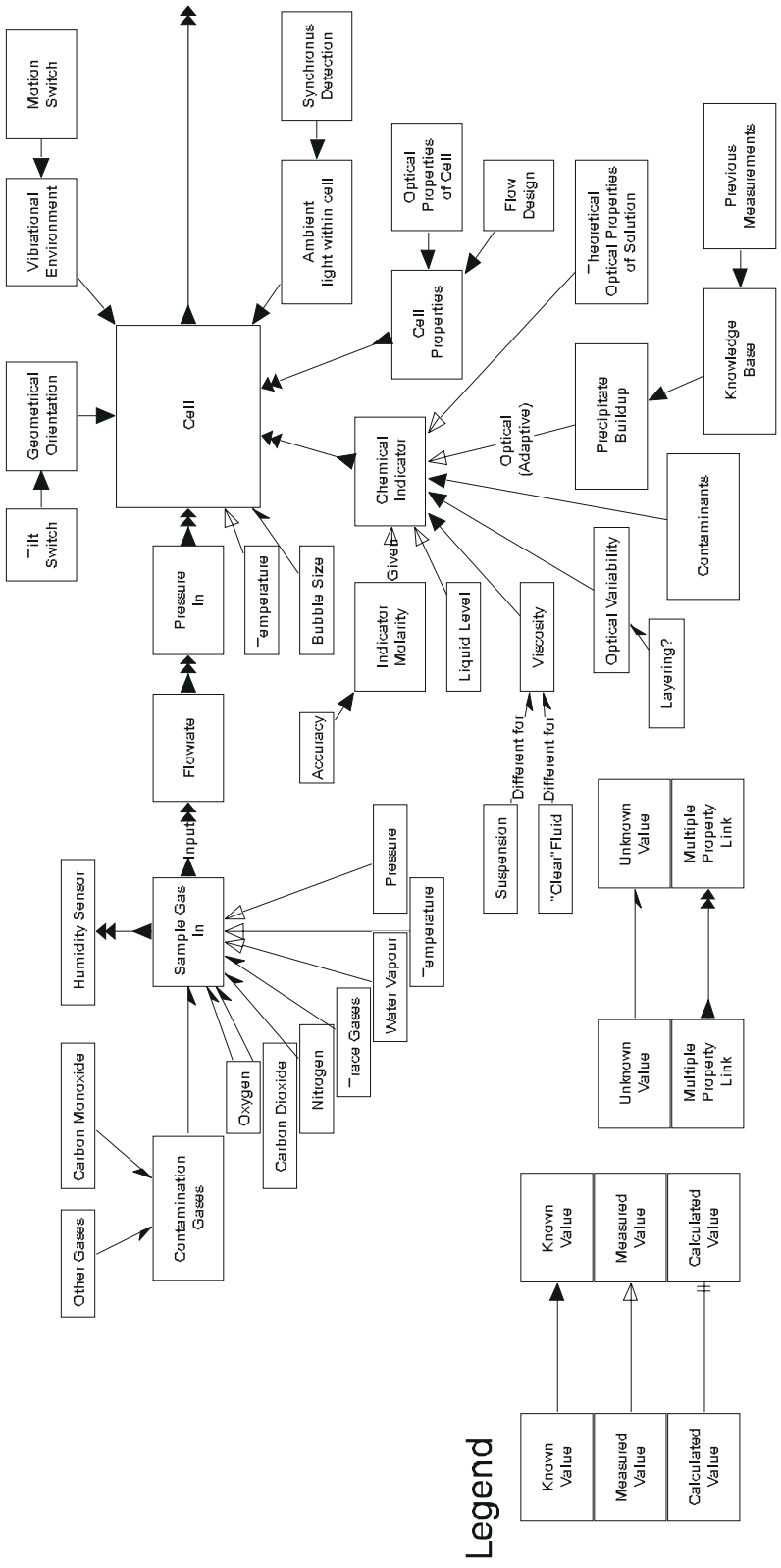

Figure 3.8: Overall instrumentation concept showing signal flows and all possible variables and influences. Continued on Figure 3.9.

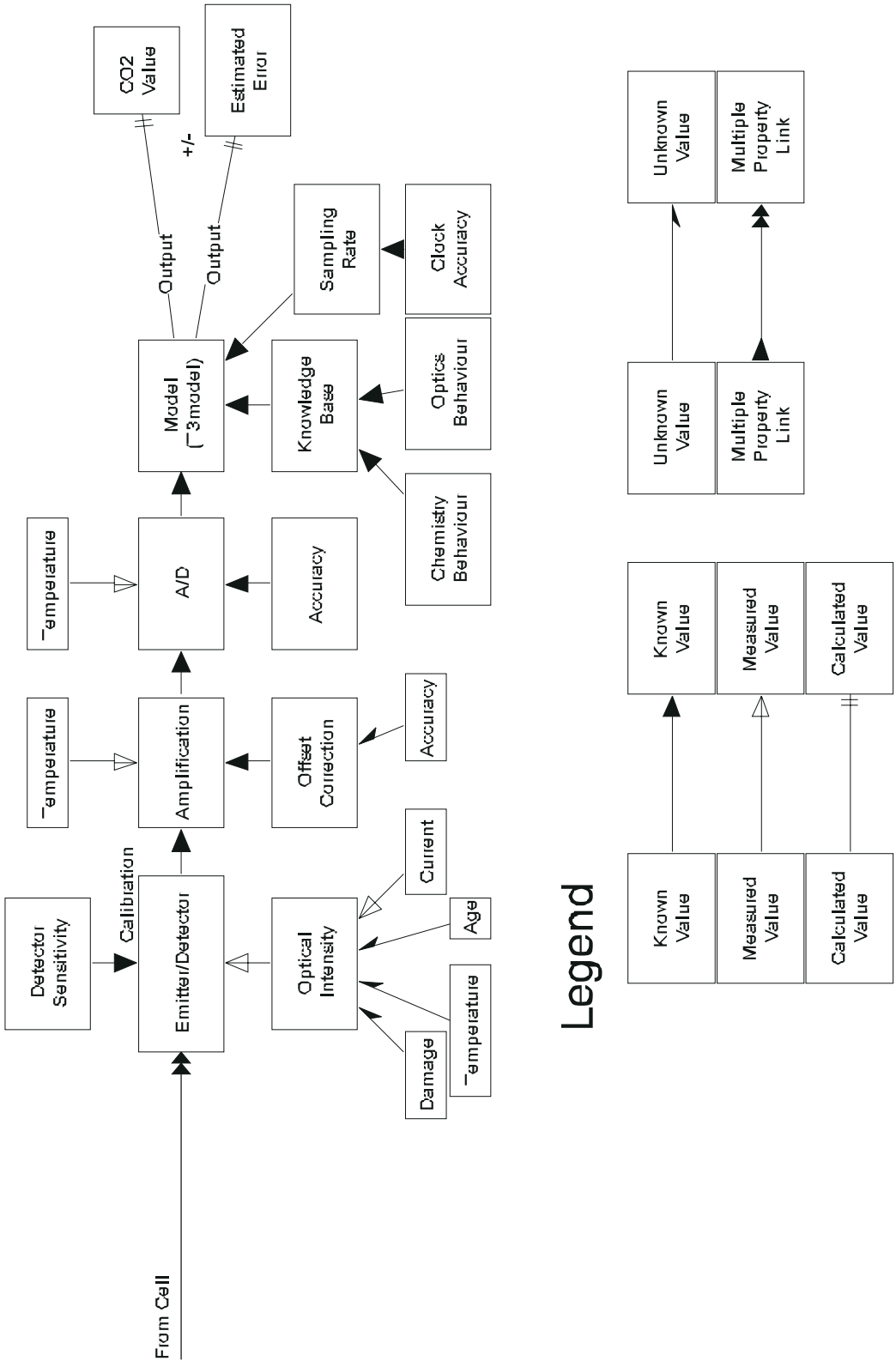

Figure 3.9: Overall instrumentation concept showing signal flows and all possible variables and influences. Continuation of Figure 3.8.

Chapter 4

Chemical Containment Cell Design I - Fluid Interactions

4.1 Introduction

To contain the chemical reaction between the chosen indicator solution and the sample gas being measured, a containment vessel or "cell" was devised to not only contain the chemical reaction but also permit the turbidity of the indicator solution to be measured extrinsically and the CO_2 concentration derived.

4.2 Reaction Cell Design Requirements

In addition to the basic purpose of the cell, there were several functional requirements of the cell in order to make it useful and compatible with a turbidity sensing mechanism. The cell had several distinct functions to perform within the sensor system. These primary functions are to:

- contain the chemical indicator solution;

- allow mixing of the sample gas with the chemical indicator solution;
- permit measurement of the optical transmittance through the cell (thus measuring the turbidity of the indicator solution); and
- allow connectors/ports or facilities for sample gas flow, and chemical indicator solution interfacing.

A development of these requirements follows.

4.2.1 Environmental Specifications

Several environmental specifications can be drawn as a guide to protect the cell from external environmental influences. The cell should ideally be protected from:

- ambient light;
- excessive temperatures that would affect the structural integrity of the plastics and other materials used;
- high humidity conditions especially where condensation might occur (due to there being optoelectronics involved);
- gases or other materials which affect or attack the plastics and materials used; and
- mechanical shock or impact.

4.2.2 Containment Volume and Geometry

The internal volume of the vessel containing the reaction needed to be of a sufficiently large volume to permit a homogenous reaction between the indicator reagent and the sample gas. The volume and internal shape also needed to permit mixing and easy

flow of solutions in and out of the vessel. The external shape of the containment vessel needed to be able to easily attach to the optical measurement system, the cell control system (pumps), and the instrument in general.

4.2.3 Mixing Requirements

As a homogeneous distribution of the precipitate was considered highly desirable to permit consistent measurements, thorough mixing of the solution throughout the measurement cycle was desired. Motorised mixers could have been employed, however these would have added extra and unwanted complexity to the cell. As a constant flow of the sample gas to the cell was presumed to be available for the envisaged CO_2 measurement applications, this gas/bubble stream was used to perform the mixing function within the cell. This avoided the use for bulky mechanical mixers thus removing the need for motors and mixing blades.

4.2.4 Measurement Area

In order for the extrinsic optical measurement to be made, an area within the cell needed to be set aside specifically as a measurement zone. Hence the cell needed to be made of a clear plastic or ceramic/crystal, or have a clear windowed area suitable for the infra-red optical path.

A secondary consideration was that of the possibility of bubbles obscuring the measurement optics. Any bubbles in the measurement zone (where the turbidity of the chemical solution was measured) would cause spurious optical transmittance measurements. The measurement zone was therefore positioned in an area that exhibited good flow but minimal bubble activity. Four cells were therefore empirically designed to permit a circular flow pattern which provided the necessary mixing action to achieve the homogeneous solution required for consistent measurements and minimise optical signal noise due to bubbles.

4.2.5 Optics Coupling

In order to measure the required optical properties, some method of coupling the optical components to the cell was also required. Coupling should introduce minimal optical attenuation and must be sealed such that changes in the exterior of the cell do not cause optical changes (i.e. dust, other vapours).

4.2.6 Mechanical Considerations

The cell must be designed with several mechanical considerations as well. The cell must be mechanically robust so that handling will not damage the sensing head, and must allow easy assembly and disassembly for when the cell would be replaced or cleaned.

The mechanical arrangement must also allow consistent and repeatable interfacing of the optics and be tolerant of small positional mis-alignments with the sub components.

Also the cell must be leak free as it would be containing the aqueous reagents. Also because the sensor may be placed inside movable containers it would be advantageous to have a cell which would continue to operate under various cell orientations.

4.2.7 Chemical and External Compatibility

The cell must be impervious to chemical attack by either the chemicals being used or possible chemicals/gaseous conditions the entire sensor system may possibly be exposed to under normal operating conditions (i.e. be chemically compatible with all chemicals being used).

The cell must also be able to withstand typical aging processes resulting from exposure to heat, light, radiation, steam, etc.

4.3 Preliminary Cell Prototypes

Several prototype cells were initially constructed to ascertain the optimal design for a cell to satisfy the functional specifications. The main focus of this experimentation was to determine the optimal geometry for the cell to obtain the best possible mixing between the sample gas and the indicator solution (since most of the functional specifications could be obtained with minimal design effort).

There were four major evolutions in the conceptual cell design before arriving at the implemented cell.

4.3.1 Inline Flow Cell

This cell (Figure 4.1) was designed around a tube containing two "gate" valves to cordon off section of the tube into a chamber. A constantly flowing chemical indicator could be temporarily stopped by the valves forming a reaction chamber. The sample gas could then be injected into this cell and an optical measurement of the precipitate level taken over the measurement cycle. When the measurement cycle had finished, the valves would be re-opened and the expended solution flushed out by the fresh solution in preparation for the next measurement cycle. Thus cleaning and removal of waste solution could be performed in the single action.

This would allow very small chamber volumes but would be complicated by the need for miniature electronically controlled gate valves. By positioning several sets of optical detectors and gas injection points around the perimeter of the cell, measurements could be taken which would be unaffected by changes in the orientation positioning of the cell. It would be therefore anticipated that the incoming solution should enter at the top side of the cell such that the flow direction of the chemical indicator would be vertical top to bottom. This would allow any precipitate that fell out of suspension to settle on the outward side valve and minimise interference with any future measurements should the precipitate not be removed effectively.

This cell design was not pursued due to the envisaged problems in the gate mechanism fabrication.

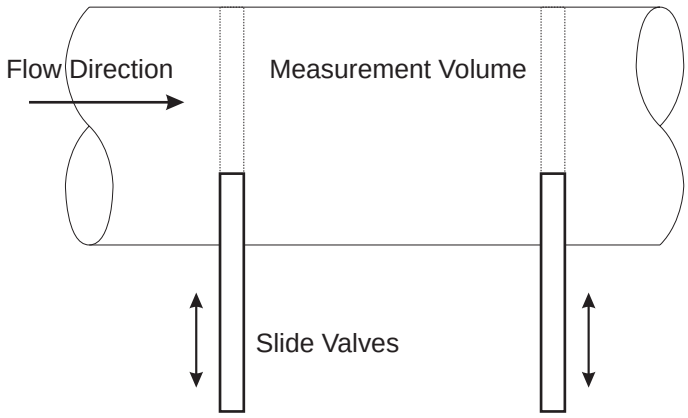

Figure 4.1: The first conceptual design for the chemical reaction cell. An inline flow cell using two slide valves to form the sides of the chamber. A center measurement area was reserved for the turbidity measurement.

4.3.2 Circular Flow Tube

It was presumed that mixing of the indicator solution would need to be performed to prevent the observed effect of precipitate falling out of suspension and coating any non-vertical wall of the containing vessel. Thus a circular flow pattern was deemed suitable. A gas injection tube was used to inject the sample gas into a brass chamber, with connecting "U" tubes to form a complete fluidic circuit (Figure 4.2). The premise was that rising bubbles would generate an upward flow of nearby fluid, and provided that the volume of the bubble stream was of sufficient size when compared to the total chamber volume a total bulk upward flow would occur.

The gas injection tube was inserted through the top to avoid problems associated with sealing of this tube if the gas flow was injected at the base of the tubing.

This cell was manufactured however construction inaccuracies resulted in poor final performance with fluid flow failing to complete the fluidic circuit due to port placement and sealing issues. This cell design was not pursued.

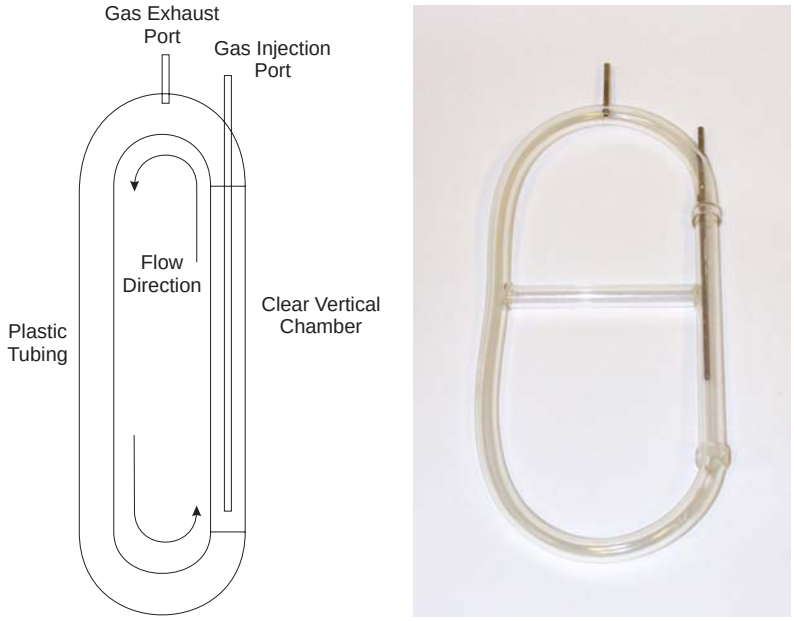

(a) Mechanical construction and expected flow directions.

(b) Photograph of the prototype.

Figure 4.2: The second conceptual design for the chemical reaction cell. This used a circular flow pattern to achieve adequate mixing of the indicator solution.

4.3.3 Divided Cell

Because of the relatively large size of the previous prototype (15cm high), a similar effect was considered easily reproducible by using a simple container with a perforated center divider constructed from "Veroboard" (perforated PCB material) to allow the fluid to complete the circular flow circuit through the perforations (Figure 4.3). It was also envisaged that this center divider would perform the necessary bubble separation to prevent any bubbles entering the settling flow region of the cell which would be set aside to allow measurement of a stable and bubble free flow zone.

This cell was designed and tested and showed adequate bubble separation and overall behavior in agreement with the concept from which it was designed.

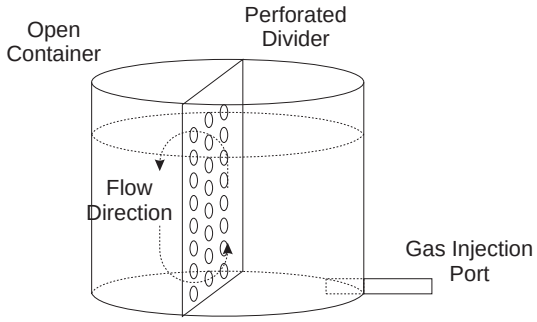

(a) Mechanical construction and expected flow directions.

(b) Photograph of the prototype.

(c) Photograph of inside configuration of the prototype.

Figure 4.3: The third conceptual design for the chemical reaction cell. The divided cell allowed simpler fabrication whilst providing a region suitable for bubble free optical measurement.

4.3.4 'Teardrop' Cell

The final step in the evolution was based on miniaturising the divided cell concept into a planar structure. This cell design was based on three pieces of polycarbonate plastic milled out to form an internal cell void (Figure 4.4 and 4.5). Two outer pieces would form the cell walls whilst a third inner piece was cut out to provide a the cell shape with a divider 'island' in the center to help direct fluid flow. All these pieces were then glued together to form the final cell. Barbed brass access ports for the necessary connections were then added as well as bolts to maintain structural integrity should the cell be dropped.

This cell construction technique proved both practical and versatile, such that different internal geometries could be easily implemented. Hence this design concept was used throughout the remainder of the project.

4.4 Final Cell Design and Construction

4.4.1 Mechanical Geometry

In order to aid in assembly and disassembly of all cells, a standard form factor was decided upon. The designed cells conformed to a face dimension of 50mm×50mm. Cells could be two ply, or three ply thick, but had to retain this face form factor. This would allow easy replacement of cells as a standard holding bracket could be used. This would also allow mounting of the optics with a high degree of repeatable alignment precision and hence preserve optical calibration values should the cell be reassembled.

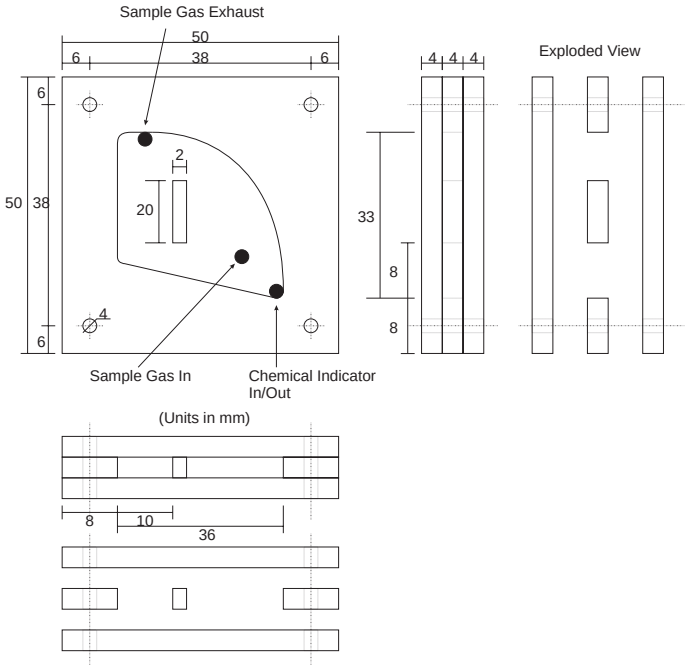

(a) Mechanical construction.

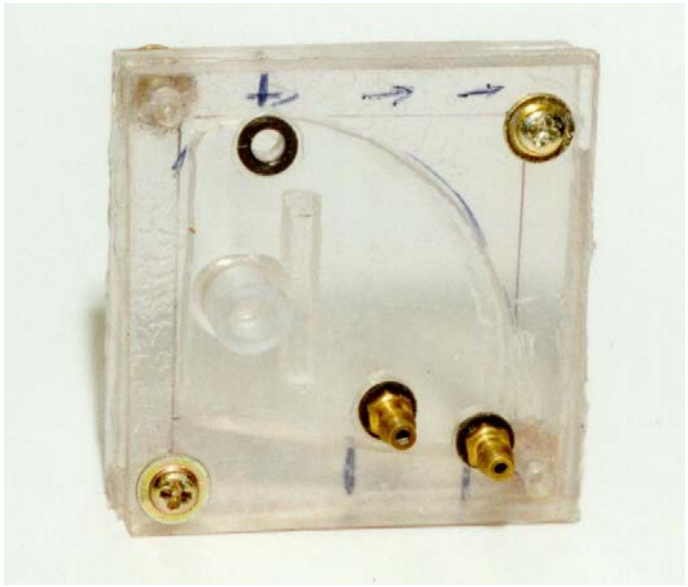

(b) Photograph of the prototype.

Figure 4.4: The fourth conceptual design for the chemical reaction cell. An upside down 'teardrop' shape formed the internal cell void. This design combined the circular flow and simple fabrication techniques and allowed easy filling/draining of the cell.

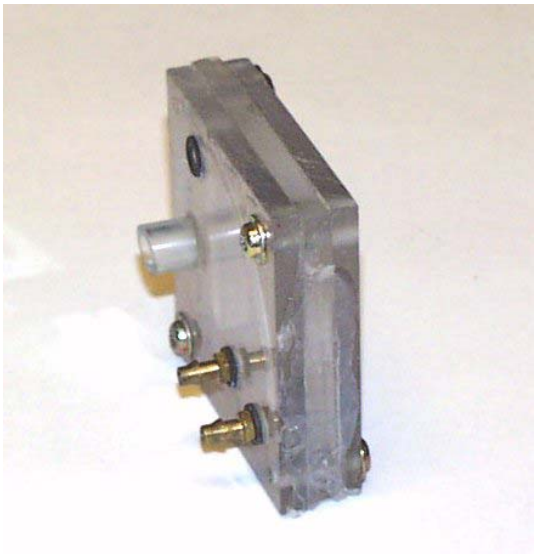

(a) Side view.

(b) Rear view.

Figure 4.5: Photographs of alternative views of the 'teardrop' cell.

4.4.2 Internal Cell Design

As previously stated, an important requirement was to have consistent mixing of the indicator chemical to prevent precipitate falling out of suspension too rapidly and provide a homogeneous solution.

Several designs were manufactured and evaluated, namely:

- Teardrop cell;
- Teardrop cell with baffles;
- Teardrop cell with mesh bubble guard;
- Circular cell;
- Oval cell; and
- Triangular cell.

and each is presented and analysed in Section 4.5 below.

4.4.3 Measurement Zone Placement

The measurement zone is positioned in an area that exhibited good flow but minimal bubble activity. Four cells were therefore empirically designed to permit a circular flow pattern which provided the necessary mixing action to achieve the homogeneous solution required for consistent measurements and minimise optical signal noise due to bubbles.

4.4.4 Interfacing of Optics

In order to permit interfacing of the measurement optics to the cells, all cells need to be constructed of clear plastic with good optical properties. Acrylic plastic was deemed suitable with good optical transparency. Polishing of the milled surfaces using "Brasso™" metal polish was essential to avoid light scattering in the optical measurement path.

External PCBs are used to mount the measurement optics to the plastic cell, with these components being bolted together to form a single sensor assembly.

4.4.5 Cell Component Alignment Invariance

As four alignment bolts were used to fix all the necessary components of the cell, minimal alignment variation between cell assemblies would occur. Minor mechanical variations between the halves of the cell would have negligible effect on the cells performance. Any variations in optics placement was easily removed via the use of preliminary calibration techniques to determine baseline optical levels.

4.4.6 Gas/Liquid Access Ports

In order to interface the cell with the outside world and also with the indicator solution, barbed brass access ports were added to the three strategic locations on the cell. Three ports were used to allow sample gas in, sample gas out, and indicator solution/cleaning solution in/out. Again, placement of these ports was determined empirically (Section 4.5).

4.4.7 Cell Sealing

Sealing of the cell to provide a leak free environment was accomplished by using custom made "O" rings. These seals were made from "O" ring cord of diameter 2mm, cut and joined to fit the custom "O" ring groove milled into each cell. The groove was slightly undersize and allowed the seal to stay in place during assembly/dissasembly and needed no further attention provided it was not damaged. It was assumed that the cord was made of either neoprene, or rubber (as there was insufficient manufacturers information available). These two materials have chemical resistance as seen in Table 4.1 (Cole Parmer Instrument Company, 1997–1998). As no major chemical incompatibilities were seen, the "O" ring cord was judged suitable for use in the cell.

Table 4.1: Chemical susceptibility for Acrylic, Neoprene, Natural Rubber, and Brass to the chemicals used in the cell (reproduced from ColeParmer Catalog, 1997–1998, pp1364–1372).

Chemical	Acrylic	Neoprene	Natural Rubber	Brass
Calcium Hydroxide	No Effect	No Effect	No Effect	No Data Available
Calcium Oxide	No Effect	No Effect	Minor Effect	No Data Available
Carbon Dioxide (Wet)	No Effect	Minor Effect	Minor Effect	No Data Available
Carbon Dioxide (Dry)	No Effect	Minor Effect	Minor Effect	Minor Effect
Water (Deionised)	No Effect	No Effect	No Effect	No Effect
Water (Distilled)	No Effect	No Effect	No Effect	No Effect
Water (Fresh)	No Effect	No Effect	No Effect	Severe Effect

4.4.8 Chemical Compatibility

The main chemicals coming into contact with the cells and their "O" ring gaskets were water (H_2O), carbon dioxide (both as a dry gas and also in a "wet" form, i.e. carbonic acid, $CO_2 + H_2O \rightleftharpoons H_2CO_3$), calcium hydroxide ($Ca(OH)_2$), and calcium carbonate ($CaCO_3$). As seen in Table 4.1, minor or no effect was expected between these chemicals and the cell materials used.

The supplied acrylic sheet, of thickness 4mm, was also mechanically robust able to and be milled by a numerically controlled (NC) milling machine.

4.4.9 Cleaning

It was apparent that an effective cleaning regime for the cell was imperative as the cell walls would quickly become coated with calcium carbonate precipitate after several measurement cycles. This would then affect the turbidity measurement. Hence by minimising this precipitate coating, the dynamic range and overall performance of the sensor would be preserved.

It was considered likely that any roughness in the internal finish of the cell void would accelerate the deposition of calcium carbonate precipitate. It was also assumed that once this initial seeding of precipitate has occurred, rapid buildup would follow with the roughness in the cell walls acting as a catchment area for precipitate particulates. Therefore, during construction of the cell, the interior walls were polished using a commercial polisher ("Brasso™"). Also when the cell was in operation it was kept in a vertical orientation to minimise the coating of the precipitate onto the inner vertical walls.

In addition to simple orientation considerations, cleaning methods were also considered (for the second instrument prototype, 'Mk.II'). Scraping and mechanical cleaning systems were considered impractical due to the need for a miniature electromechanical device to drive the scraper mechanism. Instead, a chemical cleaning system was considered suitable. This would involve a cleaning solution coupled to an external mechanism of injecting it into the cell to flush out and dissolve any precipitate deposits.

4.4.10 Cell Chamber Fabrication, Preparation & Assembly

The cell configuration was designed to be easily fabricated using computer controlled milling processes with minimal manual finishing labour. All cells were designed to be easily coupled to the optics PCBs and plumbing subsystems. The disassembled and assembled components of the cell are illustrated in Figure 4.6 and Figure 4.7 respectively.

(a)

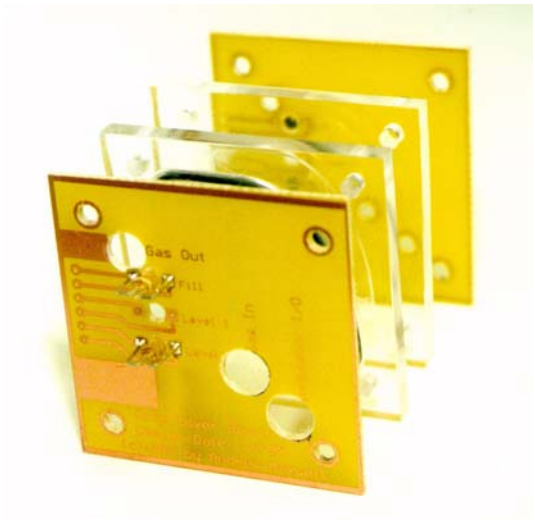

(b)

Figure 4.6: Two views of the expanded cell and associated optical alignment boards. The access holes for the plumbing ports and one half of the optics can be clearly seen.

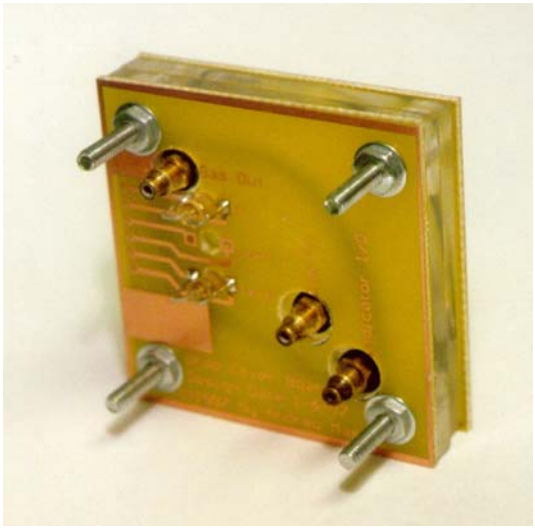

(a)

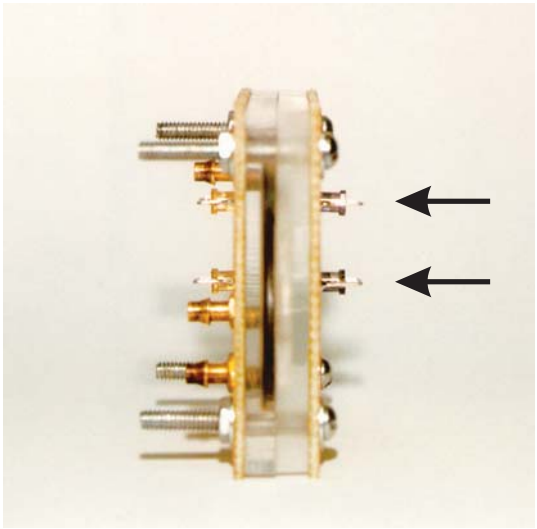

(b)

Figure 4.7: Two views of the assembled cell and associated optical alignment boards, (a) showing the access ports, (b) showing the alignment of the LEDs and the photodiodes (arrowed).

Preparation of the internal cell void was necessary before the cell could be used as part of the sensor head. Thorough cleaning of the cell to remove any particulates, or acrylic dust produced during the milling process, was considered essential. This was done by firstly washing the cells in water and then by using Brasso metal polishing liquid. Other techniques such as wet and dry polishing could also be used and by using optical grade wet and dry sandpaper a good final finish to the insides of the cell could have been prepared.

Whilst it was important to clean and prepare the entire cell void, particular attention was paid to the cell measurement region where the optics would "see" through the chemical indicator, and was prepared to be as optically smooth as possible.

4.4.11 Alternative Cell Geometries

A total of four cell geometries were developed and fabricated within the same square mechanical form factor (Section 4.4.1) . These were labelled ; 'teardrop', 'circular', 'oval', and 'triangular' as illustrated in Figure 4.8.

In each case a void space of depth 4mm was milled out giving an internal cell thickness of 4mm and internal volumes as shown in Table 4.2.

Other cell designs have eventuated from this work. These cells, whilst not fully fabricated or tested are presented in Appendix E.

Table 4.2: Internal cell volumes for the four cell designs, 'teardrop', 'circular', 'oval', and 'triangular'.

Cell Type	Volume [mL]
teardrop	2.0 ± 0.2
circular	2.5 ± 0.2
oval	2.5 ± 0.2
triangular	1.5 ± 0.2

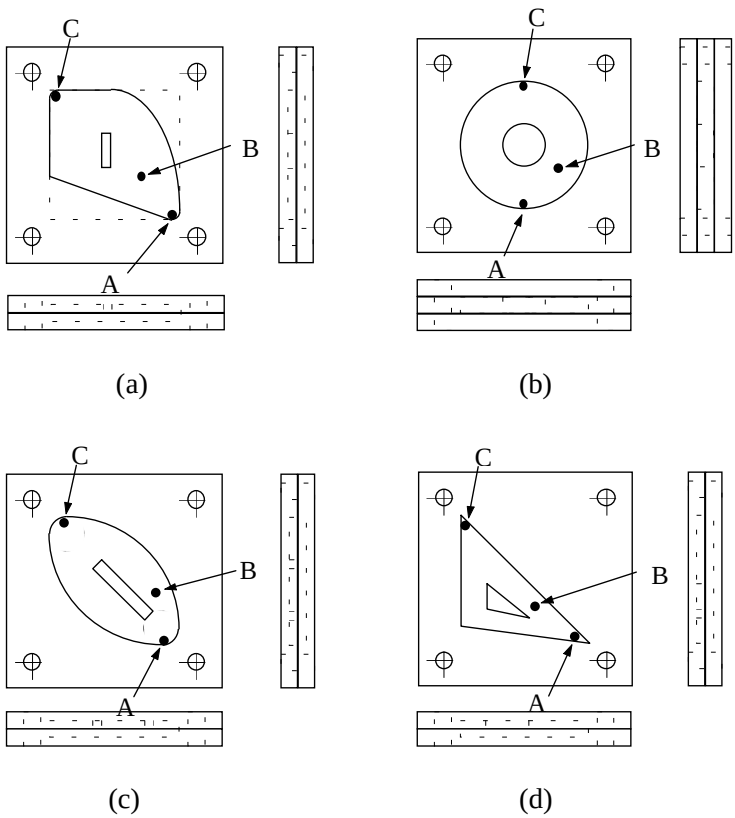

Figure 4.8: The cells, (a) 'teardrop', (b) 'circular', (c) 'oval', and (d) 'triangular'. In each case A is the chemical indicator inlet/outlet port, B is the sample gas inlet port, and C is the sample gas output port(exhaust).

4.5 Empirical Cell Analysis

Due to the chronological order of the research, initial development of the cells was performed using an empirical approach. The initial approach allowed rapid optimisation of the cell shape to a final design which could be quickly implemented yielding initially satisfactory results. Multi-phase fluid flow analysis was also unavailable at the time, however was able to be performed at a later date as shown in Section 4.6.

4.5.1 Empirical Analysis

The four cell geometries (Figure 4.8, and geometry variations) were analysed empirically using video footage of each cell under operating conditions. Each cell was filled with coloured food dye diluted in water. This allowed internal transients to be observed for matching later with computation modelling.

Each of the four cells (and their variations) presented here were operated and observed with respect to their flow characteristics. The intended flow arrangement was as illustrated in Figure 4.9.

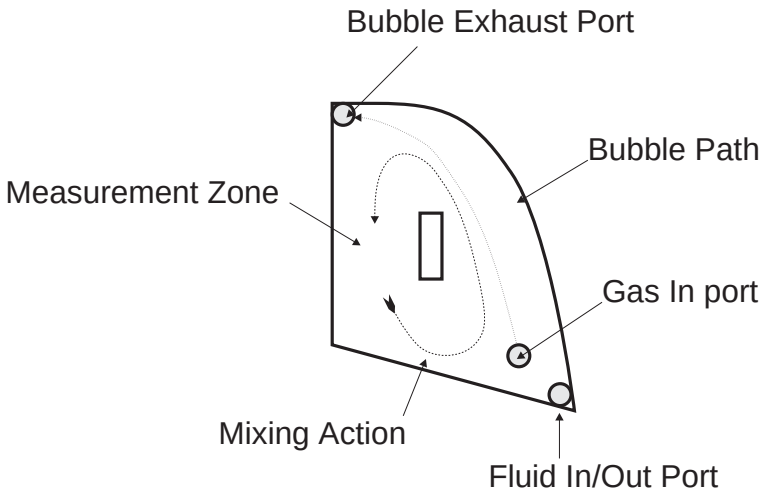

Figure 4.9: Intended fluid flow within the 'teardrop' cell.

4.5.2 Teardrop Cell

Figure 4.11 shows the typical 'teardrop' cell (Figure 4.10) flow characteristics under very high flow rates. Clustering of bubbles are clearly visible where excess bubbling prevents these formed bubbles from dispersing and the sample gas escaping out of the exhaust port (at top left). The flow circulation desired has been largely stopped due to insufficient volume of chemical indicator to complete the fluidic circuit, although some mixing would occur as the bubbles moved from the right to the left and carry some of the indicator solution into the measurement area on the left. Hence operation of the cell is still possible, but this distribution of colour indicated that a nonhomogeneous solution is produced.

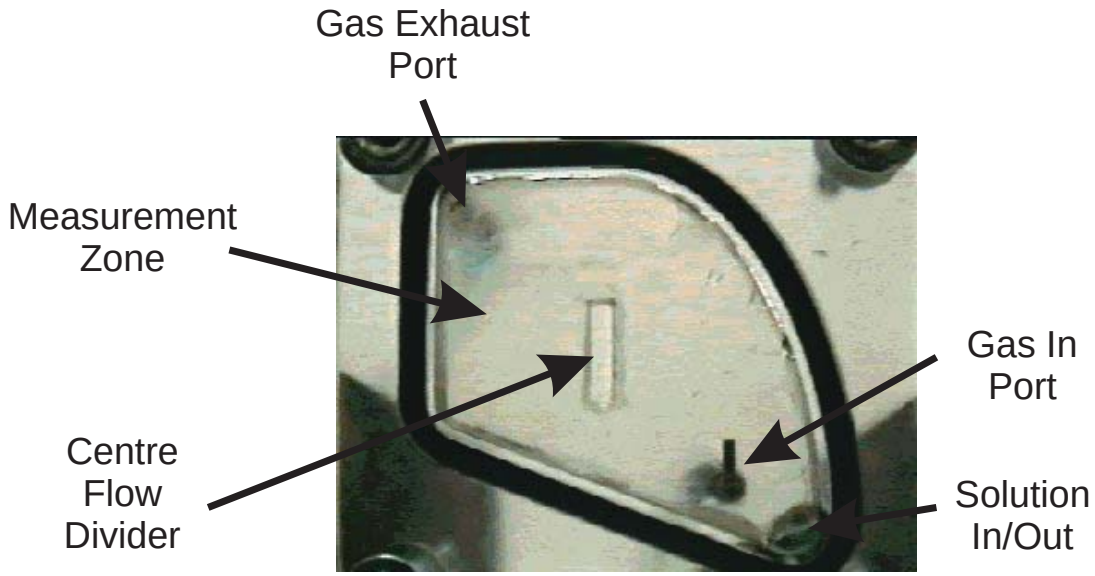

Figure 4.10: The empty 'teardrop' cell. Visible is the cell void, the center flow divider, and the three ports for the combined indicator chemical in/out (bottom), the sample gas in (towards the center), and sample gas out (top).

(a) 8 seconds after commencement of bubble injection.

(b) 24 seconds after commencement of bubble injection.

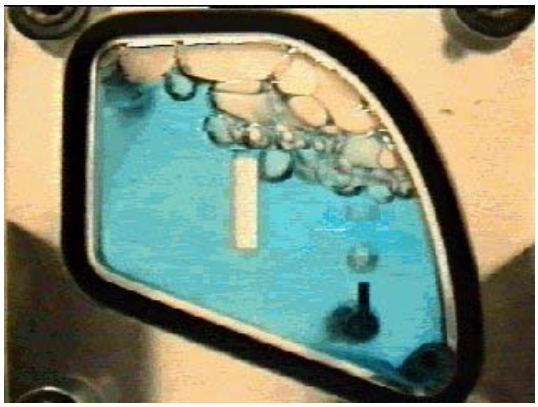

(c) 53 seconds after commencement of bubble injection. Blue dye was injected 38 seconds after commencement of bubble injection.

Figure 4.11: An example of the flow characteristics of the teardrop cell at ~8mL/s. Shown are snapshots in time during normal operation of the cell (Note that the low quality video capture system used resulted in vertical strobing effects. These can be seen on all following cell analysis images where rapid motion is present. i.e. bubble movement.)

4.5.3 Teardrop Cell with Baffles

A 'teardrop' cell was modified by adding some plastic baffles. These baffles were intended to prevent the transition of bubbles from the bubbling region on the right to the measurement area on the left, whilst still allowing a full circular fluidic circuit. Figure 4.12 shows the modified cell ready for testing. Figure 4.13 shows the poor flow characteristics of this modified cell at high flow rates. Instead of preventing the accumulation of bubbles the upper divider as desired, these baffles encourage the formation of bubble clusters by initially trapping bubbles near the center divider, and then, due to the high gas flow rates, these bubbles are reinforced by miniature counter-clockwise eddies behind the lower baffle.

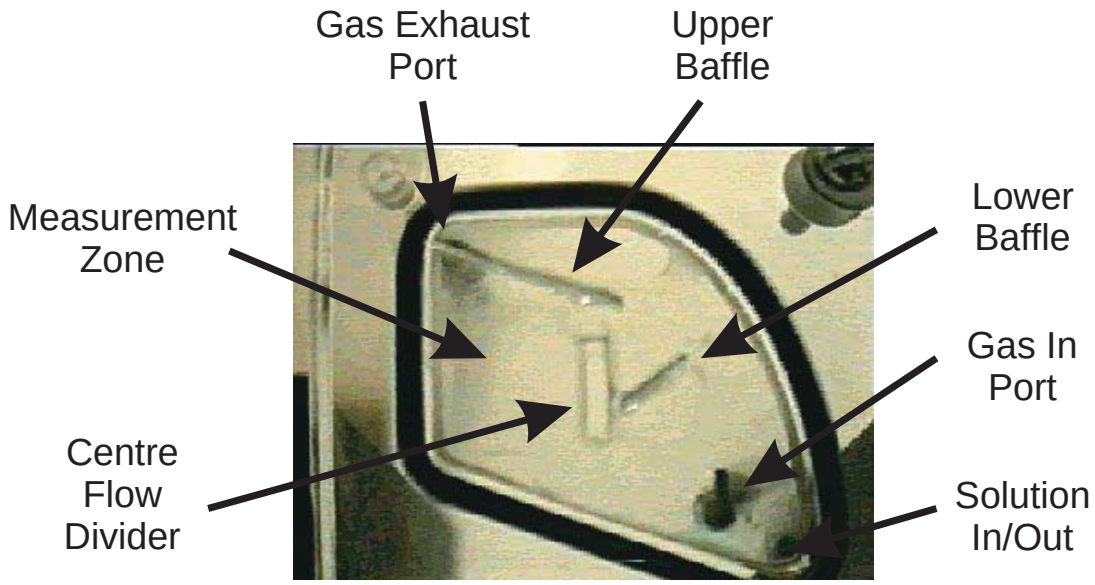

Figure 4.12: The empty 'teardrop' cell with two plastic baffles. Visible is the cell void, the center flow divider, and the three ports for the combined indicator chemical in/out (bottom), the sample gas in (towards the center), and sample gas out (top).

(a) 4 seconds after commencement of bubble injection.

(b) 10 seconds after commencement of bubble injection.

Figure 4.13: An example of the 'teardrop' cell with plastic baffles at ~8mL/s. Shown are snapshots in time during normal operation of the cell (from video capture).

4.5.4 Teardrop Cell with Mesh Bubble Guard

The previous cell was again remodified through the removal of the baffles and the inclusion of a 'bubble guard' using fibreglass fly-screen mesh. This comprised approx 0.5mm diameter wire woven to form a 2mm mesh. This bubble guard was located to guide the bubbles away from the center divider, and up towards the exit port for the cell. The mesh was considered to have the major advantage over baffles in that fluid would flow through it, but large bubbles (typically 2mm scale) would be stopped due to surface tension interactions. Figure 4.14 shows the newly modified cell ready for testing.

Figure 4.15 shows the new flow characteristics of the modified cell. It is clearly seen that the mesh allows this cell to handle the same high flow rates used for all these tests, with bubbles being prevented from entering the measurement area on the left of the cell.

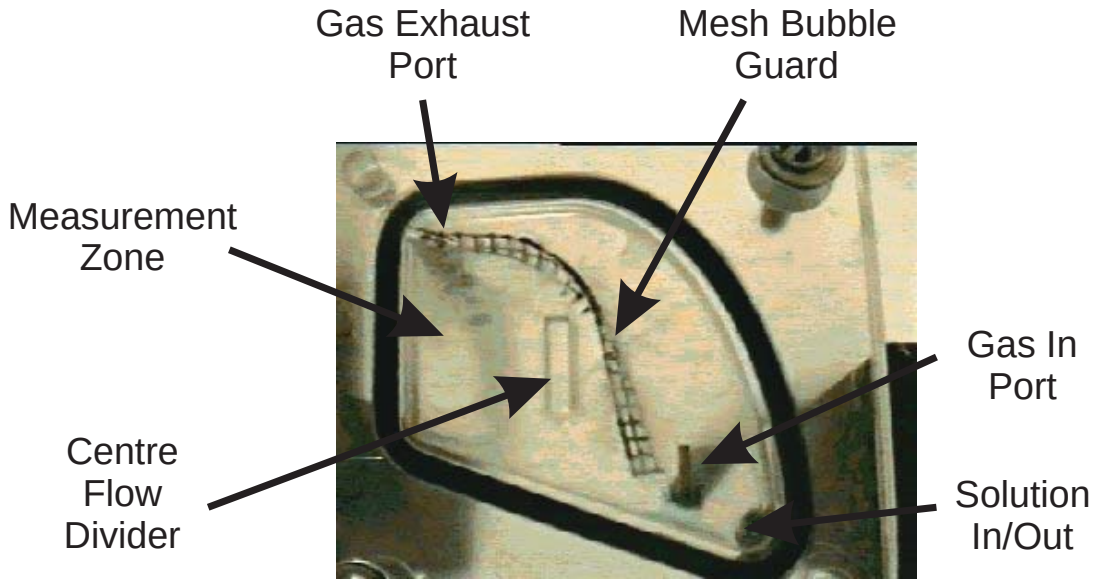

Figure 4.14: The empty 'teardrop' cell with plastic mesh bubble guard. Visible is the cell void, the center flow divider, and the three ports for the combined indicator chemical in/out (right), the sample gas in (towards the left), and sample gas out (top).

(a) 5 seconds after commencement of bubble injection.

(b) 9 seconds after commencement of bubble injection.

(c) 51 seconds after commencement of bubble injection.

Figure 4.15: An example of the flow characteristics of the drop cell with plastic mesh bubble guard at ~8mL/s. Shown are snapshots in time during normal operation of the cell (from video capture).

4.5.5 Circular Cell

The circular cell is different in construction to all the other cells shown here. It used a three ply construction rather than a two, with a milled internal void. The center divider is a plastic button milled out and then glued to the back piece. When all three ply pieces are reassembled the internal circular void results. Figure 4.16 shows the circular cell ready for testing.

Figure 4.17 shows the cell with the same flow rate sample gas injection. Clearly visible is the large bubble cluster to the left of the exhaust port. The buoyancy of this bubble is insufficient to compete with the sample gas flow rate to the right, hence forcing the bubble block to remain in this position. However once established the pressure in this bubble appeared to cause subsequent gas flow to exit through the exhaust part as intended. Some circular fluid flow is occurring in the small space between the center divider and the bubble block. Figure 4.17(b) shows a similar case this time with blue indicator to show up the presence of bubbles more clearly.

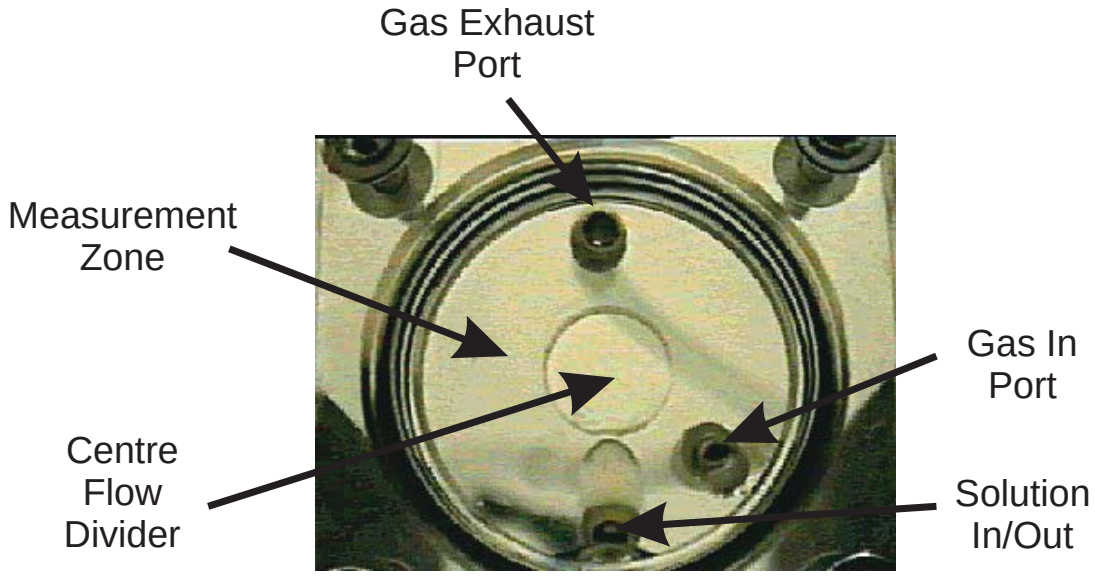

Figure 4.16: The empty circular cell. Visible is the cell void, the center flow divider, and the three ports for the combined indicator chemical in/out (bottom), the sample gas in (towards the left), and sample gas out (top).

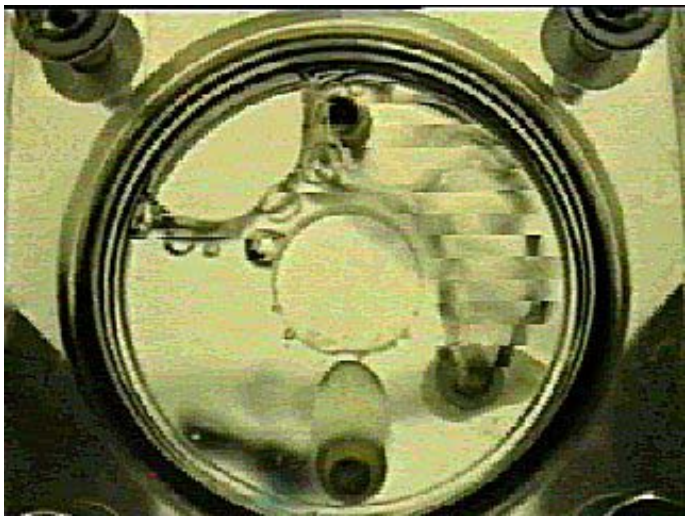

(a) 12 seconds after commencement of bubble injection.

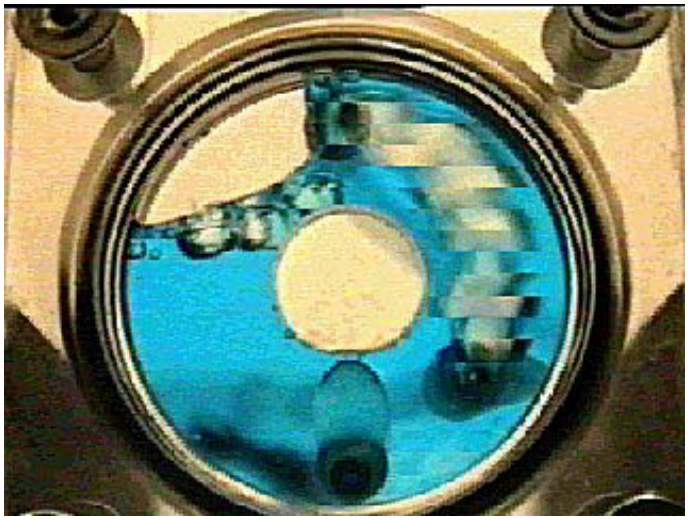

(b) 36 seconds after commencement of bubble injection. Blue dye was injected 25 seconds after commencement of bubble injection.

Figure 4.17: An example of the flow characteristics of the circular cell at ~8mL/s. Shown are snapshots in time during normal operation of the cell (from video capture).

4.5.6 Oval Cell

Figure 4.18 shows the oval cell ready for testing. The orientation and offset of the center divider. Figure 4.19(a) shows the general flow characteristics of the cell at the same high flow rate where a large bubble block had formed. This cell was capable of handling higher flow rates than the other cells (except the mesh-modified drop cell) due to the large mixing area above the gas port. Figures 4.19 shows a three part time lapse of the flow characteristics and flow patterns generated within the cell.

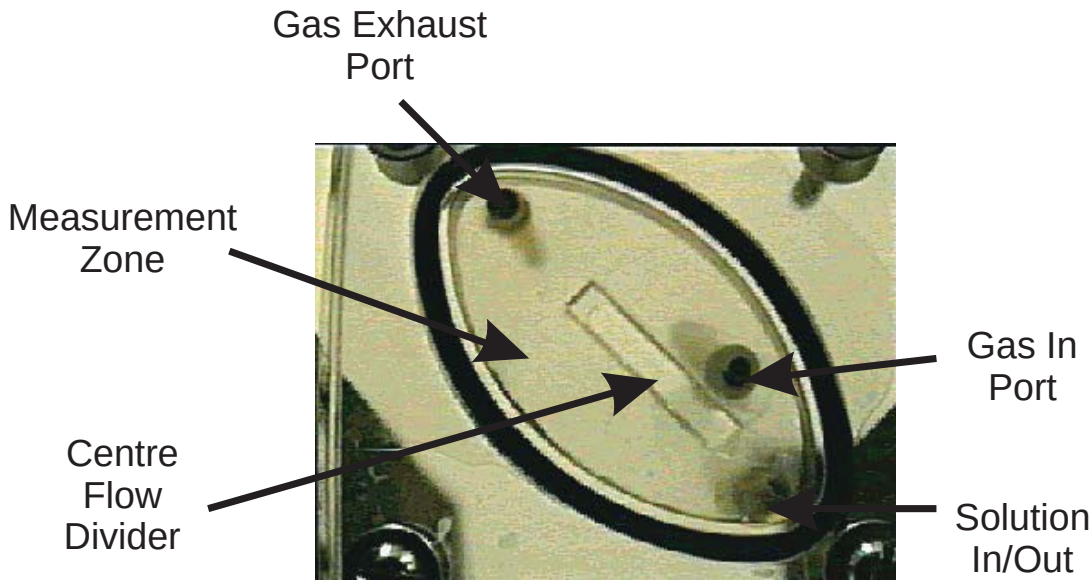

Figure 4.18: The empty oval cell. Visible is the cell void, the center flow divider, and the three ports for the combined indicator chemical in/out, the sample gas in, and sample gas out.

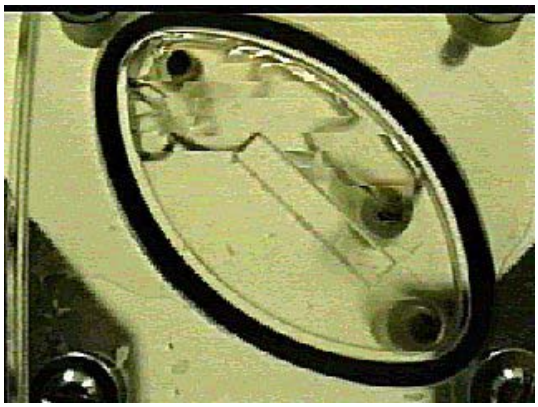

(a) 1 second after commencement of bubble injection.

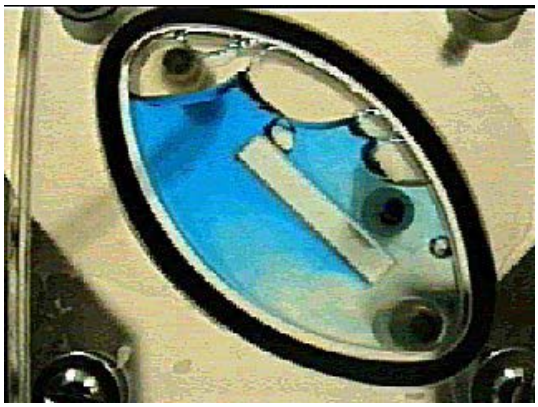

(b) 13 seconds after commencement of bubble injection. Blue dye was injected 11 seconds after commencement of bubble injection.

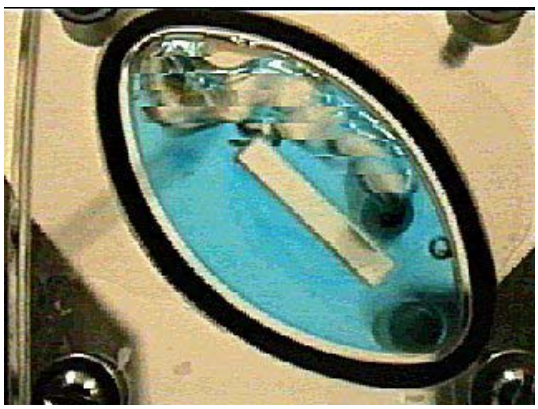

(c) 18 seconds after commencement of bubble injection. Blue dye was injected 11 seconds after commencement of bubble injection.

Figure 4.19: An example of the flow characteristics of the oval cell at ~8mL/s. Shown are snapshots in time during normal operation of the cell (from video capture).

4.5.7 Triangular Cell

Figure 4.20 shows the triangular cell ready for testing. Figure 4.21(a) shows the general flow characteristics of the cell at high flow rates. This cell whilst showing very good capability to handle high flow rates (due to most bubble activity being constrained to the top flow channel) still encouraged the formation of bubbles blocking the return path for the chemical solution. Figure 4.21 shows a three part time lapse of the flow characteristics and flow patterns generated within the cell.

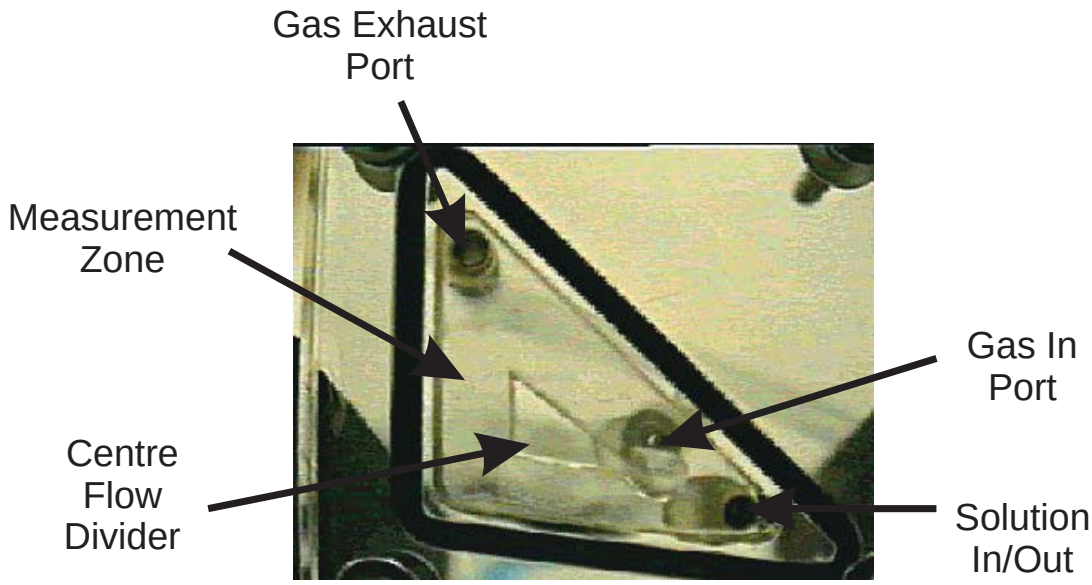

Figure 4.20: The empty triangular cell. Visible is the cell void, the center flow divider, and the three ports for the combined indicator chemical in/out, the sample gas in, and sample gas out.

(a) 6 seconds after commencement of bubble injection.

(b) 28 seconds after commencement of bubble injection. Blue dye was injected also at 28 seconds after commencement of bubble injection.

(c) 30 seconds after commencement of bubble injection. Blue dye was injected 28 seconds after commencement of bubble injection.

Figure 4.21: An example of the flow characteristics of the triangular cell at ~500mL/min. Shown are snapshots in time during normal operation of the cell (from video capture).

4.5.8 Discussion of Flow Performance

The cells perform the mixing function well for low gas flow rates ($\sim$16μL/s) allowing the circular flow pattern to actively mix the indicator solution into a homogeneous state (judged by uniform colour). The 'teardrop' cell achieved good bubble dispersion with minimal microbubble interference in the measurement area hence was used as the primary cell design for the prototype.

Problems with the current cell designs remain however. In particular their ability to handle high flow-rates and disperse bubbles is limited, due principally to excess bubble formation and frothing of the sample solution at the exhaust port. This results in insufficient solution being able to complete the circular flow route and hence developing a non-homogeneous solution. There is also a development of microbubbles (of order 0.1mm diameter) in the measurement area of the cells. Due to surface tension these microbubbles are of insufficient internal volume to be transported to the exhaust port as desired, and instead pass through the measurement zone interfering with the turbidity measurement.

Because the cells presented here have very low working volumes, any high flow rate of injection of the sample gas will indeed cause bubble blocks. These bubble blocks can be alleviated to some extent through several means (baffles or flow attenuation and mesh, as shown) but overall it was determined that the flow rate should not exceed 200μL/s.

4.6 Theoretical Modelling & Analysis

Preliminary computational fluid modelling of two cells has been conducted in collaboration with Prof Thanh Tran-Cong[1]. The fluid flow within the teardrop cell and an alternative design (conceived by Tran-Cong) was analysed using computational fluid dynamics software "FLUENT".

[1]Faculty of Engineering & Surveying, University of Southern Queensland, Toowoomba, Q, 4350, Australia

This analysis yielded two types of results, namely:

Streamfunction plot representing the flow rate flux. The graphed lines within the cell represent points which have the same flow rate in arbitrary units. This plot is useful in determining how well the fluid is mixed; and

Phase plot representing the proportion of a particular phase (gas or liquid phases) based on mass. This plot is useful in determining the overall effect of the bubble on the fluid mass as it travels upwards towards the exhaust port.

Due to the lengthy computational time required to obtain results from the model used for the two cells, no further analysis into the other cells was performed. Also because of this only two time points were analysed, 0.1 seconds , and at 0.2 seconds after the first bubble was injected into the cell.

4.6.1 Teardrop Cell Analysis

The 'teardrop' cell of Figure 4.10 was approximated by line segments as shown in Figure 4.22. The results from this analysis can be seen in Figures 4.22 and 4.23. The `streamfunction` plot for the 'teardrop' cell shows that a high sheer rate flow regime develops near the upper left region. This indicates that a majority of the interphase mixing (sample gas and indicator reagent) will occur at the top of the cell rather than at the point of sample gas entry. This would increase the likely-hood of bubbles affecting the turbidity measurement due to the mixing occurring close to the measurement region.

4.6.2 Alternative Cell Design

An alternative cell design was suggested by Tran-Cong in collaboration with the author resulting in the cell shape as seen in Figures 4.24 and 4.25.

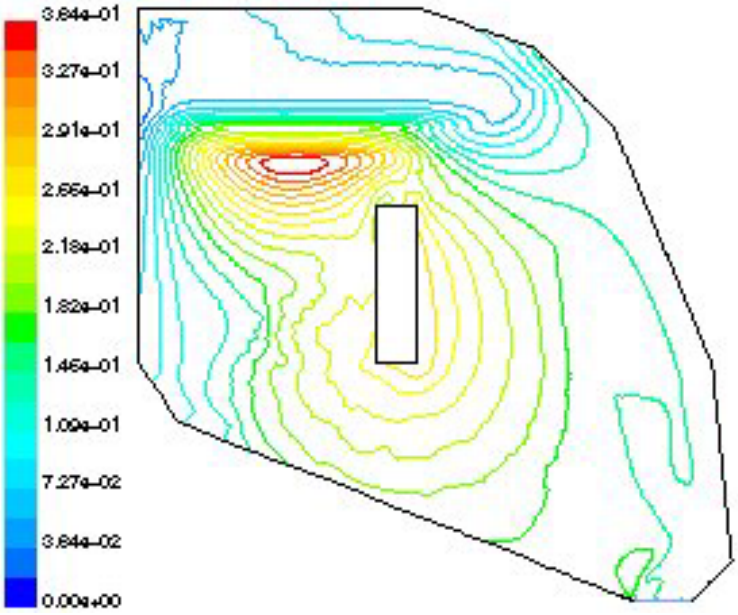

(a) 0.1 seconds after commencement of bubble injection.

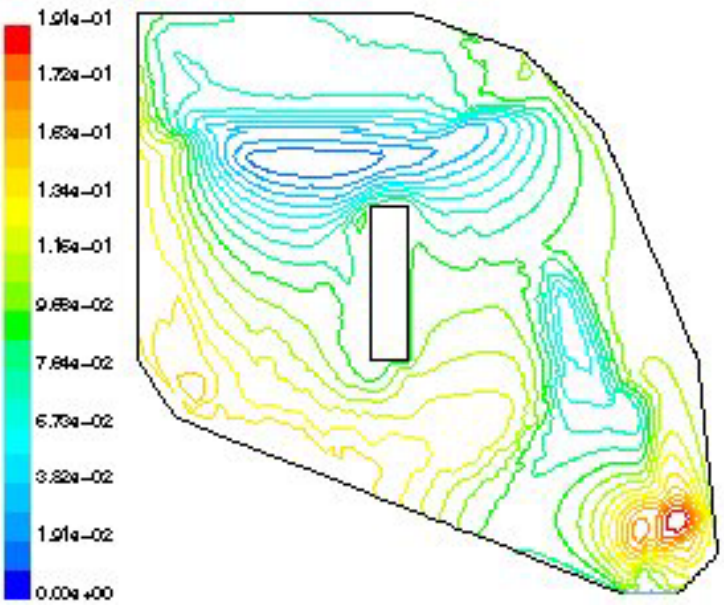

(b) 0.2 seconds after commencement of bubble injection.

Figure 4.22: Graphical representation of the shear rate (`streamfunction` plot) for the approximated 'teardrop' cell. The units are arbitrary with higher values (coloured red) indicating a higher shear rate.

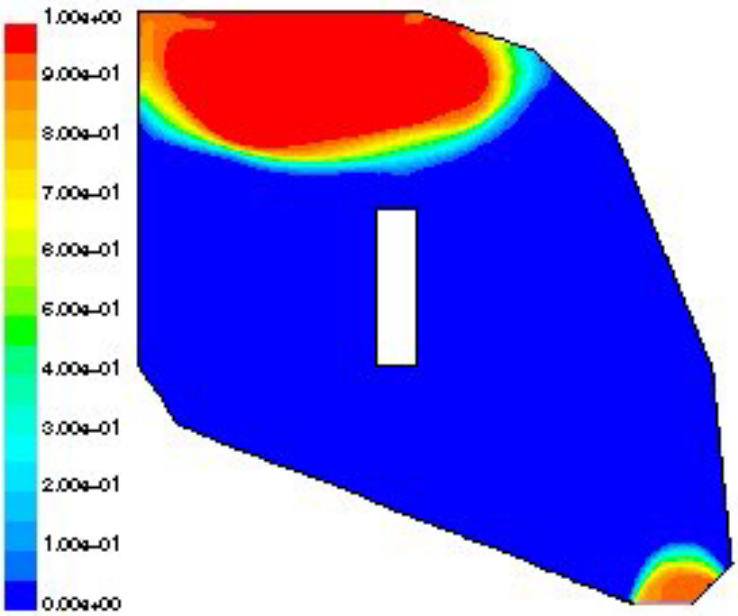

(a) 0.1 seconds after commencement of bubble injection.

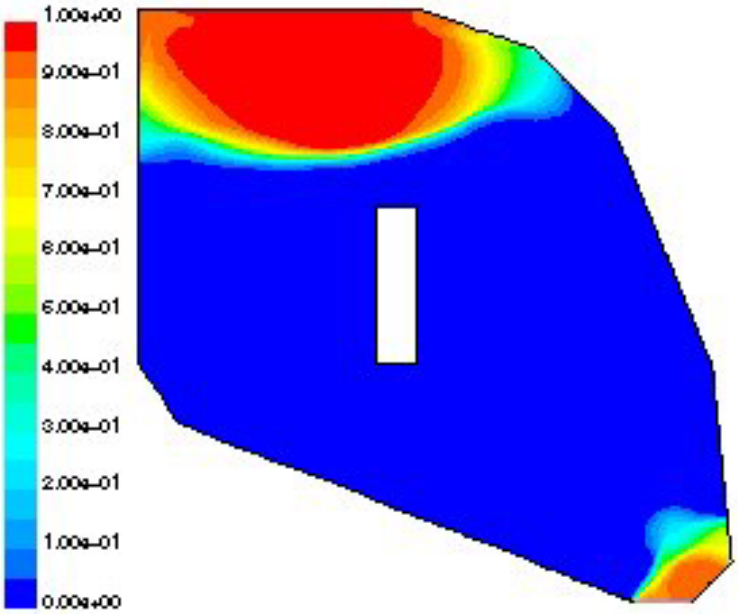

(b) 0.2 seconds after commencement of bubble injection.

Figure 4.23: Graphical representation of the gas/liquid phase (`phase` plot) for the approximated 'teardrop' cell. The units are arbitrary with lower values (coloured blue) indicating the liquid phase, and higher values (coloured red) indicating the gas phase.

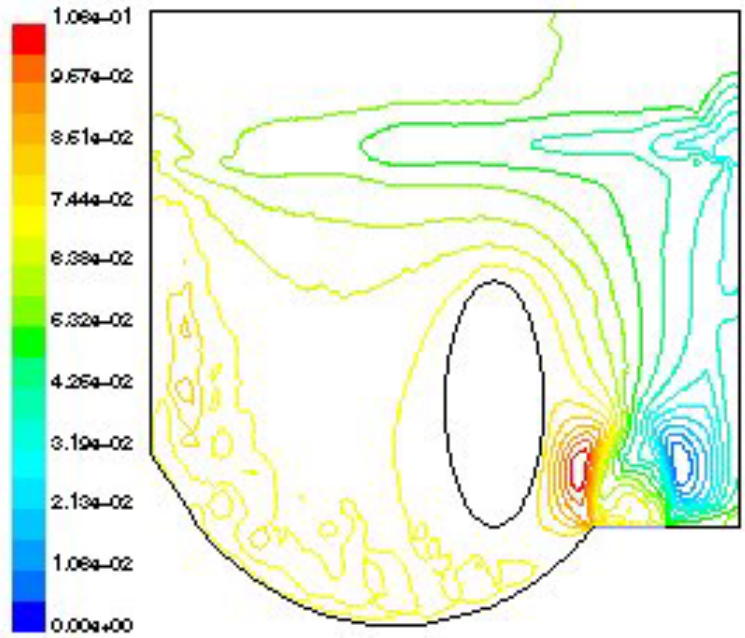

(a) 0.1 seconds after commencement of bubble injection.

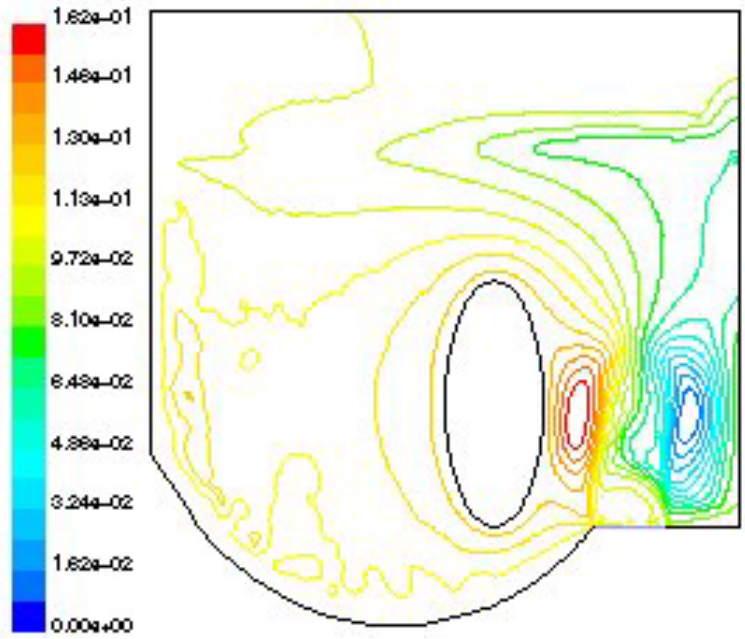

(b) 0.2 seconds after commencement of bubble injection.

Figure 4.24: Graphical representation of the shear rate (`streamfunction` plot) for the alternative cell suggested by Tran-Cong. The units are arbitrary with higher values (coloured red) indicating a higher shear rate.

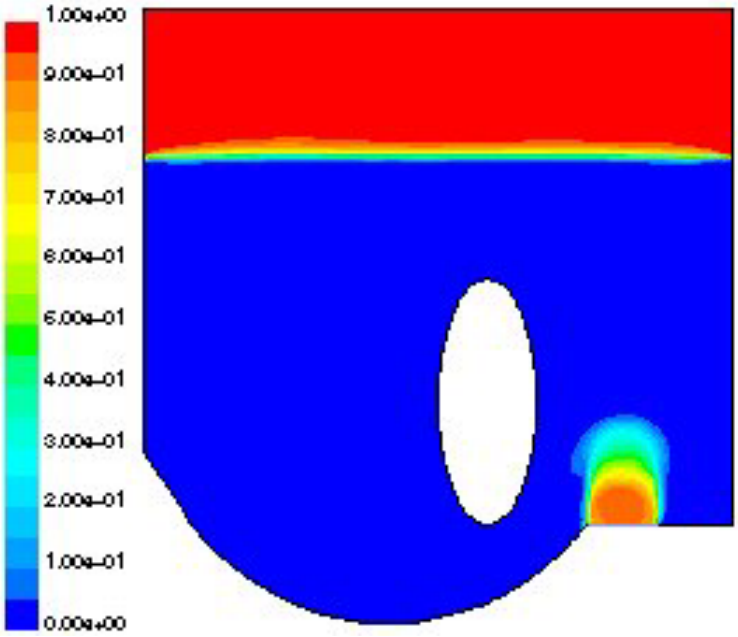

(a) 0.1 seconds after commencement of bubble injection.

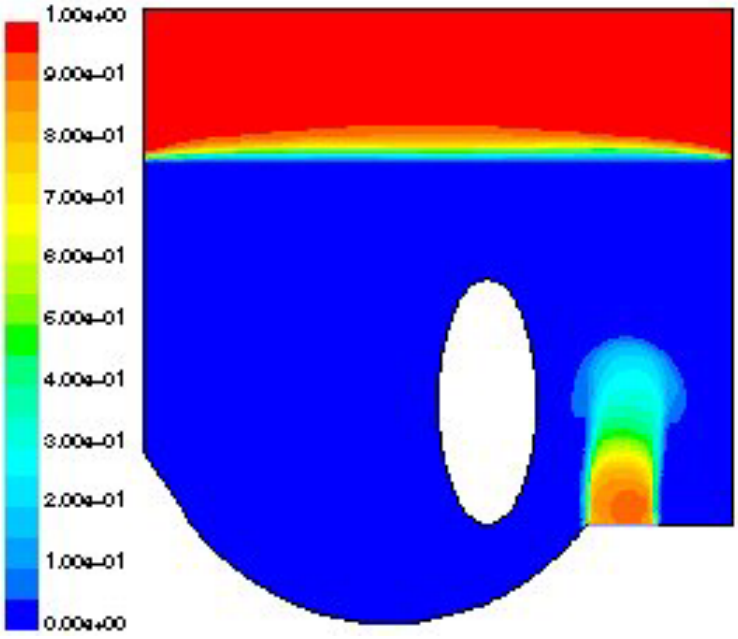

(b) 0.2 seconds after commencement of bubble injection.

Figure 4.25: Graphical representation of the gas/liquid phase (`phase` plot) for the alternative cell suggested by Tran-Cong. The units are arbitrary with lower values (coloured blue) indicating the liquid phase, and higher values (coloured red) indicating the gas phase.

This new shape was designed to initially allow better mixing at the point of gas injection rather than rely on mixing to occur at the top of the cell close to the optics as seen in the case of the 'teardrop' cell. Hence this (conceptual) cell has an elliptical flow divider close to the gas inlet to give a broad measurement zone (Figure 4.24 right hand side).

The flow pattern in this cell shows high shear rate flow regime next to the bubble injection point. This is highly desirable as it facilitates far better mixing and facilitation the chemical reaction than seen in the 'teardrop' cell. These results however were preliminary and incomplete, and were aimed at showing that computational modelling was possible if more computing resources were available.

4.7 Discussion of Cell Performance

Whilst the results from current tests indicate that the cells are reasonably stable, there are several problems with the existing cell design.

Because the cells were made from a reasonably brittle material namely acrylic, the machining in process to excavating the internal cell mechanism results in course internal cell walls.

To overcome this problem, two possible methods can be used, namely:

- The cell material could be chosen to be paid less brittle material, possibly Polycarbonate or another suitable material; and
- The final machining procedure could also include a polishing procedure with the cell walls are finished off to be optic a flat.

The cells perform the mixing function well for low flow rates ($\sim$1mL/min) allowing the circular flow pattern to actively mix the indicator solution into a homogeneous state. The 'teardrop with mesh bubble guard' cell achieved extremely good bubble

dispersion with minimal microbubble interference in the measurement area and hence was used as the primary cell design for the prototype. The interfacing of the optics to the cell using the PCBs proved effective, allowing accurately repeatable alignment through the cell with positional discrepancies causing optical/electrical errors less than the discrimination of the 8-bit A/D converter within the system microcontroller.

However, problems with the current cell designs remain. In particular their ability to handle high flow-rates and disperse bubbles is limited, due principally to excess bubble formation and frothing of the sample solution at the exhaust port. This results in insufficient solution being able to complete the circular flow route and hence a non-homogeneous solution. There is also a development of microbubbles (of order 0.1mm diameter) in the measurement area of the cells. Due to surface tension these microbubbles are of insufficient internal volume to be transported to the exhaust port as desired, and instead pass through the measurement zone. This is the principal cause of the optical signal noise as seen in Figure 7.3.

Chapter 5

Chemical Containment Cell Design II - Turbidity Measurement

5.1 Introduction

The purpose of the turbidity measurement is primarily to ascertain the time-dependent turbidity curve of the indicator solution as it reacts with the sample gas. This turbidity curve is then analysed to deduce the carbon dioxide concentration of the gas stream.

This chapter sets out design research to achieve the second and third transductions within the measurement system, i.e. turbidity to optical; and optical to electrical. This is illustrated in Figure 5.1 (which is a subset of Figure 2.15).

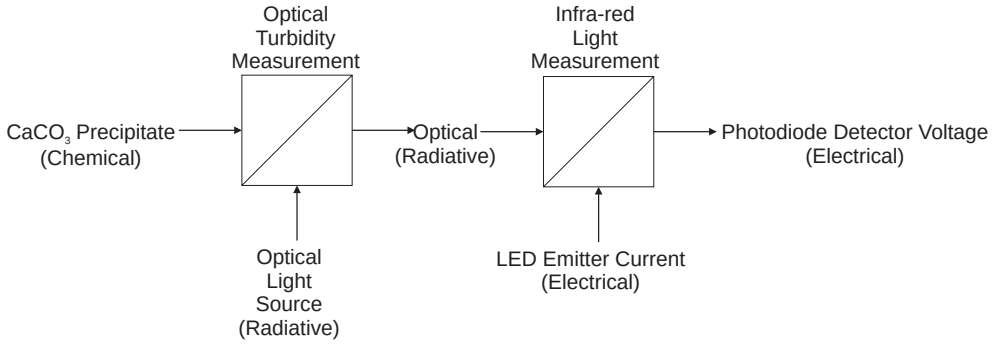

Figure 5.1: Transduction necessary for optical turbidity measurement.

5.2 Review of Turbidity Measurement Options

Turbidity is defined as the optical property of water (or other aqueous mixture) which causes light to be scattered and absorbed rather than transmitted (Gippel, 1988, p2). This scattering process is labelled Rayleigh Scattering (e.g. Hallett, 1996). The basis of the measurement is that the number of scattered photons can be related to the particle size distribution (e.g. Watts, 1983, p1185).

There are two fundamental types of turbidity measurements, namely attenuation measurements and nephelometric measurement. As light travels through the medium being measured, light is scattered by particles suspended within the medium resulting in a net optical signal loss. Should optical energy be absorbed by the particle, it will be retransmitted at a different wavelength (Nakamoto, 1970) often beyond the measurement spectrum of the detector. This then results an optical attenuation measurement such that as the number of particles increase, the light transmitted will decrease.

In contrast, nephelometric measurements measure the amount of light scattered by the suspended particles. The detector is placed out of the direct line of the incident beam, often at right angles (90°) to the incident light beam. Thus as the number of particles increase, the signal of the nephelometric measurement will also increase.

For this work, only the attenuation measurement was considered (see Section 5.3.1

for further details on Nephelometric measurements). The response of the attenuation turbidity measurement system was based on the performance of four components:

- optical source;
- optical detector;
- optical orientation and geometry; and the
- optical properties of the medium being measured.

Ideally, the optical source, detector, orientation and geometry of the measurement system will be constant for any given optical measurement. This will result logically in an attenuation measurement which will be a direct function of the optical properties of the indicator solution.

Turbidity , τ, is defined by the Beer-Lambert Law (for example Watts (1983, pp1176); Gippel (1988)):

$$\tau = \ln(\frac{I_o}{I_L L}) \tag{5.1}$$

where:

I_o is the incident radiation;
I_L is the measured intensity; and
L is the distance between the source and detector.

Rearranging gives:

$$I_L = \frac{I_o}{L} e^{-\tau} \tag{5.2}$$

with respect to the 'teardrop' cell the optical path length L is fixed.

In a situation where the precipitate suspension geometry is similar to a homogeneous solution with a population of monodispersive non-absorbing spheres, the turbidity has been derived as (Gippel, 1988):

$$\tau = N\pi r^2 K_t \tag{5.3}$$

where:

- N is the concentration of spherical particles in the solution;
- r is the average radius of the spherical particles; and
- K_t is the scattering coefficient.

However, in the case of $CaCO_3$ precipitate it cannot be assumed that the precipitate will consist of spherical particles. In this situation, the scattering coefficient K_t is usually replaced with a general factor K which combines both the scattering and absorption properties of the precipitate. Thus it is reported (also Gippel, 1988) that the turbidity-particle concentration relationship is:

$$\tau = MK \tag{5.4}$$

where:

- M is the mass concentration of spherical particles is in the solution [kg m^{-3}]; and
- K is the extinction coefficient [m^3 kg^{-1}].

Hence it is shown that the theoretical turbidity of the indicator solution is directly related to the concentration of $CaCO_3$ precipitate present in suspension.

5.3 Possible Optical Configurations

Several optical configurations were tested for use within the turbidity measurement system to observe their performance and identify any significant advantages or disadvantages of their design. (This work was performed before the final cell design was arrived at, and as such this work assisted in the preparation of the guidelines for cell development.) For these tests a single test tube was used filled with the chosen indicator reagent, $Ca(OH)_2$, and the general performance of the experimentation optics was observed. The four optic configurations tested were:

- vertical intrinsic optical detectors; and
- horizontal intrinsic optical detectors;

(having optical components within the reaction chamber) and:

- reflective extrinsic horizontal optical detectors; and
- transmissive extrinsic horizontal optical detectors.

(with optical components located outside the reaction chamber).

The vertical intrinsic optical detector, shown in Figure 5.2, was the first prototype sensor arrangement designed to measure the amount of precipitate in the vertical column of indicator solution. Both the emitter (type OP165A) and detector (type TDET500) were glued to a small PCB to which the signal wires were attached, and the assembly sealed watertight with silicone sealant. This resulted in a small and compact optic head assembly which could be placed into very small reaction vessels. Testing was performed during precipitate production as the sample gas reacted with the indicator solution. It was observed that bubbles would intermittently make their way between the emitter and detector pairs despite the sample gas injection tube being inserted some distance

away such as to minimise this effect showing that in an open cell, microbubbles would still be transported throughout the cell despite a primary bubble column. Significant coating of $CaCO_3$ precipitate on the lower optic (LED emitter) was also observed resulting in a lower incident emitted power to the detector (with slightly less coating occurring on the upper optic).

The vertical placement of the optic head in relation to the bottom of the reaction vessel and the gas injection tube also played a significant part in the observed performance. Because the precipitate was being maintained in suspension by the incoming gas stream bubbling through the reagent solution, placement of the optics lower than the sample gas tube injection point would result in little mixing of the precipitate in the region of turbidity measurement, and would result in the optics measuring principally the unsuspended/descending precipitate. Conversely, in the reverse configuration, with the optics higher than the sample gas injection point, significantly more bubbles would obscure the optics and measurements of the precipitate would lag or not reach full opacity due to inadequate mixing of the solution in the region of the optics. The geometry of these two configurations was also undesirable due to their invasiveness nature, the need for waterproofing and possible failure as a result of inadequate sealing. For these reasons this alignment geometry was not pursued.

A variation of this sensor, the horizontal intrinsic optical detector, was also examined. This sensor differed from the vertical sensor only in the alignment direction of the optics. The sensor consisted of the optic pair (optical components removed from a commercially available slot detecting module) with leads attached directly to the optical components and the entire assembly waterproofed in a similar manner to the previous version. Each optical component was then attached to a metal "U" bracket to maintain their separation and alignment as shown in Figure 5.3. This sensor performed similarly to the previous vertical version in that the optical components would quickly become coated with precipitate from the chemical reaction, with position variations generating different performance characteristics. Should the optics be placed too low in the reaction chamber, they would measure predominantly fallen-out precipitate, and

if placed too high in the fluid column, mixing problems would cause non homogeneities in the solution resulting in inconsistent readings. Again, because of the invasiveness nature of this sensor design, it was not pursued.

The third tested sensor type was the reflective extrinsic horizontal optical detector, as shown in Figure 5.4. The optical module used was a commercially available reflective type sensor, configured to measure the reflectance of the precipitate particles through the reaction cell walls. Using this method it was hoped that effects from bubble streams and precipitate coating could be minimised, and this was observed for certain cases. Whilst the actual optics would not be coated with precipitate, the cell wall was still susceptible to this effect (however at a much reduced rate of coating due to the smooth nature of the glass walls). Also the reflected signal did not exhibit adequate signal strength for reliable measurement. This was mainly due to the limited opaqueness of the solution when precipitate was produced and also the highly reflective nature of the reaction vessel glass walls (a test tube). Whilst this method did exhibit potential, it was also not pursued in favor of the final tested sensor type.

The fourth tested sensor type was the transmissive extrinsic horizontal optical detectors, Figure 5.5. This method measured the optical transmission through the entire width of the cell, and as such overcame many of the problems experienced with the previous sensors. This optical configuration would permit the optics to remain dry and clean of any precipitate fouling whilst still allow for good measurements of the turbidity within the measurement cell. Issues relating to the fouling of the optic path with bubbles whilst in a simple test-tube cell were overcome by using the special cell designs as shown in Section 4.5. Thus the final chosen optical configuration was based on the transmissive extrinsic horizontal configuration.

However, in all cases ambient light levels were found to affect the results of the turbidity measurement as the entire measurement chamber was open to ambient light levels. To prevent this all subsequent cell designs were isolated from the optical environment.

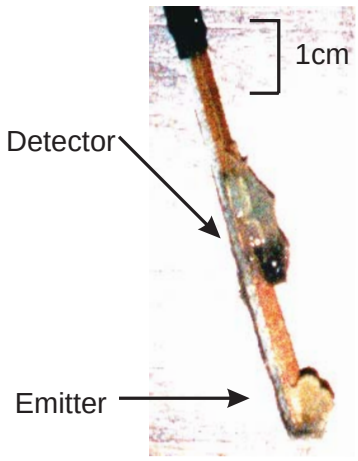

(a) A photograph of the sensor.

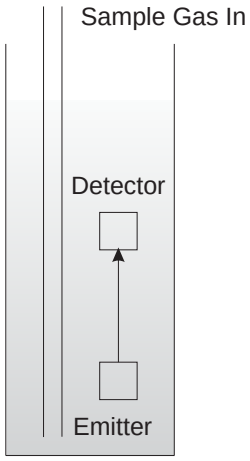

(b) The measurement orientation.

Figure 5.2: Vertical axial intrinsic optical detector as used during testing of possible optical turbidity measurement configurations.

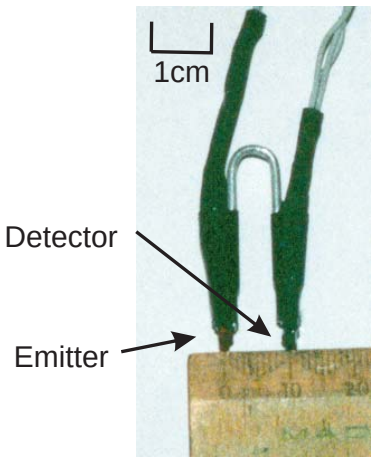

(a) A photograph of the sensor.

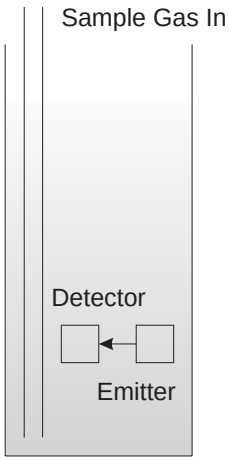

(b) The measurement orientation

Figure 5.3: Horizontal intrinsic optical detector as used during testing of possible optical turbidity measurement configurations.

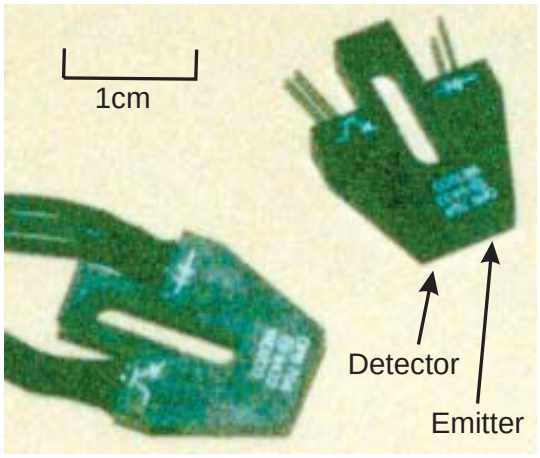

(a) A photograph of the sensor.

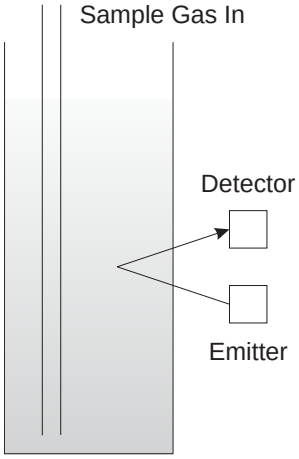

(b) The measurement orientation.

Figure 5.4: Reflective extrinsic horizontal optical detector as used during testing of possible optical turbidity measurement configurations.

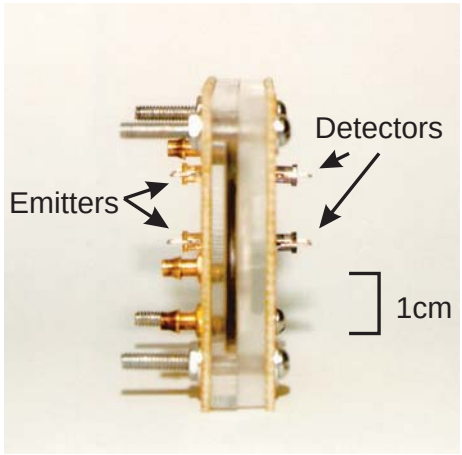

(a) A photograph of the sensor.

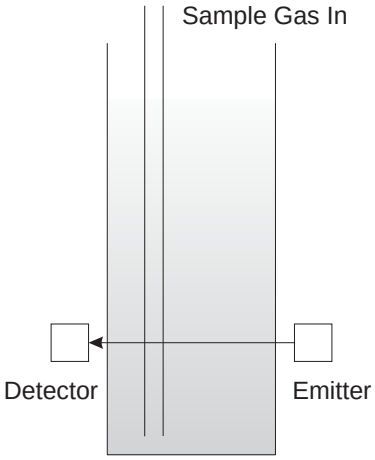

(b) The measurement orientation.

Figure 5.5: Transmissive extrinsic horizontal optical detectors as used in both hardware prototypes.

5.3.1 Other Possible Geometries

The optical geometries presented in the previous section were by no means a complete representation of all possible geometries: many other arrangements may be of potential use in this application. In particular, no experimentation was performed with off axis optical systems, where the optical emitter and detector were not on the same axis (as typically used in nephelometric measurements). An example of this geometry is shown in Figure 5.6. This alignment type would not have shown significant advantages over the transmissive extrinsic horizontal configuration (Figure 5.5) for the $CaCO_3$ precipitate, and would have required the reaction vessel to have a clear optical path at 90°to the incident beam. In the case of the implemented cells, this was not feasible as an "O" ring seal, required to maintain a watertight enclosure, was blocking the required path.

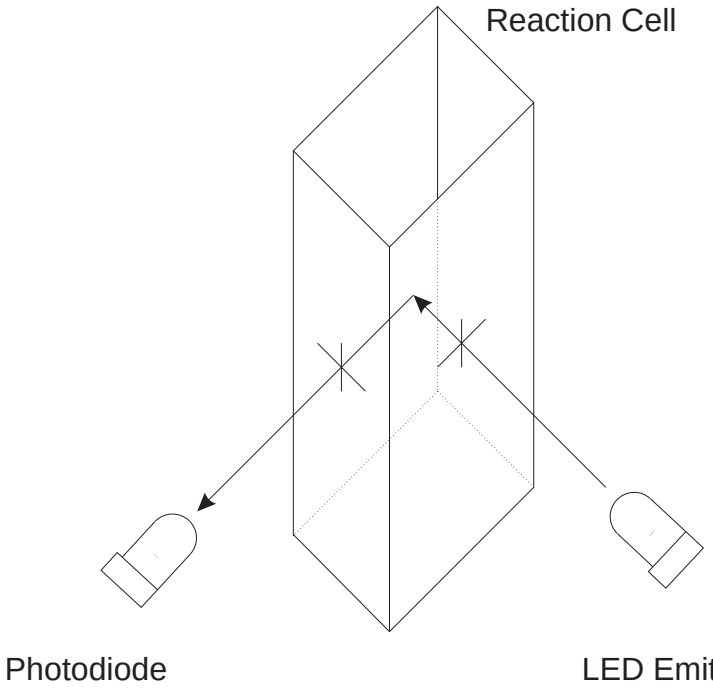

Figure 5.6: Example geometry of an off-axis optical sensor suitable for measurement of precipitate produced within a reaction cell. The emitter and detector alignment are rotated by 90°with the detector measuring optical scatter instead of transmissive attenuation.

5.3.2 'Digital' Optical Sensors

In addition, some work was conducted into using preamplified optical detectors that would produce a binary output based on an internally set optical threshold point, instead of relying on an analog measurement and performing the optical threshold measurement using models. Several commercial preamplified optical detector modules were available for use using this technique. Whilst this type of sensor could have greatly simplified the design of a smaller and simpler wet chemical instrumentation system, it would not have allowed for determination of optical baseline values, and the need to adjust these values in subsequent measurement cycles caused by the progressive fouling of the cell walls.

Additionally, through the use of analog optical sensing, it was possible to construct a model such that only a small amount of precipitate would have to be produced to obtain a measurement rather than waiting for the peak precipitate production to occur (This is presented in Chapter 7). For these reasons binary output optical modules were not used.

5.4 Prototype Implementations

Once the turbidity measurement type was chosen (namely the transmissive extrinsic horizontal configuration), investigation into the actual measurement hardware could begin.

5.4.1 Selection and Evaluation of IR Components

As an attenuation measurement was required, suitable optical components were required to be chosen based on their predicted performance measuring the $CaCO_3$ precipitate in suspension. As such the selection of the optics was primarily a function of the optical effects produced by the precipitate itself.

The average particle size of the $CaCO_3$ precipitate was unfortunately able to be estimated only very approximately and hence the effects of individual precipitate particles on light at the wavelength scale could not be assessed. It was therefore assumed (as was reasonable) that the precipitate would act to cause bulk attenuation by the mechanism of Rayleigh Scattering. As such it was assumed that if it would cause scattering in the visible range, it would also perform a similar function (and possibly somewhat reduced, due to the longer wavelength) in the infrared range. This had been confirmed in previous experiments and as such infra-red optical components were deemed suitable. Infra-red optics operating at the 935nm wavelength range were then selected not only because of their abundance, low cost and simple implementation, but also because the spectral range of the optical pair would also assist in masking effects from visible light.

The optical emitter chosen was type-OP165A and the matched detector chosen was the TDET500 (Specifications presented in Appendix A). This optical pair would then form the basis for the turbidity measurement system.

5.4.2 Optics Mounting and Alignment

In order to mount the chosen optics onto the cell, a printed circuit board (PCB) mounting system was used to hold the optics (Appendix Section A.1). A specially designed PCB (to match the cell for which it was designed) had tracks printed onto it to provide electrical signals to the optics as well as provide a simple means of attaching these signals to the control system. Holes were drilled into this PCB plate which directly related to the positions where the optical components would be placed. Each cell design had a specific measurement zone, and as such this PCB would account for that positioning, thus if the internal design of the cell changed or the locations of the optical components needed to be revised, new versions of these mounting PCBs would be created to ensure that repeatable optics alignment was maintained.

Up to three optical pair observation stations were located for each measurement zone for the respective cells. These were usually arranged in a vertical column (with the

exception of the oval and circular cells which were arranged in an arc). Each of the individual emitters and detectors were individually wired so that they could be controlled independently of each other. Whilst three stations were available, only two were ever used, being the uppermost and the lowermost, leaving the center station free of components.

As the optics mounting PCB was mounted close to the cell exterior, the LEDs were inverted and mounted through holes in the PCB so as to allow a high level of repeatability in the construction (Figure 5.7). Each LED or photodiode mounted onto the PCB was aligned manually to be as close to perpendicular to the PCB surface as possible.

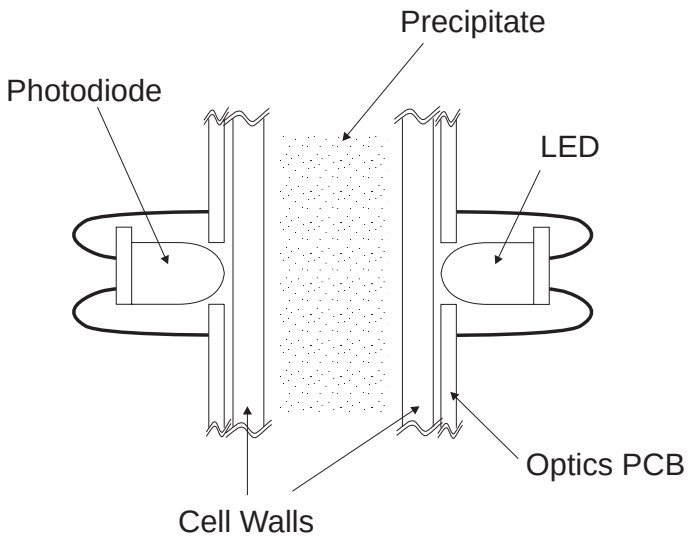

Figure 5.7: Mounting diagram for the optical components being soldered to the alignment PCB. Shown is the method to mount the LEDs and photodiodes to the PCB as well as the required optical-pair alignment desired.

The PCB was 50mm×50mm×1mm with mounting holes matching that on the cell such that the entire assembly of the optics mounting PCB and the cell could be bolted together to form a single rigid sensor. The optical component mounting PCB as well as the alignment of the entire assembly is shown in Figure 5.8.

(a)

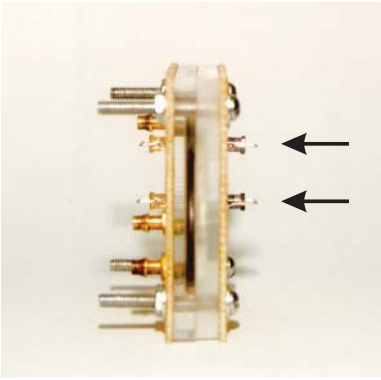

(b)

Figure 5.8: Two views of the optical configuration, (a) showing the expanded view of the cell as well as the placement of the IR LED emitters; (b) showing the alignment of the emitters and detector components (arrowed).

5.4.3 Optical Energy Dispersion

The selected IR LED (OP165D) and photodiode (TDET500) were both packaged in traditional LED packaging such that the emitted or detected light would pass through a window with a specific aperture. In both cases the aperture window would radiate or collect 50% of the energy within a cone subtending 10° to the centerline, with no other lenses attached other than the curved shape of the LED packaging. Analysis was performed to ensure that enough energy would be transmitted through the cell to the detector. Using the known refractive indexes of the materials present (Table 5.1) the

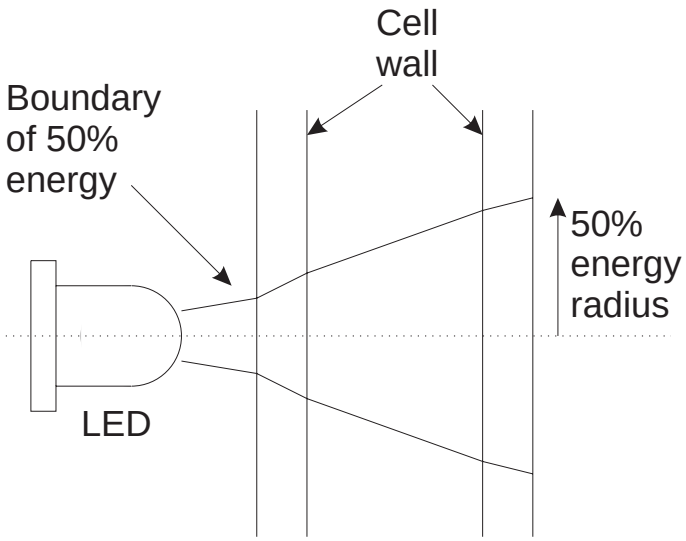

Figure 5.9: Demonstration of the refractive effects on the 50% energy radius through the cell.

total refractive properties of the cell were determined.

Table 5.1: Refractive index of materials in the optic path of the cell.

Material	Refractive Index
Acrylic	1.5
Clear Epoxy (assumed same as acrylic)	1.5
Water	1.33

As seen in Table 5.2, the final energy radius (for 50% of emitted energy from the LED assuming no internal reflection or other losses) was calculated as being 2.03mm at the cell wall surface where the emitter would be mounted, as illustrated in Figure 5.9. The detector was likewise estimated to have a 50% sensitivity radius of 0.35mm at this point, thus showing that a moderate amount of energy would not reach the detector, however the photodiode would still function properly. Note that no consideration was made to the approximately 1mm air gap between the curved sides of the LED and the acrylic surface, which if accounted for would slightly increase the energy dispersion radius. Therefore the optics could be mounted directly onto the face of the cell without any compensation lens. Should there have been a significant effect (which was highly unlikely), the energy coupling could have been improved by milling small lenses into

Table 5.2: Effects of LED emitter aperture radius by materials in the optic path of the cell.

Position	Refractive Angle	Thickness	50% Energy Radius Displacement
LED	10°	2mm (assumed)	0.35mm
Cell Wall	10°	3mm	0.53mm
Cell Void (water)	8.85°	4mm	0.62mm
Cell Wall	10°	3mm	0.53mm
Total Displacement			2.03mm

either the outer or inner surface of the cell walls to correct for this refraction, however as only a moderate amount of energy would be lost, the use of uncorrected LEDs was considered acceptable.

5.4.4 Emitter and Receiver Drive Circuitry

The drive circuits for both the emitter and receiver optics were initially based in simple voltage divider circuits (Figure 5.10- 'Mk.I'). This circuit would drive the LEDs with a fixed forward current of 10mA (5 volt supply), whilst the detector forward current could be varied. This variability of the optical detector allowed experimentation to select the best optical conditions within the cell. Should the LED be too bright, or the detector too sensitive, the detector would saturate rendering the optic pair unusable at those settings, and likewise, should the LED be too feint, or the detector too insensitive, insufficient dynamic range would be available for the optical measurement. Thus by trial and error the detector forward current and hence sensitivity was set so as to achieve a reasonable amount of dynamic range to be able to measure an almost clear liquid to one saturated with suspended $CaCO_3$ precipitate.

Note that the detectors were configured such that an increase in precipitate would result in an increase in measured voltage, which was not only easy to implement in hardware, but also logically convenient to assist in interpretation of the recorded data. This was the implemented circuit for the Mk.I hardware prototype.

The Mk.II prototype however used a more advanced approach. The implementation

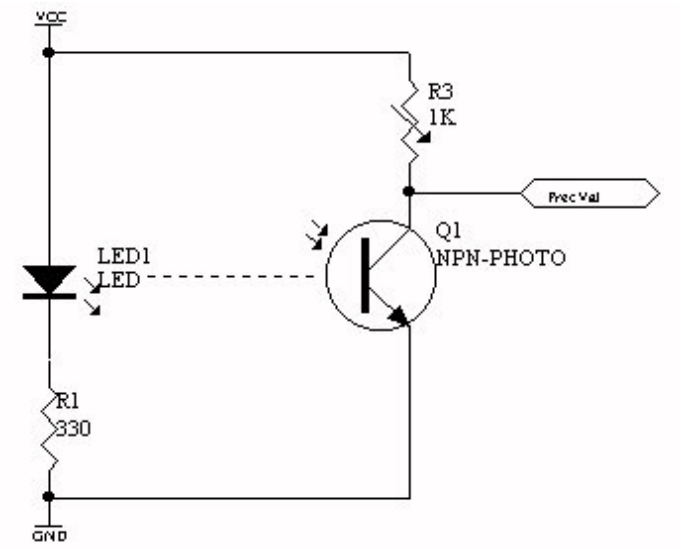

Figure 5.10: Mk.I current drive schematic for the LED emitter and Photodiode detector pair. (Two such emitter/photodiode pairs were installed on the reaction cell - Figure 5.5(a)).

used allowed the forward current of the emitters and the detectors to be independently controlled via the microcontroller system, to permit smart sensing functions and automatic selection of the two forward currents. For example, the output intensity from the emitter LED could be varied to impose a modulation of the infra-red signal (and hence permit synchronous detection), or to increase output intensity to counteract the effect of high optical loss materials such as calcium hydroxide heavily saturated with calcium carbonate particulates.

Likewise control of the detector (photodiode) bias current was implemented to allow varying of the overall sensitivity of the photodiode. By allowing the control of these two parameters it was hoped to explore adaptive optical control where the best possible operating parameters (for output intensity and detector sensitivity) could be selected for the given operating conditions and state of the indicator chemical in the cell.

The implementation of the control for both currents was performed by using four individual Howland Voltage to Current converters (Figure 5.11(a) (Stanley, 1990, p73)).

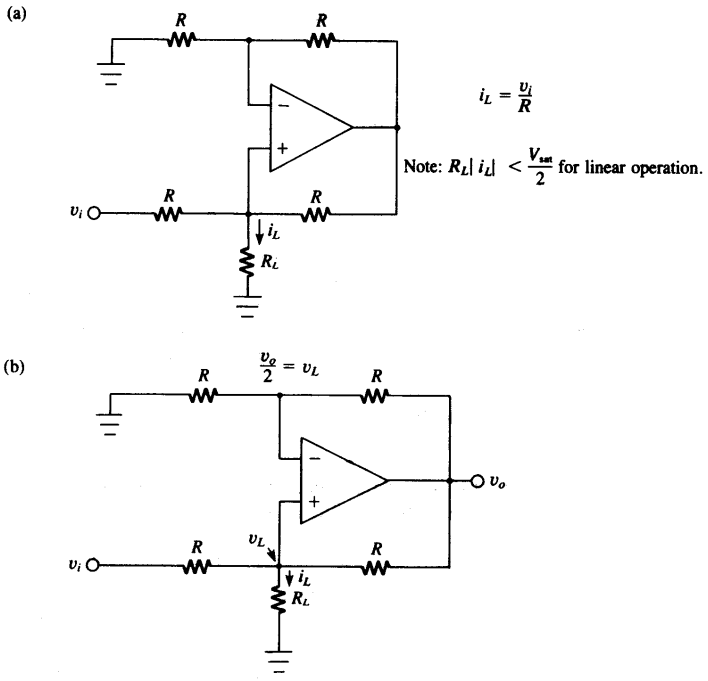

(a) Howland voltage controlled current source example (reproduced from Stanley, 1990, Figure 2-16, p73).

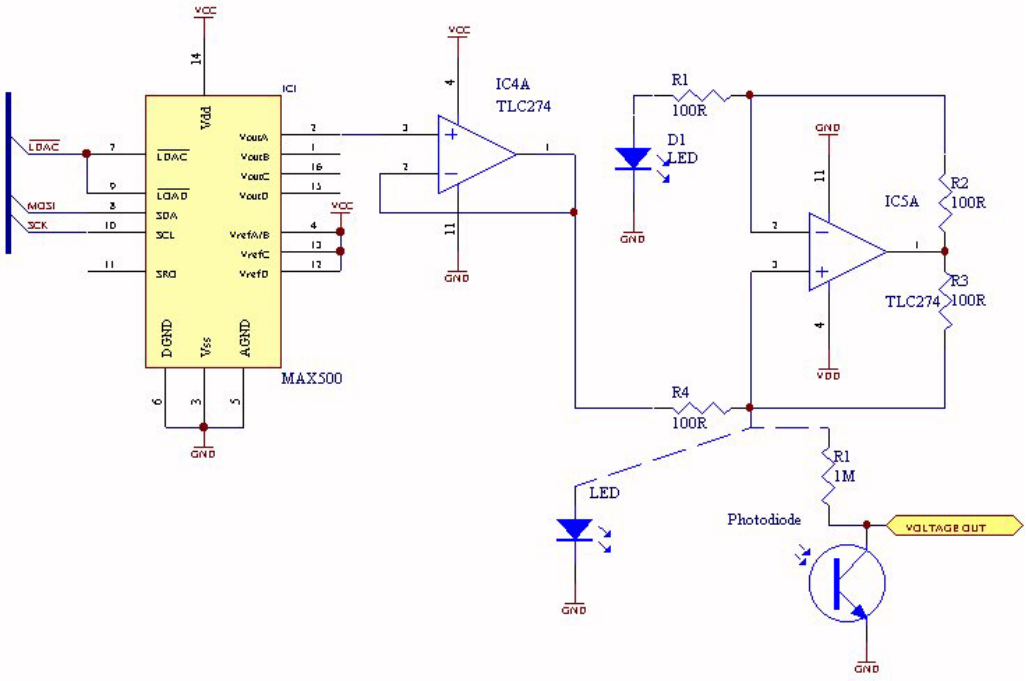

(b) The implementation of a Howland voltage controlled current source. Seen are the four stages for the LEDs and photodiodes for the two separately controllable emitter/detector pairs.

Figure 5.11: The Howland voltage controlled current as used in the Mk.II hardware prototype to control the LED and photodiode forward currents.

These converters were based around the TLC274 OPAMP. The voltage used to control the converters was derived from a quad output DAC (MAX500). Only two of the four available outputs of the DAC were used to control the converters, with a pair of converters sharing each DAC line. (The other two outputs from the DAC were used to control the adaptive analogue electronics). A schematic of the four voltage to current converters appears in Figure 5.11(b). Additional LEDs (such as LED "D1") were used to balance the circuit such that a smooth linear output could be achieved. This implementation allowed each current line to be variably selected from 0mA through to 20mA. However, as the output voltage would tend to follow the current, the LEDs connected to their respective current sources would not operate below a certain point set point due to the need to overcome the LEDs on-voltage.

5.4.5 Synchronous Detection

Although synchronous detection was highly desirable, no hardware based synchronous detection systems were implemented in either hardware prototype. However as previously mentioned, synchronous detection could have been employed using a software based method within the Mk.II hardware prototype. Synchronous detection would have enabled the effects of external lighting to be minimised, and also drift effects of the driving/detecting circuitry and analogue electronics to be removed or greatly reduced. For a commercial application or extension of the prototypes presented here, the addition of synchronous detection would be essential to assist in improving the signal dynamic range and minimise the effects of noise both internal/system based, and external influences.

Chapter 6

Fluid Transport & Control

6.1 Introduction

In order to transport the indicator and cleaning solutions into and out of the chemical containment cell and control the sample gas flow, a fluid transport and control mechanism was developed for each prototype version. This chapter presents the components and methods used to perform these functions and the control strategies adopted.

6.2 Purpose & Requirements

Carbon dioxide measurement using the chemical containment cell requires a sequence of four events, namely:

- indicator solution injection into the cell;
- sample gas injection into the cell;
- waste products removed from the cell; and
- cell cleaning.

All of these events required some form of gas and fluid transport mechanism. The solution transport system also had to interface to the three ports available on the cell. These events also needed to be performed under microcontroller control and would therefore require the pumping system to be easily interfaced. The transport system would also require reservoirs for the indicator reagent and cleaning solution (if required) as well as for the waste generated by the cell.

6.3 Mk.I Prototype

6.3.1 Introduction

As previously noted, the 'Mk.I' prototype was designed as a 'proof-of-concept' unit. As such, the fluid control system was built up as necessary rather than designed from scratch and several iterations were required in order to achieve a workable result. There were several possible configurations for the transport mechanism with the method chosen being only one of many possible designs. With hindsight, this prototype fluid control design was not optimal and did suffer from several deficiencies.

6.3.2 Function Definition

In the first prototype, only three fluid/gas control tasks were required, namely:

- filling of the cell with the indicator reagent from the reagent reservoir;
- injection of the sample gas into the cell from the sample gas source (e.g. from ambient atmosphere, sample tube, or gas standard); and
- draining of the used reagent from the cell and into the waste reservoir.

The reaction cell used for this prototype version was the 'teardrop with mesh guard' cell which had three available access ports being; fluid in/out port; the gas in port;

and the gas out (exhaust) port (Figure 4.14). Separating the fluid transport functions between gas and liquid reveals that there was only one gas function (sample gas in), with two separate liquid functions (reagent in; and waste out). Three pumps were chosen to perform these duties, with each dedicated to one function. Whilst it was conceivable that only two pumps could be used (by combining the reagent in/waste out functions), this would have require one of the fluid pumps to permit bi-directional control. This extra complexity would have typically involved a 'H' bridge arrangement using 4 switching FET devices (Figure 6.1(a)), and therefore additional complexity in the control of the device. Thus it was decided to use an extra pump to perform the reverse pumping action. Simple microcontroller controlled switches with a simple on/off function could then used to control each of the three pumps independently (Figure 6.1(b)).

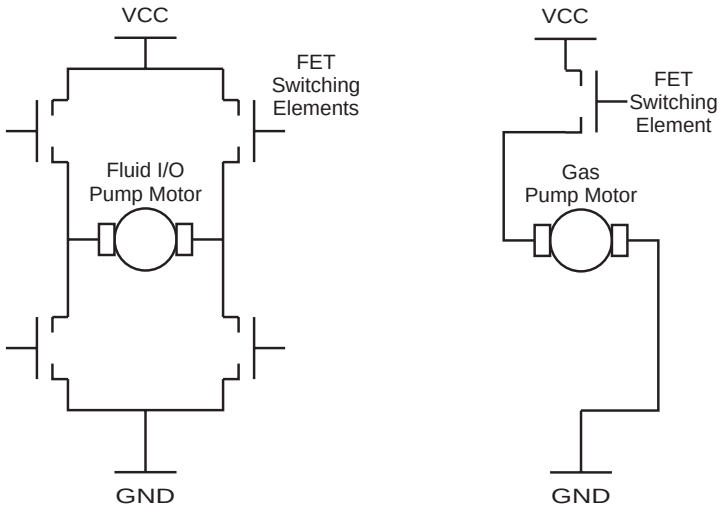

(a) 'H' bridge configuration required to control the flow direction of a bi-directional pump.

(b) The simple on/off switching control required for a uni-directional pump.

Figure 6.1: Comparison between the two types of FET switching circuits required for a bi-directional versus uni-directional pumping.

6.3.3 Selected Pumps

The selected pumps were miniature positive displacement 'gear' pumps (type Ming Yang Model Co. Ltd, Fuel Pump, No.200, Figure 6.2), and were originally intended for pumping fuel like substances however were deemed suitable for use with this prototype. These pumps were compact and rated for operation between 3 to 6 volts which was well suited to the application. They ran adequately at 5V and at this voltage were capable of pumping 5mL/s (= 300mL/min). These pumps were miniaturised further by removing their outer casing and mounting them using a smaller custom mounting bracket, such that the final volume occupied by these three pumps was reduced to 80mm×80mm×15mm (Figure 1.2(a)).

These gear pumps were used not only for the fluid transport lines but also for the gas injection line (Performance results shown in Section 10.3.2).

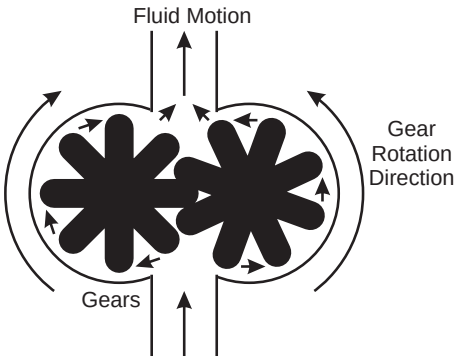

(a) Rotating inter-meshing gears in a specially designed channel, force fluid entrapped within the gear teeth from the inlet, around the outside of the channel, to the outlet.

(b) Photograph of the gear mechanism of a typical gear pump.

Figure 6.2: Photograph and diagram of the gear pump mechanism used within the fluid transport system.

6.3.4 Interconnection Scheme

The connection scheme for the prototype (Figure 6.3) consisted of the three pumps, check valves, plastic tee pieces, and standard 4mm plastic (polyurethane) tubing.

The gas flow line used a dedicated pump attached to the gas in port on the cell. A check valve (Figure 6.4) was used to prevent indicator solution from draining back into the pump or the gas sample source during filling or draining operations when the gas pump was inactive.

The indicator solution-in and waste-out functions were combined through the same port and a 'tee' connector was used to join these two pumping lines. The indicator solution section used a checkvalve to prevent drainage of reacted indicator solution back into the fresh solution reservoir, contaminating the indicator solution. Another check valve was used between the indicator source pump and drain pump to provide some flow restriction to prevent leakage of the fresh indicator solution through to the drainage collection reservoir, as would be caused by the positive pressure before the checkvalve during transport of the indicator solution into the cell.

An extra line was used from the exhaust port to the waste reservoir to allow escaping gas to make its way out of the system and to cope with indicator solution overflow from the cell, should it occur. Finally, small plastic containers (500mL volume) were used as the reservoirs for the indicator and waste solutions.

6.3.5 Pump Motor Interfacing

Interfacing of the pumps to the microcontroller system was achieved through the use of TTL level controllable Field Effect Transistors (FET). These FETs were arranged such that ground switching was used (Figure 6.5). This circuit would accept a TTL logic signal from the microprocessor (be it a simple on/off signal or a more complex

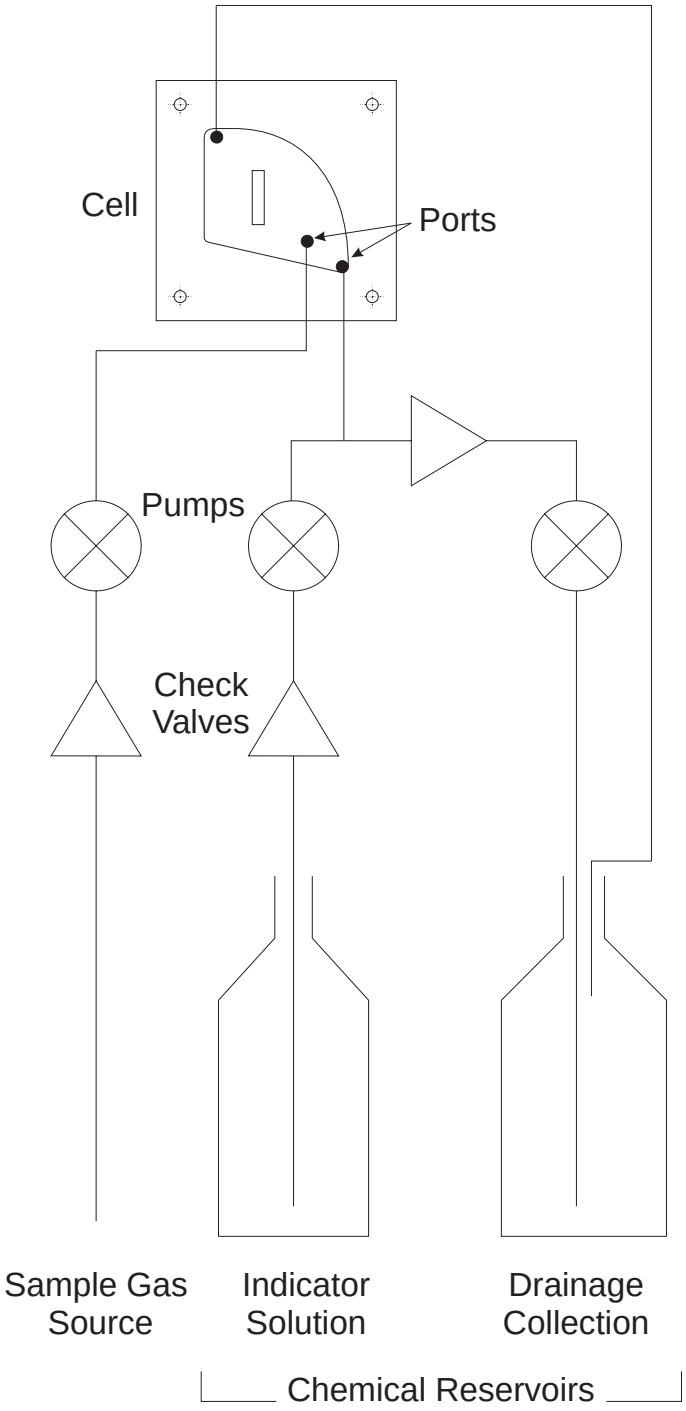

Figure 6.3: Connection scheme used for the Mk.I prototype. Three pumps (two for fluid control, and one for gas control) were connected to the cell using check valves, 'tee' pieces, and 4mm polyurethane tubing.

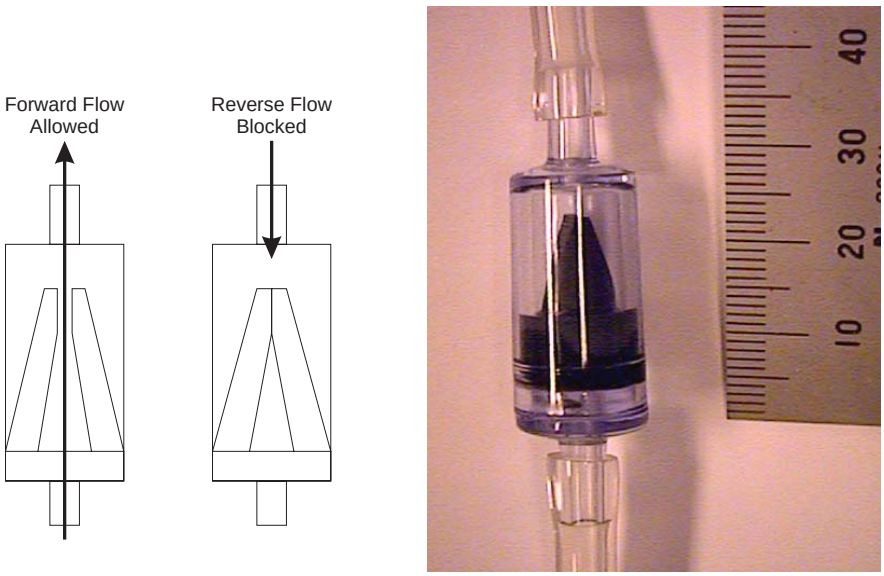

(a) The checkvalves used a small rubber valve to prevent backflow.

(b) Photograph of a typical check valve used within the CO_2 measurement system.

Figure 6.4: Photograph and diagram of the check valve mechanisms used within the fluid transport system.

modulation) and switch the ground line for the motor, where a low TTL signal would turn the motor 'on', and a high TTL level would turn the motor 'off'. Initially no power filtering of the voltage applied to the motor was supplied and subsequently significant voltage spikes were observed across the FETs and motors introducing noise back into the main system voltage supply. This would then affect the optical components (and turbidity measurement) which were energised from the same supply voltage. By placing a capacitor and flyback diode across each motor (components C1, and D1 of Figure 6.5), acceptable noise suppression was achieved.

6.3.6 Pump Motor Control Scheme

As a Motorola MC68HC11 microcontroller was used as the main system controller, it became possible for advanced control of the transport system. As such, a Pulse Width Modulation (PWM) control system was developed that allowed the microcontroller to

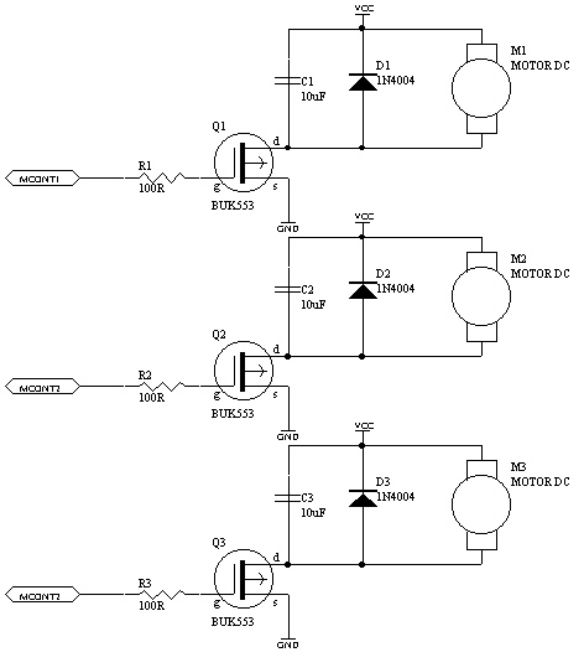

Figure 6.5: Pump motor control schematic showing the three FET switching devices.

select variable speeds for the pumps. This was highly desirable for fluid pumping as the full speed flowrate of the pumps was excessive (5mL/s) for the small cell volume (∼2mL). This high flowrate would result in the cell being filled in under one second, typically with wastage of indicator reagent as it was forced out the exhaust port before the pump could be turned off. By using PWM control of the motor, the flow rate could be controllably slowed so that the cell would typically be filled in 4 to 5 seconds.

6.3.7 Automated Cell Filling

The microcontroller control of the pumps allowed for the cell to be serviced and maintained with a fair degree of intelligence as provided by the microcontroller. During a typical measurement cycle, the cell would be flushed with fresh chemical indicator to clear any debris or contaminants, then drained and refilled again with fresh indicator in preparation for the optical turbidity measurement (with further information on the

measurement procedure is presented in Chapter 7).

Another significant advantage of the microcontroller controllable pumps was that when coupled with optical measurements from the two optical pairs attached to the cell, 'automated filling' could be performed by using optical liquid level measurements. The sequence of events is illustrated in Figure 6.6.

When the cell was empty, both of the optical detectors would see a clear path with some internal optical refraction (Figure 6.6(a)). As fluid was pumped into the cell, the lower optics would become obscured by the surface meniscus of the reagent (Figure 6.6(b)) which would result in a higher turbidity measurement. As the surface wave moved past the detector, the turbidity would become much lower due to the reduction of internal refraction (due to the indicator solution having a refraction index closer to perspex than air previously). As the surface wave continued to rise the same effects would be present at the upper optics (Figure 6.6(c) and 6.6(d)). Once the cell was full, both turbidity measurements would remain at their lower value (Figure 6.6(e)). The draining process would result in the exact reverse order of the above description. Turbidity measurements from an example filling and draining cycle are illustrated in Figure 6.6(f), showing that the lower detector during filling observes the increasing then decreasing turbidity, shortly followed by the upper turbidity measurement showing the same pattern. Should the cell be filled with this monitoring system the pump connected to the indicator solution would be turned on, these turbidity measurements made, then once both optical pairs reached the lower turbidity state, the pump would be stopped. It would also be possible to perform a similar function by just using the turbidity information of one optic pair.

Further information could also be derived from these turbidity measurements. As the distance between the optical pairs was known (13mm), the fill rate could be calculated from the time delay between the two filling or draining patterns. For example, in the case of Figure 6.6(f), the filling surface rate was calculated to be 1.4mm/sec. This feature however was not implemented, but is presented as a future consideration for the smart sensor programming.

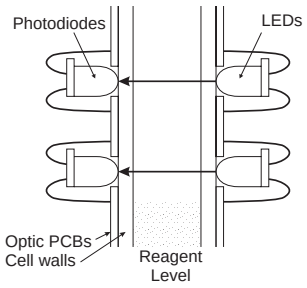

(a) Beginning of the filling process. Both optic paths exhibit moderate optical transmission.

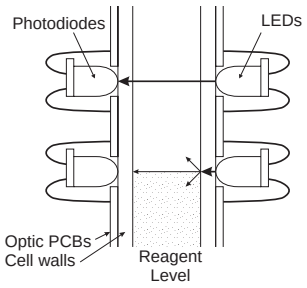

(b) Bottom optic inline with fluid level. Scattering of the incident light results in lower transmission to the detector.

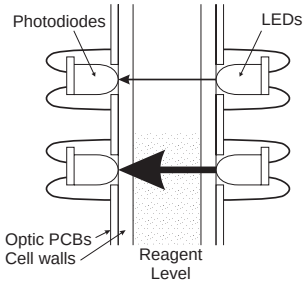

(c) Fluid level above the bottom optics. Maximum transmission through the solution results (Assuming the reagent's refractive index is closer to that of the acrylic cell walls than to air.).

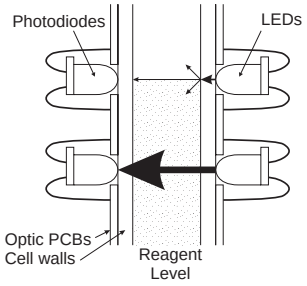

(d) Top optics inline with fluid level. Scattering of the incident light results in lower transmission to the detector.

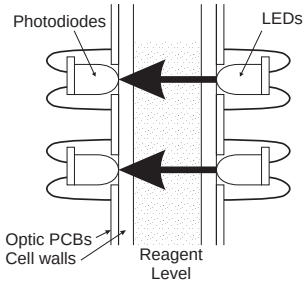

(e) Fluid level above the top optics. Maximum transmission through the solution results (Assuming the reagent's refractive index is closer to Acrylic than to air.).

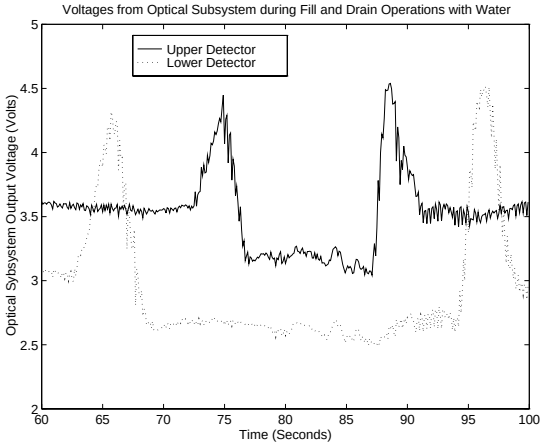

(f) Optical transmittance signal resulting from the above filling operation (ending at 78 seconds) and subsequent emptying action (commencing at 88 seconds).

Figure 6.6: Example of the 'automated filling process' of the chemical reaction cell utilising information from the turbidity measurement optics.

6.4 Mk.II Prototype

6.4.1 Introduction

The 'Mk.II' prototype was designed as a more robust test platform which would permit a more comprehensive evaluation of the instrument. The fluid control system was therefore designed to perform the stated functions as well as overcome the deficiencies of the Mk.I transport system.

One of the most significant deficiencies of the Mk.I system was its inability to make use of a cleaning solution to clean the cell. As shown in previous chapters, $CaCO_3$ coating of the optics and cell significantly interfered with the optical turbidity measurement. The Mk.II system addressed this issue.

6.4.2 Function Definition

Because of the inclusion of cleaning operations, the second prototype required four fluid/gas control tasks, namely:

- filling of the cell with the indicator reagent from the reagent reservoir;
- injection of the sample gas into the cell from the sample gas source (ambient atmosphere/sample tube/gas standard);
- draining of the used indicator/cleaning reagent from the cell into the waste reservoir; and
- filling of the cell with the cleaning solution from the cleaning reagent reservoir.

The same reaction cell (the 'teardrop with mesh guard' cell) was used for this prototype. As only one extra fluid function was added compared to the previous Mk.I system, an additional uni-directional pump was used to transport the cleaning solution. Again,

functions for the supply of indicator and draining could have been combined but this would have added extra complexity to the control circuit required for bi-directional pump motor control.

6.4.3 Selected Pumps

The pumps selected were different to those used in the first prototype. This was due to a desire to keep the Mk.I system operational and intact, and also to select pumps which had a more suitable direct drive coupling. Slightly larger positive displacement 'gear' pumps (type MFA 650) were selected for all transport functions. These were manufactured as a single module with the pump integrally mounted to the motor (unlike the Mk.I pumps which used a long fitting to join the motor shaft to the pump shaft). This permitted higher flow rates (undesirable but controllable with PWM), more precise speed control and the removal of motor/pump shaft misalignment as was common with the previous pump type. The selected pumps however required a higher operating voltage (12v) and consequently had a higher maximum flowrate (14mL/s, 857mL/min)

These pumps were used for all fluid lines and initially for the sample gas line after initial pump performance testing proved them suitable for pumping of gases (Section 10.3.2). However due to the increased inter-tooth leakage of these particular pumps (Section 10.3.3) an alternative gas pumping system needed to be designed and constructed: this is described in Section 6.4.7.

6.4.4 Chemical Cleaner

The chemical cleaner chosen was a citric acid, commonly available as the cleaning product "Shower Power™", and was able to rapidly dissolve the $CaCO_3$ precipitate from the cell walls.

6.4.5 Interconnection Scheme

The interconnection scheme utilised for the Mk.II was very similar to the previous version except for several modifications to cope with the added reagent pump. It likewise consisted of the four pumps, check valves, 'tee' pieces, and chemically inert (Tygon) 4mm plastic tubing (as the polyurethane tubing previously used was found to deteriorate over time due to exposure to CO_2). Large 2L containers were used as the reagent and waste reservoirs. The interconnection scheme was as seen in Figure 6.7. As seen in this figure, both the indicator solution-in, cleaner-in and waste-out functions were combined through a single port. Checkvalves served to prevent expended chemical indicator flowing back into the reservoirs for the indicator and cleaning solutions as well as to allow easy priming should any gas make its way into the tubing. The gear pump configuration can be seen in Figure 6.8.

Due to some inadequacies in the cell's ability to properly 'de-bubble' the mixing solution in the cell, a 'cell debubbler' was added which allowed any trapped bubbles to be expelled from the system and also allow any expelled fluid to be drained by the draining pump. Had the cell design been optimised for reliable proper in-cell debubbling and gas/liquid phase separation, this extra de-bubbler would not have been necessary, thus simplifying the overall pipework system.

6.4.6 Pump Motor Interfacing

The microcontroller interfacing for the Mk.II transport system was very similar to the Mk.I version. The only variation to the design was that the supply voltage was provided independent of the system power supply, reducing the effects of motor coupled noise onto the turbidity measurements. The supply voltage for the pumps was also increased to 12 volts. The detailed schematic for this system can be seen in Appendix A.

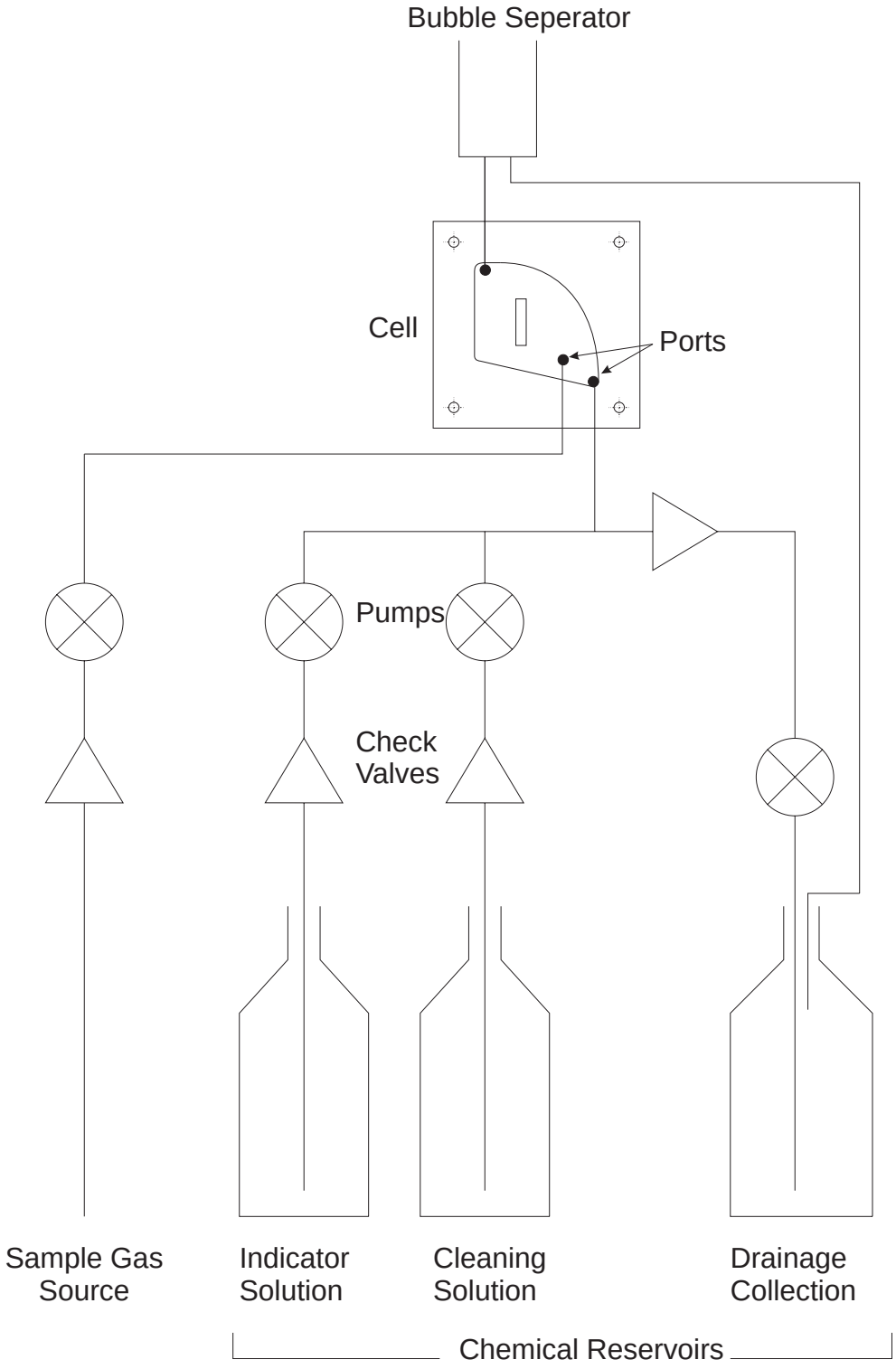

Figure 6.7: Interconnection scheme used for the Mk.II prototype.

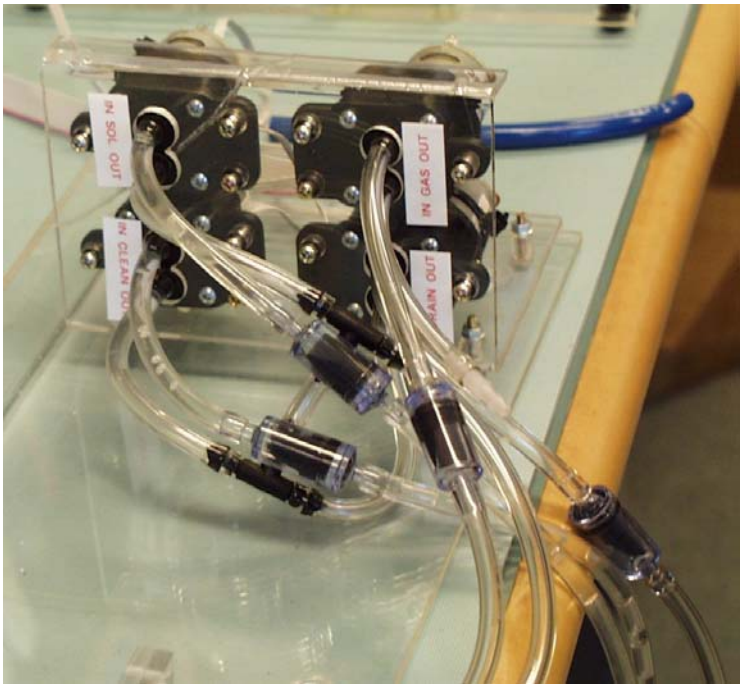

Figure 6.8: Photograph of the fluid/gas transport system used for the Mk.II prototype showing four pumps mounted on the perspex bracket) and four inline check valves (foreground).

6.4.7 External Gas Pump

As previously stated, the gear pump implemented in the Mk.II prototype was not ideally suited for pumping gases (unlike that of the Mk.I prototype), and would suffer from the inability to reliable pump gas at a constant rate. This was due to the thin metal gears used within the pump and their loose inter-tooth fit. To overcome this problem, a 'bellows' type pump system was used. This comprised of an off-the-shelf aquarium-type bellow air pump and a 240VAC mains voltage controller (unfortunately, at the time a suitable bellows pump able to be driven by a DC motor was not available) as seen in Figure 6.9. The gear pump used for gas transport in the Mk.I prototype was not used as a possible replacement, again due to a desire to keep the Mk.I prototype operational and intact.

The controller for this bellow pump used a single channel TTL triggered solid state relay which optically isolated the 240V mains section and the TTL input section. This allowed control of the mains powered pump by the low voltage microcontroller system. Extra protection and isolation circuitry was also included with the final schematic employed as seen in Appendix Section A.3.1.

Figure 6.9: Photograph of the external 'bellow' type pump and its control system (lid has been removed for the photograph).

It was discovered during testing of the gas pump that some leakage current would pass through the solid state relay in the 'off' state causing the pump to operate, although at a reduced flow rate. The fault was isolated to the solid state relay used. As the flowrate of the bellows pump was far greater than that required for correct operation of the reaction cell, the flowrate was restricted by means of a special clamp. This had the added bonus of minimising the leakage flowrate of the pump in the 'off' state such that gas injection bubbles would not be formed in the cell due to back pressure of the liquid column in the cell.

6.4.8 Precision Gas Mass-Flowmeter

As previously observed, fluctuations in the sample gas injection flowrate would affect the reaction speed of the indicator chemical reaction, and hence affect the time to reach

the turbidity thresholds. In order to adequately monitor the flowrate a high precision gas mass-flowmeter was designed to provide highly accurate metering of the injection gas into the instrumentation system prototypes. (This flowmeter would not form part of the eventual low-cost instrument but was introduced here for evaluation purposes only.)

The flowmeter was required to interface to the prototype instrumentation systems both mechanically (via plumbing necessary to route the gas flow in and out of the sensor and flowmeter) and electrically (to carry the necessary flow rate signals to the micro-controller).

The flowmeter sensor was based on the Honeywell AWM3100V precision gas flowmeter which featured a microbridge mass airflow sensor chip measuring heat transfer fluctuations caused by gas flow across the chip surface. This device however had a non-linear output characteristic as shown in Table 6.1 and Figure 6.10 with an operational range from 0-200 sccm [1]. This calibration data was then modelled to provide interpolation between the calibration points. Two models were considered, with both being modelled in "MATLAB™".

A 3rd order least square error polynomial fit was examined and showed a reasonable degree of accuracy. A cubic spline fit was also examined which provided a better fit than the polynomial, due to the spline passing through the provided data points unlike the polynomial model which smoothed around the points (not necessarily passing through them). The fit of both models is shown in Figure 6.11. Whilst the cubic spline fit provided less error, the polynomial fit was deemed suitable as it would adequately describe the behavior of the flowmeter within the flowmeter modules tolerances and required far fewer terms to describe the model than for the cubic spline model. The polynomial model parameters for this fit are shown in Table 6.2. Support electronics were constructed for the AWM3100V sensor head and provided signal buffering and basic processing of the raw analog signal. The signal flow for this device and the support electronics is shown in Figure 6.12.

[1] Standard Cubic Centimeters per Minute

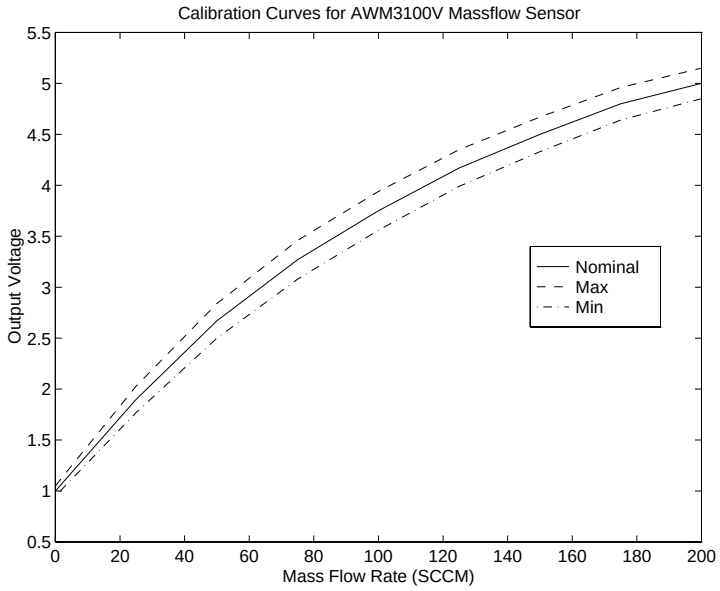

Figure 6.10: AWM3100V microbridge mass airflow sensor calibration curve.

Table 6.1: AWM3100V microbridge mass airflow sensor calibration data as supplied by the manufacturer.

Flowrate sccm	Nominal Voltage DC	Tolerance ±[Volts DC]
0	1.00	0.05
25	1.90	0.13
50	2.67	0.17
75	3.27	0.19
100	3.75	0.19
125	4.17	0.18
150	4.50	0.17
175	4.80	0.16
200	5.00	0.15

Table 6.2: Calculated parameters for the 3rd order polynomial fit to the Honeywell microbridge AWM3100V precision gas flowmeter calibration data. The polynomial function was $y = p_1.x^3 + p_2.x^2 + p_3.x + p_4$

Coefficient	p_1	p_2	p_3	p_4
Value	1.1809	-3.0833	25.4686	-0.3899

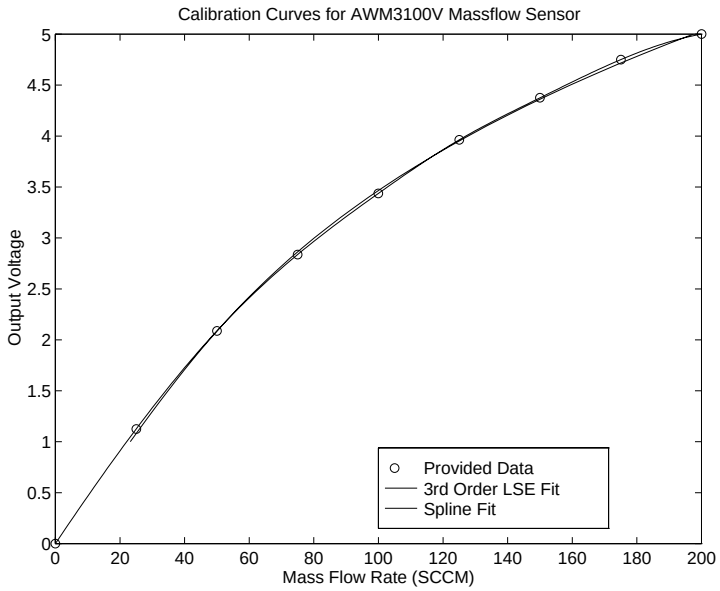

Figure 6.11: Two models used to interpolate the AWM3100V manufacturer provided calibration data.

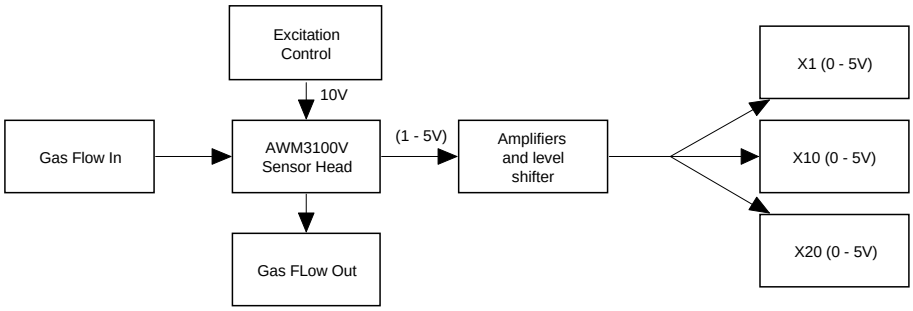

Figure 6.12: Signal flow diagram for the support electronics as part of the precision gas mass-flowmeter.

The excitation control would maintain the excitation voltage at a stable 10 Volts (as required) to prevent any output variation caused by power supply fluctuations. The signal correction section used a differential amplifier to subtract 1 volt from the AWM3100V output voltage and then amplify this by $\times 1.25$. This resulted in an output range of 0 to 5 Volts representing 0 to 200 sccm respectively. The signal amplification section consisted of additional amplifiers which applied gains of $\times 10$ and $\times 20$ and were used to improve the accuracy and output voltage range of the flowmeter for low flow rates in the order or 0 to 10mL/min.

The flowmeter prototype was then packaged in a case with access to the gas flow In/Out ports at the front, with power, data and signal lines accessible through the back (Figure 6.13). The precision flowmeter was then used to assist in determining the performance of the pumps, cell, and measurement instrumentation.

6.4.9 Final Interconnection Scheme

The final Mk.II interconnection scheme used was as shown in Figure 6.14. Components added to the scheme were the bellows pump, precision flowmeter, and flow restrictor. Although the fourth gear pump was not used for gas supply, it was still present in the system as an unconnected device.

(a) Front view showing the gas interfacing ports.

(b) Rear view showing the power switch and electronic interface connectors.

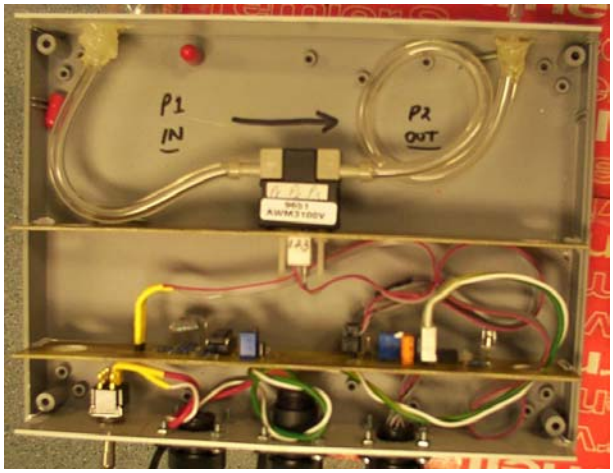

(c) Inside view of the electronics. Shown in the center is the Honeywell AWM3100V sensor.

Figure 6.13: Photographs of the precision gas mass-flowmeter incorporating the Honeywell AWM3100V microbridge flow sensor.

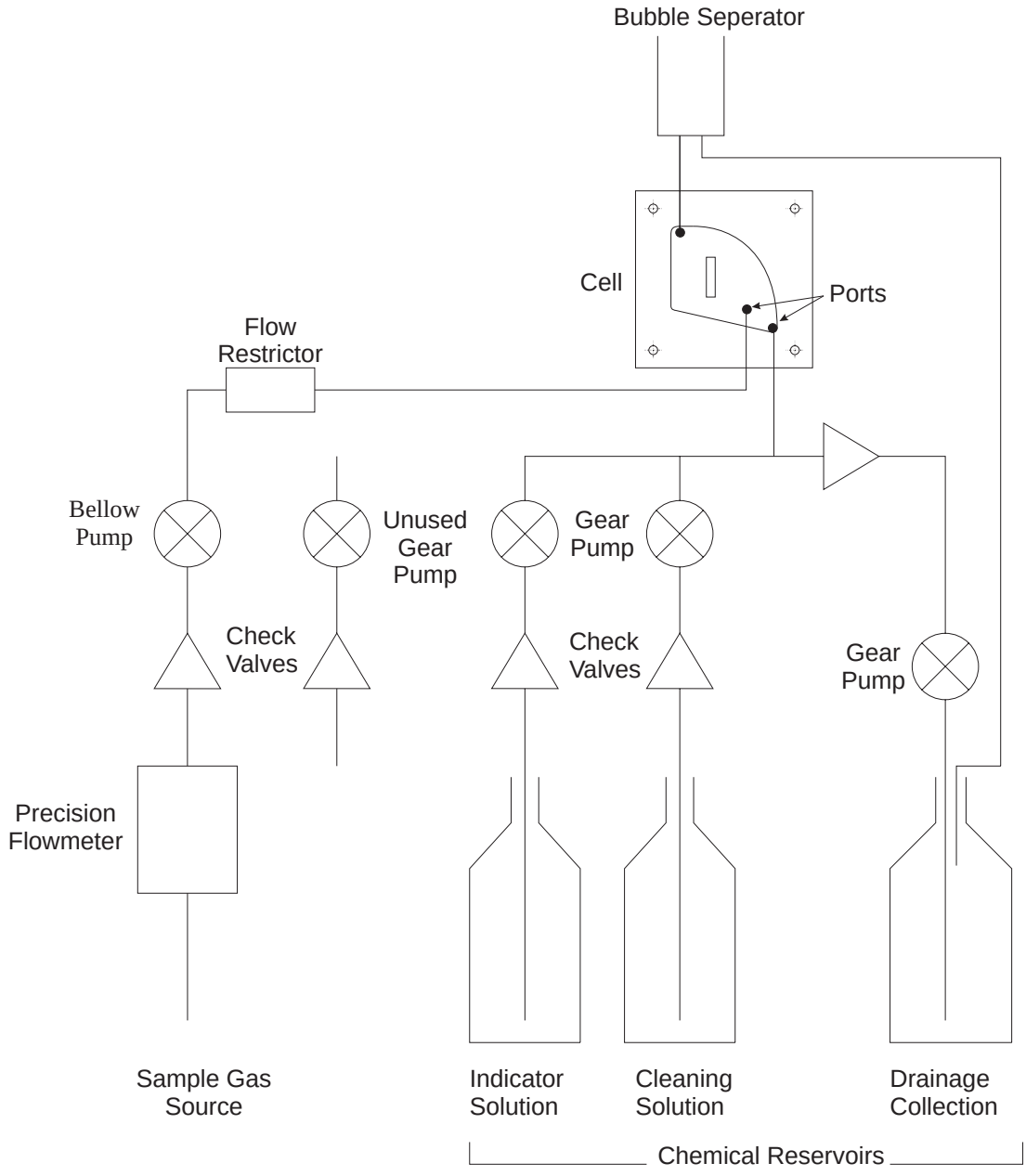

Figure 6.14: Final connection scheme used for the Mk.II prototype. Additional components include the bellow pump, precision flowmeter, and flow restrictor.

Chapter 7

System Calibration Model

7.1 Introduction

In order to derive a suitable gaseous CO_2 concentration value from the measured turbidity acquired from the cell optoelectronics, models to describe this behavior were developed. These models were then used off-line for calibration and measurement evaluation with capability to be implemented in realtime.

7.2 The Calibration Model and Calibration Procedure

Real time computer models processing were required for embedding in the instrumentation microcontroller and PC controlling systems to allow the sensor to calculate the percentage CO_2 concentration based on the measured turbidity. The model used to perform this was the "Time-To-Threshold" ("T3") model which took advantage of the observed optical turbidity effect that the chosen chemical indicator would typically produce in the presence of CO_2. An example of a typical turbidity waveform is shown in Figure 7.1. This effect of rising turbidity is clearly seen as $CaCO_3$ precipitate is produced within the cell. This turbidity then reaches a maximum and then starts to

decay as precipitate would fall out of suspension or is further chemically converted.

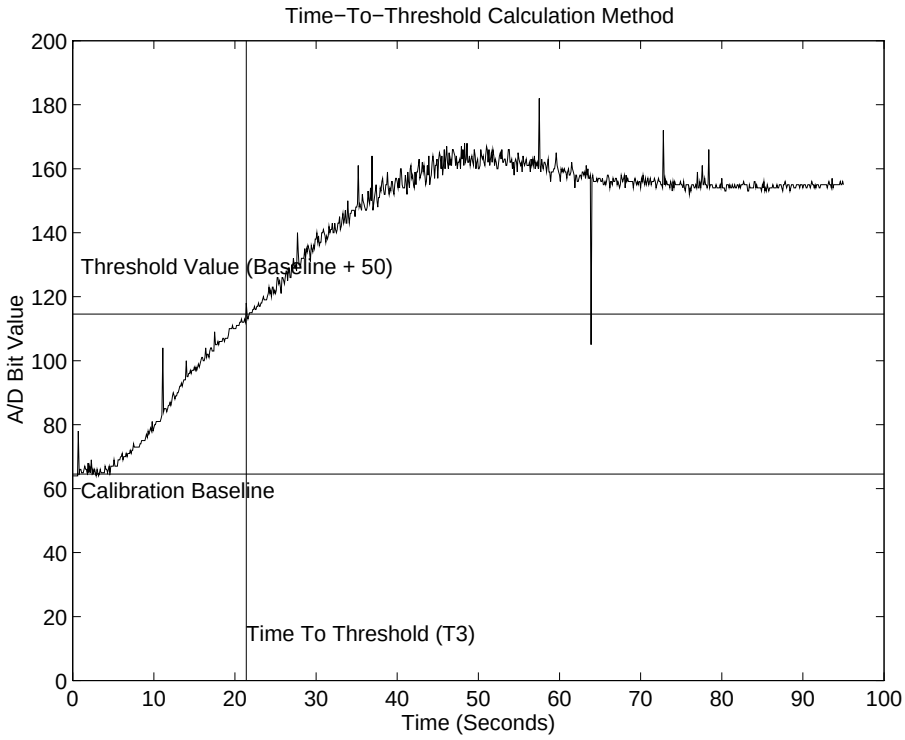

Figure 7.1: Example of a turbidity measurement from the Mk.I prototype for 100% CO_2. Spikes within the data were the result of noise generated by the gas pump motor during operation.

The "T3" model measures the time duration for the turbidity to reach a particular threshold from the start of the test, defined as the commencement of active bubbling in the cell with the sample gas. A threshold is arbitrarily chosen at a convenient point on the observed turbidity waveforms which is sufficiently above the noise floor of the instrument and also sufficiently below the peak turbidity point. This threshold is defined to be an offset above the calibration baseline taken by the instrument at the start of the test. In this way it was hoped to substantially remove any optical drift effects caused by $CaCO_3$ precipitate coating the cell wall and hence falsely increasing the measured turbidity. The particular threshold point shown in Figure 7.1 was 50 A/D converter bits above the baseline measurement.

When a series of calibration gases (of varying CO_2 proportion) are used to generate

a series of optical turbidity curves, the times to this particular threshold for each turbidity curve is measured and a model derived to fit these times. When an unknown concentration of gas is then injected into the instrumentation system, the time to the threshold is measured by the control system, and the model used to translate this time back to a CO_2 concentration.

It was also possible to use multiple threshold points and apply similar models to that data. This then allows a certain degree of flexility in the measurement. If a smaller offset is chosen for one of the thresholds then the measurement time required to reach that point will be short (approximately 10 seconds for high concentrations, such as 50 to 100% CO_2) thereby making measurement cycle times short. The disadvantage of this however is that as the turbidity measurement range will be very small compared to the rest of the turbidity waveform, significant errors in the measured time could be present due to possible false triggering by noise, or minor artifacts in the turbidity measurement. Also because the sample period used for the turbidity measurements is one second (due to relatively slow speed of the microcontroller used), significant discretisation of the time measurement would occur for fast acting (high CO_2 concentration), short time duration reactions.

Should a larger offset be used for the threshold measurement, it is clear that the time resolution for that measurement would increase with minor artifacts in the turbidity curve having less effect. The disadvantage however is that the measurement cycle would increase to possibly unacceptable duration times between measurements (approximately 10 minutes for 10% and longer for lower concentrations of CO_2).

Clearly there is a tradeoff between large offsets having long cycle times, and small offsets (increasing the possibility of noise being accidently identified as valid data), and lower time measurement resolution. For this reason five multiple threshold offsets were considered and modelled in order to examine the effects of variable offsets on measurement times and instrument accuracy in the final instrumentation device.

7.2.1 Data Fusion Issues

As five threshold models existed to describe the time-concentration relationship, five separate concentration values would hence be calculated for a single measurement cycle. These values would either be similar in value, should the measurement be 'well behaved', or would have some discrepancy between the values, if there was some artifact in the data causing a false threshold detection. Whilst a means of selecting between these models would be required in a final commercial instrument, a selection system was not implemented in the present study, but rather the effects on the instrument accuracy and cycle time were evaluated.

Several possible methods could be used however to arbitrate between the five models. The simplest is averaging of the calculated values, and more sophisticated data fusion includes the use of a 'smart' selection system to identifying erroneous calculations to be disregarded. Other schemes could include weighted averages where the weighting vector (W_i) could be determined by the variance for each model (Equation 7.1).

$$[W_i] = [\frac{1}{{\sigma_i}^2}] \tag{7.1}$$

Multiple weighing vectors could also be developed for various CO_2 concentrations such that subtle variations in the arbitration accuracy could be encapsulated. When fast measurements are required the smaller offset threshold could be selected, or if a potentially more accurate measurement were desired, the larger offset model could be selected. The selection system would however have a signal flow as shown in Figure 7.2, where each submodel would determine the time to reach the threshold for its particular offset, use the predetermined model to calculate the concentration value for that particular model, then have the final concentration value selected or determined based on the most appropriate calculated concentration, or combination of. The development and testing of an instrument embedded arbitration system was however not explored.

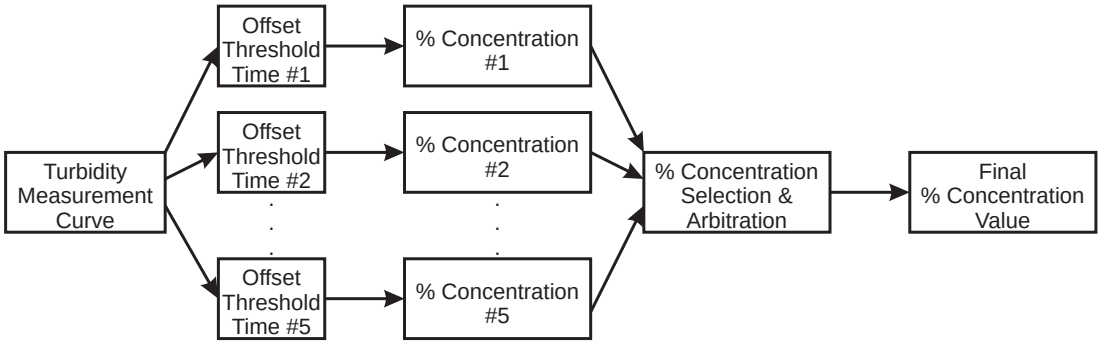

Figure 7.2: The signal flow for the "Time To Threshold" Model.

7.3 Mk.I Calibration Model

To generate the 'Mk.I' calibration model, a series of calibration gases were used comprising in order 100%[1] , 50%, 20%, 10%, and 5% CO_2 with the remaining fraction dry N_2. Turbidity measurements for each of these gases were obtained (Figure 7.3) from the 'Mk.I' hardware system running a special calibration routine. These turbidity data were sent directly a personal computer (PC) for post-processing.

During each turbidity measurement the cell was filled with the chemical indicator (calcium hydroxide solution) and a baseline calibration measurement taken. This baseline measurement permitted compensation for $CaCO_3$ precipitate buildup on the cell surface, variation in output intensity of the optics over time, and temperature effects in the optics and instrumentation electronics.

Offset values above the baselines measurement were selected for each of the five threshold points (Table 7.1), and the times to each threshold determined using a "MATLAB™" script (Table 7.2). These times were then used to produce a simple linear interpolation model as shown in Figure 7.4. Hence in order to translate from a measured threshold time back to a CO_2 concentration value, the time to reach the threshold is found on the "Time To Threshold" axis, and projected upwards to intersect with linear curve associated with the baseline offset for which the time was measured, and the concentration

[1]Strictly 99.95%, the certified purity of the reagent as stated by the manufacturer.

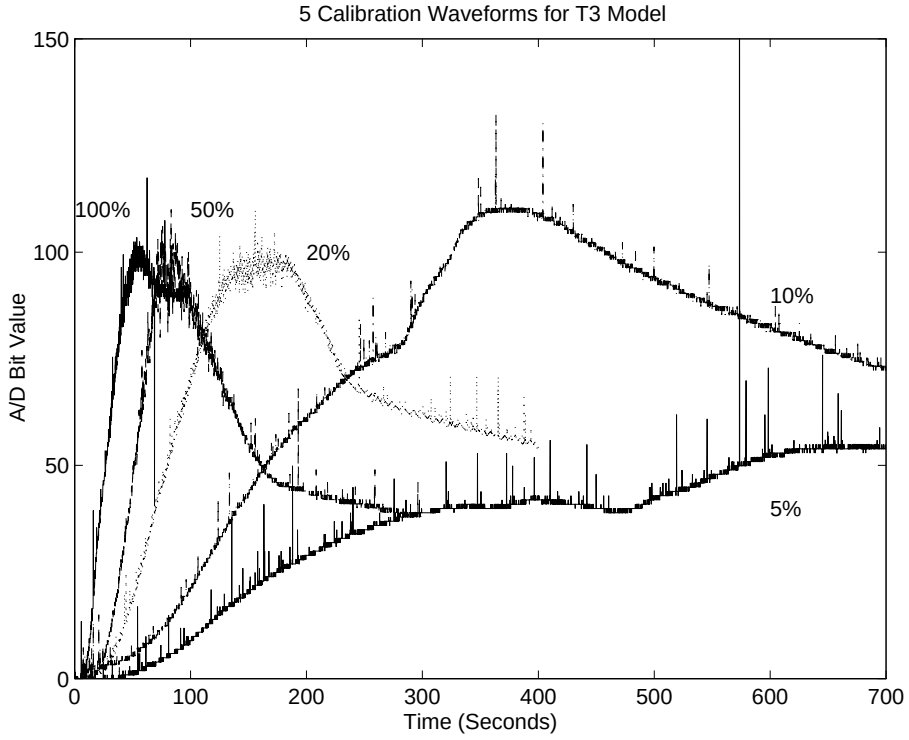

Figure 7.3: The five calibration turbidity waveforms used to generate the 'Mk.I' model. Spikes within the data were the result of noise generated by the gas pump motor during operation.

of CO_2 obtained.

Table 7.1: Threshold values chosen to use for the Mk.I model. Shown are the offset values and the absolute values selected.

Threshold	Threshold Offset	Absolute Threshold
Threshold 1	10 [A/D Bits]	baseline + 10 [A/D Bits]
Threshold 2	20 [A/D Bits]	baseline + 20 [A/D Bits]
Threshold 3	30 [A/D Bits]	baseline + 30 [A/D Bits]
Threshold 4	40 [A/D Bits]	baseline + 40 [A/D Bits]
Threshold 5	50 [A/D Bits]	baseline + 50 [A/D Bits]

7.3.1 Interpolation of Calibration Data

Whilst the linear model of Figure 7.4 used for initial 'proof-of-concept', more suitable interpolation models were examined to adequately describe the calibration data. These

Table 7.2: Measured threshold times for the Mk.I calibration data (baseline + 10, 20, 30, 40, and 50) for varying carbon dioxide sample gas concentrations.

% Concentration CO_2	10	20	30	40	50
100	8.6	11.4	14.1	17.5	21.4
50	22.5	32.0	37.3	42.7	46.0
20	35.3	47.6	56.0	64.8	75.1
10	62.8	92.6	113.6	136.9	158.4
5	100.6	143.8	211.1	329.7	580.6

were:

- an exponential function;
- a polynomial function;
- a power function;
- a cubic spline interpolation; and
- an interpolated (table-lookup) cubic spline.

Of these, only the first, the exponential function (Appendix Section B.1.1, Figure B.2 and B.3), was tested in the Mk.I prototype. This model was initially judged to be adequate due to its ability to describe the general trend of the calibration data with an adequate accuracy for the 'proof-of-concept'.

After further analysis was performed and further models explored, it was observed that the interpolated (table-lookup) cubic spline (Section B.1.5, Figure B.8) best fit the data due to the nature of the piecewise polynomial used. This model was however not used for testing of the Mk.I system but was considered for the Mk.II.

The details of each of the above five possibilities and the results obtained are set out in Appendix B.

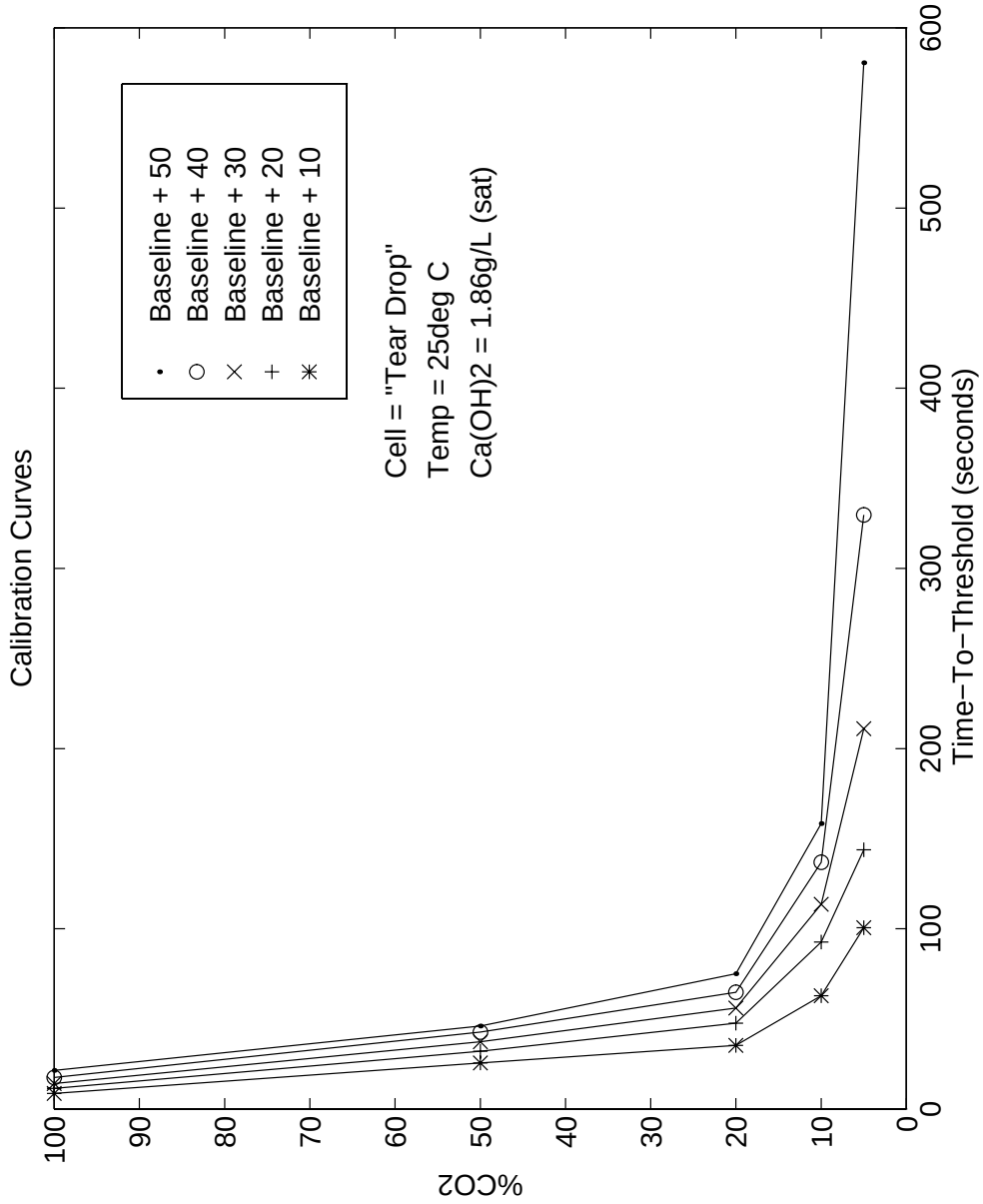

Figure 7.4: Linear interpolated calibration curves of the Mk.I prototype to translate measured threshold times back to CO_2 concentrations.

7.4 Mk.II Calibration Model

The Mk.II calibration data was obtained in a similar manner to that of the Mk.I. Five calibration gases (containing 100%, 50%, 20%, 10%, and 5% CO_2 respectively) were used to obtain five calibration waveforms. These waveforms were obtained using non-adaptive optics (Section 10.3.6) with the detector sensitivity set to its maximum and the LED emitter output power set to achieve the greatest dynamic range, as obtained by prior testing.

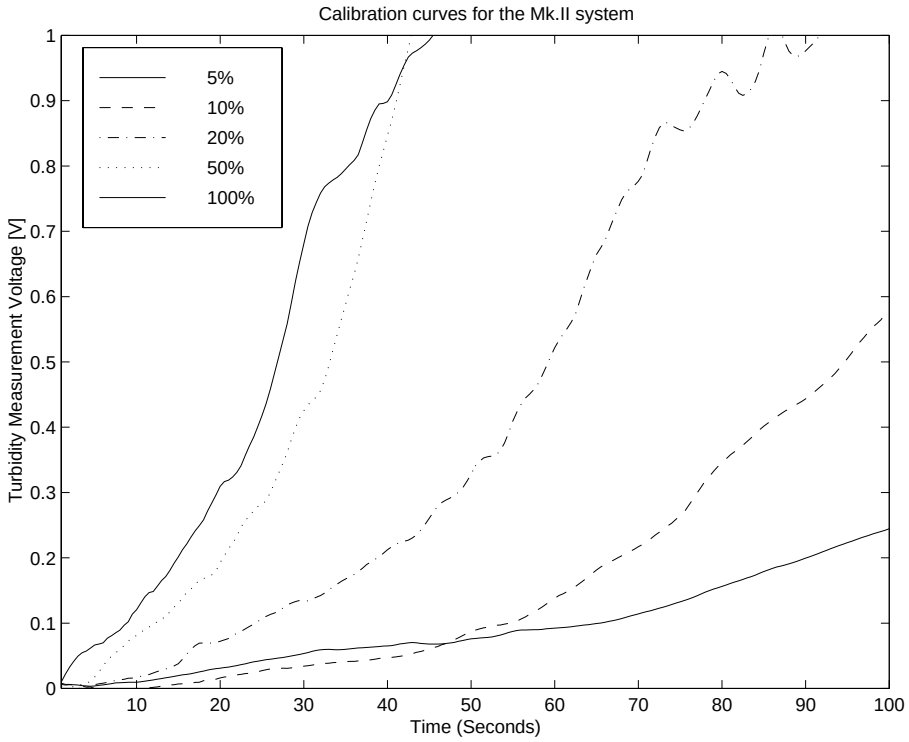

Figure 7.5: The five turbidity waveforms used to generate the Mk.II model.

Once these waveforms were obtained (Figure 7.5) the times to reach the particular turbidity thresholds were calculated (using a similar MATLAB script to that used for the Mk.II) as illustrated in Figure 7.6. Because the A/D converter electronics used in the Mk.II system were more advanced compared to those previously used, greater accuracy in the turbidity measurement could be seen. Also because the scale of the

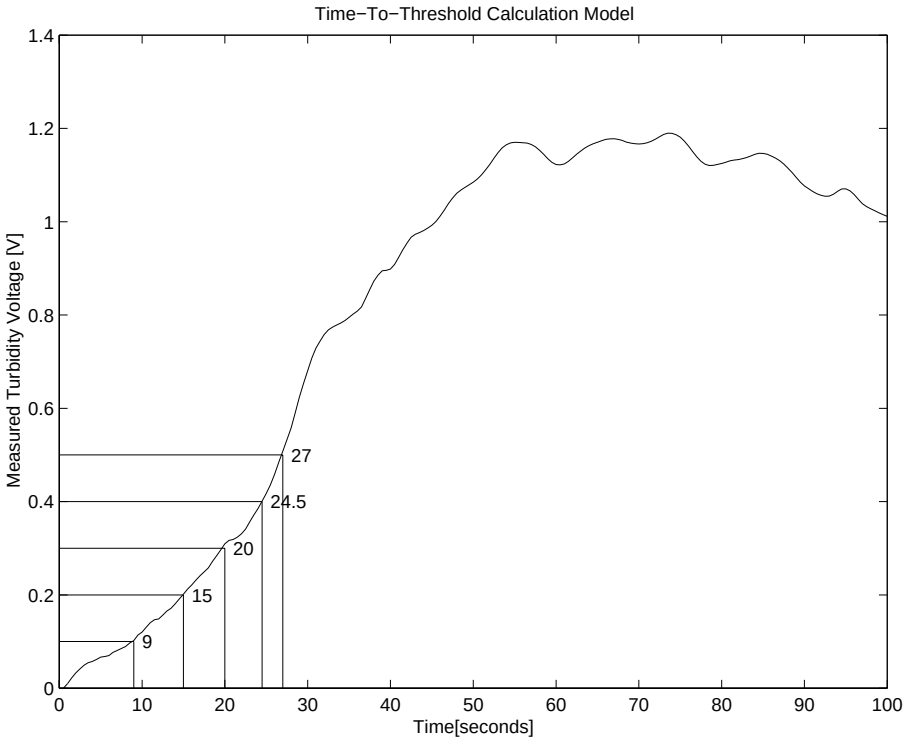

Figure 7.6: Example of a turbidity measurement from the Mk.II prototype for 100% CO_2.

turbidity measurement was now in volts rather than a pure A/D bit value as used previously, the definition for the thresholds needed to be modified. It was observed in the calibration waveform data that the maximum voltage achieved during the maximum turbidity was just over 1.5V. Hence, instead of using bit values to describe the offset points, five voltage offsets were used, $baseline + 0.1V$, through to $baseline + 0.5V$ (Table 7.3). These offsets were also selected as they were sufficiently above the noise floor during measurement and also below the maximum voltage seen during maximum turbidity (specific to the optical emitter and detector parameters set via the variable current control system).

The measured threshold times (Table 7.4) were then modelled. Following the Mk.I research, only three models were explored, namely:

Table 7.3: Threshold values chosen to use for the Mk.II model. Shown are the offset values and the absolute values selected.

Threshold	Threshold Offset	Absolute Threshold
Threshold 1	0.1 [Volts]	baseline + 0.1 [Volts]
Threshold 2	0.2 [Volts]	baseline + 0.2 [Volts]
Threshold 3	0.3 [Volts]	baseline + 0.3 [Volts]
Threshold 4	0.4 [Volts]	baseline + 0.4 [Volts]
Threshold 5	0.5 [Volts]	baseline + 0.5 [Volts]

Table 7.4: Measured threshold times for the Mk.II calibration data (baseline + 0.1V, 0.2V, 0.3V, 0.4V, and 0.5V) for varying CO_2 sample gas concentrations.

% Concentration CO_2	0.1V	0.2V	0.3V	0.4V	0.5V
100	9	15	20	24.5	27
50	12.5	20.5	26.5	29.5	33.5
20	25	39.5	49	55	59.5
10	57.5	70	78	86.5	95.5
5	68.5	92	122	157.5	181.5

- exponential function;
- power function; and
- an interpolated (table-lookup) cubic spline.

and the details are set out in Appendix B.

The performance of all three models was examined, as presented in Section 10.3.14. In summary, the exponential model performed similarly to that of the Mk.I implementation where a loose fit to the calibration data was observed, in addition to having significant errors between the model and the calibration data for both 20% CO_2 concentration and for long threshold times. The power function, whilst showing a loose fit to the data, did show its usefulness for lower concentrations and for calculation of values beyond the lower calibration limit of the instrumentation system. The interpolated (table-lookup) cubic spline function showed an exact fit to the calibration data but was unable to be used for threshold times beyond the calibration data boundaries.

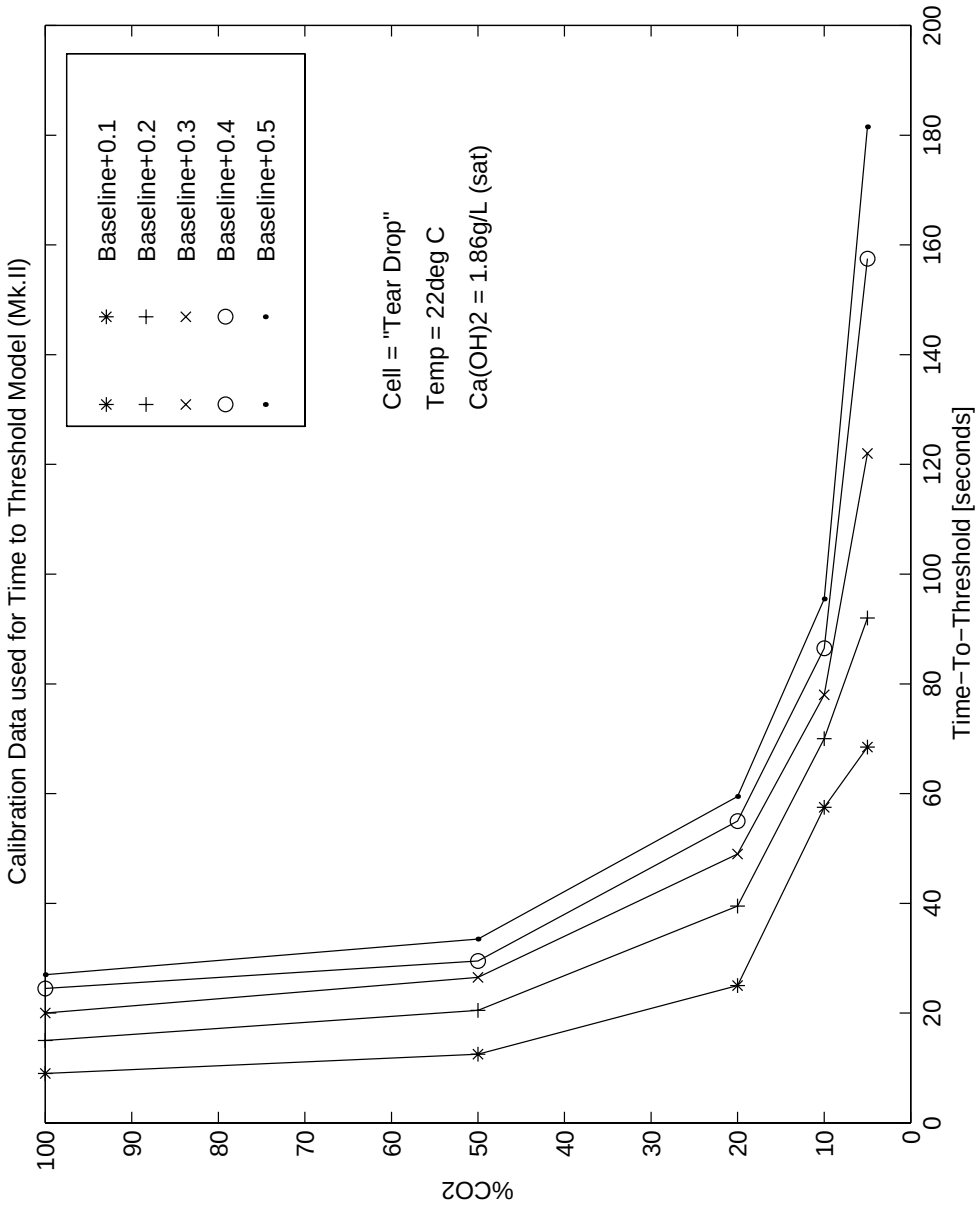

Figure 7.7: Linear interpolated calibration curves of the Mk.II prototype to translate measured threshold times back to CO_2 concentrations.

Chapter 8

System Implementation

8.1 Introduction

To complete the implementation of the two prototype measurement instruments, extra support hardware components were required. This chapter presents an overview of the extra electrical components required to complete each measurement instrument and their interconnection with the previously presented sub-systems. Further specific details are available in Appendix A.

8.2 Hardware Overview

As previously shown in Section 3.5, each complete measurement instrument required four critical components, namely:

- chemical containment cell;
- turbidity measurement system;
- fluid transport and control system; and

- microcontroller, software and modelling systems.

The development of the first three components has been presented in Chapters 4, 5, and 6 respectively. Of the remaining components in this list, the modelling structures were presented in Chapter 7, and the software is presented in Chapter 9. The microcontroller, its support electronics and the implementation of each hardware phototype is presented below, in Section 8.3 for the 'Mk.I' and Section 8.4 for the 'Mk.II'.

8.3 Mk.I Hardware Prototype

As the Mk.I measurement instrument was built up as necessary, its sub-systems were designed to be modular to allow easy removal and replacement as the measurement instrument was developed. The instrument prototype consisted of the sub-systems shown in previous chapters (cell, fluid transport mechanism, turbidity measurement) coupled with additional control structures to yield a complete measurement instrument.

8.3.1 Chemical Containment Cell

The chemical containment cell used in the prototype instrument was the 'teardrop with mesh screen' cell (Section 4.5.4). This was chosen due to its observed ability to adequately remove bubbles from the measurement zone and achieve homogeneous precipitation within the cell. It was subsequently discovered that this cell did not perform as intended and did have significant disadvantages (Section 11.3.1), however its performance was adequate for testing of this 'proof-of-concept' prototype.

8.3.2 Turbidity Measurement System

The turbidity system was implemented as shown in Section 5.4, where the 'transmissive extrinsic horizontal optical alignment' was used (Figure 5.5), with the optical compo-

nents being mounted onto the exterior face of each cell half by the use of an alignment PCB (Figure 5.8). The entire cell assembly was then bolted together.

Each of the two LEDs were then provided with a constant current by a fixed resistor, with the two photodiodes having an adjustable resistor (potentiometer) to vary the forward current and hence the sensitivity (Figure 5.10). The voltage across each photodiode was then connected to two of the internal 8 bit A/D converters on the microcontroller below (Section 8.3.4). The current supply components for the optics were placed on a separate modular board.

8.3.3 Fluid Transport and Control System

The fluid transport and control system was implemented as shown in Section 6.3, where each of the three pumps had a single FET switch (Figure 6.1(b)) to control their activation. Each FET was then connected to a digital output line of the microcontroller (Section 8.3.4). The FETs and their associated support components were also placed on a separate modular board.

8.3.4 Microcontroller System

The microcontroller system to control the hardware, used a small 8 bit microcontroller from Motorola, the MC68HC11E2. This microcontroller was selected due to its versatility, able to provide general purpose digital interfacing, as well as featuring an integral 8 channel-8 bit A/D converter, timing capture devices, and a multitude of bi-directional digital ports. Other features included onboard serial ports, internal RAM and EEPROM (Electronically Erasable Programmable Read Only Memory). This particular microcontroller was also readily available and low-cost.

This microcontroller was configured to operate in 'single-chip' mode where internal RAM and EEPROM were used for the software program, thereby freeing all physical

interface I/O lines. An alternative operating mode, 'Expanded Memory Mode' would have allowed external RAM and ROM to be used, however would have required many of the interface I/O lines to be dedicated to memory control functions (i.e. memory addressing, and data bus functions). The available memory within this microcontroller was 2kbytes EEPROM, and 256 bytes of RAM (Table 11.2). Due to this memory space limitation, the complete model (Section 7.3) could not be embedded into the onboard firmware. Data was therefore gathered from the device and sent to an external PC which then subsequently processed the data.

The microcontroller and all the necessary support components were mounted onto a general purpose prototyping PCB, with an 8MHz resonator provided the system clock for the processor (resulting in a 2MHz operation cycle speed), and a 5V regulator then providing the system supply voltage. In order to connect the prototype instrument to the controlling PC, a small RS232 level shifter was used to translate the serial TTL signal levels to those as required by the RS232 specification. This also resided on a separate module.

These two modules (the microcontroller and serial interface board) where then connected to the other modules (for Fluid Transport/Pump Control, Turbidity Measurement/Optics Control) to form the complete instrument.

The three pumps were connected to three digital output lines (PC0, PC1, and PC2). The two electrical turbidity signals were connected to two of the A/D lines (PE0, PE1).

8.3.5 Final System Implementation

The final measurement system when implemented had the structure as shown in Figure 8.1, with a photograph of the final system presented in Figure 1.2(a). The schematics and PCB artwork for the Mk.I is presented in Appendix A, Section A.2.

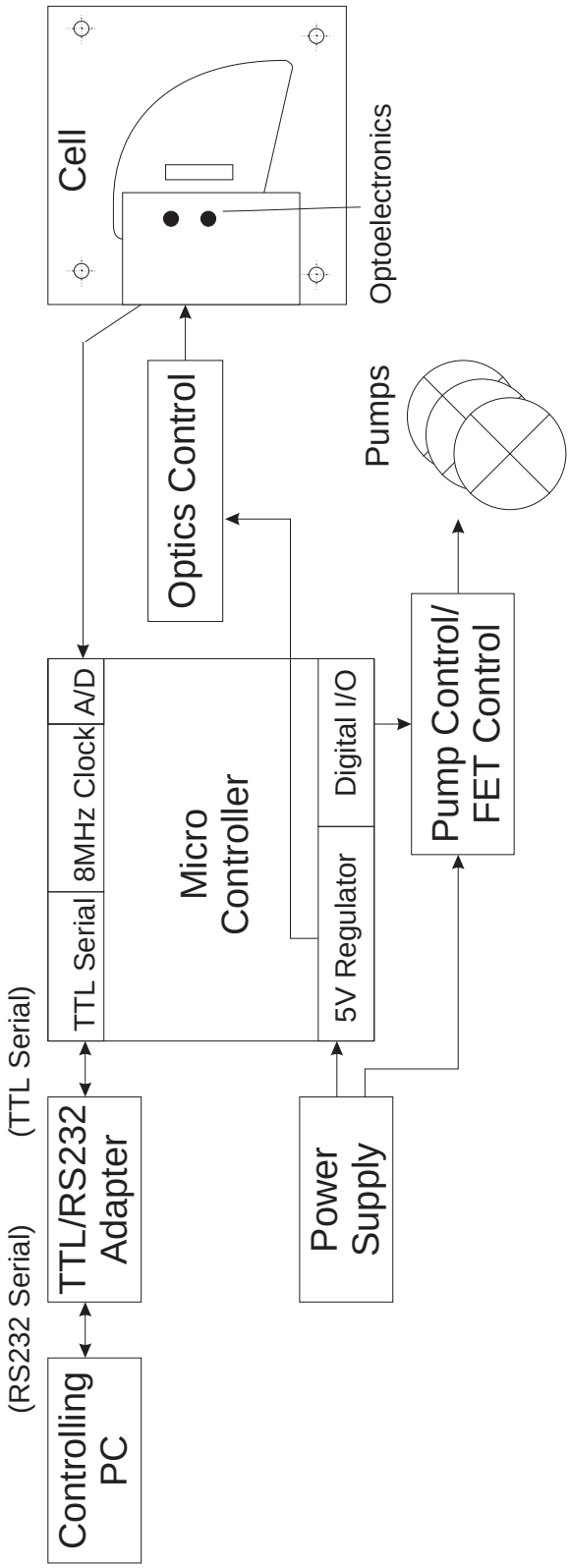

Figure 8.1: Block diagram of the Mk.I electronics.

8.4 Mk.II Hardware Prototype

The Mk.II instrument hardware was an expanded version of the Mk.I where deficiencies of this first hardware prototype (Section 10.2.5) were addressed. These deficiencies presented areas where the next instrument prototype (Mk.II) could be improved. Hence several additional features were incorporated into the electronics of the Mk.II instrument, namely;

- use of an adaptive A/D converter and associated electronics to allow reduction of its input span and hence improved discrimination of the electrical turbidity signal (to potentially increase the dynamic range of the instrument);
- inclusion of a 16 channel analogue multiplexer allowing the monitoring of up to 16 analog channels;
- incorporation of a four channel variable current source to provide microcontroller variable emitter intensity, and detector sensitivity for exploration of smart sensing regimes;
- addition of temperature sensors spread throughout the system including the cell, gas in, indicator solution, analog electronics, and exhaust gas temperatures; and
- inclusion of a relative RH (Relative Humidity) sensor to allow exploration of the effects of humidity on the instrumentation system.

8.4.1 Chemical Containment Cell

The chemical containment cell used for the second prototype was the same as that used for the first for the same reasons as already discussed in Section 8.3.1.

8.4.2 Turbidity Measurement System

The turbidity measurement system was as shown in Section 5.4, where the same cell optics and arrangement for the Mk.I were used.

Up to three LED and photodiode pairs were allowed to be mounted onto the cell, however only two of the three positions were used (the upper and the lower). Each LED had an adjustable forward current (unlike the constant current of the Mk.I turbidity measurement system). This was achieved through the use of a microcontroller adjustable Howland voltage to current converter (Figure 5.11). Likewise, each of the photodiodes were connected to separate channels of this converter. The voltage across each photodiode was then available as 3 separate channels of the 16 channel multiplexer. For diagnostics, the voltage across each LED was also available as 3 separate channels of the multiplexer.

8.4.3 Fluid Transport and Control System

The fluid transport and control system implemented was as shown in Section 6.4 and was very similar in structure to the Mk.I version. Each of the four pumps had a single FET switch to control their activation, with extra componentry to minimise switching noise.

8.4.4 Analog Electronics

Additional analog electronics were incorporated into the Mk.II instrument to permit flexibility in testing and for future experimentation.

The input stage of the analogue electronics was a 16 channel analogue multiplexer (type DG506A) which could select between many on board or off-board voltage sources (e.g. photodiode voltages, temperature sensors, flowmeters - Section 8.4.5 below).

The output of the multiplexer was then connected to a level shifting differential amplifier (type TLC274 OPAMP, which adjusted the measured zero voltage), and a 12 bit A/D (type LTC1286). This A/D also featured a variable full-span voltage which permitted variation of the full span voltage that it would measure. The combination of these two controls allowed the A/D a degree of flexibility in measuring voltages much smaller than the full span voltage (5V) whilst still maintaining a high degree of discrimination.

This was designed to allow any voltage within the 0 to 5V range to be zoomed in upon by firstly adjusting the zero level the A/D would observe, then adjust the span of the A/D to measure only up to the maximum voltage of interest. In this way a fully adaptive analog voltage sampling system was designed to maintain a reasonable accuracy (within the operational limits of the components used) across the entire voltage range.

Both the span voltage, and the offset voltage for the differential amplifier were provided by a 4 channel 8 bit Digital to Analogue Converter (DAC, type MAX500). The two spare channels of this DAC were then used to provide voltages to the two pairs of Howland voltage to current converters.

Two precision temperature sensors were also embedded into the design. One was placed directly under the 12 bit A/D converter, with the other being placed under the OPAMP used for the differential amplifier function. In this way it was hoped to perform temperature compensation of the analog electronics if required. It is however noted that should there be any signal drift in the analog electronics due to temperature effects, it would also affect the temperature measurement, and so possibly provided limited usefulness. This feature was however not used and was added only for future use.

8.4.5 Additional Sensing

Several additional onboard and external sensors were catered for in the Mk.II instrument prototype. These extra sensors were both analog and digital.

Additional on-board analog sensors were installed to measure the temperature of the critical analogue signal conditioning components. These were as follows:

A/D temperature allowing the measurement of the onboard LTC1286 A/D converter temperature via a surface mounted device (SMD), the LM45 precision temperature sensor; and

Analogue electronics temperature specifically of the differential operational amplifier (TLC274), also using an (SMD) LM45 precision temperature sensor.

Additional analog sensors (external to the circuit board) were installed as follows:

External flowmeter rate allowing recording of the external flowmeter value, potentially to allow for compensation of gas flowrate variations (Section 11.4.7);

Motor temperature allowing monitoring of the external pump motors temperature (by an SMD LM45) to potentially prevent overheating during high load, or due to motor stalling;

In-cell temperature measuring the temperature of the fluid within the cell (by an SMD LM45) where a specially modified version of the cell could be used which mounted the temperature sensor inside the cell's center divider;

Gas-in temperature allowing monitoring of the sample gas temperature before it entered the cell;

Gas-out temperature allowing monitoring of the sample gas temperature once it exits the cell;

Indicator temperature allowing recording of the chemical indicators reservoir temperature;

2.5 Volt reference source to allow verification of the accuracy and stability of the A/D and analogue electronics operation (Section 10.3.4); and

Zero Volt reference source to allow also verification of the accuracy and stability of the A/D and analogue electronics operation.

These additional analog inputs, together with 3 inputs for the LED voltages, and 3 inputs for the photodiode detector voltages made up the 16 total inputs for the 16 channel multiplexer (MUX).

The additional digital sensors were:

Tilt sensor ensuring the cell was being operated in the correct orientation;

Vibration sensor ensuring that the cell was being operated with a minimum of vibration caused by external means; and

Relative humidity sensor permitting recording of the relative humidity (translated to a frequency by an astable circuit and a C3M3 resistive humidity sensor, Appendix A.4).

All of these additional sensing inputs (except the 2.5V and zero voltage reference sources) were not used in the testing of the instrument, but were added to allow future experimentation, specifically into the effects of temperature on the measurement instrument (Section 11.4.5).

8.4.6 Microcontroller System

The microcontroller used for the Mk.II measurement instrument was the same as that for the Mk.I, namely, the Motorola 8 bit MC68HC11E2. The microcontroller was again run in 'single-chip' mode with an external controlling PC attached by a serial cable. Whilst it was learnt from the previous hardware version that this microcontroller had insufficient memory for the calibration routines, it was decided to stay with a single chip configuration and specifically design the system to interface to an external

controlling PC. Provision was also made for the Motorola MC68HC11E9FN1 (and the EPROM version MC68HC711E9CFS2 variant) which both featured extended memory areas (12K (E)EPROM, 768 bytes RAM, Table 11.2), such that a larger program could be embedded and still run in the single chip mode if required.

All of the necessary microcontroller, microcontroller support hardware, optics control, pump motor control and additional systems were built onto the one board, rather than the modular approach. This was required due to the complexity of the integration of each subsystem.

The microcontroller was also interfaced to an externally mounted LCD display and keypad board. The LCD display was used to display both the firmware version, as well as data from the serial protocol, to help verify operation. The keypad was added should a complete autonomous instrument be constructed to permit user controlled features should they be embedded into the design. This aspect was not for this research, but was included for future use.

8.4.7 Final System Implementation

The block diagram for the final system integration is shown in Figure 8.2 with a photograph of the measurement instrument presented in Figure 1.2(b). The schematics and PCB artwork for the Mk.II is presented in Appendix A, Section A.3.

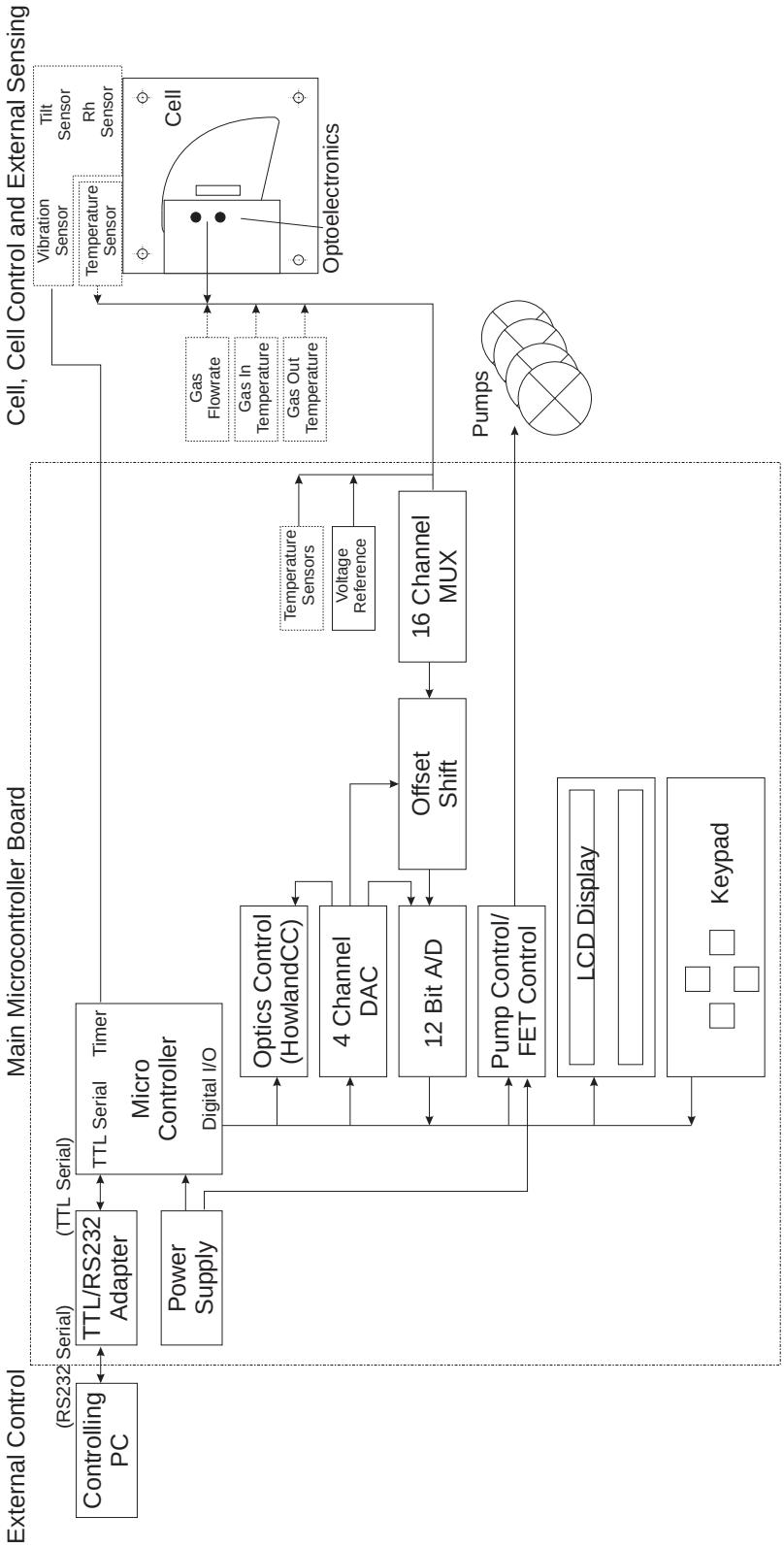

Figure 8.2: Block diagram of the Mk.II electronics.

Chapter 9

Software Development

To provide functionality to the completed measurement instrument hardware, software was written to perform the basic and more complex measurement processes required for the instrumentation system. Software components for both instrument prototypes, for the host PC controller, as well as for system simulation are presented.

9.1 Mk.I Prototype Software & Firmware

The 'Mk.I' software consisted of three separate components, namely:

Mk.I firmware which was the software running on the Mk.I hardware prototype to provide sensor functionality, calibration and data gathering functions;

Mk.I offline calibration software executed within the "MATLAB™" package to calculate the calibration model parameters for the "T3" model; and

CO2_SCS - CO_2 Sensor Control System software simulation package to process acquired data from the Mk.I hardware platform, and apply the "T3" model to resolve the CO_2 concentration value.

9.1.1 Mk.I Hardware Prototype Firmware

The firmware embedded into the instrument prototype was required to control the hardware components as well as provide further complex control and automation. The firmware was written in assembly language specific to the Motorola MC68HC11 type microcontroller, and was compiled using the Motorola compilation tools[1] specific to this microcontroller type. This software was then transferred to the prototype hardware microcontroller's EEPROM using a purpose written download package[2].

This software performed the following tasks:

1. initialise all hardware components including enabling the serial port, the A/D ports, the software based pump speed control system (PWM), and the interrupt systems;
2. clean the measurement cell in preparation for the first measurement;
3. fill the cell with the indicator chemical; and
4. continuously record the optical turbidity signal from the bottom optic pair and send this data to the master PC via the serial port, until the sensor was turned off.

The turbidity data was then captured by a PC running a serial data capture tool. This captured data was then saved to a file in preparation for use with the `CO2_SCS` software (Section 9.1.3). Extra software drivers were also embedded into the firmware specifically to control the inbuilt serial port, pumps, and internal 8 bit A/D converters. The internal software structure was as shown in Figure 9.1. Whilst analysis and calibration lookup tables were present in the firmware, insufficient memory space within the chosen microcontroller did not allow these functions to be completed.

[1] "as11.exe" as supplied by Motorola at "http://www.mot.com/pub/SPS/MCU/ibm/"

[2] Written by John Leis, Faculty of Engineering & Surveying, University of Southern Queensland, Australia

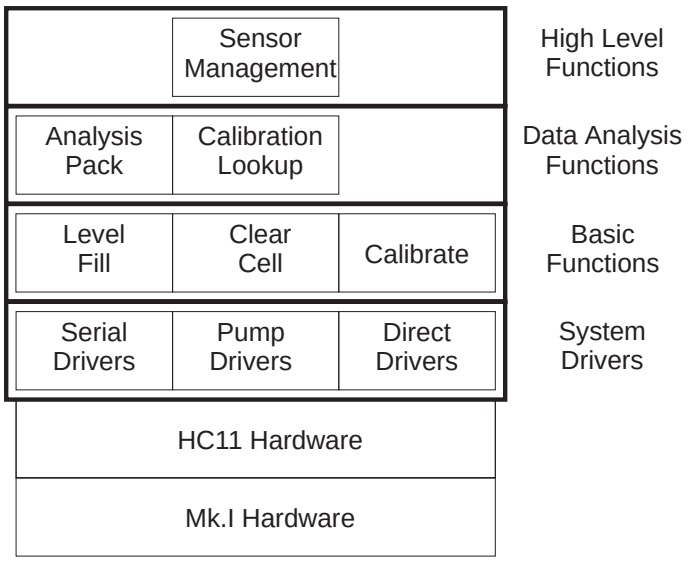

Figure 9.1: Structure of the firmware for the Mk.I Prototype.

Motor speed control for the Mk.I pumps was achieved through the use of PWM (Pulse Width Modulation) techniques. This allowed a wide range of pumping speed to be selected as required by the microcontroller. In this manner all three motors (with the software easily able to manipulate up to 8 motors) could have independent speed control. This same motor control drivers were used in the Mk.II firmware with further advancements to allow further speed control precision. The PWM firmware executed as a background interrupt process on the microcontroller, allowing the all measurement and data manipulation processes to run in the foreground.

Additional software was also written to allow the microcontroller to use external A/D converters and multichannel multiplexers (Appendix Section A.2.1) during the development and component testing of the Mk.II prototype instrument.

9.1.2 Mk.I Offline Calibration Software

The Mk.I calibration software was written to operate within MATLAB (on an external PC) as this allowed rapid development and testing of the models (Section 7.3) rather

than having them directly embedded into the Mk.I firmware. This software would take the previously recorded turbidity data from the prototype instrument and calculate the "T3" calibration model parameters to represent the system.

The initial "Time-To-Threshold" model generator would perform the following functions:

- filter the data using an un-weighted average function, $data[t] = \frac{\sum_{n=t}^{t+4} data[n]}{5}$;
- obtain the first data value in the series and make this the 'baseline' value;
- scan each value in the series until it exceeds the chosen 'baseline + threshold offset' value; and
- determine the time to this particular threshold.

This software was used to generate the times as shown in Table 7.2.

9.1.3 Mk.I Simulation Software - CO2_SCS

To simulate the fundamental measurement system in order to prove the "T3" model's effectiveness, a simulator was written which would take previously acquired turbidity data from the Mk.I hardware prototype, apply the "T3" model and derive the CO_2 concentration. This took the form of the software package "`CO2_SCS`" (CO_2 Sensor Control System).

The purpose of this software was to simulate the overall measurement system excluding the actual realtime acquisition of the turbidity data, which was obtained by another software tool running on the prototype instrument hardware. `CO2_SCS` was designed to display and validate the method of threshold models as shown in Chapter 7.2.

This software was written using "Microsoft Quick-C v 2.5" for MSDOS. Also included was a windowing graphical user interface previously written by the present author.

Whilst `CO2_SCS` was originally written as a simulator for the entire measurement system, extra facilities were built-in to allow further development into a larger control package for the sensor hardware at a later date. This extension of functionality was however not pursued due to difficulties in the serial communications code and problems with serial interrupt programming in the Quick-C programming environment.

The `CO2_SCS` software performed the following functions (ignoring graphical components):

1. read in the first optical data point and save as the '*baseline*' value for which all other thresholds were referenced from;
2. calculate each target threshold for the 5 simultaneous models (baseline + 10, 20, 30, 40, and 50 arbitrary optical units);
3. obtain the next optical data point;
4. filter the data as it is read using an un-weighted average function as shown in Equation 9.1;
$$data[t] = \frac{\sum_{n=t}^{t+5} data[n]}{6} \tag{9.1}$$
5. check if the newly read data point exceeds the next pending threshold (would be 'baseline + 10' at the beginning of the test);
6. as each threshold point was identified, the reverse lookup equation (Equation B.2) would be implemented and the CO_2 concentration for that threshold point identified (this model in this software implementation was preprogrammed from prior experiments and applied as seen in Figure 9.2); and
7. repeat from item 3 until all sub-models have been resolved.

Figure 9.3 shows a typical screen from the `CO2_SCS` software after a measurement has been performed. Clearly shown are the separate windows used to display the optical data, measured threshold times as well as the resolved CO_2 concentration. Also shown

```
float calc_mod_value(int model,float x){
    struct _ans modeldat[5] = {{2.786,−5.678,1.905},
                               {2.803,−4.481,1.326},
                               {2.841,−3.919,0.996},
                               {2.889,−3.445,0.671},
                               {3.032,−3.579,0.871}};
    float answer;

        answer = (10*exp(modeldat[model].a +
                  modeldat[model].b * (x/1000.0) +
                  modeldat[model].c * pow((x/1000.0),2)));
    return(answer);
}
```

Figure 9.2: Sample code for the calculation of the concentration value based on the time measured and the selected model.

is the cell status window to be used for later versions of the software as it was to be developed into a full control package for the sensor hardware, however this functionality was not used any further.

Figure 9.4(a) shows the raw optical data as obtained either from a retrieved file or from the serially (RS232) connected MC68HC11 hardware (Mk.I). Also shown are each of the threshold points (referenced from the baseline measurement). At the intersection of each of these thresholds, the time to that threshold is marked and used in further calculations. At some of these intersections spikes are clearly seen, which are the result of electrically unsuppressed pump motors at the time. This was corrected for later versions of the hardware prototype. These spikes are highly undesirable as they clearly show that the determined time to that threshold could be advanced in error when compared to the overall averaged data trend. For this reason, it was found to be imperative that a noise-free optical signal be recorded, i.e. free of bubble errors, or other abnormalities caused by either internal influences (motor and pump switching) or external variables. A 2nd order polynomial least squares approximation fit is also shown with this data. This trend was calculated in real-time as data was obtained and the results were investigated as a possible alternative method of determining the CO_2 concentration. Some initial work was performed using this method but was not pursued in favor of the "T3" model.

Figure 9.4(b) shows the reverse calculation from the time determined at each threshold back to the concentration value (shown by the five sets of translational lines from the bottom axis up to the curves then across to the vertical concentration axis). These values, as well as the threshold times, were shown in the "T3" model window (Figure 9.4(c)). Additionally the fit polynomial coefficients were also presented in the "Predictive Model" window (Figure 9.4(d)).

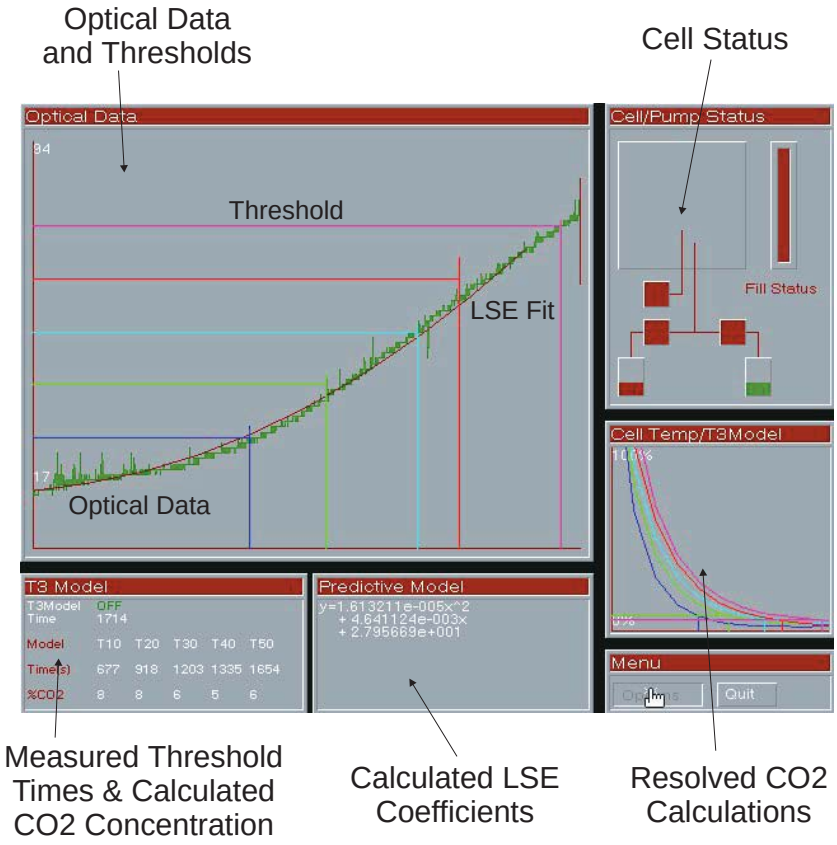

Figure 9.3: Screen capture of the `CO2_SCS` software during the processing of some optical data (100% CO_2). (A clearer presentation of the data of this figure is set out in Figure 9.4.)

Although multiple models were employed for the five threshold offsets (baseline + 10, 20, 30, 40, and 50) no decision algorithm was imposed. As such this software simply rendered the five separate CO_2 calculations which would then have to be resolved to a single concentration value. (This issue of 'data fusion' is discussed in Section 7.2.1.)

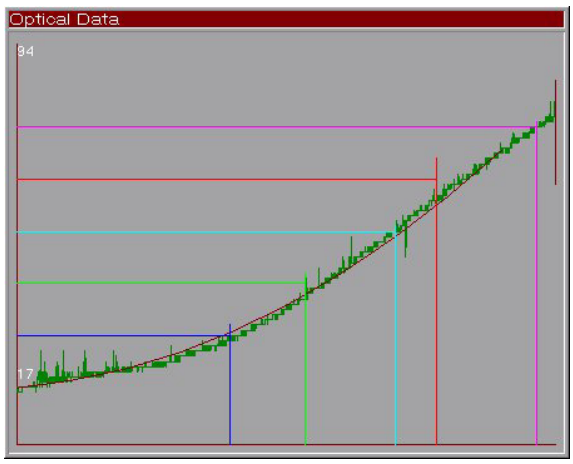

(a) Optical data, threshold points and times to each threshold. The horizontal axis shows time in seconds, whilst the vertical axis shows the arbitrary optical data values (A/D bits).

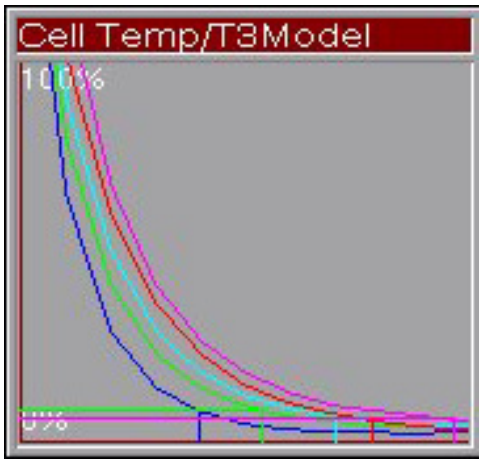

(b) The reverse calculation curves for each of the models to translate the measured threshold time back to a CO_2 concentration. The horizontal axis shows the measured time in seconds to each threshold, whilst the vertical axis shows the concentration of CO_2.

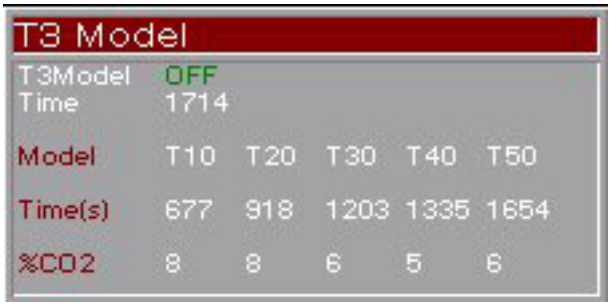

(c) The time in seconds to reach each of the five thresholds as well as the calculated CO_2 concentration for each of the threshold models.

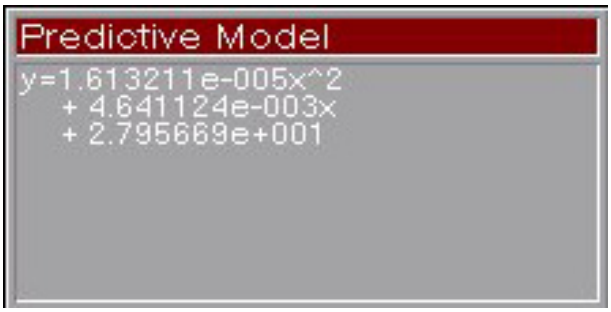

(d) The calculated coefficients for the 2nd order polynomial fit.

Figure 9.4: An expansion of the windows present within the `CO2_SCS` software package (from Figure 9.3).

9.2 Mk.II Prototype Software & Firmware

The Mk.II originated as a 'single chip' microcontroller design that was required to be fully autonomous with no external control (from PC or otherwise). This was found to be difficult to implement given the relatively small program space available in the microprocessor chip (2kbytes for the MC68HC11E2). Variations of this microcontroller were examined with the anticipation that the code could be written in C, this too was found to be difficult due to the need to port a large amount of software routines that had already been written assembly language.

A solution to this problem was to use an external PC (personal computer) as a controlling master system with the Mk.II instrument hardware acting in a slave capacity. The master would request tasks to be performed, the slave would obey and return relevant results data for further analysis back to the PC. The detailed software structure of these two systems is presented in Figure 9.5. The PC hardware would provide all the user interface and data analysis functions. All physical hardware functions were then managed by the slave system providing the necessary drivers to control the hardware. These two systems would then communicate via the RS232 serial line forming the complete measurement system.

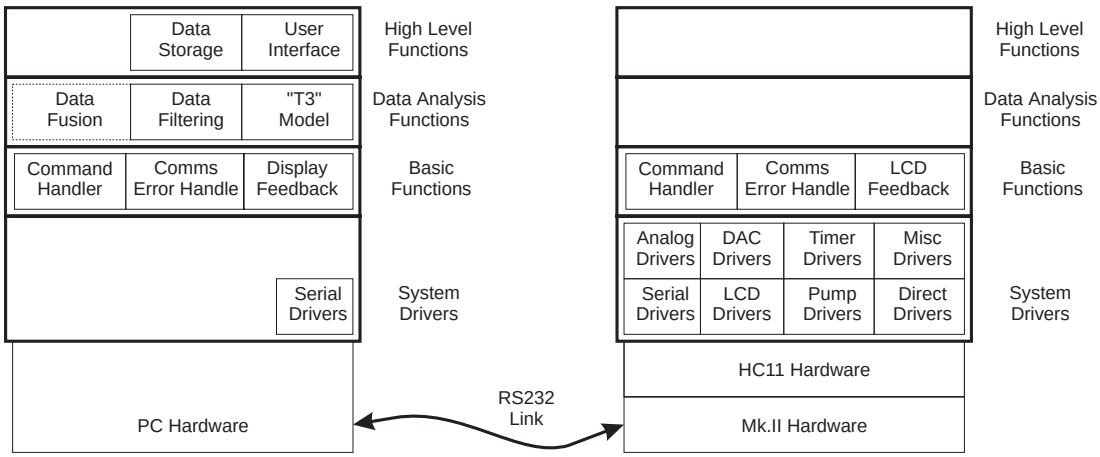

Figure 9.5: Pictorial view of the functional relationship between the master controlling program and the slave system.

9.2.1 Master - Slave Communications

In order for the master PC to reliably communicate with the slave system, a small inherently but stable communications protocol was implemented. This protocol transmitted small two-byte packets of data between the master and slave systems. The first byte was the command byte, with the second being the data command, or returned data result byte, as presented in Figure 9.6. Fault tolerance was written into the serial driver software on both the PC and the Mk.II instrument firmware allowing reliable communications between the two systems.

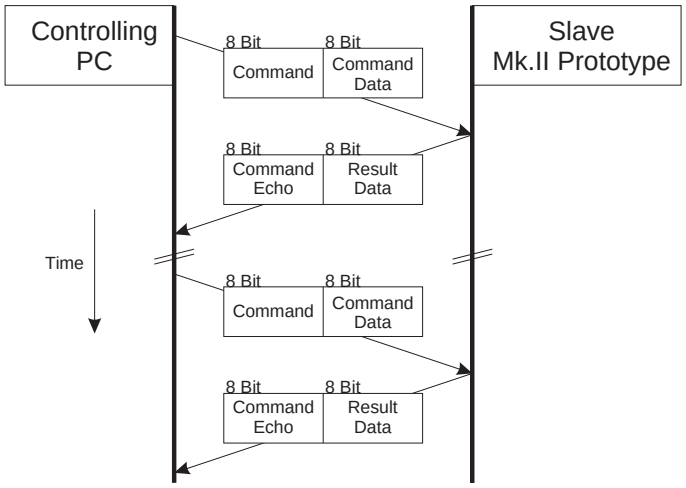

Figure 9.6: Pictorial view of the master/slave serial communications protocol developed. Two separate command exchange are shown.

When requesting data from the slave, the procedure for the master controlling PC was:

1. send first packet containing the command byte, and data byte;
2. set a timer and wait for a returned packet. If no packet was received within 1 second, the original command packet would be retransmitted;
3. if an incomplete or badly-formed packet was received, that received packet would be ignored and the master would retransmit the original command packet;

   and when successfully received:

4. process the returned packet.

The slave would perform the following procedure;

1. wait for a packet to arrive;
2. if an incomplete of badly formed packet was received, that packet would be ignored;
3. if an invalid command was received, the packet would be ignored;
   and when a packet judged complete and valid was received:
4. process the packet, perform the required operation; and
5. transmit a return packet consisting of the same command byte but with a new data byte containing the requested data (if the requested operated resulted in result data), or otherwise a default return value of $FF.

9.2.2 Mk.II Hardware prototype Firmware - GenHC11

Firmware was written to run on the Mk.II hardware, named `GenHC11`. This firmware was written in assembly using the same software development tools as for the Mk.I. This firmware was written as a small operating system with a driver layer, a basic functions layer and a higher order data analysis layer (Figure 9.5).

The Mk.II firmware (`GenHC11`) would wait within a message handling loop for the next command packet. Once the command was received it would determine the command function and pass this onto the specific driver for that command. Any data returned from the driver would then be sent back to the controlling PC in another two-byte packet (the returned command byte was an echo of the received command byte). Should communication time-out or data packet errors be encountered, by either the controlling PC or Mk.II instrument, these would be handled accordingly to maintain data synchronisation between both systems.

Table 9.1 and Table 9.2 list all the available commands on the Mk.II instrument hardware grouped by common hardware feature. These commands allowed numerous functions including initialization and configuration of hardware systems, control of pump speeds, as well as obtaining data from the 16 channel multiplexer through the 12 bit A/D converter. Because only 8 bits in each packet of the serial protocol were reserved for returned data, any command normally returning 16 bits of data had two functions, one to retrieve the high byte, and one for the lower, with the two values combined at the controlling PC end (for example `HC11F_EADH` and `HC11F_EADL` to obtain the high and low bytes respectively from the 12 bit A/D).

Both the Mk.II testing software `HC11term` software (running on the PC) and the firmware `GenHC11` shared a single protocol description file (`HC11prot.h`) containing these command descriptions. This allowed any variations of the protocol to be reflected in both the master and slave software. Additional software to translate this C header file information into assembly suitable for the `GenHC11` firmware was written for this purpose.

Table 9.1: Command set of the Mk.II hardware prototype firmware. Part 1 of 2.

Command Name	ID #	Data Sent	Data Received	Description
Generic Commands				
HC11F_ALIVE	0	NULL	NULL	Is HC11 Alive?
HC11F_HWV	1	NULL	NULL	Obtain Hardware Version
HC11F_SWV	2	NULL	NULL	Obtain Software Version
HC11F_ECHO	3	Data to Echo	NULL	Echo Characters
Internal Analogue to Digital Converter Commands				
HC11F_ADBANK1	4	A/D Bank	NULL	Select A/D Bank 1
HC11F_ADBANK2	5	A/D Bank	NULL	Select A/D Bank 2
HC11F_ADBANK3	6	A/D Bank	NULL	Select A/D Bank 3
HC11F_ADBANK4	7	A/D Bank	NULL	Select A/D Bank 4
HC11F_AD0	8	NULL	A/D Value	Obtain A/D 0
HC11F_AD1	9	NULL	A/D Value	Obtain A/D 1
HC11F_AD2	10	NULL	A/D Value	Obtain A/D 2
HC11F_AD3	11	NULL	A/D Value	Obtain A/D 3

Table 9.2: Command set of the Mk.II hardware prototype firmware. Part 2 of 2.

Command Name	ID #	Data Sent	Data Received	Description
Special Reserved System Commands				
HC11F_Nothing	12	NULL	NULL	Ignore
HC11F_RESET_NO	13	NULL	NULL	Deny Remote Reset
HC11F_RESETYES	14	NULL	NULL	Allow Remote Reset
HC11F_RESET	15	NULL	NULL	Perform Remote Reset
HC11F_SERVER	16	NULL	NULL	Perform Server Action
Frequency Measurement Commands				
HC11F_FREQ1H	17	NULL	Freq 1 MSB	Obtain Freq 1 MSB
HC11F_FREQ1L	18	NULL	Freq 1 LSB	Obtain Freq 1 LSB
HC11F_FREQ2H	19	NULL	Freq 2 MSB	Obtain Freq 2 MSB
HC11F_FREQ2L	20	NULL	Freq 2 LSB	Obtain Freq 2 LSB
HC11F_FREQ3H	21	NULL	Freq 3 MSB	Obtain Freq 3 MSB
HC11F_FREQ3L	22	NULL	Freq 4 LSB	Obtain Freq 4 LSB
Reserved Commands				
HC11F_RES1	23	NULL	NULL	Ignore
HC11F_RES2	24	NULL	NULL	Ignore
Analogue Multiplexer Switch Commands				
HC11F_SETC	25	MUX Channel	NULL	Select MUX Channel
External A/D Converter Commands				
HC11F_EADH	26	NULL	A/D MSB	Obtain A/D MSB
HC11F_EADL	27	NULL	A/D LSB	Obtain A/D LSB
General HC11 Port Commands				
HC11F_CLPA	28	NULL	NULL	Clear HC11 Port A
HC11F_SETA	29	Set Value	NULL	Set HC11 Port A
HC11F_CLPB	30	NULL	NULL	Clear HC11 Port B
HC11F_SETB	31	Set Value	NULL	Set HC11 Port A
External DAC Commands				
HC11F_SETD1	32	Set Value	NULL	Set DAC Port 1
HC11F_SETD2	33	Set Value	NULL	Set DAC Port 2
HC11F_SETD3	34	Set Value	NULL	Set DAC Port 3
HC11F_SETD4	35	Set Value	NULL	Set DAC Port 4
Pump Motor Control Commands				
HC11F_PUMP1	36	Speed (0-3)	NULL	Set Pump 1 Speed
HC11F_PUMP2	37	Speed (0-3)	NULL	Set Pump 2 Speed
HC11F_PUMP3	38	Speed (0-3)	NULL	Set Pump 3 Speed
HC11F_PUMP4	39	Speed (0-3)	NULL	Set Pump 4 Speed
Pump Motor Variable Speed Control Commands				
HC11F_MOTO	40	Off PWM Value	NULL	Set Variable PWM Speed
HC11F_MOTI	41	On PWM Value	NULL	Set Variable PWM Speed

9.2.3 Mk.II HC11 Testing Software - HC11term

During the development of the Mk.II firmware, a generic control package was written to allow testing of the hardware components of the Mk.II. This package took the form of `HC11Term` (Figure 9.7). This software was written using "Borland C++ Builder" incorporating 3rd party serial communication and data graphing code objects.

This software was designed to test specific hardware components the Mk.II instrument, including:

- the MC68HC11 internal 8 bit A/D inputs (used for microcontroller board diagnostics);
- the input capture system (used for the humidity sensor);
- system identification to ensure that both software and hardware versions matched;
- the external 12 bit A/D and its 16 channel multiplexer;
- the 4 channel, 8 bit DAC system for controlling the LED output current, photodiode sensitivity current level, 12 bit A/D converter voltage range, differential amplifier offset voltage; and
- the four pumps under PWM speed control.

The menu items within `HC11Term` were:

File provided simple file operations (such as saving transcripts of testing sessions).

Transcripts provided a means of clearing the display windows.

Serial Port allowed changing of the serial port and speed through which communications would take place.

System provided system level functions.

Versions requested the hardware or/and software version of the Mk.II hardware/firmware.

Reset enabling remote resetting of the Mk.II hardware.

Is Alive? requested a check to ensured the system was powered, and operating normally.

Become Server placed the Mk.II into a server mode where it could operate autonomously, sending data back through the serial port to be recorded for later analysis.

Ports allowed direct manipulation of the interface ports on the microcontroller.

PORT A allowed the modification of the PORT A interface lines on the MC68HC11 PORT A (connected to the interfacing system for the external 12 bit A/D and other system components).

PORT B allowed the modification of the PORT B interface lines (connected to the pump motor controls).

A/D allowed requesting the values of any of the internal MC68HC11E2 A/D inputs.

SPI allowed control of any of the devices connected to the SPI bus (Serial Peripheral Interface, part of the digital I/O, Figure 8.2).

A/D allowed requesting data from the external 12 bit A/D.

DAC allowed the setting of either of the two DAC channels to any one of 5 values from 0% to 100% in 25% intervals.

Switch allowed selection of which of the 16 analog input channels the external A/D was sampling from.

Frequency allowed requesting of the value of any of the three frequency counters running on the system.

Commands for manipulation of the external 12 bit A/D, the 4 channel-8 bit DAC, the 16 channel multiplexer, and the pump speeds could also able to be controlled by

using the onscreen slider bars and toggle controls within the `HC11Term` software (Figure 9.7(b) for example).

Because of the object orientated programming environment of "Borland C++ Builder", construction of a full measurement instrument control system within this environment was not able to be completed in the style of the `HC11term` package. This was due to the difficulty of writing a procedural program to control the sensor hardware whilst at the same time allowing the serial port and graphical interface update to occur simultaneously. For this reason, `HC11term` was maintained only as a diagnostic tool. Had the 3rd party serial tool code objects been able to operate seamlessly within a procedural programming environment, "Borland C++ Builder" would have made an excellent platform for the construction of a virtual instrument environment based around the Mk.II sensor hardware platform.

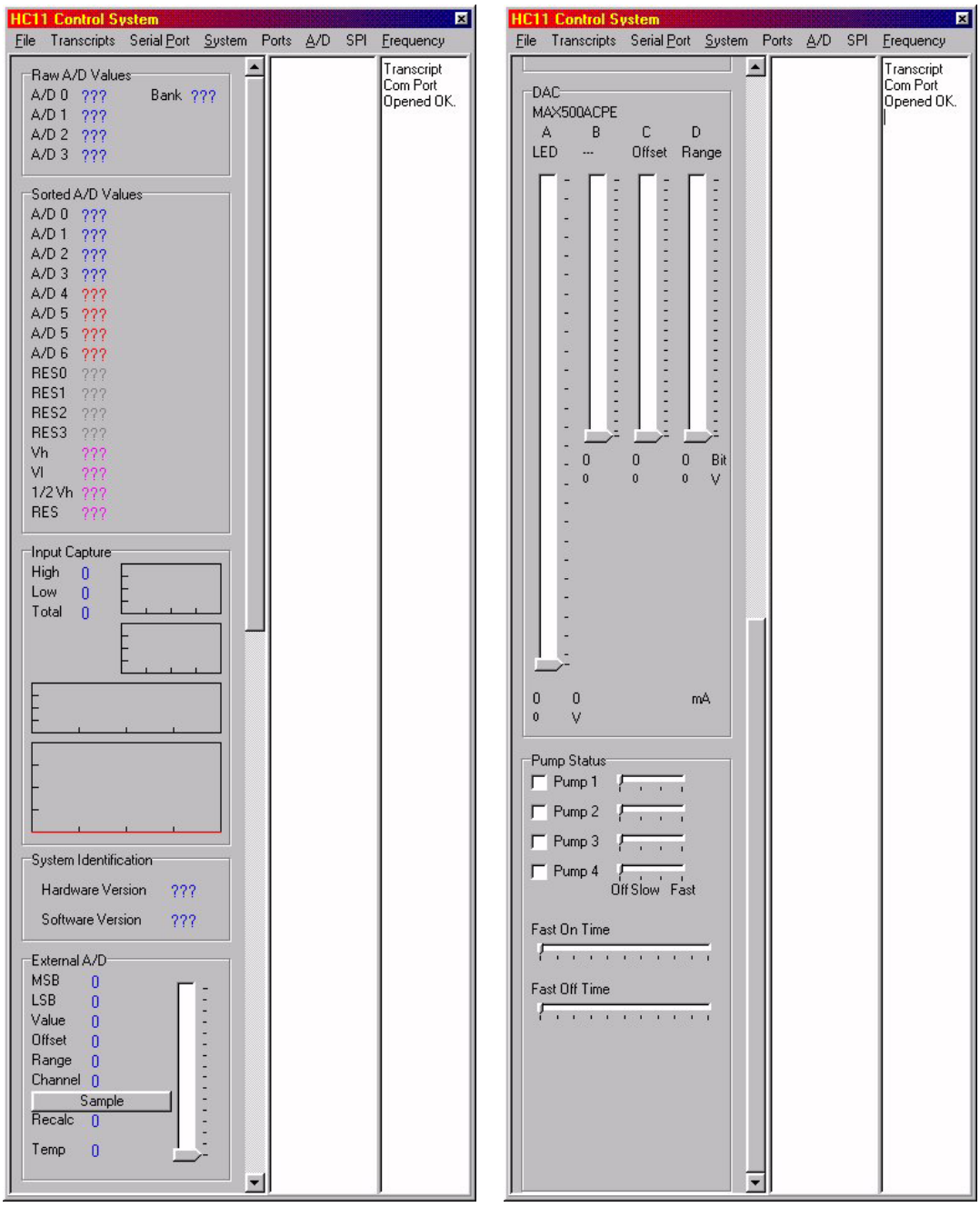

(a) Upper components. (b) Lower components.

Figure 9.7: Screen captures of the `HC11Term` testing software for the Mk.II measurement instrument prototype. Shown are the main menu items, and the onscreen controls. Question marks ("???") indicate currently unobtained values.

9.3 Mk.II Control Procedures

The duties of the Mk.II control software running on the PC were to control the slave's hardware, perform analysis of measured data received from the hardware, present the user with the relevant results, and store data to disk for further analysis. This software was originally intended to be written as an extension of the `GenHC11` software (Section 9.2.2) however difficulties in writing procedural software routines within the object orientated environment of "Borland C++ Builder" were discovered. The software was then written in "QBasic" for MSDOS which allowed rapid software development incorporating the serial (RS232) communication protocol. This software was then able to command the MK.II instrument hardware to perform any of the commands shown Table 9.1 and 9.2.

The controlling structures consisted of software routines as illustrated in Figure 9.8. Each of these items is covered in the following subsections.

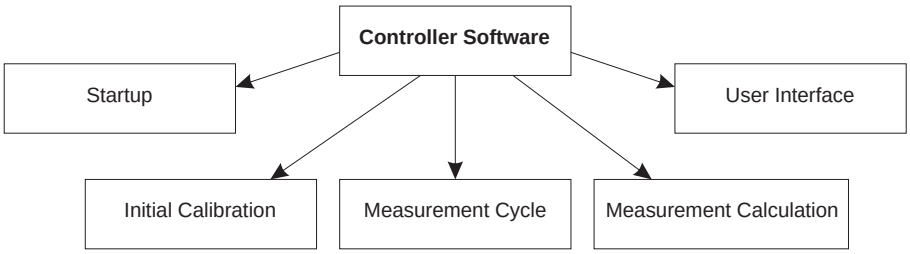

Figure 9.8: Pictorial view of the functions the master controlling system performed.

9.3.1 Startup

When the measurement system was initialised, several logging, data analysis and cell preparation tasks were required to be performed.

The startup procedure was:

1. ensure that the slave system is present and operating properly;
2. prepare disk files for data storage;
3. initialise the computer graphics, and user interface; and finally
4. instruct the Mk.II instrument hardware to clean the cell.

9.3.2 Initial Calibration

Before turbidity measurements could be performed, initial calibration of the optical turbidity was required to determine the state of the optics and the cell with respect to precipitate coating. This was done by measuring the optical turbidity both when the cell was empty and when the cell was full of indicator solution. These measurements allowed for the optical baseline to be derived ensuring that the cell was still in a useful condition. The initial calibration procedure was:

1. clean the cell (by filling with cleaner, waiting, then emptying the cell);
2. measure empty (cleaned) turbidity calibration values;
3. fill cell with indicator solution;
4. measure full (cleaned) turbidity calibration values;
5. empty the cell; and
6. reclean the cell.

9.3.3 Measurement Cycle Control

The central procedure of the measurement instrument was the measurement cycle control function. Through this function, the instrument would gather the time-based

turbidity curve for further processing. The basic procedure was:

1. clean the cell;
2. record the turbidity measurement; and
3. re-clean the cell.

During the cleaning of each cell, a cleaning function was performed, before and after each turbidity curve measurement (for single measurements) or only before each turbidity measurement during continual operation. This cleaning procedure would maintain the cell and return the steady-state turbidity measurement to a known value. This cleaning procedure was:

1. drain the cell;
2. pause (4 seconds, to allow the water film on the cell wall to drain);
3. re-drain the cell;
4. pause;
5. fill the cell with cleaning solution;
6. pause (4 seconds, to allow the water film on the cell wall to drain);
7. drain the cell;
8. pause (4 seconds, to allow the water film on the cell wall to drain); and
9. re-drain the cell;

The turbidity measurement cycle then consisted of the following procedure.

1. clean the cell (using the above procedure);

2. measure empty (cleaned) turbidity calibration values.
3. fill cell with indicator solution;
4. begin injecting the sample gas into cell;
5. measure optical turbidity at the preset sample rate;
6. continue to take optical measurements until the last threshold is reached ('baseline+0.5v');
7. empty the cell;
8. re-clean the cell; and
9. return to item 3 for next measurement.

9.3.4 Measurement Calculation

The measurement calculation procedure would take the threshold data from the prior turbidity measurements, and determine the concentration of CO_2 according to the chosen models (Section 7.4). This procedure performed the following:

1. obtain the first threshold time ('baseline + 0.1v');
2. determine the CO_2 concentration according to the model (exponential, power, interpolated cubic spline);
3. obtain the next threshold time ('baseline + 0.X v');
4. determine the CO_2 concentration according to the model (exponential, power, interpolated cubic spline);
5. repeat items 3 and 4 for all baseline thresholds; and
6. apply data fusion procedures to all calculated concentration values (Section 7.2.1).

9.3.5 User Interface

The user interface procedures were to provide detail about the state of the Mk.II hardware, serial communications data, and of the CO_2 calculation values. However, these procedures were not implemented, with all data that would normally have been displayed on screen having been stored to file for further processing.

9.4 Additional Software

Many additional software packages were written during this research to aid in the development and usage of the measurement instrumentation systems. This software included:

Modelling software exploring the use of a 2nd order polynomial fit to the turbidity curves of the Mk.I measurement instrument (which were not pursued in favor of the "T3" model system);

AWM3100 flowmeter calibration software to allow calibration of the flowmeter component based on the supplied calibration data;

AWM3100 flowmeter sensor software developed to generate a stand alone instrument from the AWM3100 flowmeter (using a single chip MC68HC11E2 and LCD to display the flowrate in realtime);

Gas lab flowmeter calibration software to calibrate the precision rotameter flowmeters used as part of the gas laboratory (Appendix F);

Common header packages which allowed a single 'C' header file containing the command-set for the Mk.II hardware prototype to be shared between both the Mk.II firmware and the `HC11term` testing software to maintain synchronisation of feature sets;

LCD graphic generator software used to generate custom characters for the LCD display used in the Mk.II hardware prototype; and

Analysis/plotting scripts which assisted with the analysis and plotting of data throughout this dissertation.

9.5 Software Listings

Software listings for the software packages described in this chapter can be found in Appendix C.

Chapter 10

System Performance

10.1 Introduction

Once construction of each prototype was finished, critical areas of performance were investigated. These areas were:

- cell performance;
- prototype hardware performance;
- pumping performance;
- analogue electronics performance; and
- modelling performance.

This chapter details these performance results with Chapter 11 providing an insight into the performance of the overall sensing methodologies employed.

10.2 Mk.I Instrument Performance

As previously shown, the 'Mk.I' system implementation employed microcontroller systems, reagent containment systems as well as mechatronic fluid control structures and strategies. The performance of the Mk.I measurement instrument was therefore evaluated within three main areas, namely cell performance, instrumentation hardware and implementation performance, and overall sensor performance (encompassing accuracy, discrimination and repeatability).

10.2.1 Cell Performance

The performance of the cell utilised ('teardrop' cell with mesh bubble guard) has already been presented in Section 4.5 and 4.6. As shown this cell was able to perform adequate mixing of the indicator solution and sample gas bubble stream for low flow rates (~1mL/min) whilst maintaining homogeneous state of any precipitate produced, and exhibiting good bubble dispersion. It was also clearly able to perform the physical and interconnect functions easily and reliably.

The utilised cell however did suffer several problems particularly with the ability to function at high flow rates (typically above 15mL/min). At these high flow rates, escaping bubbles would tend to force significant volumes of indicator solution through the exhaust port thereby lowering the volume of indicator available for reaction with the sample gas within the cell. This would continue until either a bubble block formed beneath the exhaust port, for example Figure 4.13(a) (a different cell type is pictured), interrupting the fluid circuit around the center flow divider, or the fluid level would fall (as also seen in Figure 4.13(a)) below the sight line of the optics (the upper optic pair, Figure 4.7(b)). Both of these effects would result in incorrect turbidity recordings for the measurement. A temporary solution was found (if operating the cell with high flow rates) by slowly running the reagent pump to counter the reagent loss in the cell. This was able to be run in a closed loop control system using optical fluid level measurements

within the cell however this would also result in a change of the chemical dynamics as fresh reagent would take the place of partially reacted indicator, which was highly undesirable. Therefore the sample gas flowrate was carefully selected so as to minimise this solution loss.

It was also noticed after each calibration run for the sensor (commencing in each case with fresh chemical indicator), that the walls of the cell would become quickly coated with the calcium carbonate precipitate (Figure 10.1). This buildup would affect and interfere with the optical transmittance measurement through the cell. The dynamic range of the optical measurement would decrease. This is shown in the 5% calibration curves of Figure 7.3 in which the 5% CO_2 does not show the expected 100-bit (approximately) A/D range from commencement to complete reaction.

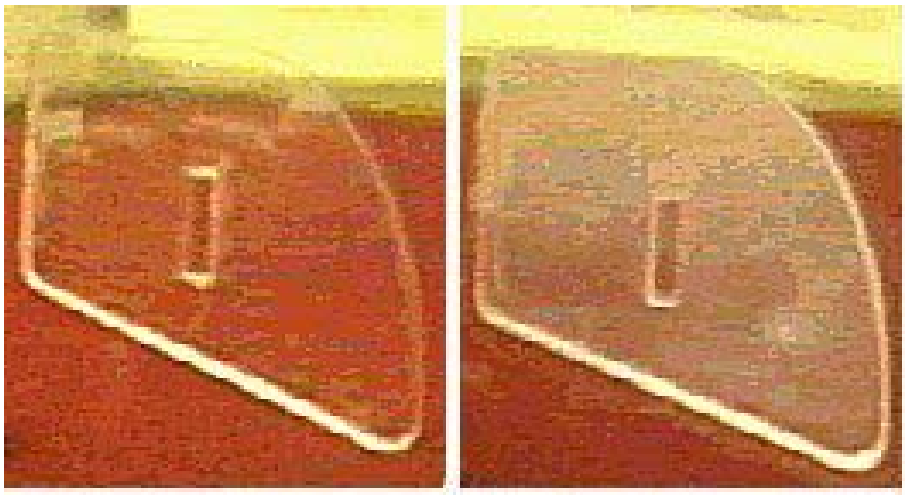

Figure 10.1: An example of calcium hydroxide ($Ca(OH)_2$) precipitate buildup on the inner walls of the cell (the 'teardrop' cell in this case). The left image is a cleaned cell, whilst the right image is clearly shows the internal cell wall coated with a thin film of precipitate. These images were obtained by video capture and hence both images exhibit significant rasterisation.

The optics alignment method utilising a standard 50mm×50mm geometry for the cell and matching PCBs worked well and allowed repeatable alignment of the cells optics whenever the cell was rebuilt. Misalignment did however occur whenever the optical components mounted onto the PCBs were physically damaged or bent as a result of mishandling of the PCBs during mounting onto the cell but would not normally present itself under normal operating conditions. Solutions to this problem were considered

including setting the optics set in epoxy, or a PCB conformal coating, however as misalignment occurred only rarely, no further action was warranted.

10.2.2 Hardware Performance

As previously set out in Section 6.3.6 the Mk.I hardware platform was based around the single-chip Motorola MC68HC11E2 microcontroller and as such much of the systems performance was directly attributed to the specifications of this device. As the initial software used in this device was simple, it proved adequate for initial experimentation however many of the limitations of this chip did degrade the performance of the Mk.I instrumentation system.

In particular, the 256-bit quantisation of the in-built A/D converter proved inadequate, resulting in severe discretisation of the recorded optical signals. In turn, this resulted in significant errors in detecting the threshold points as required by the "T3" model. Also, as the memory size within the chip was small (2kbytes), all recorded data had to be sent back to a controlling PC.

The three pumps used within the fluid control system (Section 6.3.3) were simple off-the-shelf gear pumps which were modified in order to make them direct drive coupled to the pump motors (whereas the pumps as obtained used loose friction connections). Whilst this allowed more precise speed control, it did result in difficulties of alignment; and drive misalignment over time (due to increased load on the pumps from wear and $CaCO_3$ fouling) caused pump stalling. Other problems existed such as pump leakage (Section 10.3.3), where fluid could leak back through the teeth of the gears in the pump potentially draining parts of the fluid transport system of indicator solution, or fouling of the pump by $CaCO_3$ precipitate. Also, as the pumps were connected to the incoming power source, the speed of pumps was largely governed by the input voltage. Because there was no feedback system on the pumps, the effective speed of the pumps was an unknown function of the pulse width modulation (PWM) control signal and the supply voltage. In future designs it would be highly advantageous to have metered pumps

with a feedback feature so that accurate dosage levels could be maintained.

Despite the testing of an optic level control system to precisely fill the cell (Section 6.3.7), this method was unpredictable due to unknown pump filling speeds and time delays between detection of the correct level and ceasation of the pumping operation. Due to the formation of bubbles the optics would also sometimes erroneously detect the level resulting in insufficient filling or failing to recognise that the cell was full, hence overflowing the cell.

10.2.3 Modelling Performance

As previously shown in Section 7.2, the primary model used was the Time-To-Threshold ("T3") model, which used measured duration times to reach specific parts of the measured optical waveform (Figure 7.1), and from this deduce the CO_2 measurements via a reverse lookup model.

After the calibration model was developed (Section 7.2) it was tested by injecting various concentrations into the measurement instrument, calculating the concentration from the threshold duration times and comparing with the actual concentration. Because there were in effect 5 different models in operation (each of the form 'baseline + x'), the performance of all five models is presented in Figure 10.2. Ideally, all curves should fall on the 1:1 line shown in the figure.

Inspection of Figure 10.2 and Table 10.1 reveals that:

- all five models perform similarly;
- the average characteristic slope for the instrument is 0.758 (This then implies a general calibration error of -24.2% at full scale, or -0.242% error per CO_2% unit);
- a problem exists with the 20% CO_2 curves with respect to the rest of the data. This was caused by the exponential model itself which would consistently calculate

higher concentration values around 20% than for other CO_2 concentrations (as shown in Section B.1.1); and

- scatter with respect to the 5 models is roughly a slope error of ± 0.1 across all models.

Table 10.1: Mk.I "T3" model slope performance for the five versions ('baseline + x').

	CO_2%				
Threshold	5%	10%	20%	50%	100%
+10	0.60	0.70	1.10	0.70	0.76
+20	0.60	0.70	1.10	0.74	0.84
+30	0.60	0.60	1.10	0.78	0.83
+40	0.40	0.50	1.10	0.80	0.83
+50	0.40	0.50	1.00	0.82	0.83
Average Slope	0.52	0.60	1.08	0.77	0.82

10.2.4 Other Effects

During the obtaining of the turbidity calibration waveforms, two significant effects were observed, namely:

- variations in the starting rate of the precipitation chemical reaction; and
- effects on the turbidity measurements due to lack of cleaning of the reaction cell.

The chemical reaction rate variations during the starting of precipitation can be seen in Figure 10.3, where the turbidity curve for two measurements of 20% CO_2 exhibit differing reaction rates at the start of the precipitation cycle. Once the chemical reaction is underway, both turbidity curves exhibit the same reaction rate during the precipitation development but due to the initial rate difference, the curves are shifted in time. This shift would result in higher concentration values being calculated for the initially faster reacting turbidity curve. This rate variation could have been caused by contaminants (such as water) within the cell during the measurement, thereby changing the molarity

of the indicator reagent. For this reason there is a requirement for further research into chemistry stabilisation (Section 11.4.2).

During the measurements, effects of not cleaning the cell were also observed. The Mk.I cell was not capable of being cleaned, apart from flushing of the cell with the indicator solution and/or full disassembly. These effects resulted in the cell wall being coated in precipitate (as previous show in Section 10.2) thereby increasing the measured steady state turbidity and shifting the baseline, as shown in Figure 10.4. As the baseline turbidity would increase the available dynamic range would also decrease, which is also seen in this figure. This thereby showed that for a successful instrumentation system to be constructed, cleaning of the cell, or some method of maintaining cell conditions, would be required.

10.2.5 Summary of Limitations of Mk.I Instrument

The Mk.I prototype did perform many of the functions required of it including and showed that it was successfully able to:

- interface a microcontroller to a photoelectric turbidity sensor structure;
- interface a chemical containment cell to small pumps to provide fluid transport;
- perform cell maintenance by injecting both indicator solution and the sample gas using pumps at appropriate times so to yield a measurement system;
- use a gear pump, typically reserved for liquid flow, as a gas supply pump;
- obtain optical turbidity measurements from a reaction cell which related to the concentration of CO_2 in the sample gas stream;
- demonstrate that the modelling structure used had merit and could form the basis of a calibration model for the instrument; and
- showed that the simple modelling structure could be easily embedded in the microcontroller if enough memory space was available.

However, this prototype also had several deficiencies:

- the overall accuracy and repeatability of the results was poor, primarily due to inefficient mixing within the cell, and cell maintenance problems causing $CaCO_3$ to interfere with the measurement results and the plumbing structure;
- the inability to account for a varying flowrate, or cope with variability in the speed of the gas supply pump;
- the inability to vary the optical emitter intensity or the detector sensitivity, which would have a large bearing on the optical dynamic range the instrument could examine;
- the inability to have the calibration model running on the hardware itself due to insufficient memory space in the onboard RAM of the microcontroller; and
- the inability to cope with serial protocol errors between the hardware prototype and the controlling PC.

Hence there was a need to develop a 'Mk.II' system to address these issues and allow investigation of methods to overcome them.

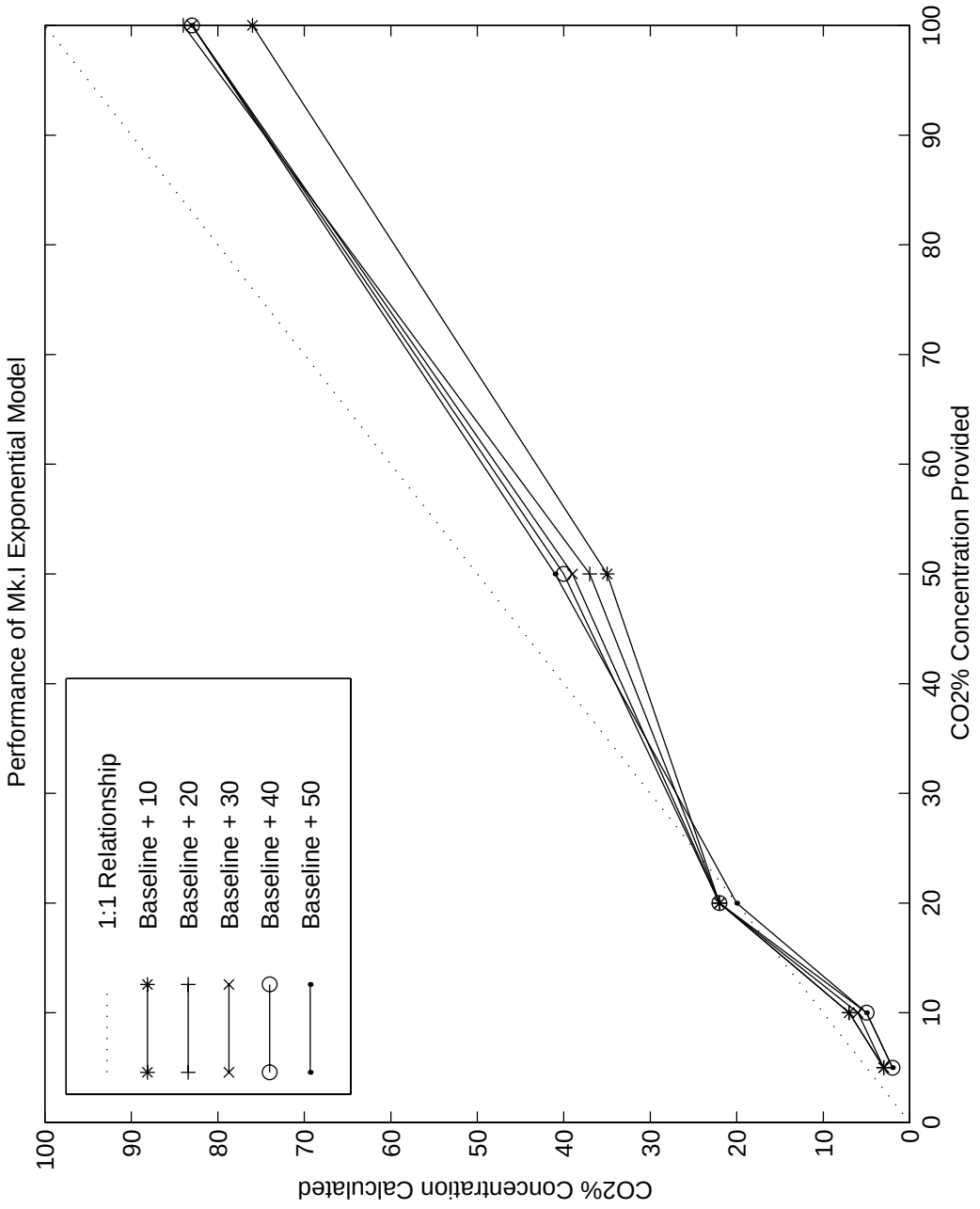

Figure 10.2: Mk.I "T3" model performance for the five versions ('baseline + x') in comparison with the ideal 1:1 line.

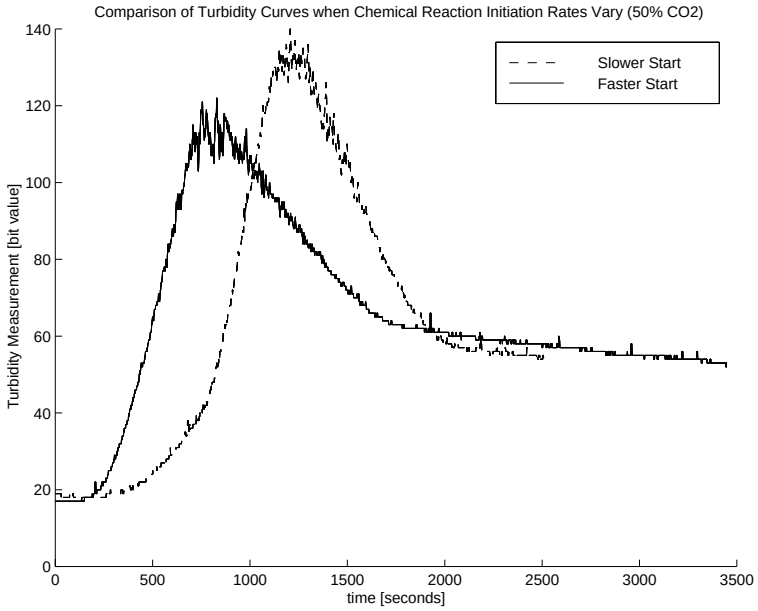

Figure 10.3: Turbidity measurement of 50% CO_2 showing how slight variations in reaction rate during the initial stages of reaction shift the expected turbidity curve.

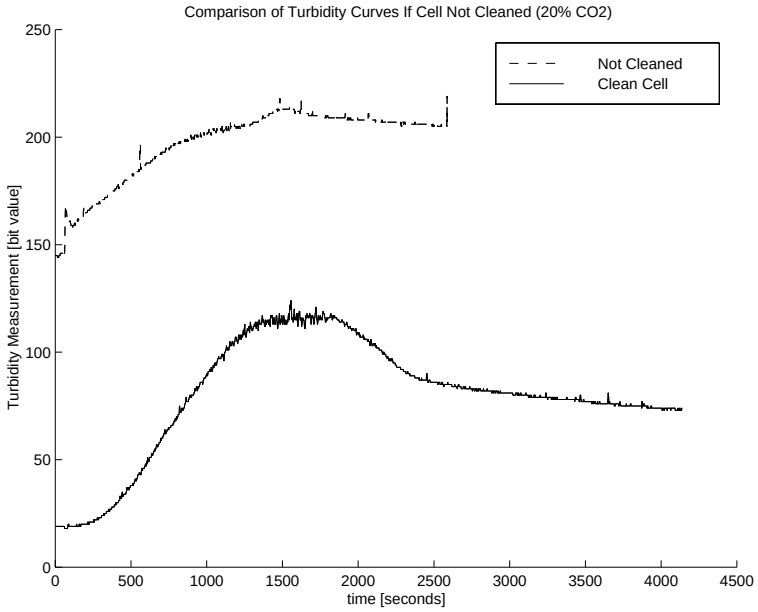

Figure 10.4: Turbidity measurement of 20% CO_2 immediately after the cell was cleaned and then again after several measurements when cleaning was neglected. Shown is the increase in turbidity and the decrease in dynamic range.

10.3 Mk.II Instrument Performance

Following the Mk.I 'proof-of-concept' prototype, the Mk.II system allowed further exploration of the measurement capabilities through its more adaptable hardware. This system differed from the previous Mk.I prototype in the following ways (as shown in previous chapters) through the:

- addition of a chemical cleaning agent to assist with cell maintenance and removal of $CaCO_3$ on cell wall surfaces;
- addition of an extra pumping channel to provide the transport of this additional chemical cleaning agent;
- replacement of the gas pump (previously a 'gear' pump) with a 'bellows' style pump;
- use of an inline flowmeter to provide information about the rate of gas injection into the cell;
- inclusion of a 16 channel analogue multiplexer allowing the monitoring of up to 16 analog channels;
- use of an adaptive A/D converter and associated electronics to allow zooming-in of the resultant electrical turbidity signal to potentially increase the dynamic range of the instrument;
- incorporation of a four channel variable current source to provide microcontroller variable emitter intensity, and detector sensitivity for exploration of smart sensing regimes;
- addition of temperature sensors spread throughout the system including the cell, gas in, indicator solution, analog electronics, and exhaust gas temperatures; and
- inclusion of a relative humidity sensor to allow exploration of the effects of humidity on the instrumentation system.

Unfortunately a full autonomous Mk.II prototype was unable to be completed due to deficiencies in several of the low cost components. However, testing of many of the embedded systems as well as the model performance was able to be performed, and the results of these experiments and analysis are shown below. A discussion of these deficiencies appears in Chapter 11.

The performance of the Mk.II prototype sensor was assessed simillarily to the Mk.I, including:

- cell performance;
- gas and liquid pumping;
- analogue electronics;
- optics and adaptive optics system;
- turbidity practacalities;
- flowrate management;
- modelling performance; and
- overall CO_2 measurement performance.

10.3.1 Cell Performance

The measurement cell used for the Mk.II instrumentation system was the same as used for the Mk.I, however several extra observations and analyses were performed as an extension to that shown in Section 10.2.1 for the Mk.I.

The performance of the cell was further expanded on by testing the effect of excessive gas injection flow rates as well as problems caused by excessive $CaCO_3$ buildup on the walls. The results of these experiments are shown in Section 10.3.7 in association with the adaptive optics.

10.3.2 MFA-650 Gear Pump - Gas Pumping Performance

Tests were conducted on the pumps selected for use within the prototype and particularly with respect to their suitability for gas transport. These tests were conducted by measuring the gas flow rate through the MFA-650 gear pump used whilst measuring the resultant flowrate using the constructed flowmeter module. The pump had one port open, with the second port connected to the IN port of the flowmeter module (Section 6.4.8). A variable voltage was applied to the pump, being ramped up then down, with both the motor voltage and the resultant flowrate recorded. The raw results of this experiment are presented in Figure 10.5. The noise shown on both axes in this figure reflects the speed jitter of the small brushed motors causing an unevenness in the pumping rate and the measured brush voltage.

The results show that the gear pump performs linearly with respect to the applied voltage. This is to be expected as the unloaded rotation speed of the motor will be linear with respect to its applied voltage (excluding stalled situations as observed at motor voltages below 2V). Because of this characteristic, the pump flow rate will be linear with respect to the rotation speed of the gears within, hence confirming the positive displacement nature of the pumps.

Thus it was initially concluded that these particular pumps could be used to pump gases. However, under loaded conditions, back-pressure within the pump resulted in interference of the pumping action and leakage as explored in Section 10.3.3.

The required flowrate range for the cell (10.2.1), concluded that high flowrates were not desirable. However Figure 10.5 shows that these desired flowrates are within regions where the pump motor has stalled, thus requiring the pump to be operated at a higher nominal flowrate with a flow restrictor in place to increase the pump pressure but decrease the actual flowrate. It was found that due to the back-pressure generated by the flow restrictor, the gear pumps performed poorly and would suffer significant flow rate unevenness resulting in an unpredictable gas flow to the cell. Hence for gas transport the Mk.II hardware gear pump was replaced by a 'bellows' pump system

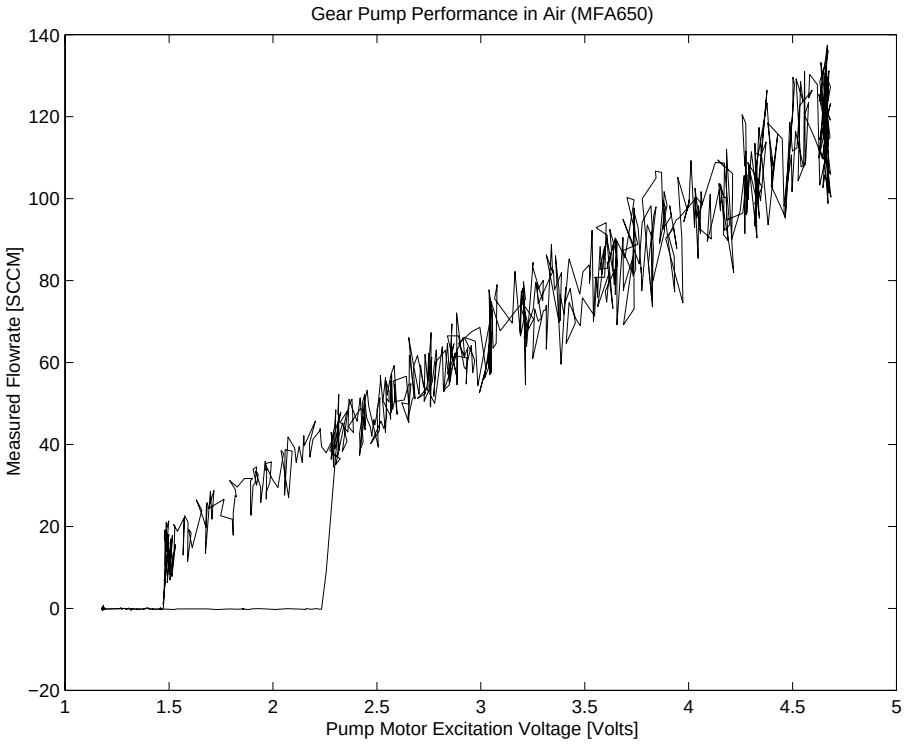

Figure 10.5: Raw data of unloaded flowrate performance of the MFA 650 gear pump for gas.

(described in Section 6.4.7) to provide a reliable and constant gas flowrate.

10.3.3 MFA-650 Gear Pump - Leakage Performance

A series of experiments performed by Buttsworth & Chin (2001), examined the intra tooth leakage of the MFA650 gear pump. These experiments varied the pressure difference between the two pump ports (IN and OUT) with the resultant leakage flowrate calculated when the pumps were static. These results can be seen in Table 10.2 and Figure 10.6.

It is seen that even for relatively low differential port pressures, $\Delta(pressure)$, high leakage flow rates are observed. These test confirm the observed deficiencies of the pumps where fluid would be drained from the reaction cell through the drainage pump

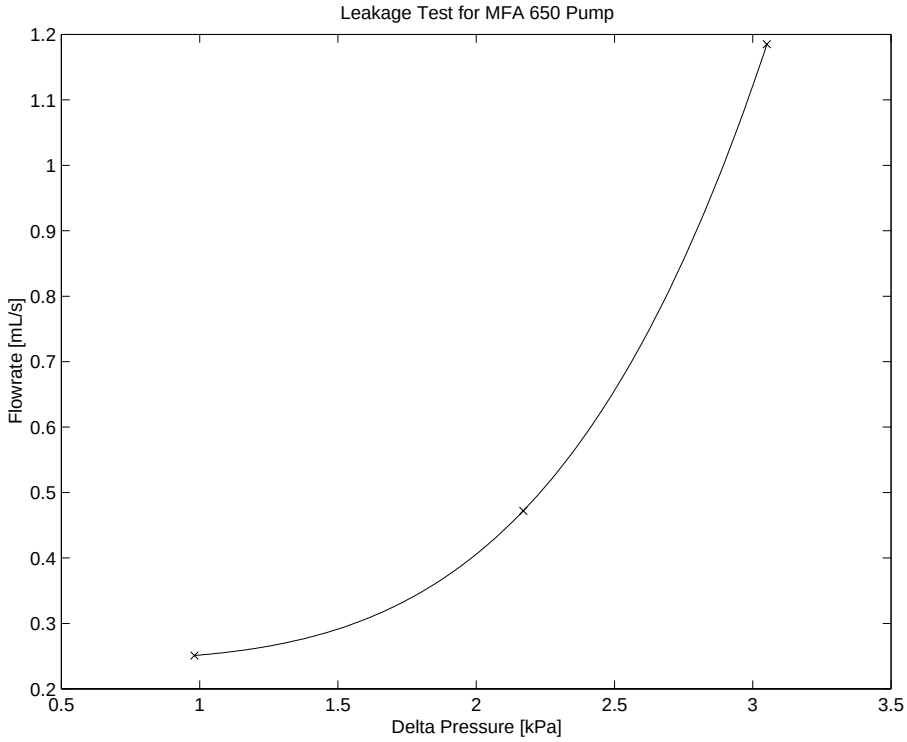

Figure 10.6: Three point plot of the flowrate through the static MFA-650 gear pump for a given port pressure differential.

to the waste reservoir. This then resulted in insufficient indicator chemical being available to react within the cell. For this reason, all instrumentation performance testing for the Mk.II system was performed with this pump deactivated and a syringe used to manually inject the required $Ca(OH)_2$ indicator solution directly into the reaction cell.

10.3.4 Analogue Electronics

The hardware prototype features several voltage reference sources to enable testing of the analog electronics, in particular offset and span errors of the DG506 16 channel multiplexer (MUX), the voltage level offset differential amplifier, and the LTC1286 12 bit analogue to digital converter (ADC). Whilst the variable offset and span features of these electronics were not used in the prototype, tests were conducted to examine the overall accuracy of these combined systems when sampling from the voltage reference

Table 10.2: Table of results for leakage tests of the MFA650 gear pump showing the leakage flowrate at three differential port pressures.

Leakage (mL)	Ambient Pressure	Pump Pressure	Flow Rate (mL/s)	Time (sec)	$\Delta(head)$ (m)	$\Delta(pressure)$ (kPa)
500	518	618	0.251	997	0.1	0.981
500	457	678	0.472	530	0.221	2.17
500	412	723	1.185	221	0.311	3.051

sources with the analog electronics at their default settings.

Figure 10.7 shows the sampled voltage as seen by the analogue electronics (A/D converter set at full span, 5V with 0V offset) over a time duration compared to the actual externally measured voltage provided of the onboard 2.5V reference source. These results are summarised in Table 10.3. A maximum signal noise level of 7.3mV was measured with an offset error of 8mV, and Figure 10.7 shows the A/D quantisation step of 1.22mV.

Table 10.3: Table of analogue signal processing and A/D system performance whilst measuring a 2.5V voltage reference source.

Actual Voltage	2.496 Volts
Measured Average	2.488 Volts
Offset Error	8mV
Maximum Value	2.4902 Volts
Minimum Value	2.4829 Volts
Span Error	7.3mV

Full span accuracy was also tested with several external voltages, provided by a potentiometer and selected via the analog multiplexer. The results of this test are shown in Figure 10.8 and Table 10.4. This figure shows that across the full voltage span of the analogue sampling system (incorporating all associated electronics), the maximum error was measured as 14.6mV with a maximum offset error of 19.5mV. The offset error was seen to be relatively constant across the entire input voltage span, except for an input of 5V or 0V. This was acceptable as the design of the optics avoided these areas of operation. The noise error span was seen to increase with the increasing input voltage. Over the full span an error of $\pm 0.3\%$ would be expected. The range of operation of the optics however was far less than this, and typically was in the range of 0.3V to

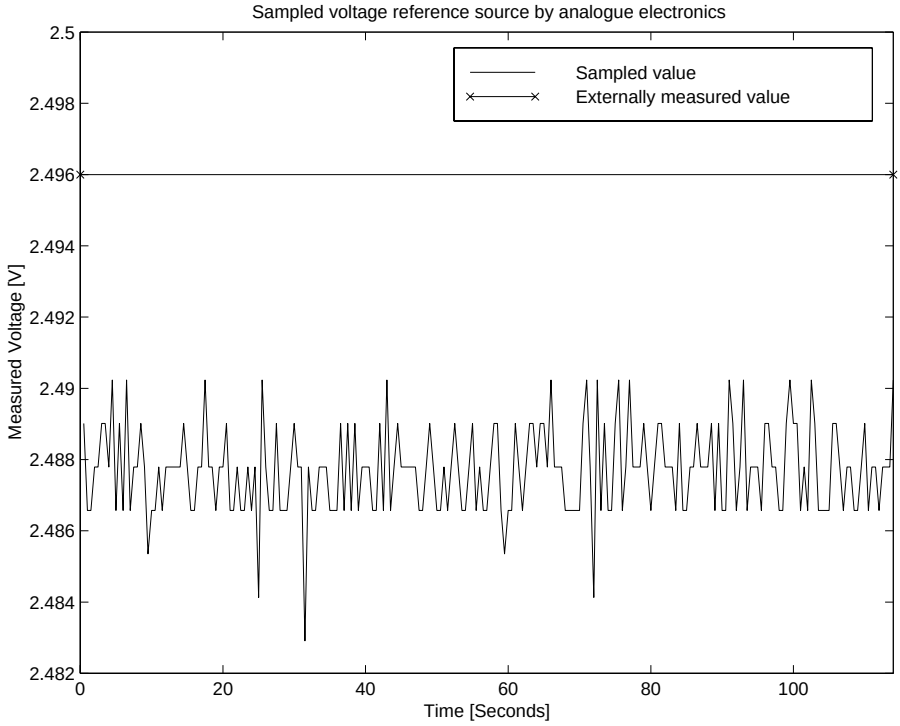

Figure 10.7: A/D converted voltage compared with the voltage of the onboard 2.5V voltage reference source.

2V. Taking this into account, the expected noise error of the analogue electronics was ±0.7%. This was deemed acceptable and within expected performance specifications of the low cost components used.

The offset errors observed would be negated by the calibration model due to the baseline measurement being subtracted from any measured turbidity data. Thus the offset voltage error was able to be ignored.

10.3.5 Howland Current Source

The output current delivered to each infra-red LED emitter via the Howland voltage-controlled current source is shown in Figure 10.9. For bitvalues below 50 the output current would fall to 0V due to the V-I characteristic of the LED. This showed that the

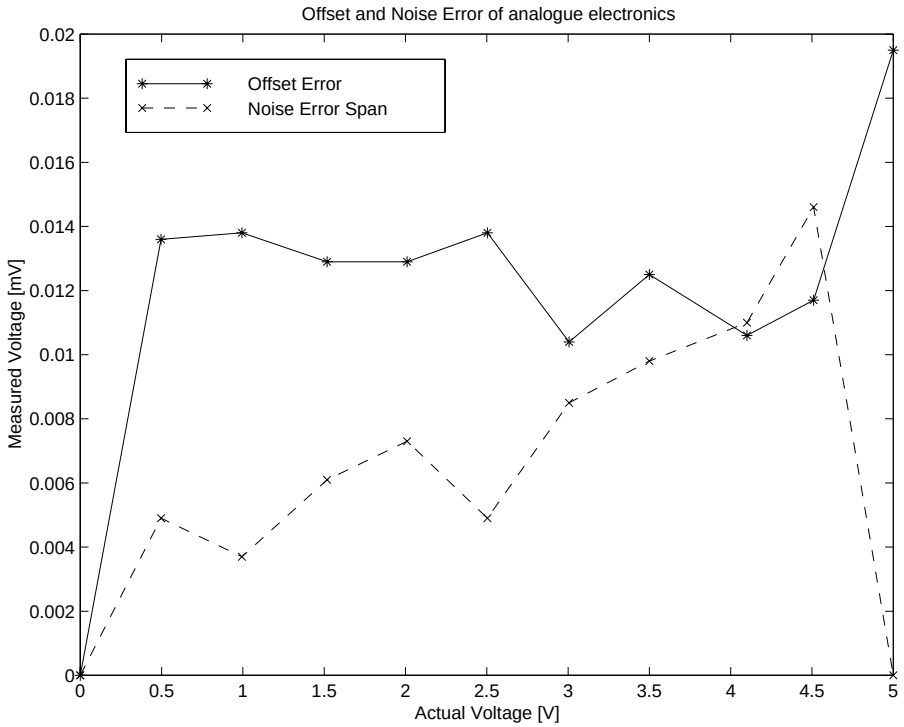

Figure 10.8: Full scale DC offset and noise span errors of the analogue electronics.

useful range of operation for the LED current control system was for DAC bitvalues between 50 (0.98V) and 220 (4.3V), providing a source current between 0mA to 20mA. The non-linearity of this response particularly below a bitvalue of approximately 110 (2.16V) and above 180 (3.53V) was accommodated by the closed loop configuration of the optoelectronics.

10.3.6 Selection of Non-Adaptive Optics Parameters

A series of tests were performed to determine the operating region of emitter power and detector sensitivity to yield maximum dynamic resolution. After preliminary experiments it was observed that there was a distinct range of usefulness of the optics pair to avoid problems such as over-saturation of the detector, or non linear output brightness from the emitter. An experiment was performed where a sample gas measurement

Table 10.4: Full span accuracy test of 12 bit A/D converter and associated electronics.

Actual Voltage [V]	Average [V]	Offset Error [V]	Error Span [V]
0	0	0	0
0.497	0.4834	0.0136	0.0049
0.994	0.9802	0.0138	0.0037
1.518	1.5051	0.0129	0.0061
2.010	1.9971	0.0129	0.0073
2.504	2.4902	0.0138	0.0049
3.006	2.9956	0.0104	0.0085
3.500	3.4875	0.0125	0.0098
4.100	4.0894	0.0106	0.0110
4.510	4.4983	0.0117	0.0146
5.000	4.9805	0.0195	0

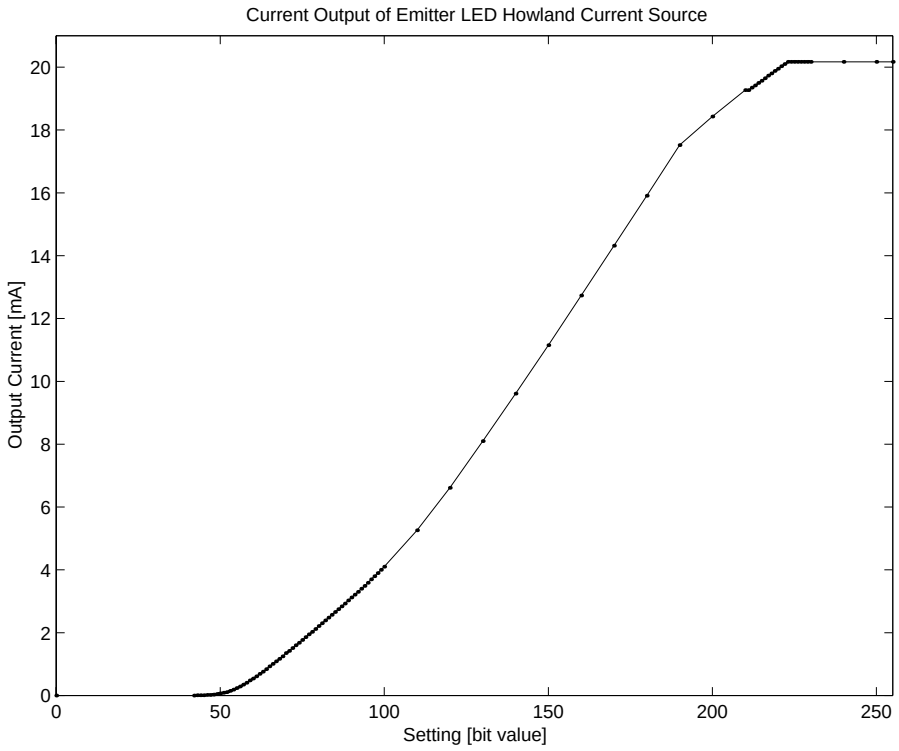

Figure 10.9: Output current from the voltage controlled current source. The actual data points used to compose the curve are shown. A deliberate increase in density of measurements at both the foot and knee of the curve was taken to improve the accuracy of the plot.

was made whilst constraining the detector sensitivity at its maximum, bit value 255, resulting in the maximum allowable current to the photodiode, and varying the LED emitter intensity.

Figure 10.10(a) shows 51 data sets acquired at each of the 51 differing emitter intensity levels, 50 to 100 bit value inclusive. The optoelectronics were configured such that as more optical energy was received by the detector, the voltage would drop. Therefore as the emitter intensity was increased, the detector steady state voltage would decrease accordingly. Also due to this configuration an increase in opacity caused by an increase in turbidity would be recorded as an increase in optical voltage. These effects are summarised in Table 10.5. As a result, Figure 10.10(a) shows this combined effect. If a single optical condition were examined it is seen that as the turbidity increases so does the detected voltage, and the optoelectronics were configured this way to simplify analysis and interpretation of the recorded data.

Table 10.5: Combined effect of turbidity measurement and variation of emitter intensity on the detected turbidity voltage.

Detected Energy $\uparrow$	$\Rightarrow$	Detected Voltage $\downarrow$
Emitter Current $\uparrow$	$\Rightarrow$	Detected Voltage $\downarrow$
Turbidity $\uparrow$	$\Rightarrow$	Detected Voltage $\uparrow$

Fluctuations observed in the turbidity curves are due to insufficient mixing occurring as a result of the sample gas being pulsed on and off during the test and can be ignored as the interest lies in the overall optical disturbance.

Figure 10.10(b) shows a 3D-surface representation of the data and allows interpretation of several interesting areas. Clearly seen is a shelf at the top of the figure where the emitter intensity was set between 50 and 55 (bit value). As shown in Section 10.3.5, at this point the forward current for the LEDs is just starting to overcome the characteristic LED voltage drop, and are just starting to operate thus resulting in a non linear operational relationship. Another critical area shown is the signal floor where the measured voltage is close to zero. This was caused by saturation of the photodiode due to excessive optical energy reaching the photodiode from the LEDs. Thus two boundaries of operation were identified which were to be avoided, namely the

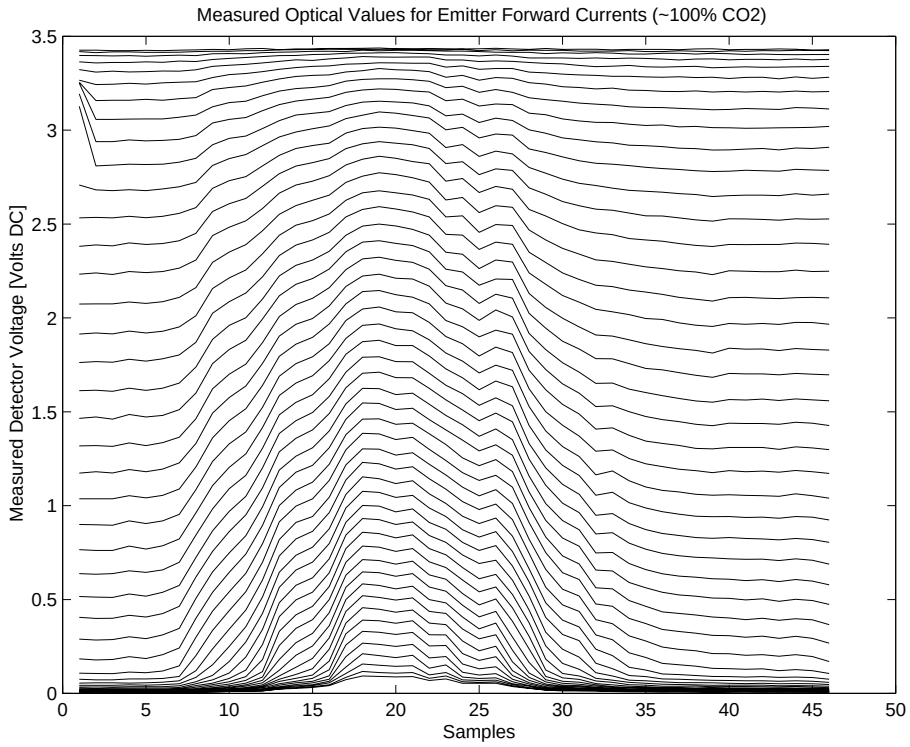

(a) Measured optical values from emitter current levels of 50 to 100 (bit value).

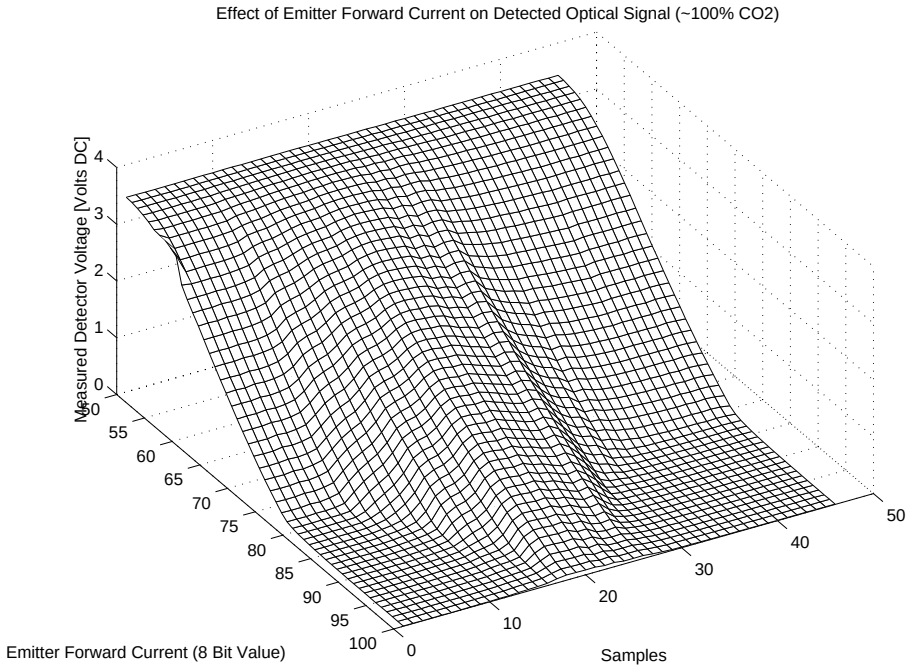

(b) 3D Surface representation of the measured optical values.

Figure 10.10: Optics dynamic range optimisation (Detector sensitivity was set to 255 bit value - maximum sensitivity).

non linear and saturation regions.

It was discovered however that within these two extremities, the dynamic range of the measurements at different emitter intensities also varied and could be optimised. As a result, the dynamic range could be calculated by examining the optical signals at their peak (the point of maximum opacity) with reference to a baseline taken from other parts of the measurement sequence. This resulted was a dynamic range plot as shown in Figure 10.11. As shown there was a specific level of optical emitter intensity where the maximum dynamic range could be expected, in this case, when the emitter intensity was set to be approximately 78 bit value (approximately 2mA). This result followed closely for all of the other similar tests, thus for further testing where no adaptive selection of the optic parameters was set, the detector sensitivity was set to be 255 (bit value) with the emitter set to be 78 (bit value).

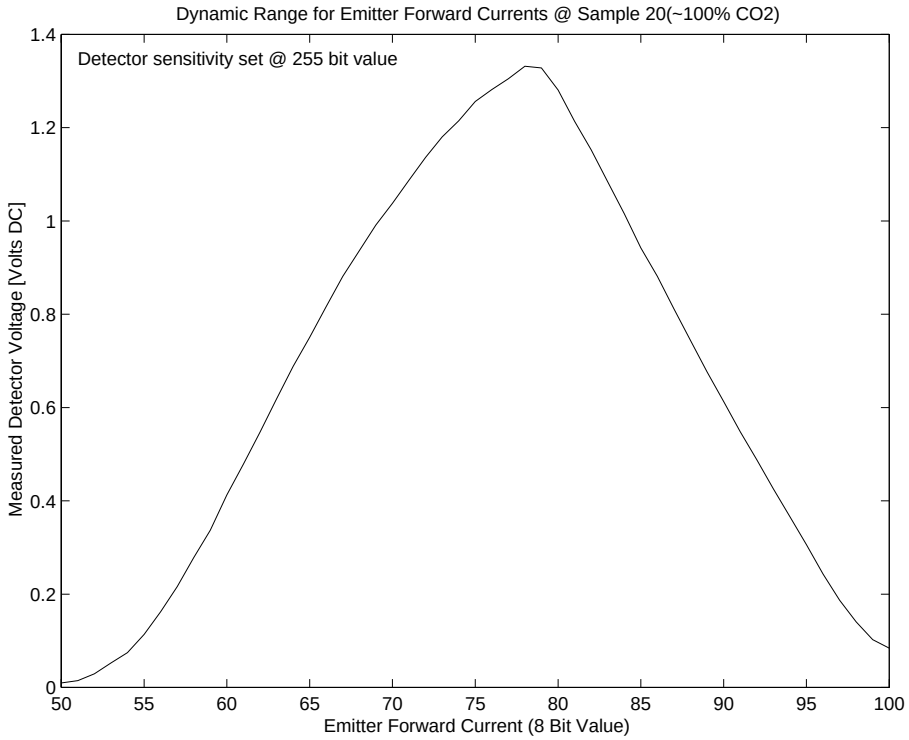

Figure 10.11: Dynamic range of the optics calculated at sample 20 (the peaks of the optical curves) using a baseline reference from the initially acquired optical data at sample 1.

It was found however that the design for the photodiode using current source presented a difficulty in that the current source would damp any response of the photodiode. This resulted in poor performance of the optical detector. This was overcome by configuring the photodiode similar to that in the Mk.I version where a resistor connected to +5V was used instead of the current source. However, doing this removed the ability to variably control the sensitivity of the photodiode via the microcontroller, but resulted in more stable turbidity measurements. After this augmentation of the electronics, another test was performed to again determine the most optimal operating point for the optics. The emitter current was varied (0 to 255 bit value in steps of 10) with the detector standby current held constant by the resistor. This result is shown in Figure 10.12.

As before, Figure 10.12(a) showed that there was a variation in the dynamic range of the turbidity measurements dependant on the LED output energy. These curves were again represented as a 3D-surface plot, Figure 10.12(b), showing the effect more clearly. The dynamic range with respect to a baseline measurement, the first sample, was calculated and appears in Figure 10.13 indicating that the maximum dynamic range is obtained when the emitter is set to its maximum forward current or bit value 255. From knowledge of the expected dynamic range curve from the previous experiment, Figure 10.11, it is seen that in this case the detector electronics could have been further optimised. This was however not performed however as the available range was deemed suitable and the dynamic range plot showed evidence that the actual maximum dynamic range point would be very close to the existing optical operating conditions.

In order to restore variable photodiode sensitivity able to be controlled by the microcontroller, a more optimal technique would use a FET device configured to behave as a variable resistor.

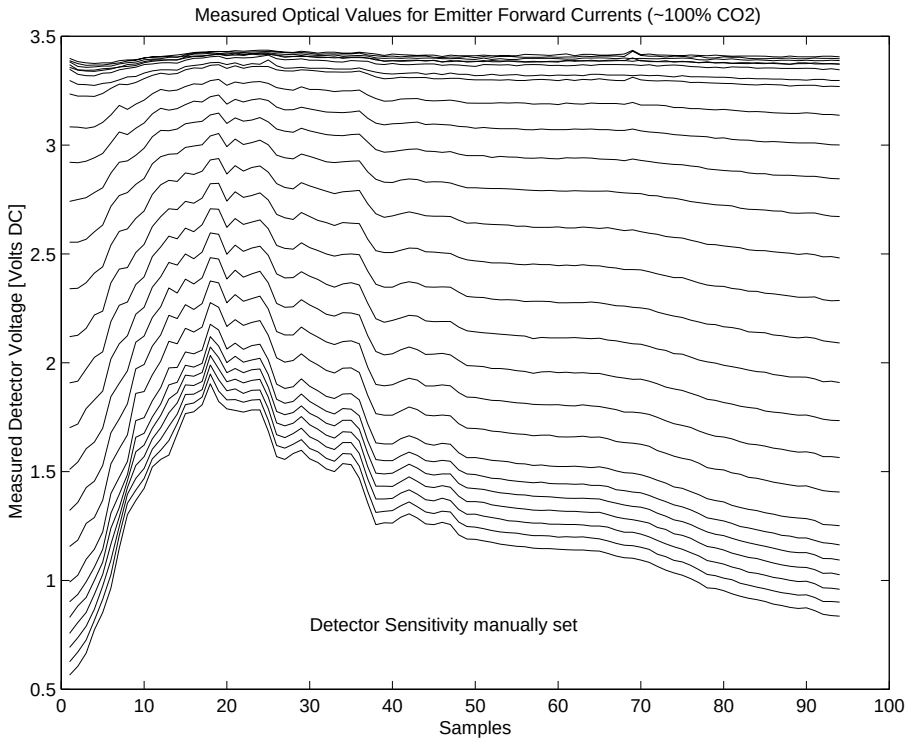

(a) Measured optical values from emitter current levels of 0 to 255 (bit value).

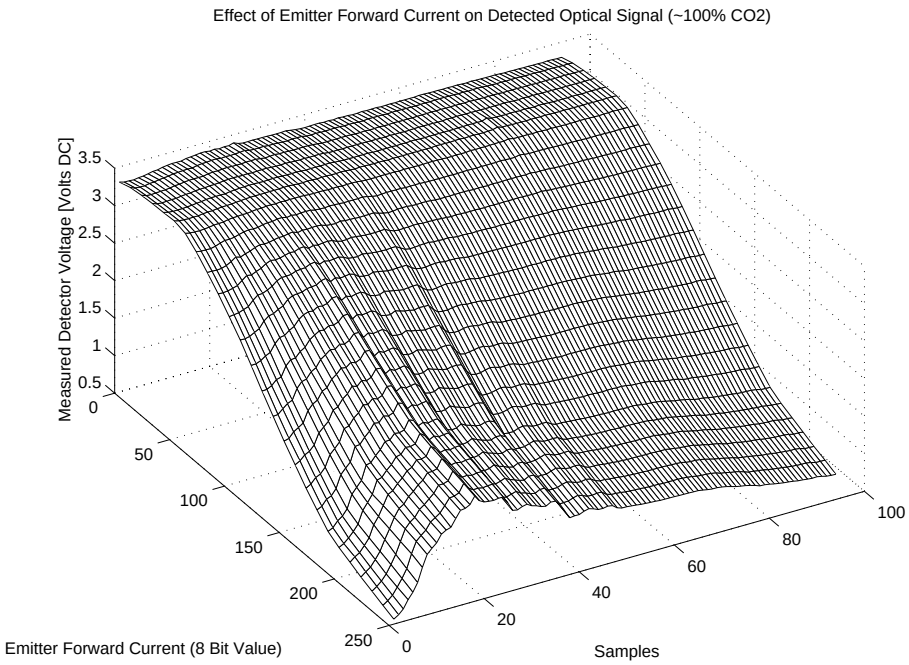

(b) 3D Surface representation of the measured optical values.

Figure 10.12: Optics dynamic range optimisation (Detector sensitivity was set manually via a precision potentiometer).

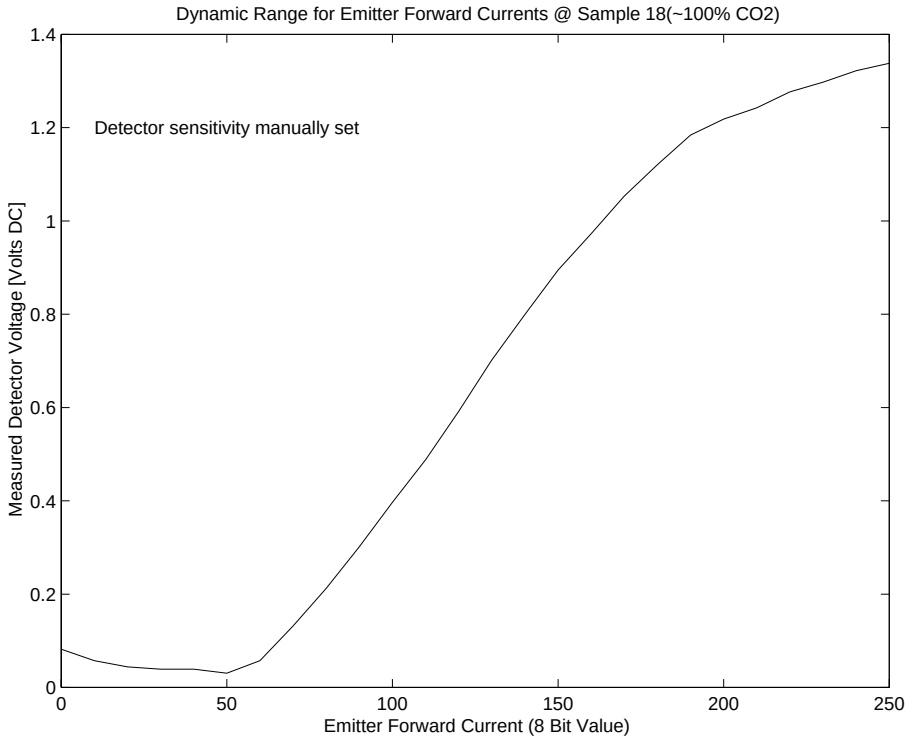

Figure 10.13: Dynamic range of the optics calculated at sample 18 (the peaks of the optical curves) using a baseline reference from the initially acquired optical data at sample 1.

10.3.7 Examination of Adaptive Optical Capabilities

As an extension to the previous experiments, further exploration of the adaptability of the optical components was performed. By using a combination of both variable LED emitter intensities and variable detector sensitives, it was considered likely that these features might prove useful in extending the operating conditions for which the turbidity measurement system could operate.

In these experiments both the emitter intensity and the detector sensitivity were varied for four known materials and an overall turbidity map derived for each. The four materials used were:

- air (i.e. empty);
- clean water;
- water and milk mixed roughly 1:1 (Sanitarium "So Good" soy-based milk); and
- undiluted soy milk.

The soy based milk was used to simulate a stable (non-settling), homogeneous suspension of $CaCO_3$ precipitate and provided the extended times required to acquire the data.

As seen in Figure 10.14(a), as the emitter current is increased the detector voltage (at any sensitivity level) also decreases in the same way as shown in Figure 10.10(a) and 10.12(a). Similar boundary regions exist being the shelf at low emitter levels (below 50 bit value) where the LED is still turned off, and at higher emitter levels (above 80 bit value) where the detector is saturated. The increase in voltage as the detector sensitivity increases is a by product of the way the optoelectronics were designed. The results for water, Figure 10.14(b), are very similar to that of the empty, air filled, state. For both these results, operational conditions are restricted by the LED-off and saturation boundaries.

The results for the diluted soy milk, Figure 10.15(a), however suggest that a much wider operational conditions can be used, where turbidity measurements are now possible across a wide range of optical parameter combinations. The initial LED-off and saturation boundaries still exist but now exist to a lesser extent. The results for undiluted soy milk, Figure 10.15(b), show that at extremely high turbidity levels, the optics are unable to make any useful measurements, where the LED cannot provide enough optical energy to sufficiently penetrate the turbid solution. Close inspection of this last figure however does show that with an increasing emitter intensity some minor variation of the turbidity measurement is made. This then shows that this optical control system is incapable of measurement at extremely high turbidity levels, however as the turbidity caused by $CaCO_3$ is substantially less, this effect will not be seen.

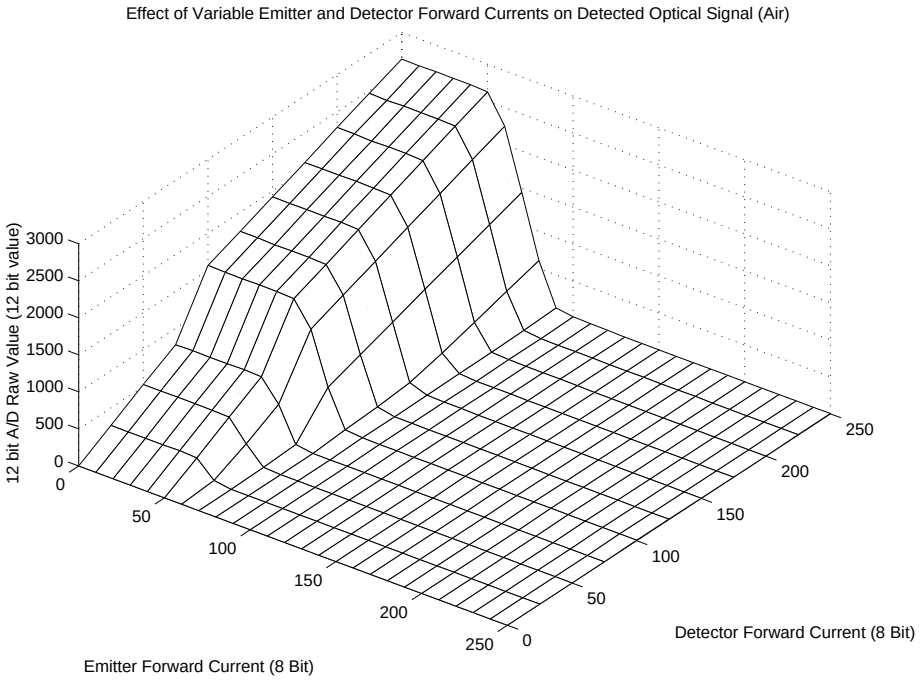

(a) Empty (air).

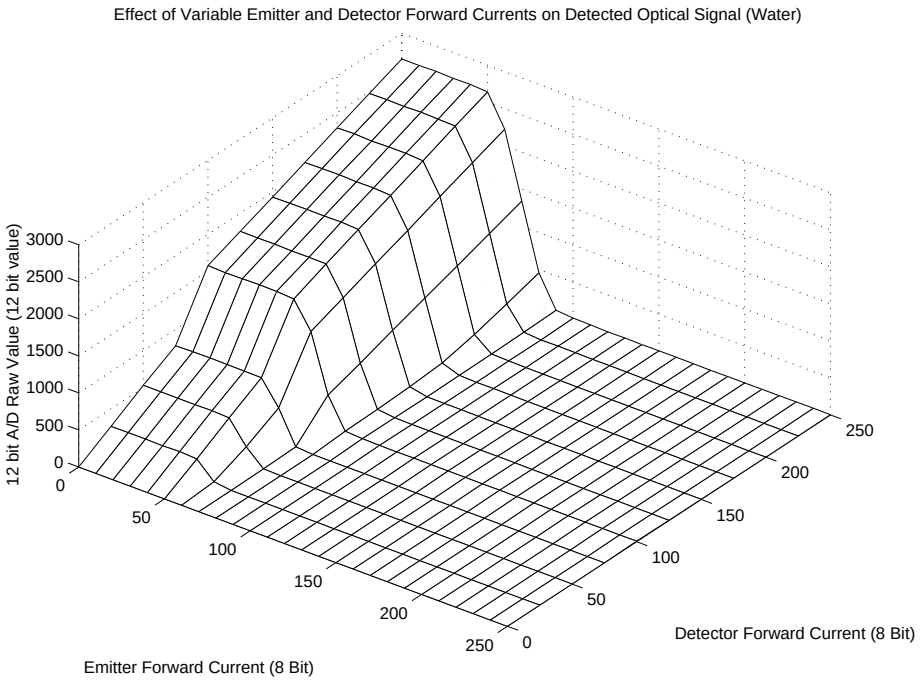

(b) Water

Figure 10.14: Multi-state optical measurement set for various materials within the cell (Part 1 of 2). As noted in the test, the results are very similar for air and clean water.

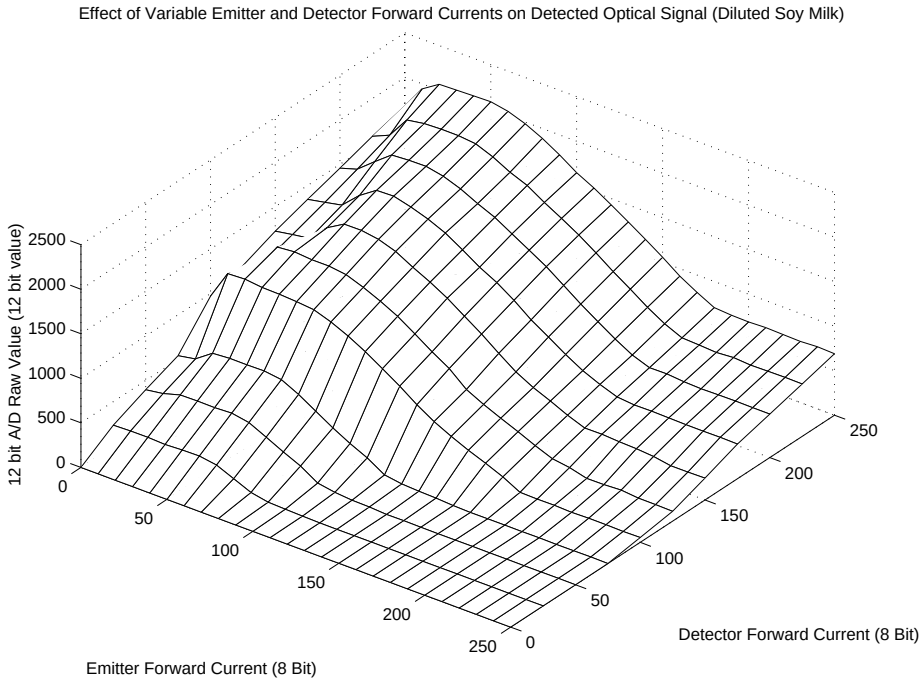

(a) Diluted soy based milk (simulating medium $CaCO_3$ precipitation).

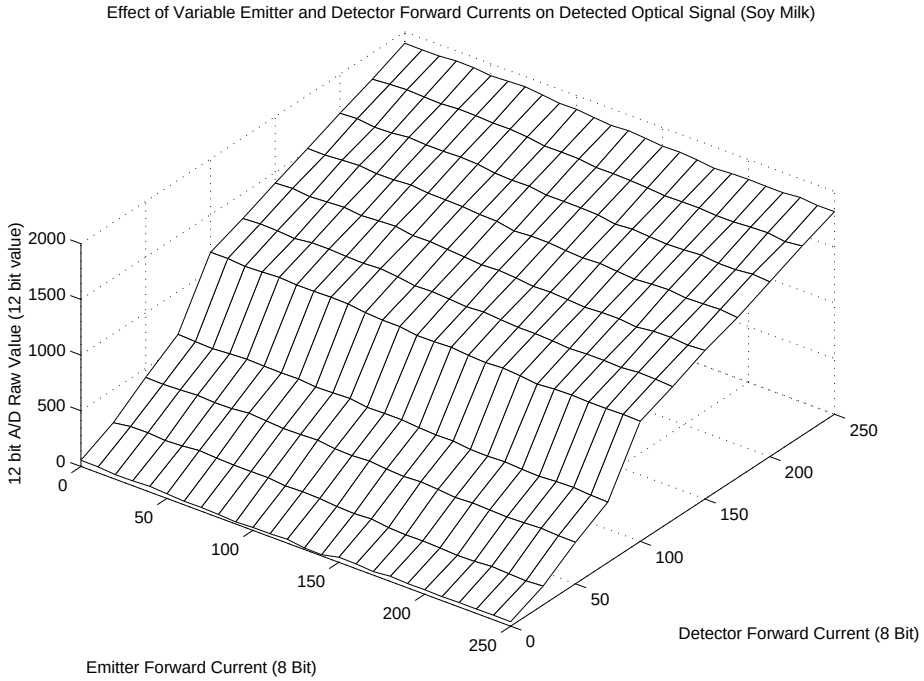

(b) Soy based milk (simulating $CaCO_3$ precipitation).

Figure 10.15: Multi-state optical measurement set for various materials within the cell (Part 2 of 2).

10.3.8 Turbidity Evaluation

Figure 10.16 shows a typical turbidity curve for 100% CO_2, i.e. the typical characteristic curve as precipitate is produced, held in suspension briefly, then falls from suspension or is further chemically converted.

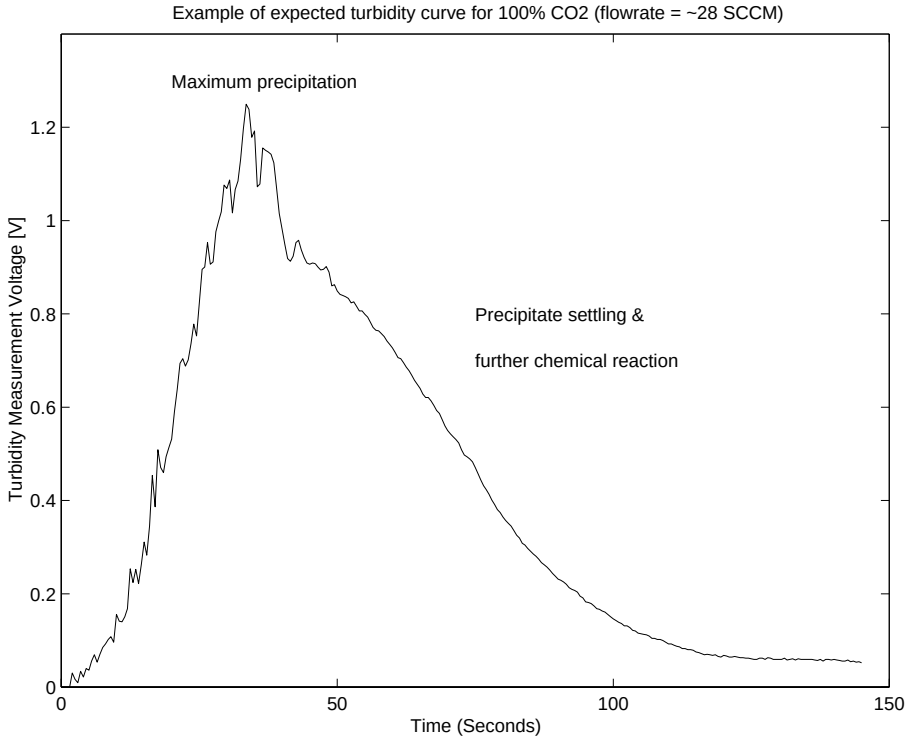

Figure 10.16: An example of the expected turbidity curve measured for 100% CO_2 at a flowrate of 28 SCCM (Standard Cubic Centimeters per Minute) from initial gas injection through to eventual removal of the $CaCO_3$ precipitate.Turbidity measurement noise during the first 40 seconds is due to non-homogeneous precipitate production and precipitate clumping.

Also shown in this figure is the effect on the turbidity measurement of $CaCO_3$ precipitate coating the interior walls of the cell. At the end of the optical turbidity curve a residual turbidity measurement of 0.05 V is observed, a direct result of the optical attenuation caused by cell wall coating.

Whilst this was the expected turbidity curve, not all turbidity measurements exhibited this response. Many of the measurements suffered from bubble noise, or non homoge-

neous precipitate formation. This resulted in an uneven turbidity rates, and other data artifacts. These are set out in Section 11.3.1 and 11.4.1.

10.3.9 Turbidity Measurement of Static Precipitation

An experiment was performed to examine the turbidity measurement during static precipitation, where a precipitate was present in the cell, but no agitation was present, or further chemical reactions were occurring. The result of these tests (Figure 10.17) shows the exponential trend of the precipitate falling from suspension decreasing the turbidity measured within the cell. This figure shows that when bubble noise is prevented, and a homogeneous solution is formed, accurate and virtually noise free turbidity measurements can be made within the cell.

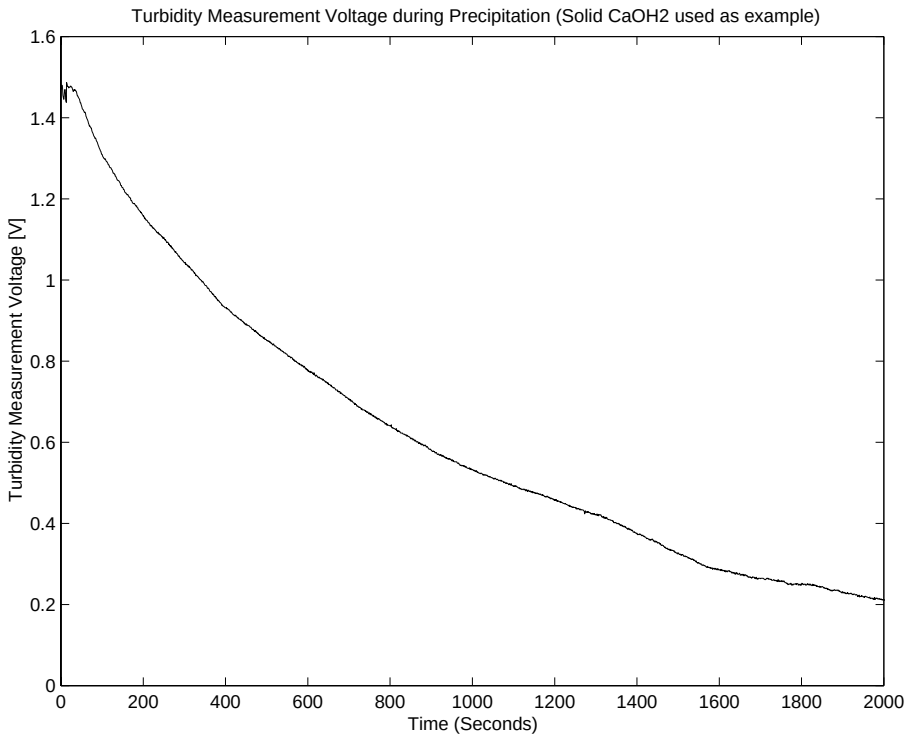

Figure 10.17: An example turbidity measurement of static precipitation as the cell filled with solid $Ca(OH)_2$ precipitate was allowed to settle. Signal noise for the first 10 seconds was due to precipitate having just been injected into the cell causing turbulence, and some non-homogeneity of the solution.

10.3.10 Turbidity Rates

A comparison between Figure 10.16 and Figure 10.17 reveals a significant turbidity rate difference depending on the conditions within the cell. When no intra-cell agitation was provided (Figure 10.17), the precipitate takes a long time duration (2000 seconds) to fall out of suspension. When agitation is provided (Figure 10.16), the latter half of the turbidity curve takes a significantly shorter time (100 seconds) to fall back to the baseline measurement. This shortened time during agitation is due to the combination of both precipitate settling, as well as further chemical reaction of the precipitate into $Ca(HCO_3)_{2(aq)}$ due to the presence of $Ca(OH)_2$ and CO_2 (This chemistry is presented in Appendix D).

10.3.11 $CaCO_3$ Initiated Optical Drift

It was observed that during measurement operation, the cell walls and in particular the region where bubbling within the cell occurred, would quickly become coated with $CaCO_3$ precipitate which would significantly affect the optical turbidity measurement. Performance results of this effect are shown in Figure 10.18. Figure 10.18(b) shows the first 25 seconds of four measurements, the initial, the 3rd, 6th, and 7th measurements of a sequence of seven. (The intermediate measurements are omitted for clarity.)

Figure 10.18(b) shows the baseline drift associated with an increase in turbidity at the start of each test. This increase in turbidity was due to the increase in optical attenuation from wall-attached precipitate, and from waste materials from previous measurements. An initial decrease in turbidity seen in the 6th and 7th data set indicates initial cleaning of the cell as waste materials from the previous measurement are dislodged or diffused throughout the solution due to initial bubble agitation from the sample gas source. This test showed that the dynamic range of the instrument diminishes significantly and a cleaning regime was essential.

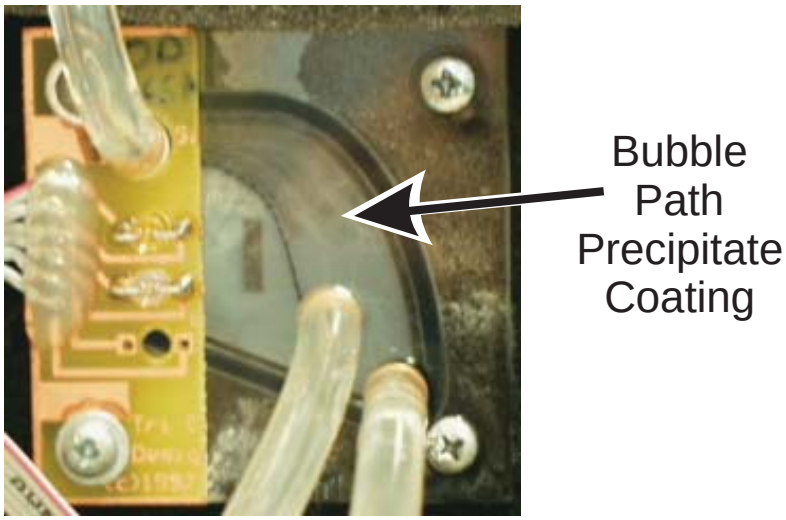

(a) Photograph of cell wall during the $CaCO_3$ initiated optical drift tests. A significant precipitate coating (light grey) has developed in the bubble injection area (above middle tube) and following the path upward of the bubbles, plus general sheet precipitate covering the rest of the cell.(The circuit card out left carries the two sets of infra-red optics.)

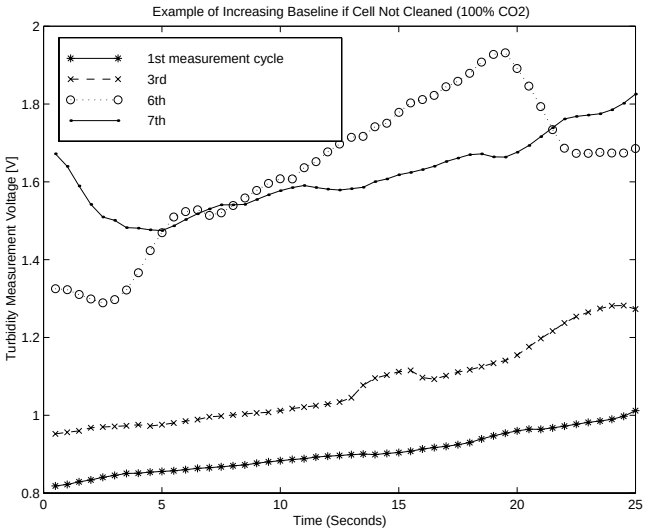

(b) Results from a sequence of turbidity measurements (at 100% CO_2), neglecting to clean inbetween measurements. Baseline drift is shown for each subsequent turbidity measurement.

Figure 10.18: Photograph of cell wall and corresponding turbidity measurements when the cleaning of the cell is omitted between tests.

10.3.12 Variable Flowrates

Because the measured turbidity curve is dependant on the rate of reaction, it follows that the flowrate that the gas is supplied at will affect the rate of precipitate production. This is demonstrated in Figure 10.19 where the same sample gas was used (100%) with the flow rate varied. Clearly shown are significant variations in the rate of turbidity change. This hence shows that strict control of the flow rate is required of the sample gas being injected into the cell.

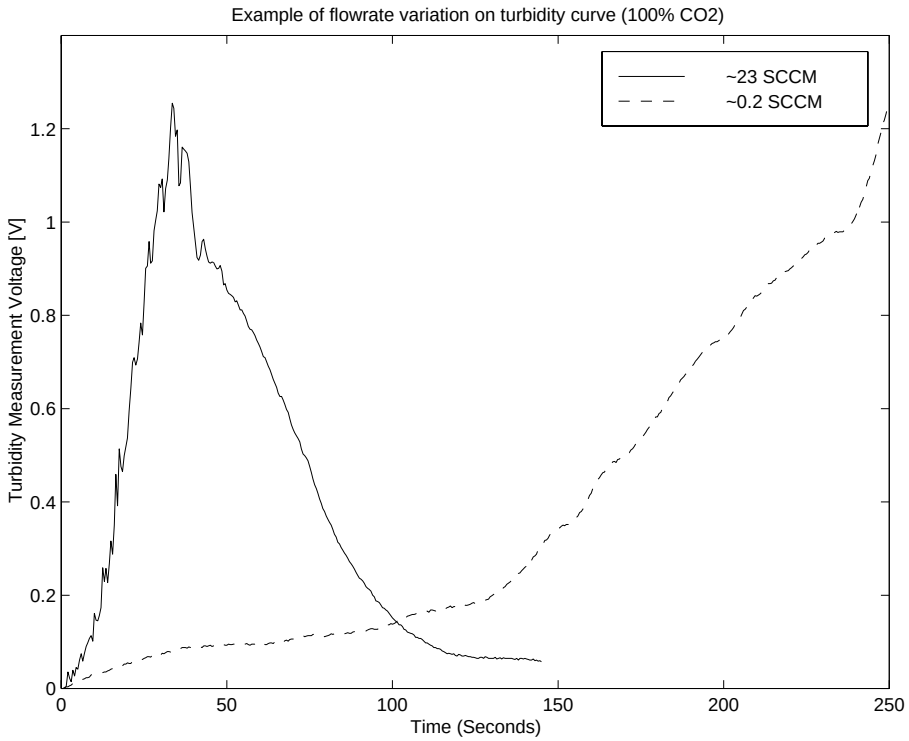

Figure 10.19: An example of how flowrate affects the characteristic turbidity curve.

10.3.13 Excessive Flowrates

A desirability of high flowrates allows for faster reaction rates within the cell between the sample gas and the indicator solution, and hence faster measurement resolving times to each of the thresholds. This would result in overall faster instrument cycle

times.

However, if excessive flowrates were used for the sample gas, it was found that a relatively large proportion (estimated to be up to 70%) of the indicator solution that was previously in the cell would be transported through the exhaust port in the form of bubbles. This would result in a net loss of solution within the cell available to react. Should the level fall significantly low, bubble blocks would form and prevent both the fluidic circuit of the indicator, thereby reducing the mixing, as well as obscuring the optic path of the detectors. This would result in false turbidity measurements as shown in Figure 10.20.

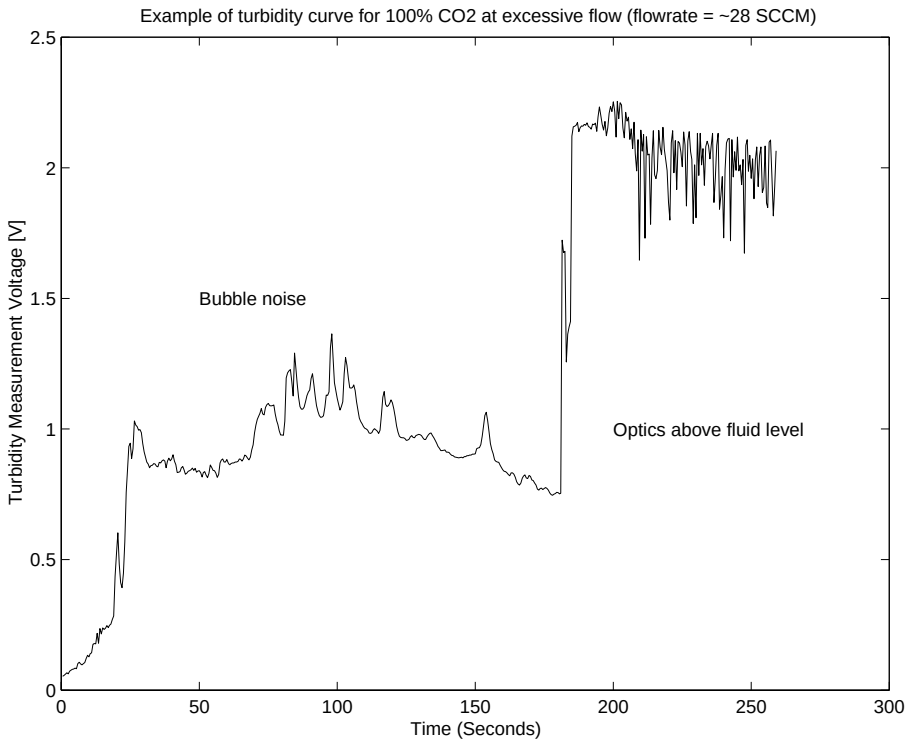

Figure 10.20: An example turbidity measurement during excessive sample gas flowrate.

As shown in this figure the turbidity measurement will start and appear satisfactory however a dip in the turbidity curve would occur. At this point a small bubble block had occurred causing stagnation and fall out of the precipitate in the measurement

region resulting in a falling turbidity measurement. Then as more fluid was expelled from the cell, a larger bubble would form blocking the upper optic pair, resulting in the interrupted turbidity measurement as shown after 180 seconds. And finally as the bubble continued to grow, the bubble would eventually obscure the lower optic pair. Thus it was imperative to optimise the flowrate such that this effect did not occur.

Significantly problems were found during performance testing of low gas concentrations, where there long measurement cycles, due to loss of even minor volumes of solution during the test would result in flawed turbidity measurements. No solution was found for this problem other than optimisation of the flow rate. Ideally the cell design would have to be optimised such that bubbles could be adequately expelled from the cell.

10.3.14 Instrument Performance with respect to Calibration Model

Evaluation of instrument performance was performed over a range of known CO_2/N_2 gas mixtures. These gases were prepared using methods shown in Appendix F.

Turbidity data was recorded from the prototype hardware using the non adaptive modified optics (Section 10.3.6) and under laboratory conditions. The flowrate was set to approximately 3sccm [1] with the ambient temperature during the tests being 22°C.

The performance of the complete instrument was assessed with respect to three calibration models (Section 7.4) , namely:

- the exponential function model;
- the power function model; and
- the interpolated cubic spline model.

Raw data was collected from the prototype hardware running calibration software routines and then modelled using "MATLAB™" running specially written calibration pro-

[1] Approximately 4 bubbles per second within the cell

cedure. Two scripts were used, the first was used to generate calibration models from the processed data, Section 7.4, and the second used to apply these models to the rest of the captured data.

Figure 10.21 and Table 10.6 shows the performance of each of the models at the actual calibration points (100%, 50%, 20%, 10%, and 5%) using the actual turbidity calibration waveforms. As seen in this figure, the interpolated spline model (solid line) shows zero error at each of the calibration points due to the nature of the model (where interpolation only occurs between the calibration points). Errors in the other two models exist due to their approximation of the overall calibration data presented in Section 7.4.

Table 10.6: Mean error for the three models using the turbidity calibration waveforms.

Model	Exponential[%]	Power[%]	Interpolated Spline[%]
baseline+0.1V	5.2	5.1	0
baseline+0.2V	4.7	3.5	0
baseline+0.3V	4.8	3.8	0
baseline+0.4V	7.1	6.9	0
baseline+0.5V	6.0	6.7	0
Average	5.5	5.2	0

These results show that the interpolated cubic spline model is the most accurate in terms of fitting the calibration data (0% mean error) but as previously noted (Section 7.4), cannot be used beyond the boundaries of its data.

Likewise, the exponential model has previously been shown to be poorly suited for use with this system (Section B.2.1), and this conclusion is reinforced by the 5.5% mean error (Table 10.6). It has also been shown that this model is incapable of being used beyond the boundaries of the data due to its exponential nature where both short and long times are translated into the high concentrations, thus showing that for low concentration calculations its use is limited.

The power function model however (5.2% mean error) shows that whilst its accuracy is less for high CO_2 concentrations, it can be used beyond the calibration data bound-

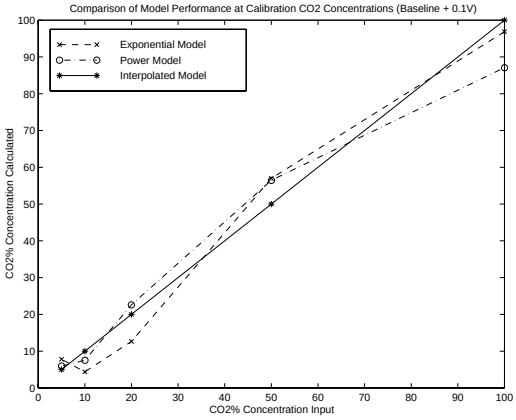

(a) Performance of baseline+0.1V model.

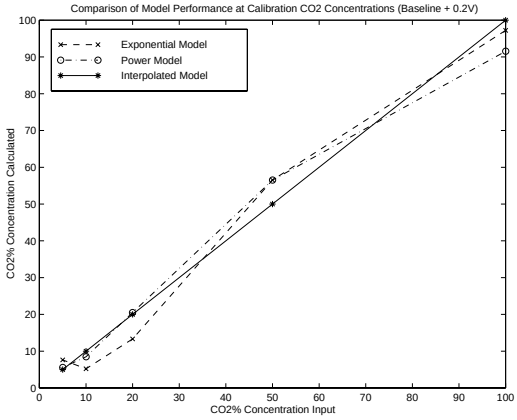

(b) Performance of baseline+0.2V model.

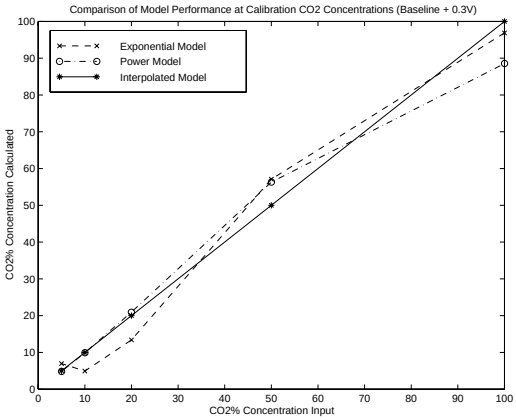

(c) Performance of baseline+0.3V model.

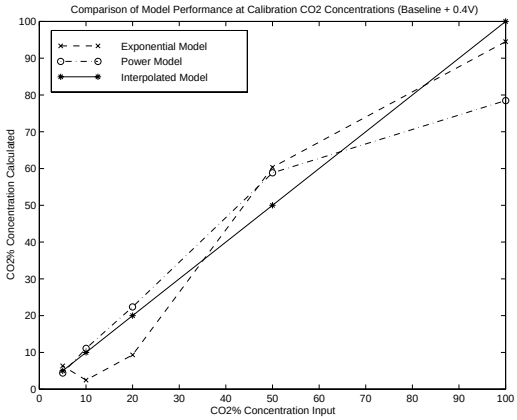

(d) Performance of baseline+0.4V model.

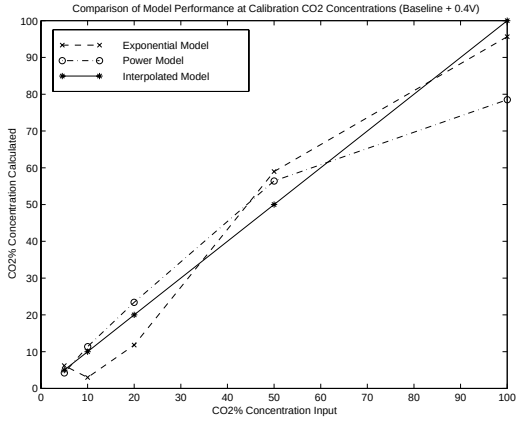

(e) Performance of baseline+0.5V model.

Figure 10.21: Comparison of the three models at the five calibration concentrations (100%, 50%, 20%, 10%, and 5%) for the Mk.II instrument.

aries for low concentration measurements. This is seen in Figure 10.21 where each power function curve shows a trend moving towards the interpolated curves for low concentrations. This shows that its accuracy increases for lower concentration values.

10.3.15 Overall Instrument performance

The performance of the models with respect to actual turbidity data was then assessed. Multiple sets of measurements at each concentration were performed with the turbidity data being recorded and then run through the simulation scripts running in MATLAB. The calculated concentrations for each gas using the exponential, power, and interpolated spline models are shown in Figures 10.22, 10.23, and 10.24 respectively.

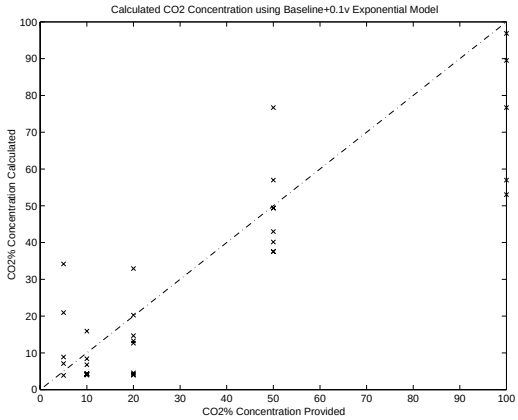

(a) Performance of baseline+10 model.

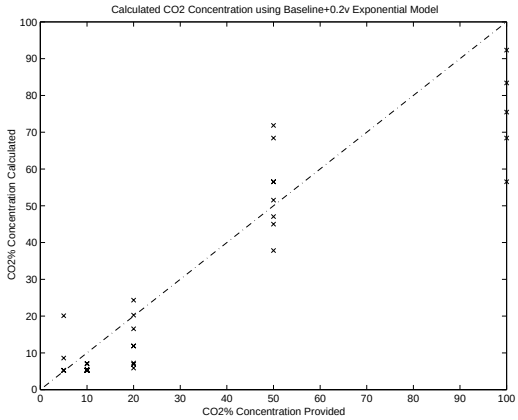

(b) Performance of baseline+20 model.

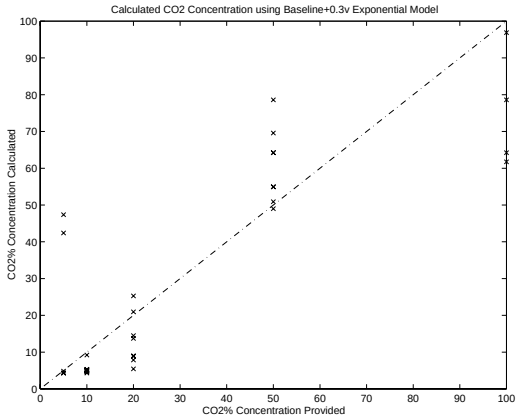

(c) Performance of baseline+30 model.

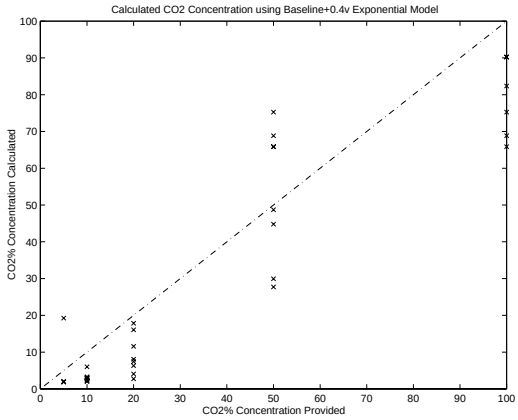

(d) Performance of baseline+40 model.

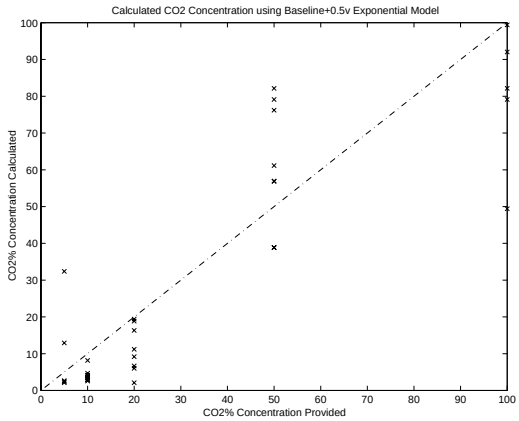

(e) Performance of baseline+50 model.

Figure 10.22: Raw calculated $CO_2\%$ concentration for various gases using the exponential model.

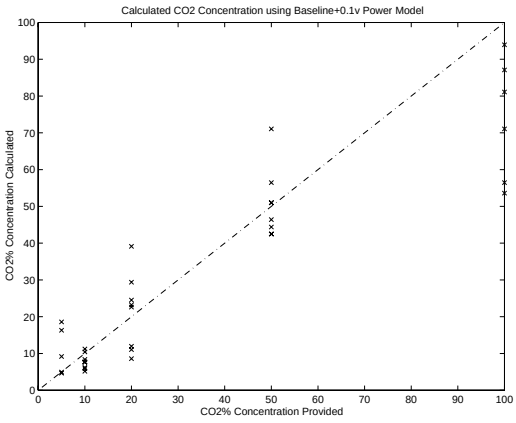

(a) Performance of baseline+10 model.

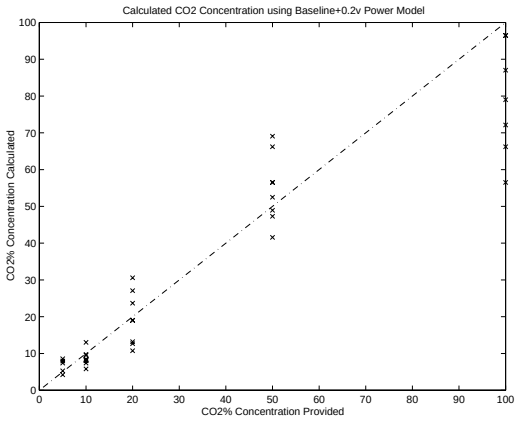

(b) Performance of baseline+20 model.

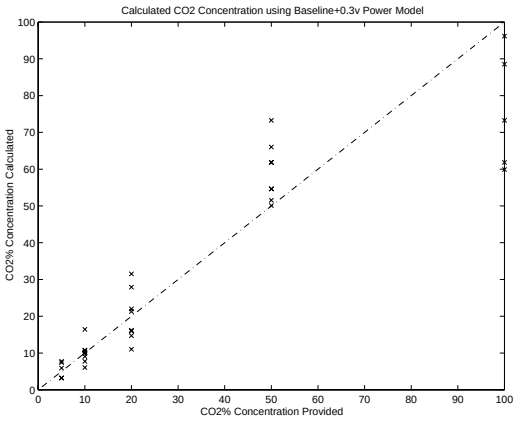

(c) Performance of baseline+30 model.

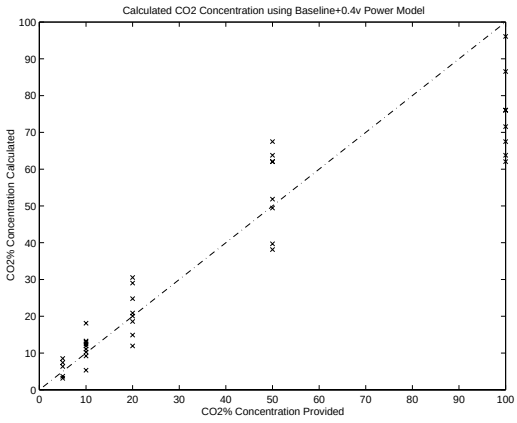

(d) Performance of baseline+40 model.

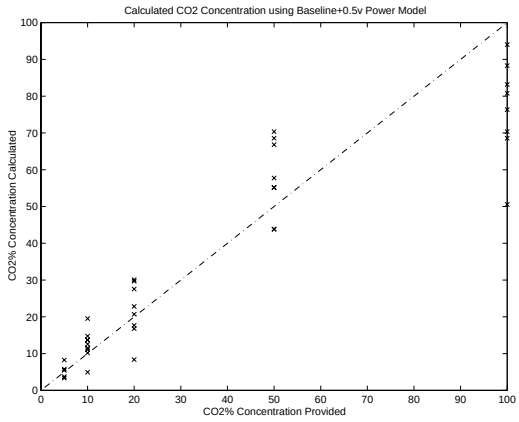

(e) Performance of baseline+50 model.

Figure 10.23: Raw calculated $CO_2\%$ concentration for various gases using the power model.

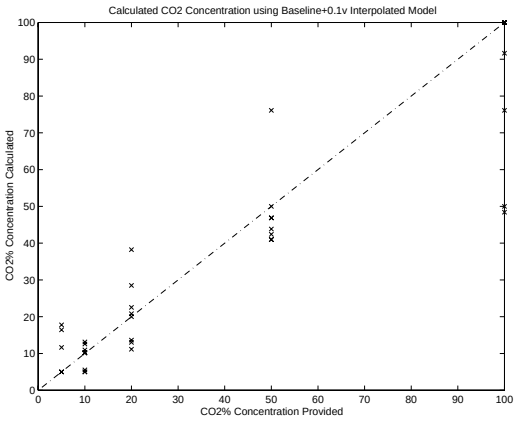

(a) Performance of baseline+10 model.

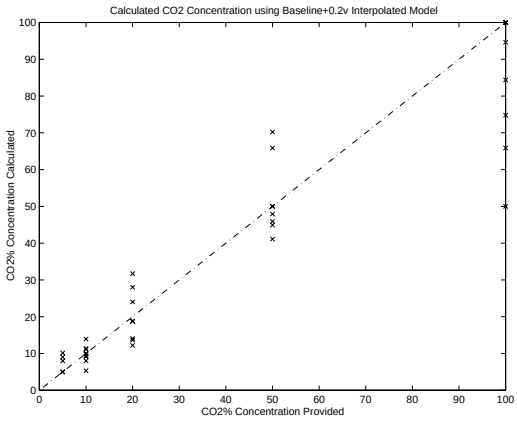

(b) Performance of baseline+20 model.

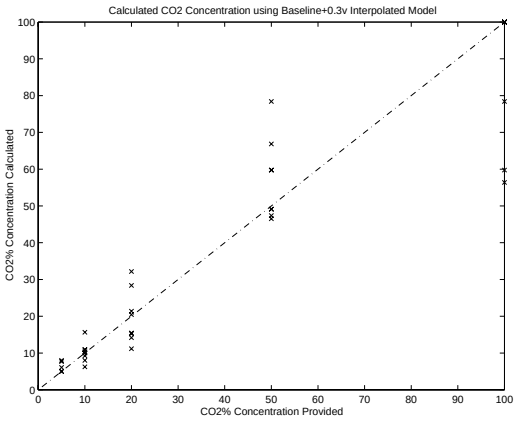

(c) Performance of baseline+30 model.

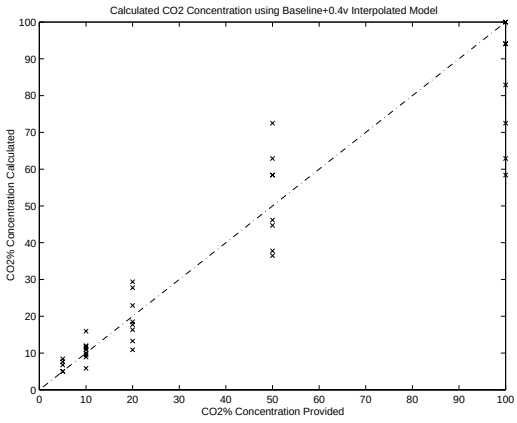

(d) Performance of baseline+40 model.

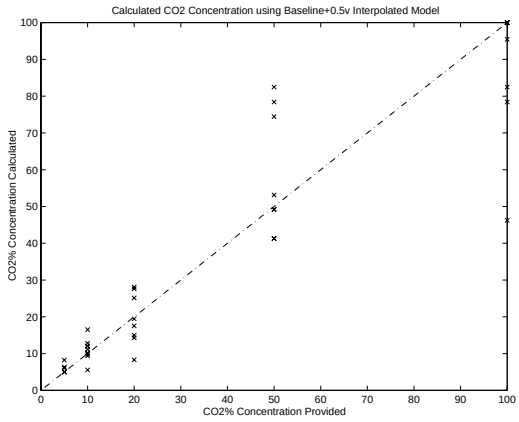

(e) Performance of baseline+50 model.

Figure 10.24: Raw calculated $CO_2\%$ concentration for various gases using the interpolated spline model.

As multiple turbidity measurements were taken at each concentration, the data recorded would exhibit a gaussian distribution for the calculated CO_2 concentration. The data in these figures were then further processed looking at the mean, $\overline{x}$, and the standard error (the Gaussian standard deviation of the mean), σ_m. These processed results can be seen in Figure 10.25, 10.26, 10.27, again for the exponential, power, and interpolated spline models respectively.

The error between the mean calculated concentration and the actual concentration were evaluated for each model and each threshold. The results are shown in Figure 10.28. As shown in these figures the mean error tends to decay with a lowering of CO_2 concentration. The average errors for each of these three models is shown in Table 10.7.

Table 10.7: Mean standard error for the three models.

Model	Exponential[%]	Power[%]	Interpolated Spline[%]
baseline+0.1V	7.6	3.4	5.2
baseline+0.2V	9.0	5.8	5.2
baseline+0.3V	11.3	7.4	5.7
baseline+0.4V	11.5	6.5	5.7
baseline+0.5V	11.2	7.3	6.5
Average	10.1	6.2	5.7

The variation in the standard error, σ_m, was then examined with respect to the three particular models as shown in Figure 10.29. The variation in the exponential model, Figure 10.29(a), is shown to be large for high and low concentrations, but shows a relatively small amount of variation for concentrations inbetween. This is due to the exponential nature of the model, where it was incapable of modelling the calibration data for both high and low concentrations.

The variation for the power and interpolated spline models however, Figure 10.29(b) and 10.29(c) respectively, show that the variation in the standard deviation decreases with the concentration level. This relationship is to be expected due to the increasing time resolution of the turbidity measurement for longer reaction threshold times. Thus showing that for longer model resolving times, which occur for lower concentrations, the accuracy of the models increase due to a decrease in the standard deviation of the sample set.

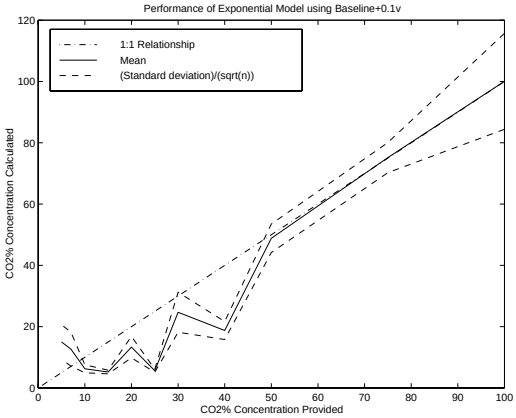

(a) Performance of baseline+0.1V model.

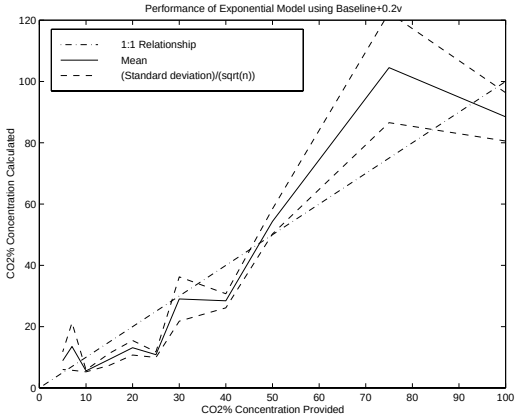

(b) Performance of baseline+0.2V model.

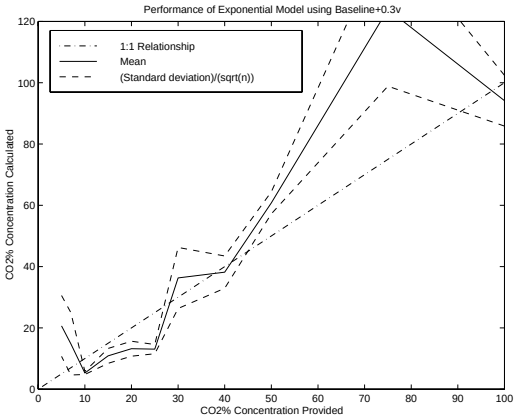

(c) Performance of baseline+0.3V model.

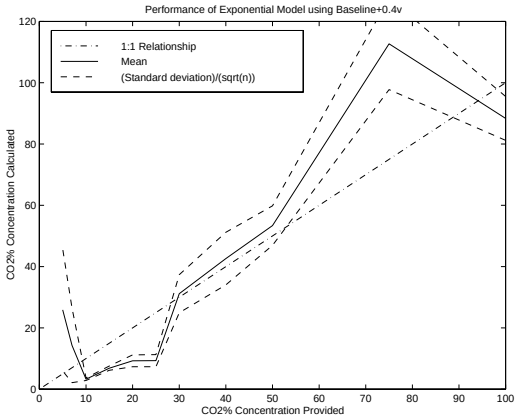

(d) Performance of baseline+0.4V model.

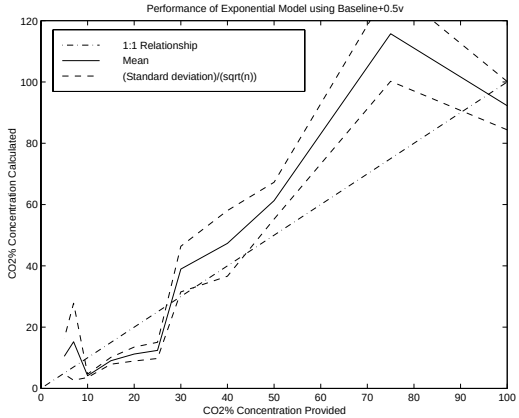

(e) Performance of baseline+0.5V model.

Figure 10.25: Mean and standard error band ($\pm\sigma_m$) for the calculated CO_2 % concentration for various gases using the exponential model.

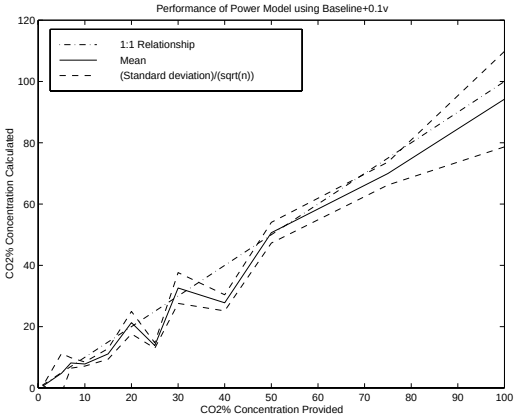

(a) Performance of baseline+0.1V model.

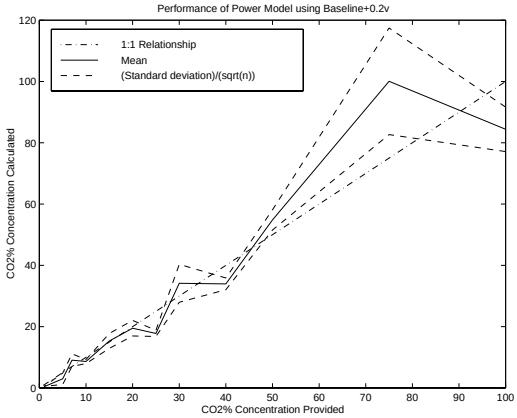

(b) Performance of baseline+0.2V model.

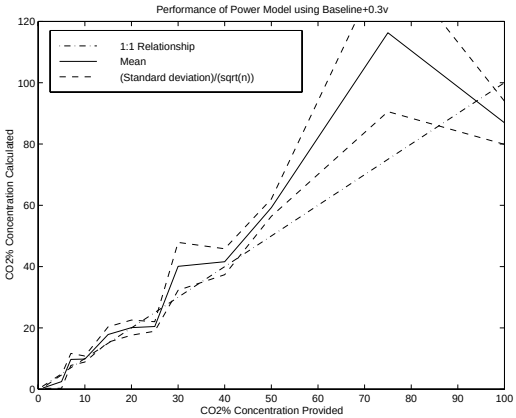

(c) Performance of baseline+0.3V model.

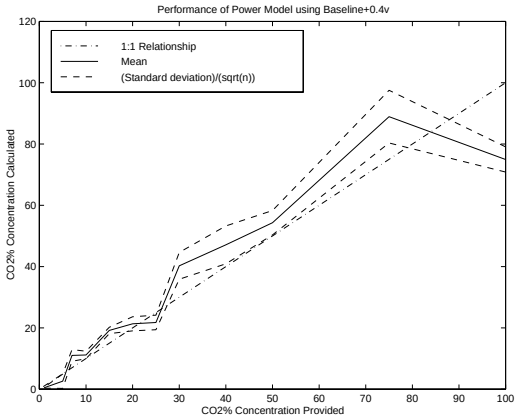

(d) Performance of baseline+0.4V model.

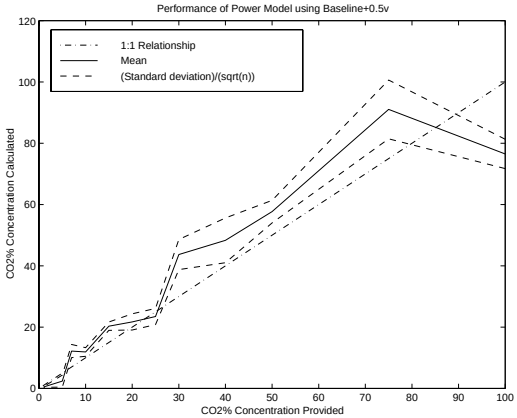

(e) Performance of baseline+0.5V model.

Figure 10.26: Mean and standard error band ($\pm\sigma_m$) for the calculated CO_2 % concentration for various gases using the power model.

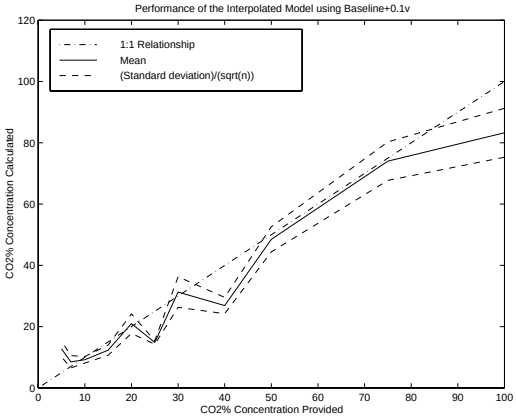

(a) Performance of baseline+0.1V model.

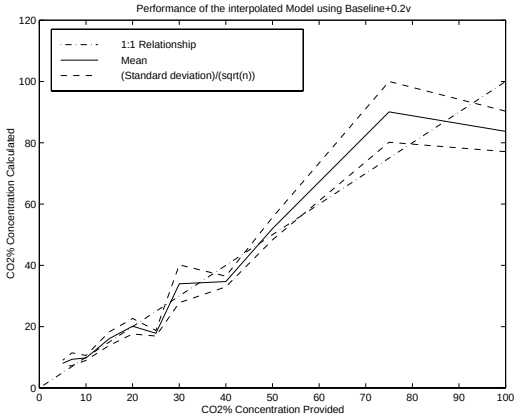

(b) Performance of baseline+0.2V model.

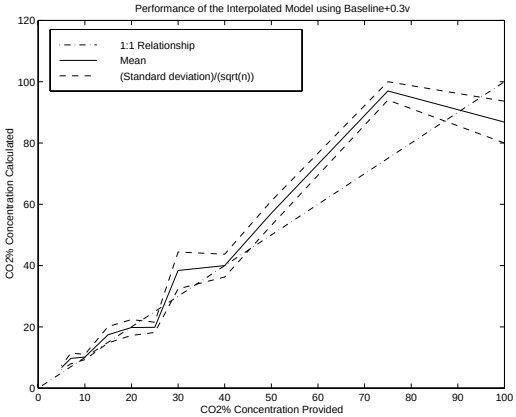

(c) Performance of baseline+0.3V model.

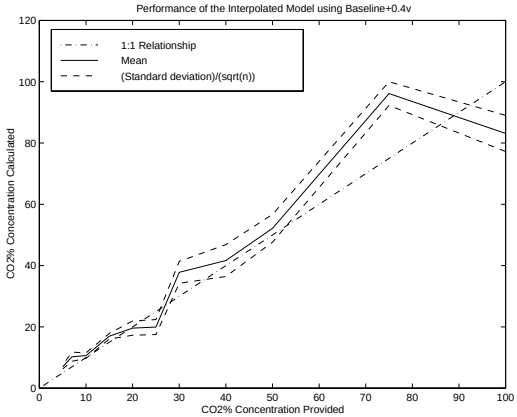

(d) Performance of baseline+0.4V model.

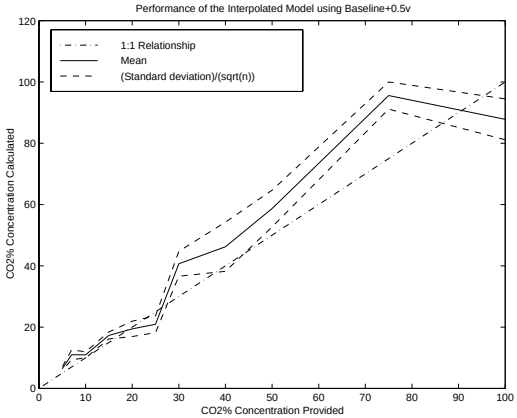

(e) Performance of baseline+0.5V model.

Figure 10.27: Mean and standard error band ($\pm\sigma_m$) for the calculated CO_2 % concentration for various gases using the interpolated spline model.

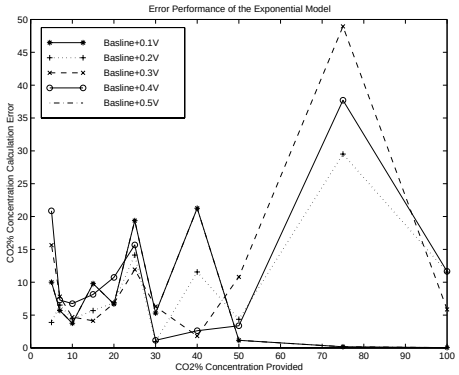

(a) Variation of mean error for the exponential model.

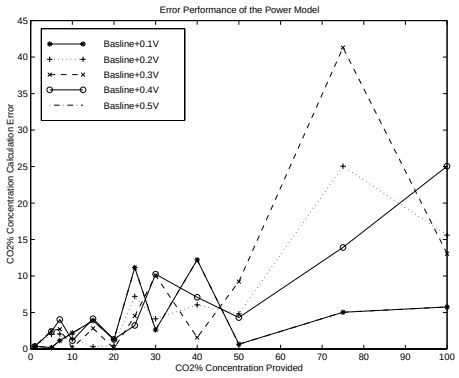

(b) Variation of mean error for the power model.

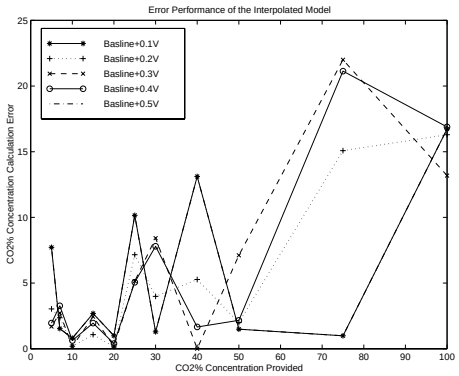

(c) Variation of mean error for the interpolated model.

Figure 10.28: Variation of mean error for the three models.

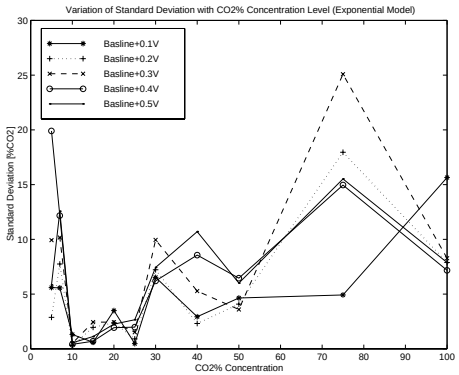

(a) Variation of standard error band ($\pm\sigma_m$) for the exponential model.

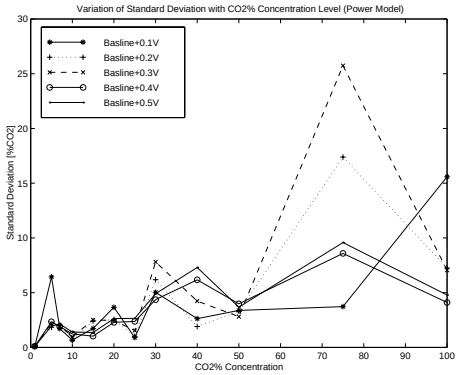

(b) Variation of standard error band ($\pm\sigma_m$) for the power model.

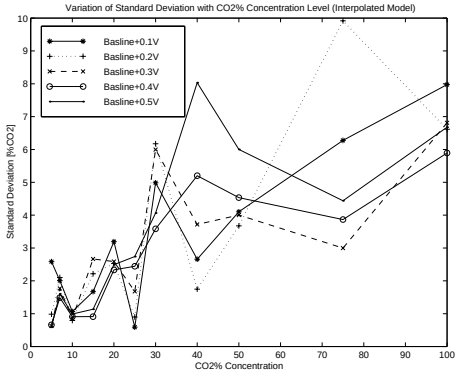

(c) Variation of standard error band ($\pm\sigma_m$) for the interpolated model.

Figure 10.29: Variation of standard error band ($\pm\sigma_m$) for the three models.

By further analysing these data, average error for each model can be determined as shown in Table 10.8. It is seen that the interpolated spline model has the greatest repeatability of all the models which was expected from previously results.

Table 10.8: Average standard error band ($\pm\sigma_m$) for the three models at each baseline (baseline + 0.1V, 0.2V, 0.3V, 0.4V, and 0.5V).

Model	Exponential[%]	Power[%]	Interpolated Spline[%]
baseline+0.1V	4.7	3.8	3.4
baseline+0.2V	5	3.9	3.4
baseline+0.3V	7.2	5	3.06
baseline+0.4V	7.3	3.2	3.06
baseline+0.5V	6.6	3.5	3.5
Maximum	7.3	5	3.5

10.3.16 Summary of Mk.II Performance

The second hardware prototype did allow further exploration of the overall concept, and demonstrated the following performance improvements including:

- RS232 communication between the controlling PC and the prototype hardware was stable and was able to recover from data faults or timeout situations;
- interrogation of all systems onboard the prototype hardware was able to be performed remotely from the controlling PC;
- all hardware parameters including analog channel selection, A/D converter range and offset, variable optical operating conditions, and pump control, were able to be reliably controlled from the controlling PC;
- all diagnostic data displayed via the onboard LCD display was accurate, and updated according to the commands and data transferred to and from the hardware prototype;
- cell mechatronics able to transport fluid in and out of the cell under controlling PC control;

- optical turbidity measurements were able to be taken with data recorded on the controlling PC;
- the hardware prototype was able to perform limited measurement cycle operations; and
- the model performance showed that it was useful from 1% to 100% with an average discrimination of 6% and an average repeatability of 4%.

Several deficiencies were also identified with this second hardware prototype. These included:

- the pumps chosen for fluid transport exhibited significant leakage as reported in Section 10.3.3;
- flowrates provided by the augmented bellow pump were variable rather than constant;
- the hardware prototype lacked the memory capacity or processing speed to perform real-time calculations of the CO_2 concentration, and as such an external PC was required to perform these tasks; and
- due to these hardware deficiencies, fully autonomous testing of the measurement system was unable to be performed.

Further discussion of the performance of the Mk.II system as well as future improvements, further areas of research, and the recommended design of a 'Mk.III' prototype are presented following in Chapter 11.

Chapter 11

Discussion

11.1 Introduction

In the foregoing chapters, many conclusions have been drawn from the two prototypes constructed and their evaluation. This chapter discusses the overall performance of the instrument prototypes, problems encountered and future work to further explore this field of study, namely the potential for low-cost chemical-transduction gas measurement systems.

The chapter concludes with the outline of a 'Mk.III' prototype instrument for carbon dioxide measurement.

11.2 Prototype Instrument Performance

11.2.1 Resolving Time versus Model Accuracy

It was shown in Figure 10.28 that the measured mean error between the calculated gas concentration and the actual concentration decreased for smaller concentrations, which

is to be expected. Due to the nature of the "T3" model, small concentration values would take a longer time duration to resolve and with this increased time, the time resolution would also increase. Also any minor variation in the reaction rate as a result of a small concentration variation would hence be easier to resolve.

This can be shown symbolically. From Equation 3.8 it was shown that:

$$c = \frac{K}{t}(I_o - I_d) \tag{11.1}$$

where:

c = the concentration of CO_2 gas in the incoming gas stream being bubbled through the sample [mol];
K = $1/k_1 k_2 I_o$, is defined as the sensitivity coefficient for the final measurement system;
t = time from commencement of bubbling [s];
I_o = the output intensity of the optical source; and
I_d = the detected intensity through the solution.

Therefore, for a constant threshold point the following holds true.

$$c = \frac{K'}{t} \tag{11.2}$$

where:

$$K' = K(I_o - I_d)$$

By differentiating the above:

$$\delta c \cong \frac{dc}{dt}\delta t \tag{11.3}$$

$$= -(\frac{K'}{t^2})\delta t \tag{11.4}$$

$$= -(\frac{c}{t})\delta t \tag{11.5}$$

Therefore, for a constant concentration c and for a constant sample rate δt:

$$\delta c \propto \frac{1}{t} \tag{11.6}$$

Hence, with any increasing time measurement to resolve a threshold time, the error in the calculated concentration will decrease. This assumes however that each turbidity measurement is monotonic, and well behaved which has been shown to not always be the case due to internal bubble influences within the cell.

However, this modelling does not account for:

- settling of precipitate;
- clumping of the precipitate; or
- further chemical reaction within the cell.

These effects cannot be easily modelled as their relationships are not directly obvious. In general however the results show that Equation 11.6 holds true.

11.2.2 Threshold Level versus Model Accuracy

Multiple threshold points were used to examine their effects on the accuracy of the measurement system. It was argued that low threshold values would allow shorter measurement resolving times whilst higher thresholds would allow more time resolution and, as seen in Section 11.2.1, increased model accuracy. In an ideal situation where the reactions were well behaved, higher turbidity thresholds would inherently increase

the model accuracy (from Equation 11.6). However under real testing conditions this was not observed.

From Tables 10.7 and 10.8, it was seen that in general no one particular baseline yielded more accurate CO_2 calculation results than any other. This is presumed to be due to the unstable nature of the turbidity measurement within the cell. This result shows that the only advantage of a particular threshold value would be the actual time to resolve the measurement. As such, should fast calculations of CO_2 be required, a lower baseline values would be chosen, however any accuracy improvements with a higher baseline and longer resolving time cannot be justified based on the particular operating conditions of these experiments.

Should more ideal conditions be achieved, with turbidity data being free of noise, higher threshold levels would indeed assist in the overall accuracy of the implemented model.

11.2.3 Cell Life

As the most critical item within the measurement system was the cell, its useable life would contribute to any early failure of the instrument. This is because each measurement results in full precipitate production within the cell (according to the chosen threshold), and hence some $CaCO_3$ coating the cell walls. The cell life was therefore a function of the number of measurement cycles where incomplete cleaning is performed.

It was seen that the number of cycles required before the cell would become significantly coated with $CaCO_3$ precipitate was approximately 10 cycles. With each measurement it was observed, Figure 10.18, that the baseline for the turbidity measurement would rise until insufficient range in the turbidity measurement (Figure 10.4) would result causing erroneous measurements. The Mk.II prototype demonstrated that cleaning of the cell was essential for extended cell life.

With the cell receiving constant cleaning after each measurement, the cell walls would

be removed of all precipitate coating. The cell life would then be extended until it mechanically failed, due to excessive external shock or impact, or was chemically attacked by either the reagents used or gas species within the sample gas. This chemical attack would be seen as the most significant of the two influences, however as shown in Table D.3, the effects of the $Ca(OH)_2$ indicator solution and dry CO_2 were minor on the materials used. The effect of the cleaning solution (citric acid) however was unknown, but was assumed to only have minor effects on the plastics and metals used within the cell, as no significant incompatibilities were observed during the research.

11.2.4 Measurement System Life

As an extension to the previous point in Section 11.2.3, the measurement system will also have a finite life before its functionality is compromised. This life is a function of the general wear on the moving mechanical components, and the material life of the plastics and other materials used in the presence of the ambient environment as well as the chemicals and gases used within the measurement system.

The two most significant components groups exposed to wear, apart form the cell itself, are the pumping systems, and the fluid and gas transport lines. As the measurement system is designed to operate from a single DC supply voltage, small DC voltage pumps are intended to be used for driving either gear pumps or other pumps types (discussed further in Section 11.4.6). These DC pumps will eventually wear out their commutator and stator contacts rendering the pump ineffective.

The fluid lines also prove a significant factor to the life of the measurement system, where calcium carbonate will eventually restrict or block the flow of the indicator chemical to the rest of the instrument. The plumbing material itself could also eventually fail due to long term exposure to ambient gases, or the reagents involved. Suitable materials such as "Tygon™", which would remain chemically inert and unaffected by the reagents, were used throughout the duration of this research. Other plastics such as 4mm polyurethane tubing, used in the first prototype, were however found to stiffen,

and whilst they did not become brittle, it did show that the polyurethane was not suitable for long term installation in the measurement instrument.

11.3 Identified System Limitations & Problems

Several problems and inadequacies in the prototype systems were identified. A majority of these issues primarily originate from the low cost and consequently low specification components used in the prototypes construction.

11.3.1 Cell Design & Shape

The geometry of the implemented cells was based on empirical observations of their operational fluid dynamics. Whilst this resulted in useable reaction cells, they did not adequately perform the task of maintaining indicator chemical consistency and homogeneity, as shown in Section 4.6 and in later results.

The most obvious cell deficiency was that the concentration of phase mixing (sample gas and indicator solution) was occurring at the top of the cell close to the measurement optics rather than at the point of sample gas injection, remote from the measurement zone as had been intended. This resulted in considerable turbidity measurement noise generated by bubbles and a non homogenous spatial distribution of precipitate. The cell was also unable to adequately vent the exhaust gas from the cell without transporting a significant volume of indicator solution from the cell in bubbles along the exhaust plumbing line. The combination of these effects resulted in poor performance of the cell under real conditions.

11.3.2 Cross Sample Contamination

Another significant problem within the instrument would appear during calibration where different gases would be injected into the system. Due to significant lengths of plumbing used for the input gas line, flushing of the entire gas line and cell was required to remove any trace of the sample gases from previous experiments cross contaminating the current measurement. Despite this, problems were still encountered as gas dead-spots within the gas plumbing did exist, particularly at the check valves, where stagnant gases from prior calibration and test runs would remain and contaminate the fresh sample gas. Also under real operating conditions, if these gas dead-spots were ignored, the long gas line lengths would result in a measurement lag dependant on the flow rate and length of plumbing used.

A secondary effect would also occur, where if the sample gas suddenly changed concentration during a measurement, the resultant chemical reaction would result in a turbidity curve with two separate reaction rates, and hence non-standard turbidity developed, related to the concentration of the gas before and after this concentration change. This would result in erroneous concentration measurements because the "T3" model was not calibrated for this situation. As such, the operational conditions of the instrument require that if measuring a variable CO_2 concentration, this variation can only occur at a very slow rate.

11.3.3 Cleaning Agent Cross Contamination

The cleaner used in the Mk.II system was a based on a citric acid and was able to quickly dissolve the $CaCO_3$ precipitate. When the cell was flushed, the cleaner would typically be injected into the cell, the $CaCO_3$ allowed to dissolve, with the cleaner then pumped out of the cell. Due to the plumbing configuration, some of the cleaner would remain in both the cell and in some of the plumbing lines. The cell would then be filled with the indicator chemical ready for the next measurement. As a result, the indicator solution within the cell would be contaminated. It is highly probable that this cleaner

would then interact and interfere with the production of the $CaCO_3$ precipitate during a measurement cycle, and hence affect the turbidity measurement. Although this effect was unable to be confirmed, it was reasonable to assume that some minor affect was present in all of the measurements due to this contamination of the indicator reagent.

11.3.4 Calcium Carbonate Contamination

As already established, the cell interior walls of the cell in both the Mk.I and Mk.II prototype instruments quickly became contaminated with a $CaCO_3$ film, despite the use of an active cleaning cycle with an aggressive cleaning agent. Whilst the amount of precipitate on the walls of the cell was initially measured as an optical baseline measurement by the sensor as part of its self-calibration, eventually a turbidity baseline level would be reached where the functioning of the optics would be seriously impaired. Only by minimising the precipitate coating could the dynamic range and overall performance of the sensor be preserved.

The cell wall surface condition was also a critical factor in the rate at which precipitate would condense. Any roughness would accelerate precipitation deposits, and once established, precipitate coating would occur more rapidly. For this work, the cell wall was prepared to be almost optically flat, but still showed serious fluctuations in surface conditions as a result of the milling fabrication process. The small size of the cells and the lack of proper polishing equipment did not make it possible to better prepare these surfaces.

11.3.5 Optical Sensitivity

It was shown with the second hardware prototype (Mk.II) that the optics were extremely sensitive to $CaCO_3$ particulates, inhomogeneities, and bubbles. These influences resulted in significant noise in the recorded turbidity measurements. In part this was due to the detector aperture being very small (roughly 2mm diameter) such that

small aggregates of precipitate or a localised non-homogeneity would cause significant errors in the turbidity measurement.

Clearly it is desirable that the overall detector sensitivity area should be increased. This would result in a larger measurement window being used for the turbidity measurement hence averaging non-homogeneities to a greater extent, and could be achieved in several ways. A optical lens or grating system could be incorporated to increase the area that the LED emitter irradiates, and the photodiode detector 'sees'. Ideally, if the cell design remained the same the entire measurement zone from the center flow divider to the cell extremities would be inclined in this new measurement zone. A second method would be to use a diffuser to also spread the energy of the emitter to a larger area, however this would however result in a lower optical density than before, therefore a condenser lens or other optical collimation arrangement would be required to increase the effective area the photodiode condenser sensitivity. Other arrangements including photodiode arrays could be employed to provide optical 'averaging' over a large measurement area.

11.3.6 Pump leakage

As much of the mechanical hardware used for the prototypes was deliberately sourced as low-cost originally intended for low technological and hence low precision use, many problems arose from the low specification componentry.

It was observed that the pumps used on the Mk.II system (and to a lesser extent those in the Mk.I system) would leak substantially when turned off and stationary. This resulted in the inability to use these pumps online when obtaining performance results. Testing of the pumps and their control system did show that 'smart' reagent transport was possible, however this leakage would result in unacceptable conditions within the cell due to reagent leakage back through the drainage pump.

Similar problems were found when using gear pumps for gas transport. This was seen with significant loss in pumping efficiency when pumping gases as opposed to pumping

liquids and was primarily due to leakage of gases through the teeth of the gears in the pumps. This would typically result in unstable and unreliable gas delivery. This was overcome in a temporary manner by using an external 'bellows' pump (Section 6.4.7).

11.3.7 Electronic Systems

Another considerable problem encountered was due to the relatively low processing power and limited memory for the Motorola MC68HC11 (again deliberately sourced as a low-cost microcontroller). Due to the inherently intensive CPU control and data acquisition required to be performed by the microcontroller, many of the specialised data analysis functions could only be performed by an external personal computer (PC) connected through a RS232 link. This meant that the control system was complicated by the process of communication to the controlling PC.

Programming this RS232 link on the various programming platforms proved the largest obstacle in development of a working system. It was found early on that many methods for programming RS232 serial ports on the PC were unreliable, or would be specific to a particular serial UART chip. Initially the "Quick C" programming language was used, however many of the initial runtime routines to control the serial port would randomly freeze or fail due to interrupt programming difficulties.

"Borland C++ Builder", in the "Windows 95" environment, was found to work well with serial ports however programming a sequential program, as required by the measurement system procedures, within an object oriented environment proved extremely difficult. Several packages were written in Windows to interface with the external hardware systems, however a full complete instrumentation package was not feasible due to the object orientated programming style required.

Finally the control software was programmed using "QuickBasic" running in the MS-DOS environment. It was found that serial programming was relatively easy and did not suffer from the deficiencies of the QuickC or Borland C++ Builder systems, and

did allow rapid development of calibration routines, and control structures. However because much time was spent trying to find a final programming environment suitable for this work, many instrument functions which were planned to be implemented, were unimplemented due to this progression of programming platforms. As a result only a rudimentary form of the measurement control system could be finished.

11.4 Future Work

There are many areas of research which have been identified to extend the work presented here. These are presented below. In addition, a combination of changes and enhancements set out in this section leads to the conceptual design for a 'Mk.III' prototype. This is presented in Section 11.5 following.

11.4.1 Cell Design & Optimisation

Whilst some analysis, both empirical and analytical, of the 'teardrop' and alternative cells was performed, further modelling is still required to assist conclusively in a new cell design. The existing model, built using the computational fluid dynamics software "FLUENT", whilst comprehensive in its modelling of a bubble stream, used significant computational resources to obtain limited results (Maxwell et al., 2000). A loosening of the finite element grid used would help alleviate this problem, however would result in lower accuracy of the model, but hopefully produce sufficient accuracy to identify key areas to further model.

Alternatively, computational modelling of just a single bubble as it travels from the gas injection point to the gas exhaust port would require far less computational resources and still yield useful flow information with respect to advancing the cell design. The results from this modelling would show how a single bubble affects the fluid flow within the cell, and by applying the assumption that continual bubbling will simply amplify the effect, dead spots (which contribute to precipitate fallout and cell wall coating) in

the flow can be minimised as well as optimisation of the mixing area within the cell.

Mechanical cleaners, additional chemical solvents, and specially coated cell wall interiors could be implemented and is also an area for further empirical research.

11.4.2 Chemical Stabilisation

In order for any cells design to function well with $CaCO_3$ (or other precipitates), further work needs to be conducted into how the addition of catalysts or surfactants could assist with limiting the deposition of precipitates on the cell walls. Through the addition of these agents, the extension of life span of the cell as well as the reduction of cleaning requirements could be achieved.

It is also suggested that through the use of these surfactants or other chemical stabilisation methods, greater control over the homogeneity of the precipitate could be achieved.

11.4.3 Multiple-Gas Sensitivity

An important ability for this sensor is not only its ability to be used for the measurement of CO_2 but for the measurement of other gases. As the primary detection principle is based on turbidity, any other gas species that, when combined with an indicator reagent, produces a turbid solution can be measured using this technique.

11.4.4 Cross-Sensitivity to other gases

Cross-sensitivity of the chosen indicator reagent to gases other than CO_2 was not investigated. It is envisioned that there will be a certain amount of cross-sensitivity with other gas species, however investigation into these was considered outside the scope of this research.

This is however an important issue for a final instrument, and would require careful selection of the indicator solution, or the addition of a catalyst to reduce the effects of other noise gases through the acceleration of the primary reaction with CO_2, or suppression of other 'noise' reactions.

11.4.5 Temperature and Other Effects

No work was performed on how temperature affected the instrument. Whilst intra-cell temperature sensors were available for use, these were not used in any of the model calculations. Temperature would affect the reaction rate and hence the times in the "T3" model. A secondary model to compensate for temperature could then be generated thus creating an extra dimension to the calibration curve set as seen in Figure 7.4, and 7.7.

Additionally no work was performed into the effects of relative humidity on the instrument. These effects, as with temperature, would affect the reaction rate, and likewise could be modelled through an extra dimension of the "T3" models.

11.4.6 Fluid/Gas Transport System

As previously shown, the gaseous pumping system employed for both hardware prototypes performed poorly. It has been shown that whilst gear pumps may be suitable for unloaded pumping of gases, in the measurement instrument their performance was questionable. Also the performance of these same pumps when used for fluid transport, was seen initially as adequate, however problems such as reverse flow leakage when the pumps were off and stationary did not allow these pumps to be used properly in an online situation.

A far better pumping system would have been to replace all four pumps with DC voltage 'bellows' pumps, Figure 11.1. These pumps couple a small DC electric motor

to a diaphragm and inbuilt valve assembly to provide uni-directional pumping, of a known volume per pump cycle. This would have allowed reliable and repeatable fluid transport of a known quantity and also allowed a metered dosage of both indicator solution and sample gas to be injected into the cell.

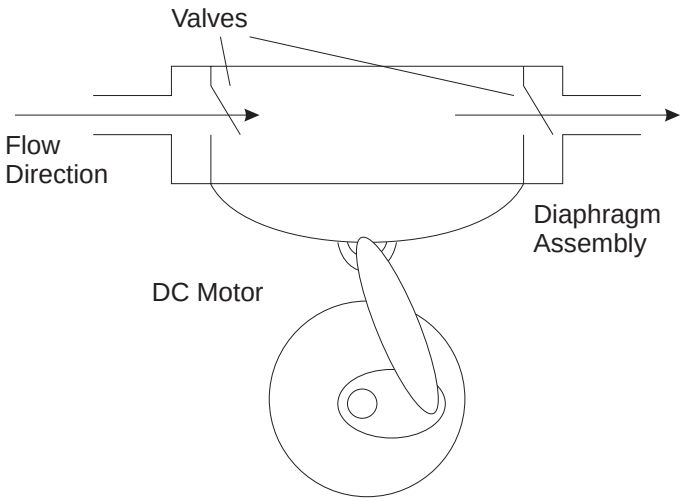

Figure 11.1: Example of a 'bellows' pump using a small DC motor for actuation.

At the time of design for both prototypes, small and low cost DC operated bellows pumps were unable, however at the end of the research, pumps of this type were located, but unfortunately unable to be obtained. Should these have been implemented, the overall size of the prototypes could be decreased with all check valves being removed and tubing lengths significantly reduced.

Future research in this area of mechatronic fluid and gas transport would significantly advance the successful implementation of this measurement technique.

Also with miniaturisation of the cell (Section 11.4.14 below) the pumping requirements also decrease such that techniques such as electrostatic pumping and the use of ultrasonics may become feasible. If either electrostatic or ultrasonic pumping methods could be developed this would remove the need for mechanical pumps and allow almost solid state cell control mechanisms to be created. Ultrasonic pumping systems have been postulated by Rife et al. (1986), with electrostatic fluid transport starting to appear in

miniature chemical cell systems (Fluri et al., 2000).

11.4.7 Gas Flowrate Compensation

It has been shown that the flowrate of the sample gas being injected into the cell affects the reaction rate, and hence the resultant turbidity curve. One possible method of compensating for variations in the flowrate would be to use the measured flowrate as a modifier to the model, for example, to produce an 'adjusted time scale' for sampling.

For example, if a faster flowrate was measured, the reaction rate would increase, and to counteract this the adjusted time scale would be lengthened. Hence the indicated time to reach a particular threshold would still remain the same regardless of reaction rate, thereby providing the same CO_2 calculation. An example of this effect is shown in Figure 11.2. The upper curve shows a varying flowrate (in this case sinusoidal for demonstration purposes), and the corresponding adjusted timescale as the lower curve. As the flowrate increases, the perceived sample rate decreases (longer sample time) thereby compensating the time measurement for the raster production rate of the precipitate. As the flowrate then decreases the perceived sample time is then shortened to compensate for a slower reaction rate.

11.4.8 Adaptive Optics Techniques

Although preliminary experimentation with the use of adaptive optics in the measurement of properties of suspensions, coagulants, and precipitates were presented in Section 10.3.7, further research is necessary to understand the effect of adjustable output power levels (at the infra-red LED source) and adjustable sensitivity (at the infra-red detector) on the overall dynamic range of an instrument.

The effects of synchronous detection on the system's performance is also another important area for further research. Synchronous detection in this specific case would

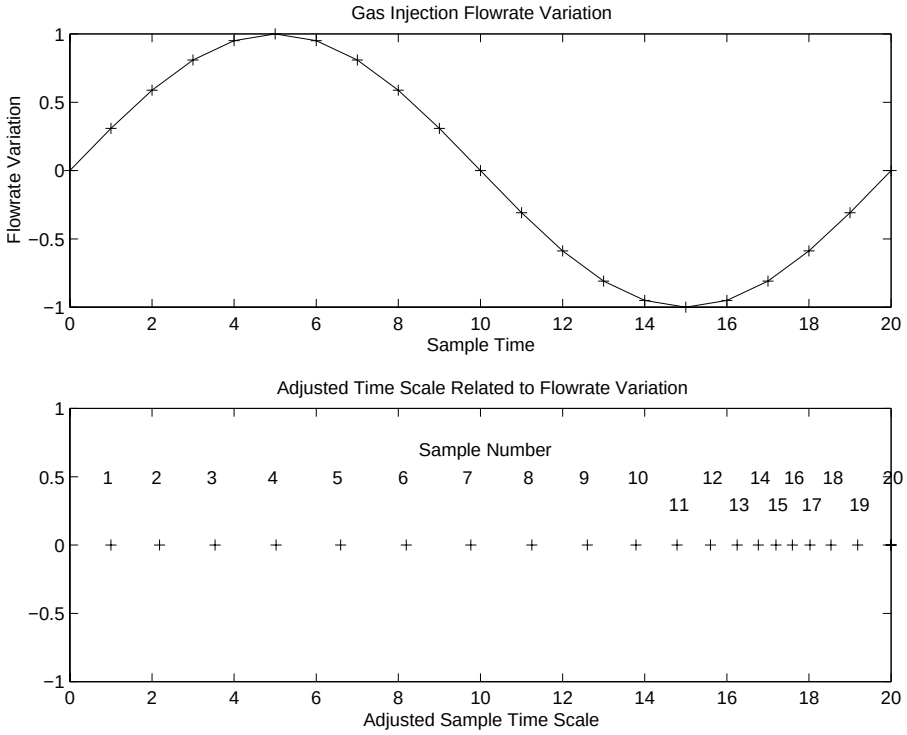

Figure 11.2: Flow rate related 'adjusted time scale' compensation for fluctuations in reaction rate caused by variable gas injection flow rates.

involve the activation then deactivation of the emitter infra-red LED such that two optical measurements would be made, one with detector measuring both the in-cell turbidity and ambient lighting noise, and then one with the detector measuring just ambient light respectively. The difference between these two measurements then yields only the turbidity measurement with suppression of the noise effects of ambient light. This technique would be necessary to significantly reduce the effects of external ambient light and external signal noise on the optical measurement system.

Whilst synchronous detection was not used for the prototypes, any further extension of the prototypes should include this detection method.

11.4.9 Prototype Hardware and Cell Control

The pipework connection scheme for the fluids in the prototypes constructed was chosen based on simple fluid manipulation principles, namely simple 'tee' junctions and check valves. However it needs to be noted that this scheme resulted in several problems, notably the inability for the pumps to properly prime themselves and inability for the gas pump to properly pump gas due to additional flow restriction caused by the plumbing tube diameter.

As previously noted, the primary pumps used were simple gear pumps, which are designed primarily for pumping liquids. Pumping gases can be achieved provided that the pump outlet pipe lengths were kept short, judged to be less than 10cm for the pipe sizes and fluid volumes of the Mk.I and Mk.II prototypes, and provided that no significant flow restrictions are present.

Also, as the gear pumps were typically suited for aqueous environments rather than for gases, this resulted in increased wear on the pumps (which would result in regular replacement or servicing in a commercial ready implementation) and also a very pulsatile flowrate rather than the required steady flow.

Various mechanical improvements to the pumping mechanism could be made to make the gaseous pumping function more efficient and stable with respect to fluid flow. The development of controllable valves would have simplified the design of the fluid handling system. Some initial work was performed (Appendix E) into these valves, however due to the inability to properly manufacture the valves at the small scale required, this work was not completed.

11.4.10 Cell Interfacing

As it was observed that the cells could become easily fouled or blocked, a mechanism for easily replacing the entire sensing head (comprising the cell and optical assemblies)

could usefully be investigated. The interfacing mechanism would require not only gas and fluid connections but also electrical signals to be separated. A far better solution would be to have the electrical and fluid/gas lines attached to the cell in a modular manner thus permitting simple and rapid removal and replacement of the sensing head. A simple connector providing three gas/fluid lines and the necessary electrical signals (6 for the optical signals, and 3 for the temperature sensor in the case of the prototype cells used here) would suffice.

11.4.11 Microcontroller Implementation

Many processor-orientated problems could have been avoided by implementing a far more powerful microcontroller into the instrumentation package to implement the control system.

It is estimated that the system microcontroller would require the minimum specifications shown in Table 11.1 to achieve fully autonomous operation. As presented in Appendix B.1.5, the minimum memory requirement to represent the interpolated (table-lookup) cubic spline was estimated to be 3kbytes (for $\pm 1\%$ accuracy). In order to achieve a greater accuracy, additional memory to store a more detailed lookup table would be required. Additionally, should any of the other models presented in Appendix B be implemented, the memory requirements would further increase due to the need for extra mathematical code libraries to perform these operations.

Table 11.1: Minimum microcontrollers specifications required for the measurement system to operate fully autonomously.

Specification	Minimum Value Speed
Speed	8MHz
RAM	4kbytes
ROM	8kbytes
A/D	10 bit (multiple channels)
Serial	RS232 (TTL) or equivalent
I/O	8 general purpose digital I/O
Other Buses	SPI

Several processors, able to be used for a future Mk.III prototype (Section 11.5), are

listed in Table 11.2. This list is organised from least processing power and capability at the top (and hence lowest cost) through to the more powerful at the bottom (and hence more expensive).

Table 11.2: Motorola microcontrollers potentially suitable for use in further measurement system prototypes.

Processor	Speed	I/O	RAM	(EP/EEP)ROM
MC68HC711E2	8MHz	8ch(8 bit), Timers, Serial	256b	2kb EEPROM
MC68HC711E9	8MHz	8ch(8 bit), Timers, Serial	512b	512b EEPROM 12K EPROM
MC68HC711E20	8MHz	8ch(8 bit), Timers, Serial	768b	512b EEPROM 20K EPROM
MC68HC11F1	8MHz	8ch(8 bit), Timers, Serial	1kb	512b EEPROM
MC68HC812A4	16MHz	8ch(8 bit), Timers, Serial	1kb	4kb EEPROM
MC68HC912BC32	16MHz	8ch(10 bit), Timers, Serial	1kb	4kb EEPROM 32kb ROM
MC68HC916X1	16MHz	8ch(10 bit), Timers, Serial	2kb	48kb Flash
MC68HC916Y3	16MHz	8ch(10 bit), Timers, Serial	4kb	96kb Flash

The processor used in both instrument prototypes was the 68HC711E2 and was able to provide basic functionality to the prototype hardware. However, more suitable devices could have been used such as the 68HC711E9 or 68HC711E20 which not only had significantly more RAM and EPROM, but are pin for pin compatible with the existing processor therefore requiring no further alteration to the instrument electronics. Other devices such as the MC68HC812A4 and MC68HC912BC32 (members of the commonly termed "68HC12" series) could be more ideal if the code could be sufficiently compressed to fit the small memory space available (4kb EEPROM) in these microcontrollers. The latter microcontroller (MC68HC912BC32) had a significant advantage due to it's higher resolution onboard 10 bit A/D converter.

Other variants such as the MC68HC916X1 and MC68HC916Y3 could also be used ("68HC16" series), which feature faster operation speeds, an 8 channel 10 bit A/D converter and large 48kbyte or 96kbyte FLASH ROM memory sizes respectively. This series of processor would be well suited to future prototype instruments. However, these latter microcontrollers are inherently more expensive than previous ones, therefore requiring cost justification of their use.

All of the possible microcontroller variants shown in Table 11.2 are also able to operate in an 'expanded memory mode', where external RAM and ROM can be used, further increasing storage and program size limits. Low cost variants such as the Motorola MC68HC11F1, designed for this purpose, could then be used which allows this expanded memory function. However, extra componentry in the form of RAM, ROM, and memory decoder chips would still be required in this mode, and may negate any cost advantages of using this method.

11.4.12 Differential Measurement

Throughout this dissertation the focus has been on absolute measurement of CO_2 gas. An extension of the mechatronics technique reported would be to implement differential measurement capability. Whilst this was outside the scope of this present research, methods of incorporating differential measurement are as follows.

An obvious extension of the absolute measurement technique presented here would be to replicate the instrument. This has an inherent disadvantage in that two completely separate instrument packages making two independent measurements will increase the measurement error particularly where the difference between the two absolute volumes is small. Differences between the two instruments will include general short and long term drift, and noise as well as unavoidable differences in calibration.

A far better approach would be to encompass the differential ability into a single instrument where cell manufacture, calibration, mechatronic variabilities are common to both sensing heads thus removing the errors caused by these variabilities. By fabricating two separate chemical reaction cells side by side and utilising common optic paths, it will be possible to create a differential instrument whose drift and noise minimisation characteristics are far greater than the case of two separate instrument packages.

11.4.13 Instrumentation Package Size

The instrument package size for the Mk.I measurement instrument was approximately 180mm×100mm×80. This did not include the chemical reagent reservoirs which were not made an integral part of this 'proof-of-concept' instrument.

The Mk.II instrument package size was partially larger, due to the size of the pumps and additional electronics. The instrument package, comprising pumps, reaction cell and infra-red optics , pipelines and electronics, occupied a total size of roughly 20cm cube and is capable of further miniaturisation (Section 11.4.14). This measurement instrument size ignores the additional components, the gas flowmeter (Section 6.4.8) and the external bellows pump (Section 6.4.7), required for performance monitoring and to overcome the deficiencies of the pumping system (Section 11.3.6).

Additionally, to perform 100 measurements, approximately 300mL of indicator reagent ($Ca(OH)_2$), and 300mL of cell cleaning reagent (citric acid) is required. These values are calculated from the internal cell volume (Table 4.2) of the 'teardrop' cell. This then requires a minimum 600mL storage capacity for waste materials. These storage vessels would then add to the total measurement instrument size.

Also, due to the design of the cell requiring bubble flow from the lower part of the cell to the upper part (e.g. Figure 4.15), there was a requirement that the entire operational package remain upright, and level during operation.

11.4.14 Instrumentation System Miniaturisation

The cells presented here were originally intended to be miniaturised, however this miniaturisation presented significant challenges. In order to miniaturise the system, the cells themselves would obviously need to be miniaturised.

Because the cells combine both the aqueous indicator solution and the sample gas, the physical interaction between these two phases would need to be considered. As the

cell size was miniaturised, the effects of bubble size would become more pronounced. However, the bubble size could be similarly reduced by using an active injection system. A miniature heating element could heat a small volume (micro-litre scale) of sample gas, actively forcing it through a miniature orifice resulting in a smaller bubble diameter. Likewise surface tension effects of the indicator reagent would increase, potentially interfering with the liquid/gas phase mixing.

At a smaller scale, and with the advent of micro-machining, it would be possible to construct microlitre-scale volume cells based on silicon or similar substrates. It would also become possible to place not only the cell on the substrate, but also the optics and signal processing systems. It then also becomes possible to either micromachine pumps to perform fluid control, or utilise electrostatic techniques to perform a similar function (Fluri et al., 2000), thereby facilitating a solid state fluidic based microsensor.

It also becomes possible to use other substrate structures for the measurement system. A novel cell design based on a structure similar to a compact disk (CD) has been presented by Madou (2000). This device merged chemical reservoirs, valves, plumbing and measurement zones onto a planar structure able to be placed into a standard personal computer CDROM drive unit. This allowed for only one moving part being the disk itself. Variations in the disks spin speed could control the valves. Centrifugal force from the spinning disk provides the "pumping" action to transport the chemicals throughout the instrumentation package (as illustrated in Figure 11.3).

This packaging could also include traditional CD software necessary to drive the CDROM drive and could use the CD drive's optical mechanism to form the basis of an optical measurement system to read the disk's measurement area. Thus a complete, possibly disposable, measurement packaging systems could be developed.

Simple and novel packaging systems for wet chemical analysis for CO_2 could also be created based on the same principle thus identifying another area for further exploration.

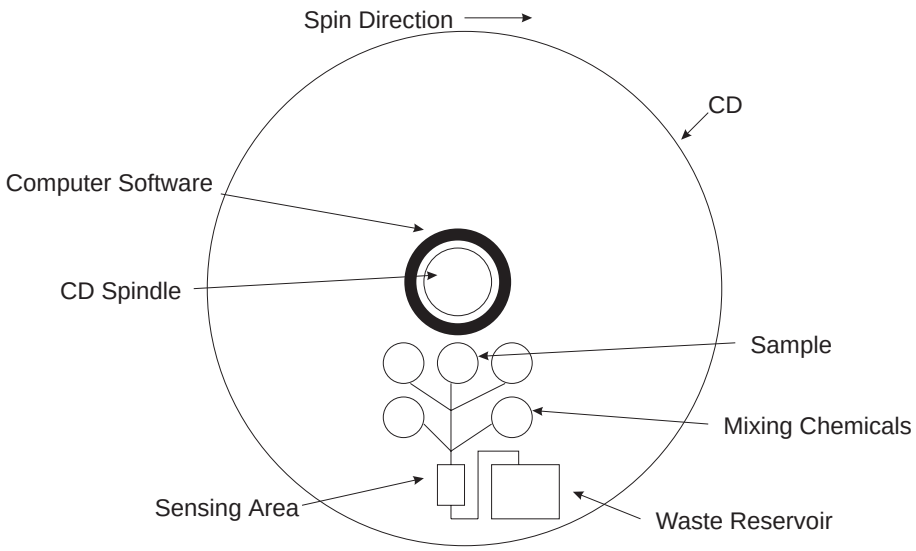

Figure 11.3: Example of a wet chemical sensor on a compact disc (CD) structure, conceptual only (after Madou, 2000). Variations in the disks spin speed controls the valves at the base of each chemical reservoir whilst centrifugal force provides the pumping action. It is possible to have integrated software on the CD providing instrumentation capabilities to a standard personal computers CDROM drive, with the drives laser providing optical measurement capability of the reagents.

11.4.15 Disposable Sensing

Although not a prescribed aim of the project, there are significant disposable sensing applications of the research presented here. If the limitations of the system can be overcome it is feasible that a disposable sensing package can be constructed.

Disposable sensors have advantages in that due to their low cost, they can easily be used on single mission trips, where the sensing package is simply discarded after logged information has been obtained.

As shown in the Section 11.4.13, all of the chemical reagents and waste materials remain encapsulated within the instrument. Additionally, as the chemistry used is benign and poses no environmental safety threat, the entire instrument package can be easily and safely disposed of.

Applications for such devices exist in the horticultural industry where produce is transported on long domestic or international trips. Information about the respiration rate and hence the freshness of the produce can be derived from the carbon dioxide concentration within a sealed container during the trip. This information is then used at the destination to grade the produce and potentially be used to take preventive action if produce, during transportation, suffers from inadequate storage conditions. At the end of the trip the instrumentation package (due to its low cost) can simply be discarded, and a new device used the next time produce is transported.

11.5 Mk.III - Conceptual Design

From the discussion above it is seen that whilst there were some deficient aspects of the Mk.II system, much of it worked as required. As an extension to this work, a potentially commercial-ready Mk.III system can be explored. This new revision could be optimised using the knowledge gained form the previous two hardware prototypes.

An outline of the necessary components for this new hardware prototype is as follows:

Cell The cell used would be a variation of the one used for the previous hardware prototypes, optimised to yield reliable, and consistent turbidity measurements free of spurious noise and exhibit homogeneous mixing (Section 11.4.1).

Pumps The pumps to be used would be miniature 'bellows' pumps (Section 11.4.6) which would be configured to provide a metered volume of sample gas or indicator/cleaning solution per rotation cycle. Optoelectronics or some other feedback mechanism would be required so that accurate knowledge of the dosage could be determined.

Chemistry The chemistry used for the Mk.III would be identical to previous versions where $Ca(OH)_2$ is used as an indicator through the production of $CaCO_3$. Stabilisation of this chemistry would be performed through the use of either a

surfactant or other chemical method (Section 11.4.2).

Signal Conditioning Synchronous detection (Section 11.4.8) would be employed hence reducing the susceptibility of the cell to ambient light.

System Processor The system processor would either be an expanded memory version of the processor used previously (Section 11.4.9, Motorola MC68HC11E2), or different package (Section 11.4.11) capable of providing the necessary processing power and onboard interfacing to perform all model calculations and interact with the rest of the hardware system.

Additional Sensing To allow further automated features, extra sensors such as fluid level sensors would be employed to ensure that sufficient indicator reagent was available and that the waste reservoir did not overflow. Other sensors such as tilt sensors could also be employed to ensure cell orientation was maintained during operation.

Power Source The power source for the entire system would be portable and consist of either a 12V sealed lead-acid gel ("gel cell") battery or other high energy density package.

System Integration The system would be integrated as shown in Figure 11.4.

User Interface The user interface would be very similar to that used in the existing hardware prototype, with extended diagnostic information being presented, such as fluid levels within the reservoirs.

Chemical Reservoirs The reservoirs would be the same as previously used (Section 6.4.5) unless more compact versions were found.

Packaging The whole system would be packaged into a 'black box' suitable for deployment in several targeted applications including horticultural storage and transport. Considerations to the disposable nature of the instrumentation system should also be considered (Section 11.4.15). As the cell is required to remain level during operation, the packaging would also require to maintain it's orientation.

Thus if further research were performed, the development of this Mk.III would be the next logical step.

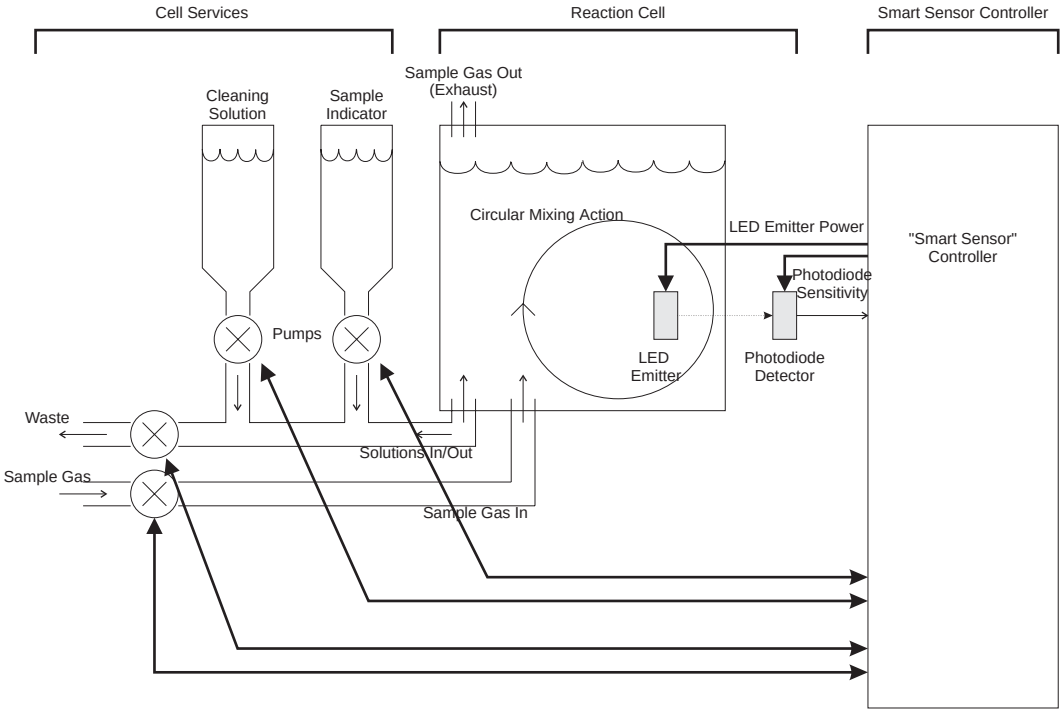

(a) Conceptual Mk.III block diagram.

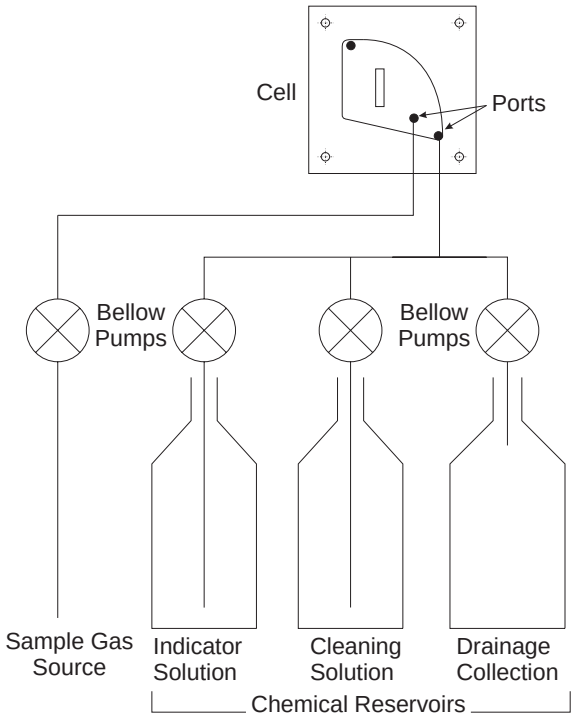

(b) Conceptual Mk.III interconnection scheme.

Figure 11.4: Conceptual view of the Mk.III block diagram and interconnection scheme.

Chapter 12

Conclusion

12.1 Summary of Research

Research commenced with an evaluation of the many possible measurement methods for the proportion of carbon dioxide in a gas stream and is presented in Chapter 2. Of these, one was seen suitable for further exploration with respect to potentially low-cost, possibly single mission instrumentation. This method was based on the use of "wet chemical analysis" methods utilising bulk chemical reactions between reagents and the sample gas to produce a detectable chemical change which was directly related to the absolute concentration of CO_2 in the gas sample. This method required several transductions from the chemical form, through the optical, then to electrical, and finally to an information value of concentration.

The theoretical basis for such an instrumentation system presented in Chapter 3 showed that this method could be used to repeatably produce an absolute measurement system. Preliminary experiments using the calcium hydroxide ($Ca(OH)_2$) indicator solution and 95% pure CO_2 showed that a repeatable reaction would occur where the fine white chemical precipitate calcium carbonate ($CaCO_3$) would be produced when exposed to CO_2. Also shown was the pattern of precipitation, and then precipitate suspension

due to agitation from the gas source. Upon removal of the gas source the precipitate suspension would start to fall out of suspension. This would, as shown in later sections, cause some problems with the turbidity measurements. This simple experiment showed that interphase mixing between the sample gas stream and aqueous indicator solution, was necessary to maintain homogenous precipitate conditions, and that many other parameters of the reaction would need to be controlled. Thus the basis for the sensor was shown to consist of a chemical reaction cell, indicator reagent, sample gas source, some mixing action, and a chemical change (turbidity) detection system.

Three transduction steps were required to convert the gaseous CO_2 concentration to an electrical signal, namely; transduction through the chemical energy regime converting carbon dioxide and calcium hydroxide to the white precipitate calcium carbonate; then from the chemical to the optical energy regime by transducing the light scattering properties of the precipitate to an optical turbidity measurement; and finally converting this optical signal to the electrical energy regime using a LED and photodiode combination. Once in the electrical form the signal could be sampled at a regular interval (typically every second) by the microcontroller and analysed using the inbuilt models yielding the final CO_2 measurement.

Other extensions to this principle were shown including both open and closed loop measurement systems, where the closed loop system took into account the ability to control the optic system's sensitivity, the pumping systems required to move the reagents to the sensor as well as allowing for compensation of fluctuations in the sample gas flow, primarily caused by the sample gas source pumping mechanism. Whilst some of these systems were not fully implemented in the final instrument, they were still discussed. With the basic sensor premise shown, detail was provided for the cell design, fluid transport, measurement microcontroller and integration systems.

The cell design was critical to the overall performance of the sensor. The cells, as shown in Chapter 4, were required to not only contain the chemical reaction but also to allow mixing of the reagents with the sample gas; to permit optical measurements of the precipitate; and also allow for convenient integration into the rest of the system both

electrically and mechanically. The cell design constituted a large factor in the overall instrument performance as it was the cell's internal void shape that primarily affected the mixing and therefore the production of the precipitate. The design of the cell also impacted the ease of cleaning and maintenance in an online situation.

Suitable regions for chemical mixing and optical measurement were built into the empirically designed cells to minimise spurious turbidity noise caused by micro-bubbles breaking free of the main vertical mixing column. Several cell prototypes were constructed and tested before arriving at the final cell type used, these others included simple inline flow cells, a circular flow tube, a divided cell, and finally the modular 'teardrop' cell. Numerically controlled machine milling was used to mill both the outside cell shape as well as the cell void. This yielded highly accurate and repeatable cell construction suitable for implementation into the sensor design.

In addition to this empirical cell design, brief computational modelling and analysis based on the "FLUENT" fluid dynamics software package was performed. The original unmodified 'teardrop' cell and a completely new cell design were modelled showing that whilst the 'teardrop' functioned well, it was shown to be far from functionally ideal. The new cell design showed significant merits over the old design (including a high shear rate at the bubble injection port which would result in significantly better mixing) however construction and testing were not able to be performed. Further computational modelling was not performed due to difficulties experienced with the FLUENT package.

Detail of the turbidity measurement method was provided in Chapter 5. This included an evaluation of the optical components and the optical orientation in order to provide the turbidity measurement. This, in addition with the final hardware components of the fluid transport system as shown in Chapter 6, provided details of all the hardware necessary for the sensor to operate autonomously. The plumbing configuration, pump selection, and motor drive circuits were presented as well as the control schemes used for the lower level control functions. A description of how the level control functions and other smart sensing operations was also presented in addition to the differences

functionally between the 'Mk.I' and 'Mk.II' instruments. Also presented was later work into the development of a precision gas mass flowmeter to assist with modelling variations in the flow rate of the sample gas and its effects on the reaction rate of the reagent.

Chapter 7 presented the developed models and techniques used to derive suitable CO_2 gas concentration values from the realtime optical data. The model described was the "Time-To-Threshold" or "T3" model. This model used rate of reaction data from the optical measurement to derive a time to a particular optical threshold (with respect to the optical baseline at the start of the test). This time was then related to a reverse lookup translational model based on a multiparameter exponential series. This then allowed translation from the time to a concentration. By utilising multiple threshold target points, a series of calibration curves could be produced which allowed fast (but less accurate) CO_2 measurements or more accurate measurements over a longer time period. Using this method the effective accuracy of the instrument became a parameter of the time chosen between measurements, and this has been shown to have significant advantages in the detection of lower concentration values.

With each component of the sensing system complete, joining of the blocks was performed and allowed extension concepts such as adaptive optical measurements and further automated functions to be explored as shown in Chapter 8. With the models came the development of the software, both the firmware operating system in the microcontroller and the software for a master PC controlling the system as shown in Chapter 9.

Performance details for both prototypes, as well as for the optical, and cell subsystems was presented in Chapter 10. Whilst high concentrations were easily measured for both prototypes, lower concentrations (below 20%) would typically take several minutes to converge to the chosen threshold point (as part of the "T3" model) which would lengthen the instrument cycle time with long delays, typically 5 minutes, between readings. The Mk.II performance was significantly better of the Mk.I system, however the programming for the Mk.II was not optimised and many automated functions were

unable to implemented. With the addition of these extra features it is estimated that the accuracy of the Mk.II system could have been increased to 1% and possibly 0.1%. Enhanced model characterisation, signal filtering and coherent detection could have also been incorporated. The unique ability of the optical subsystem to allow both the detector sensitivity and the emitter power to be adjusted independently showed that 3D optical parameter surfaces could be generated for each particular sample solution. This allowed the measurement of dispersion through the precipitate and could be used to maximise the optics sensitivity for a given precipitate condition within the reaction cell hence providing further smart sensing operation.

The first prototype (illustrated in Figure 1.2(a)) was easily constructed with minor manufacturing and off-the-shelf componentry. The sensing technique employed displayed good potential for further miniaturisation. The second prototype (illustrated in Figure 1.2(b)) required extensive construction both on the cell, optics system as well as for the microcontroller and software systems.

Discussion of the measurement instruments performance was set out in Chapter 11 and comprised of further analysis of the performance and identified limitations of both measurement instruments. Future work in this research area is discussed as well the overview of a future Mk.III prototype measurement instrument.

The latter Mk.II measurement instrument occupies roughly 20cm cube and is capable of considerable further miniaturisation. Working chamber volumes of less than 0.5mL are possible through miniaturisation of the reaction cell resulting in complete sensor packages in the order of 5cm cube. When coupled to a 2L supply of chemical indicator, the sensor could perform well over 3000 measurements before any top-up of the indicator was necessary.

12.2 Conclusion

The prototype instruments developed in this research demonstrate that simple chemical reactions coupled with mechatronic systems can form the basis of a sensing package to measure CO_2. A first prototype (Mk.I) capable of useful measurements in the range 10% to 100% (with an error slope of -0.242, Table 10.1) was constructed; and a second, more versatile prototype (Mk.II) was then constructed which delivered measurement capabilities in the range of 100% to 1% to a discrimination of $\pm 6\%$ (Table 10.7) and a repeatability of $\pm 4\%$ (Table 10.8).

As shown in Chapter 1, the primary objectives for this work were to investigate select applications, investigate existing instrumentation systems and measurement methodologies, describe and model novel and non-traditional methods and phenomenon useful for the quantitative measurement of CO_2. The objectives also included the need to devise and develop a prototype, and derive suitable evaluation procedures and employ these to evaluate the prototyped sensors to demonstrate performance capabilities and limitations. All of these objectives were met.

12.3 Further Work

There are many aspects of this research direction which require further work, as set out in detail in Section 11.4. In addition, the design of a Mk.III is outlined in Section 11.5.

References

Ayres, G. H. (1968), *Quantitative Chemical Analysis*, 2nd edn, Harper & Row, New York.

Barnes, H., Helgeson, H. & Ellis, A. (1966), Ionization constants in aqeous solutions, *in* S. Clark, ed., 'Handbook of Physical Constants', revised edn, The Geological Society of America, New York, chapter 18.

Bartolomeo, J. D. (1995), 'Detecting *CO* in the home', *Home Automation & Building Control* pp. 51–55, October.

Benson, I. B. (1993), Compositional analysis using near infrared absorption spectroscopy, *in* E. Kress-Rogers, ed., 'Instrumentation and Sensors for the Food Industry', Butterworth Heinemann, Sydney, chapter 5, pp. 121–188.

Bhatia, V., Murphy, K. A., Claus, R. O., Jones, M. E., Grace, J. L., Tran, T. A. & Greene, J. A. (1996), 'Optical fibre based absolute extrinsic fabry-pérot interferometric sensing system', *Measurement Science and Technology* **7**(1), 58–61.

Block, R., Fickler, G., Lindner, G. & Müller, H. (1992), 'Mechanical resonance gas sensors with piezoelectric excitation and detection using PVDF polymer foils', *Sensors and Actuators B* **7**, 596–601.

Butler, J. D. (1979), *Air Pollution Chemistry*, Academic Press, New York.

Buttsworth, D. & Chin, S. (2001), University of Southern Queensland, Toowoomba, Queensland, Australia. discussions with.

Choi, M. F. & Hawkings, P. (1995*a*), 'Novel dye - solvent solutions for the simultaneous detection of oxygen and carbon dioxide', *Analytical Chemistry* **67**, 3897–3902.

Choi, M. F. & Hawkings, P. (1995*b*), 'A novel oxygen and/or carbon dioxide-sensitive optical transducer', *Talanta* **42**(3), 483–492.

Cole Parmer Instrument Company (1997–1998), *Cole-Parmer Catalog*, Cole-Parmer Instrument Company / Extech Equipment Pty Ltd, P.O.Box 7, Wantirna South, 3152, Victoria, Australia, chapter T, pp. 1364–1372.

Conn, G. K. T. & Avery, D. G. (1960), *Infrared Methods: Principles and Applications*, Academic Press, New York, chapter 6.

Debéda, H., Massok, P., Lucat, C., Ménil, F. & Aucouturier, J. L. (1997), 'Methane sensing: From sensitive thick films to a reliable selective device', *Measurement Science and Technology* **8**(1), 99–110.

Dillig, B. (1994), 'Infrared analysis cost-effective with new detector says dräger', *Water & Wastewater International* pp. 39–20, October.

Doebelin, E. (1990), *Measurement Systems, Applications and Design*, 4th edn, McGraw Hill.

Durrant, P. (1964), *General and Inorganic Chemistry*, Longmans, Green and Co. Ltd, 48 Grosvenor St, London.

Fluri, K., Dodge, A., Lettieri, G., Verpoorte, E. & de Rooij, N. (2000), Design and operation of an automated microfluidic platform for heterogeneous assays based on sealed pL wells, *in* '8th International Meeting on Chemical Sensors - Abstract Book', Elsevier Science, Basel, Switzerland, p. 141.

Fredericks, P. (1995), 'Vibrational spectroscopy heads towards life', *Analysis, Separation chemistry for science and industrial markets* pp. S3–S8, April.

Frutos, A. (1998), 'SPR of ultrathin organic films', *Analytical Chemistry News & Features* pp. 449–455, July.

Future Fibre Technologies (2001), Science of fibre optic sensors.
URL: *http://www.fft.com.au/background.html*

Gippel, C. (1988), The effect of water colour, particle size and particle composition on stream water turbidity measurements, Technical Report 3, University of NSW, Australian Defence Force Academy, Campbel, ACT, Australia.

Glenar, D., Hillman, J., Saif, B. & Bergstralh, J. (1994), 'Acousto-optic imaging spectro-polarimetry for remote sensing', *Applied Optics* **33**(31), 7412–7424.

Gordon, A. J. & Ford, R. A. (1972), *The Chemist's Companion*, John Wiley & Sons, New York.

Grandke, T. & Ko, W. (1989), *Sensors: A Comprehensive Survey*, Vol. 1, VCH Publishers Inc., New York.

Gripp, J., Mäder, H., Dreizler, H. & Teffo, J. L. (1995), 'The microwave spectrum of carbon dioxide ^{17}OCO and ^{18}OCO', *Journal of Molecular Spectroscopy* **172**(2), 430–434.

Hallett, F. R. (1996), Size distributions from static light scattering, *in* W. Brown, ed., 'Light Scattering: Principles and Development', Oxford Science Publications, Oxford, chapter 14, pp. 477–493.

Hampel, C. A. & Hawley, G. G., eds (1973), *The Encyclopedia of Chemistry*, 3rd edn, Van Nostrand Reinhold Company, New York.

Harrous, M. E., Gill, S. J. & Parody-Morreale, A. (1994*a*), 'Description of a new gill titration calorimeter for the study of biochemical reactions. 1: Assembly and basic response of the instrument', *Measurement Science & Technology* **5**(9), 1065–1070.

Harrous, M. E., Gill, S. J. & Parody-Morreale, A. (1994*b*), 'Description of a new gill titration calorimeter for the study of biochemical reactions. 2: Operational characterization of the instrument', *Measurement Science & Technology* **5**(9), 1071–1077.

Hauser, P. & Liang, C. (1997), 'All solid-state instrument for absorbance based optical gas sensor membranes', *Instrumentation Science & Technology* **25**(2), 147–156.

He, X. & Rechnitz, G. A. (1995), 'Linear response function for fluorescence-based fibre-optic CO_2 sensors', *Analytical Chemistry* **67**(13), 2264–2268.

Helenelund, C. (1996), 'New from vaisala - the CARBOCAP carbon dioxide sensor', *Vaisala News* **141**, 18–19.

Hester, C. (1995), Gas analysis by packed column chromatography, *in* 'Chromatography - Techniques and Developments', The Royal Australian Chemical Institute - Queensland Branch, Sunnybank Hotel/Motel, Sunnybank, Brisbane, pp. 38–42. October 23.

Heuber, D., Stevenson, C. & Vo-Dinh, T. (1995), 'Fast scanning synchronous luminescence spectrometer based on acousto-optic tunable filters', *Applied Spectroscopy* **49**(11), 1624–1631.

Ishihara, T., Kometani, K., Hashida, M. & Takita, Y. (1991), 'Application of mixed oxide capacitor to the selective carbon dioxide sensor', *The Electrochemical Society* **138**(1), 173–176.

Ishiji, T., Takahashi, K. & Kira, A. (1993), 'Amperometric carbon dioxide gas sensor based on electrode reduction of platinum oxide', *Analytical Chemistry* **65**(20), 2736–2739.

Jackel, J. L., Baran, J. E., d'Alessandro, A. & Smith, D. A. (1995), 'A passband-flattened acousto-optic filter', *IEEE Photonics Technology Letters* **7**(3), 318–320.

Janata, J., Josowicz, M., Vanysek, P. & DeVaney, D. M. (1998), Chemical sensors, *in* 'Fundamental Reviews - Analytical Chemistry', American Chemical Society, Washington DC, chapter 8, pp. 179–208.

Johri, G. K. & Pathak, S. K. (1989), 'Theoretical study of microwave spectral linewidth of ethylene oxide perturbed by nitrogen and carbon dioxide', *Journal of Quantitative Spectroscopy and Radiative Transfer* **42**(5), 395–398.

Jory, M. J., Bradberry, G. W., Cann, P. S. & Sambles, J. R. (1995), 'A surface-plasmon-based optical sensor using acousto-optics', *Measurement Science & Technology* **6**(8), 1193–1200.

Karube, I. (1992), Biosensors, *in* P. Sydenham & R.Thorn, eds, 'Handbook of Measurement Science - Volume 3: Elements of Change', John Wiley & Sons, Brisbane, chapter 40, pp. 1721–1758.

Kennedy, G. C. & Holser, W. (1966), Pressure-volume-temperature and phase relations of water and carbon dioxide, *in* S. Clark, ed., 'Handbook of Physical Constants', revised edn, The Geological Society of America, New York, chapter 16.

Kraus, J. D. (1991), *Electromagnetics*, McGraw Hill, Sydney.

Kress-Rogers, E. (1993), Chemosensors, biosensors and immunosensors, *in* E. Kress-Rogers, ed., 'Instrumentation and Sensors for the Food Industry', Butterworth Heinemann, Sydney, chapter 17, pp. 581–669.

Langdon, R. M. (1987), Resonator sensors - a review, *in* B. E. Jones, ed., 'Current Advances In Sensors', Adam Hilger, Bristol and Philadelphia, chapter 3, pp. 19–32.

Lewis, E. N., Treado, P. J. & Levin, I. W. (1993), 'A miniaturised, no-moving-parts raman spectrometer', *Applied Spectroscopy* **47**(5), 539–543.

Li, P. C. H. & Thompson, M. (1994), 'Potential carbon dioxide sensing based on recognition by *trans*-[Carbonylhydroxybis-(triphenylphosphine)rhodium(I)] deposited on acoustic wave devices', *The Analyst* **119**(9), 1947–1951.

Lide, D., ed. (2001), *CRC Handbook of Chemistry and Physics*, 82nd edn, CRC Press, New York.

Losos, J. (1998), Carbon dioxide as a pH-adjusting agent in the production of cheese (schedule 1107). Government Notices: Department of Health: Food and Drugs Act: Interim Marketing Authorisation.
URL: *http://www.hc-sc.gc.ca/food-aliment/english/publications/acts_and_regulations/ima/1107.html*

Lueptow, R. M. & Phillips, S. (1994), 'Acoustic sensor for determining combustion properties of natural gas', *Measurement Science & Technology* **5**(11), 1375–1381.

Macbeth, A. (1945), *Organic Chemistry for Medical, Intermediate Science and Pharmaceutical Students*, Longmans, Green and Co, London.

Madou, M. (2000), Chemical and biological sensors: Beyond batch fabrication, *in* Elsevier Science, ed., 'Abstract Book', 8th International Meeting on Chemical Sensors, Elsevier Science, p. 22.

Maxwell, A., Hancock, N. & Tran-Cong, T. (2000), Automated carbon dioxide measurement via miniaturised chemical reaction chambers under mechatronic control, *in* J. Billingsley, ed., 'Mechatronics and Machine Vision', Research Studies Press Ltd, Hertfordshire, England, pp. 135–142.

McGhee, J., Henderson, I., Korczynski, J. & Kulesza, W. (1998), 'The sensor effect tetrahedron: An extended transducer space', *Measurement* **24**, 217–236.

McMurray, H. N. (1992), 'Novel thin optical film sensor for the detection of carbon dioxide', *Journal of Material Chemistry* **2**(4), 401–406.

Meyerhoff, M., Pranitis, D., Yim, H., Chaniotakis, N. & Park, S. (1988), New anion and gas selective potentiometric sensors, *in* R. W. Murray, E. Dessy, Raymond, W. R. Heineman, J. Janata & W. R. Seitz, eds, 'Chemical Sensors and Microinstrumentation', American Chemical Society, Washington DC, chapter 2.

Mills, A. & Chang, Q. (1993), 'Fluorescence plastic thin-film sensor for carbon dioxide', *The Analyst* **118**(7), 839–843.

Mills, A., Chang, Q. & McMurray, N. (1992), 'Equilibrium studies on colorimetric plastic film sensors for carbon dioxide', *Analytical Chemistry* **64**, 1383–1389.

Mills, A. & Monaf, L. (1996), 'Thin plastic film colorimetric sensor for carbon dioxide: Effect of plasticizer on response', *The Analyst* **121**, 535–540.

Miura, N., Yao, S., Shimizu, Y. & Yamazoe, N. (1992), 'High-performance solid-electrolyte carbon dioxide sensor with a binary carbonate electrode', *Sensors and Actuators B (Physical)* **9**(8), 165–170.

Moseley, P. (1997), 'Solid state gas sensors', *Measurement Science and Technology* **8**(3), 223–237.

Nakamoto, K. (1970), *Infrared Spectra of Inorganic and Coordination Compounds*, 2 edn, John Wiley & Sons, Sydney, Australia.

Nylander, C. (1987), Chemical and biological sensors, *in* B. E. Jones, ed., 'Current Advances in Sensors', Adam Hilger, Bristol, chapter 13, pp. 133–148.

Patel, N. G., Makhija, K. K. & Panchal, C. J. (1994), 'Fabrication of carbon dioxide gas sensor and its alarm system using indium tin oxide (ITO) thin films', *Sensors and Actuators B* **21**(3), 193–197.

Peterson, K. I., Suenram, R. D. & Lovas, F. J. (1994), 'Hydration of carbon dioxide: The structure of $H_2O - H_2O - CO_2$ from microwave spectroscopy', *The Journal of Chemical Physics* **1**(1), 106–117.

Pinchas, S. & Laulicht, I. (1971), *Infrared Spectra of Labelled Compounds*, Academic Press, New York.

Pride, R. D. (1993), Advanced sensors for the gas industry, *in* K. T. V. Grattan & A. T. Augousti, eds, 'Sensors VI - Technology, Systems and Applications', Institute of Physics Publishing, Bristol, chapter A, pp. 3–14.

Rife, J., Bell, M., Horwitz, J., Kabler, M., Auyeung, R. & Kim, W. (1986), 'Miniature valveless ultrasonic pumps and mixers', *Sensors and Actuators A: Physical* **86**(1-2), 135–140.

Robinson, J. W., ed. (1980), *CRC Handbook of Spectroscopy*, Vol. 2, CRC Press, Florida.

Severinghaus, J. & Bradley, A. (1958), *Journal of Applied Physics* **13**, 515–520.

Silverstein, R. M., Bassler, G. C. & Morrill, T. C. (1974), *Spectrographic identification of organic compounds*, 3 edn, John Wiley & Sons, Brisbane, Australia.

Son, V., Luc, T., Lan, T., Pho, P. & Nga, N. (2001), CO_2 sensor using perovskite oxide/NASICON structure, *in* 'Extended Abstracts of the Fourth German - Vietnamese Seminar on Physics and Engineering (GVS4)', Dresden, pp. 153–155, June 5–9.

Stanley, W. (1990), *Operational Amplifiers With Linear Integrated Circuits*, 2nd edn, Merrill Publishing Company, Singapore.

Stein, P. (1991), *The Unified Approach to the Engineering of Measurement Systems*, Stein Engineering Services Inc., Phoenix, USA.

Straughan, B. (1976), Infrared and raman spectroscopy, *in* B. Straughan & S. Walker, eds, 'Spectroscopy', John Wiley & Sons, New York, chapter 4.

Sydenham, P., Hancock, N. & Thorn, R. (1993), *Introduction to Measurement Science and Engineering*, John Wiley & Sons Ltd, Brisbane, Australia.

Tran, C. D. & Lu, J. (1995), 'Characterization of the acousto-optic tunable filter for the ultraviolet and visible regions and development of an acousto-optic tunable filter based rapid scanning detector for high-performance liquid chromatography', *Analytica Chimica Acta* **314**, 57–66.

Tsionsky, M. & Lev, O. (1995), 'Electrochemical composite carbon–ceramic gas sensors: Introduction and oxygen sensing', *Analytical Chemistry* **67**(14), 2409–2414.

Uehara, P. K. (1991), Remote detection of methane using a 1.66μm diode laser, Technical report, Anritsu Corp. Optoelectronics Technology Today.

Uttamial, M. & Walt, D. (1995), 'A fibre-optic carbon dioxide sensor for fermentation monitoring', *Biotechnology* **13**(6), 597–601.

Van Duyn, D. & Middelhoek, S. (1991), The thermodynamic classification of solid state sensors as a basis for a finite element simulation tool, *in* 'International Workshop on the Fundamentals of Sensor Science', Vrije Universiteit Brussel, Belgium.

Watts, R. S. (1983), Transducer practice: Chemical analysis, *in* P. H. Sydenham, ed., 'Handbook of Measurement Science', Vol. 2 Practical Fundamentals, John Wiley & Sons, Brisbane, Australia, chapter 27, pp. 1173–1208.

Weigl, B. H., Holobar, A., Trettnak, W., Klimant, I., Kraus, H., O'Leary, P. & Wolfbeis, O. S. (1994), 'Optical triple sensor for measuring pH, oxygen, and carbon dioxide', *Journal of Biotechnology* **32**(2), 127–138.

Weigl, B. H. & Wolfbeis, O. S. (1994), 'Capillary optical sensors', *Analytical Chemistry* **66**(20), 3323–3327.

Weldon, V., Phelan, P. & Hegarty, J. (1993), 'Methane and carbon dioxide sensing using a D.B.F. laser diode operating at 1.64 μm', *Electronic Letters* **29**(6), 560–561.

White, N. & Turner, J. (1997), 'Thick-film sensors: Past, present and future', *Measurement Science and Technology* **8**(1), 1–20.

Wolfbeis, O. & Weis, L. (1988), 'Fiber-optic fluorosensor for oxygen and carbon dioxide', *Analytical Chemistry* **60**, 2028–2030.

Wolfe, G. C. (1993), Optimal Control for the Storage of Horticultural Produce, PhD thesis, University of Queensland, Brisbane, Australia.

Appendix A

Electrical & Mechanical Design Information

A.1 Chemical Containment Cell Design Specifications

- 'Teardrop' cell mechanical drawing.
- 'Oval' cell mechanical drawing.
- 'Triangular' cell mechanical drawing.
- 'Circular' cell mechanical drawing.
- Optical alignment PCBs for 'teardtop' cell.
- Optical alignment PCBs for 'oval' cell.
- Optical alignment PCBs for 'triangular' cell.
- Optical alignment PCBs for 'circular' cell.
- Generic optical alignment PCBs.

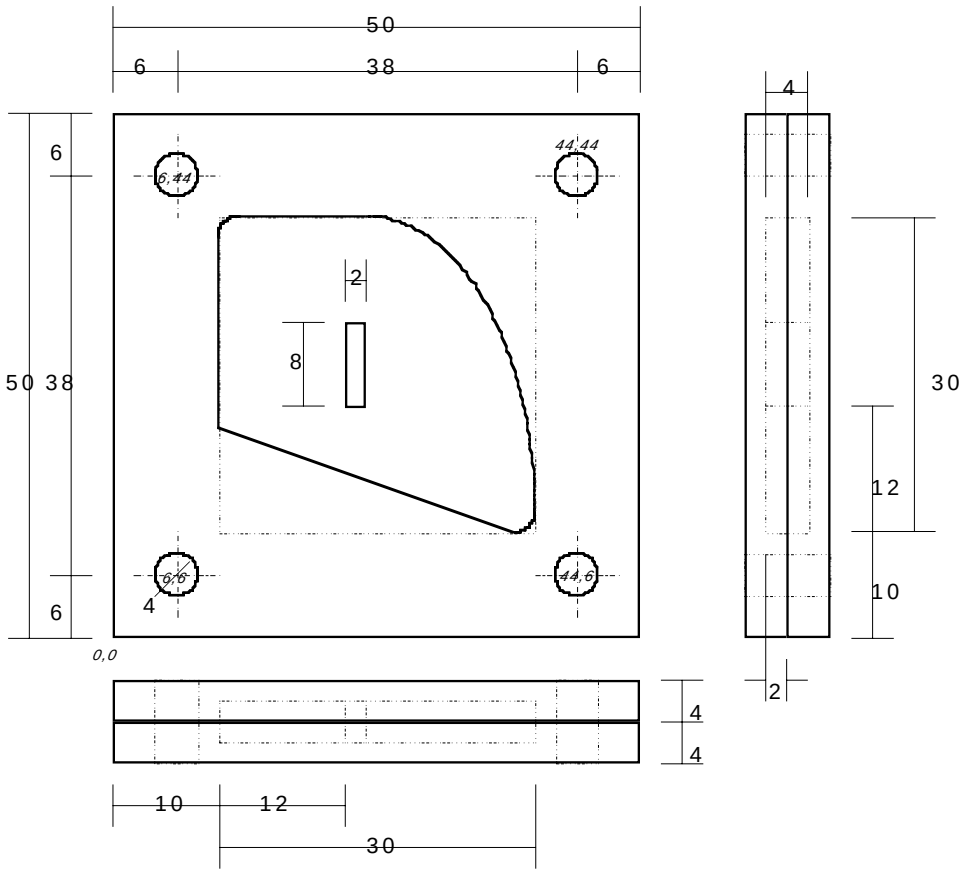

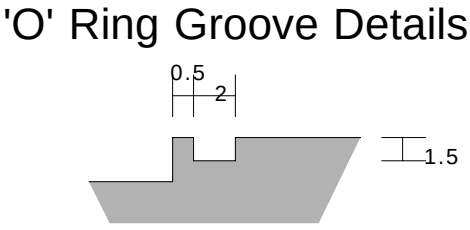

Figure A.1: Mechanical drawing for the 'teardrop' cell (units in mm). Also shown are the coordinates (in mm) for points within the cell as required by the numerically controlled (NC) milling machine, e.g. (4,66) for the top left drill hole.

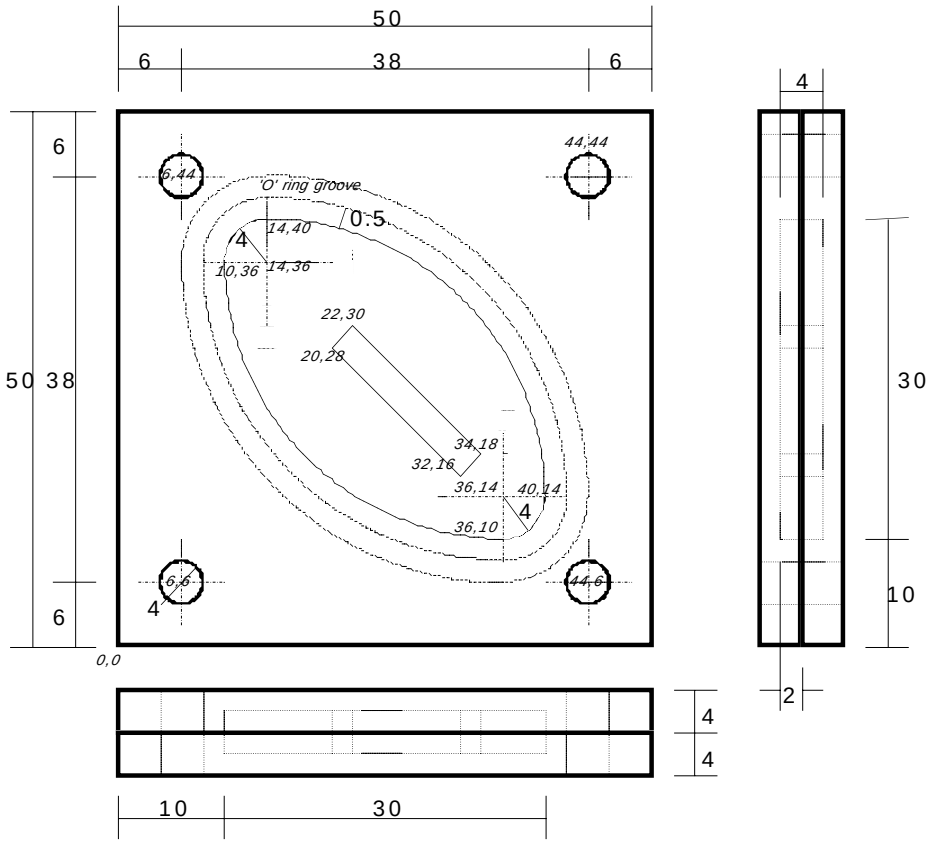

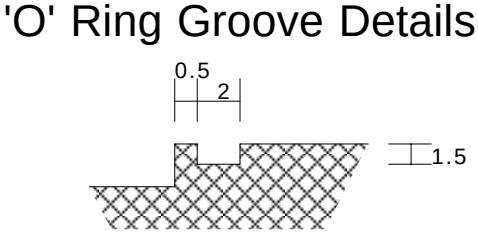

Figure A.2: Mechanical drawing for the 'oval' cell (units in mm). Also shown are the coordinates (in mm) for points within the cell.

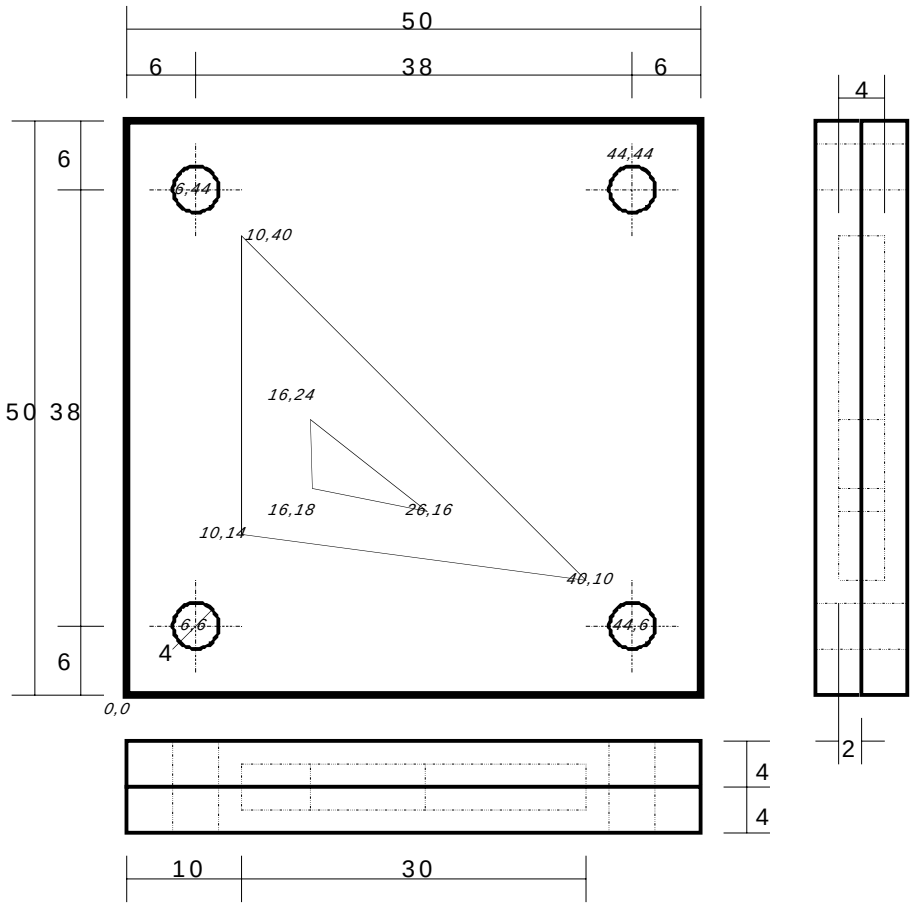

'O' Ring Groove Details

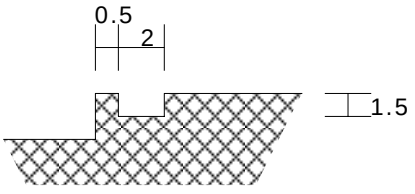

Figure A.3: Mechanical drawing for the 'triangular' cell (units in mm). Also shown are the coordinates (in mm) for points within the cell.

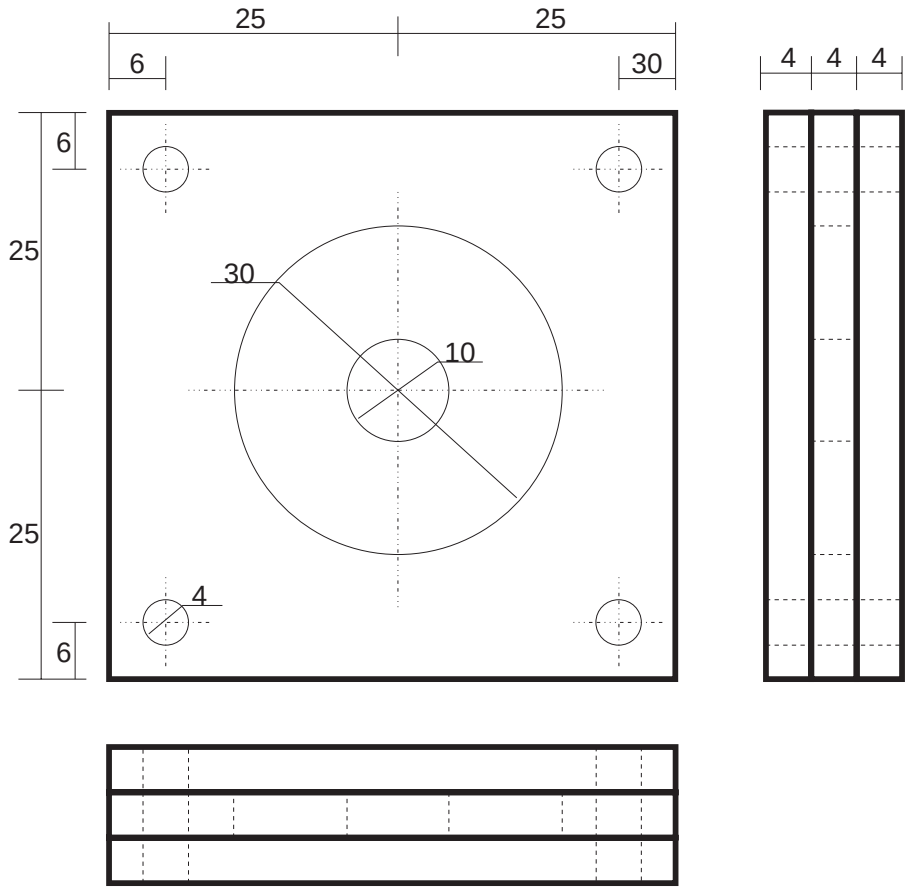

Figure A.4: Mechanical drawing for the 'circular' cell (units in mm). The "O" ring groove construction method is the same as presented in Figure A.3 and milled into the two outer plates. The inner 10mm 'island' is glued to one of the outer plates.

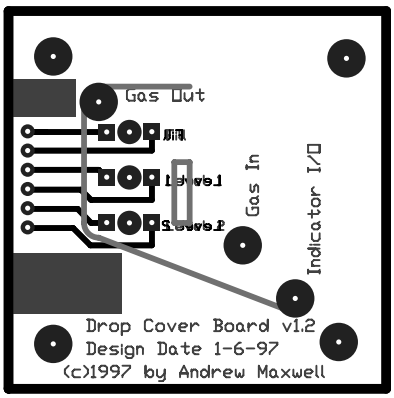

DROP Check Plot

(a)

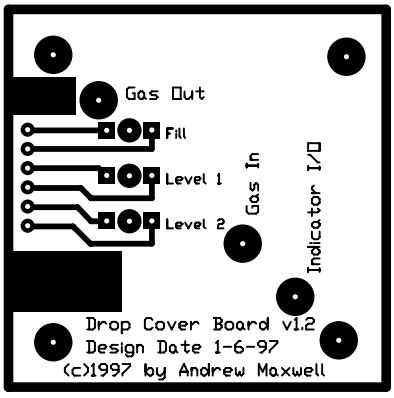

DROP Top Layer

(b)

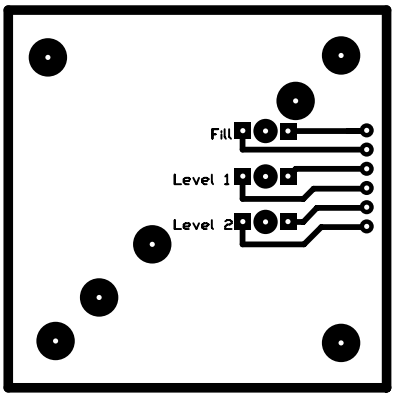

DROP Bottom Layer

(c)

Figure A.5: Optical alignment PCBs for the 'teardrop' cell. (a) overlay of both PCBs, (b) front PCB, (c) rear PCB

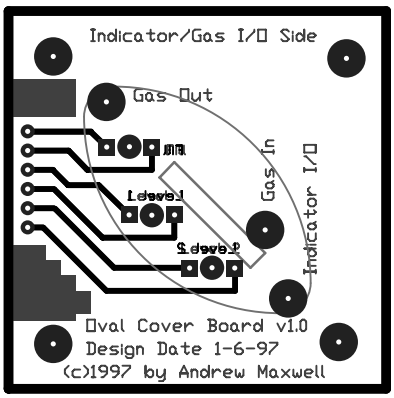

OVAL Check Plot

(a)

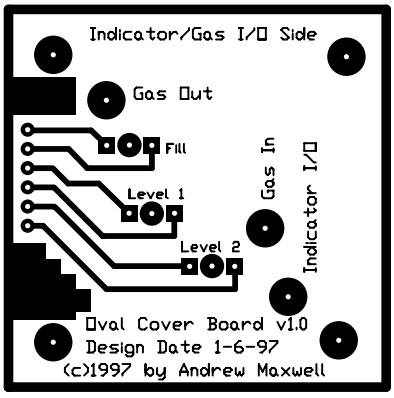

OVAL Top Layer

(b)

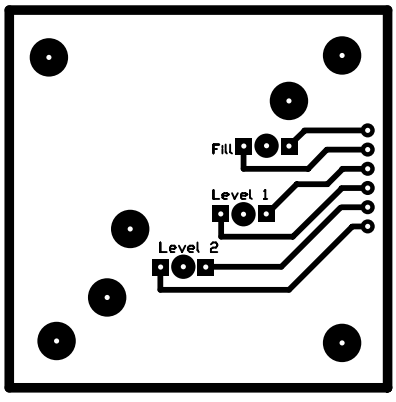

OVAL Bottom Layer

(c)

Figure A.6: Optical alignment PCBs for the 'oval' cell. (a) overlay of both PCBs, (b) front PCB, (c) rear PCB

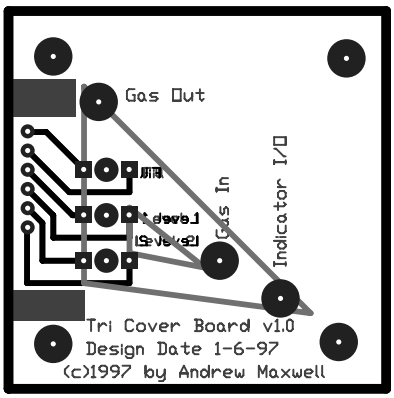

TRI Check Plot

(a)

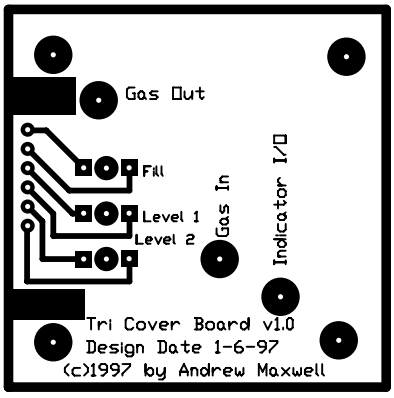

TRI Top Layer

(b)

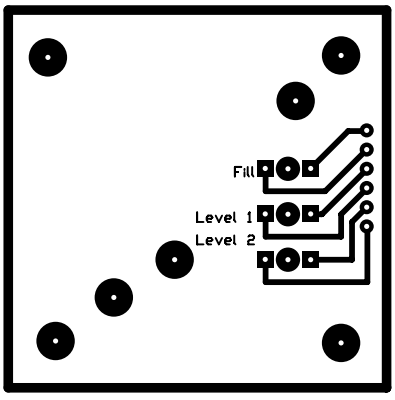

TRI Bottom Layer

(c)

Figure A.7: Optical alignment PCBs for the 'triangular' cell. (a) overlay of both PCBs, (b) front PCB, (c) rear PCB

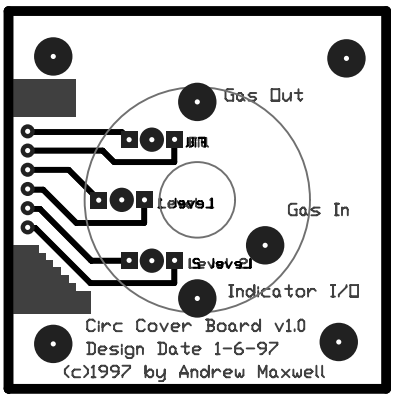

CIRC Check Plot

(a)

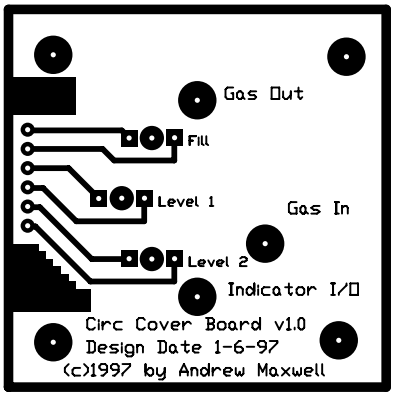

CIRC Top Layer

(b)

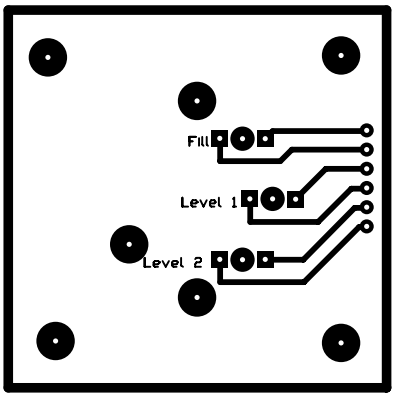

CIRC Bottom Layer

(c)

Figure A.8: Optical alignment PCBs for the 'circular' cell. (a) overlay of both PCBs, (b) front PCB, (c) rear PCB

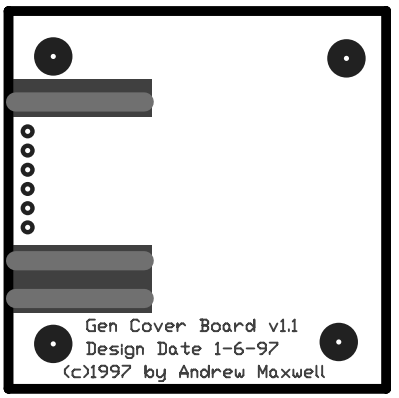

GEN2 Check Plot

(a)

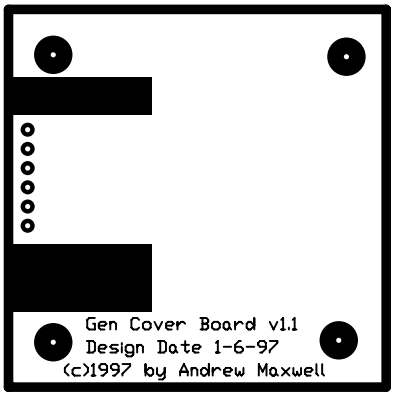

GEN2 Top Layer

(b)

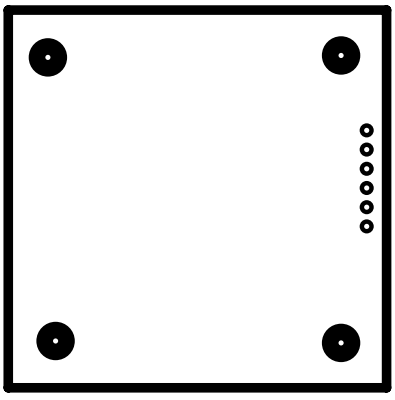

GEN2 Bottom Layer

(c)

Figure A.9: Optical alignment PCBs for 'generic' use. (a) overlay of both PCBs, (b) front PCB, (c) rear PCB

A.2 Mk.I - Schematic and PCB Artwork

- Main Mk.I microcontroller board schematic and PCB.
- Serial board PCB.
- Motor control board (v1.0) schematic.
- Motor control board (v2.0) schematic and PCB.
- Optics control board (v1.2) schematic and PCB.
- Optics control board (v2.0) schematic and PCB.
- Power supply and distribution schematic.

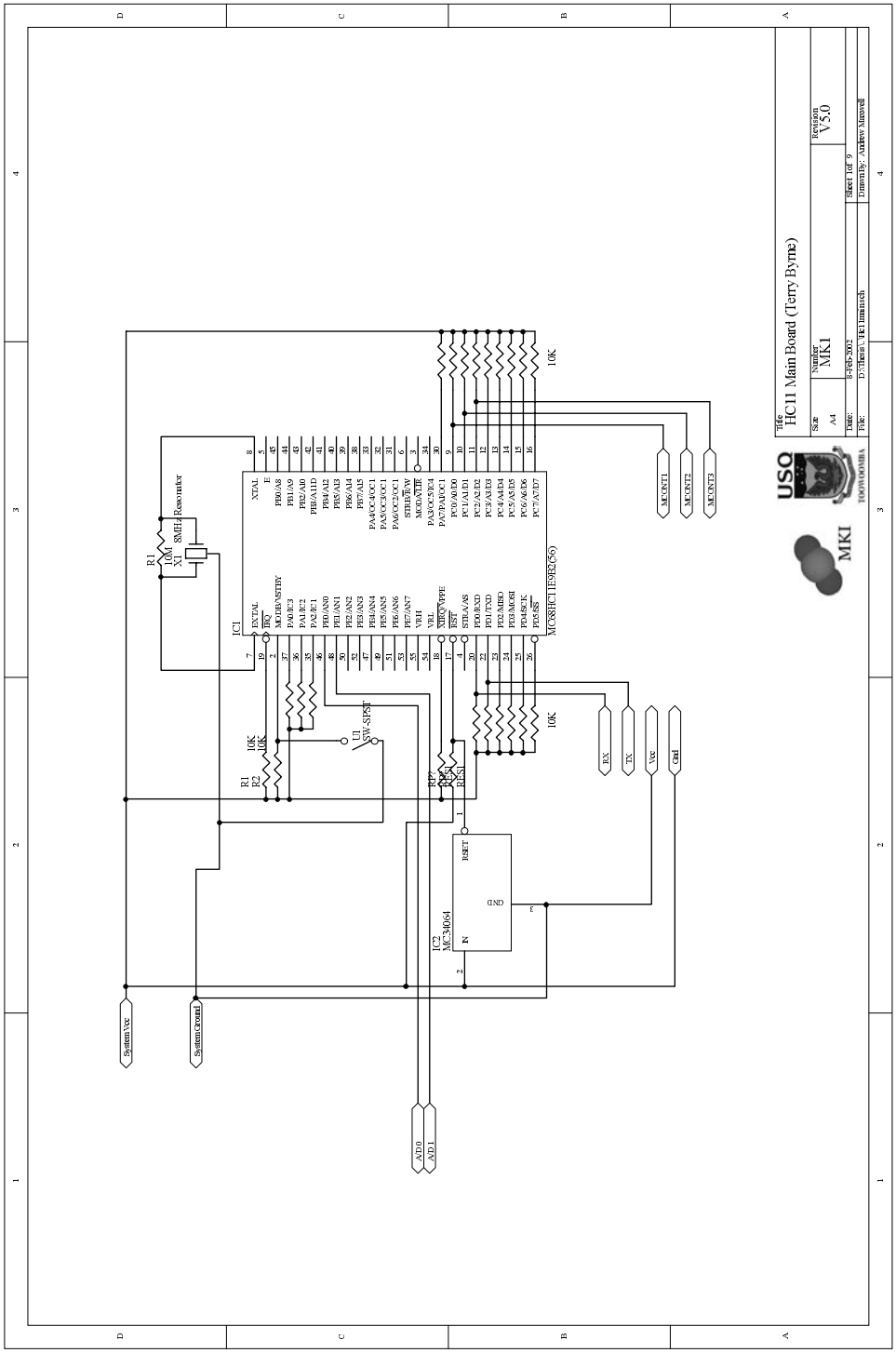

Figure A.10: Main microcontroller board schematic (Originally design by Terry Byrne, Faculty of Engineering & Surveying, University of Southern Queensland, Toowoomba, Queensland, 4350, Australia). A more legible version is available on the accompanying CDROM.

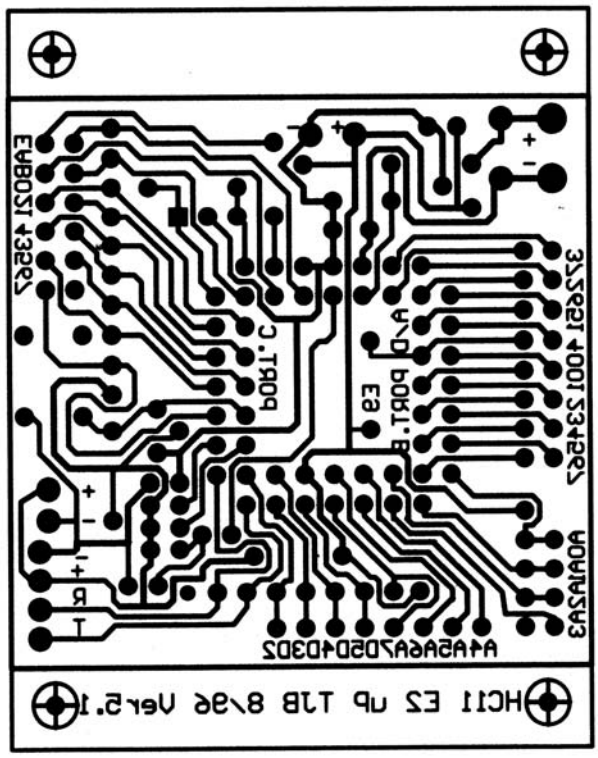

(a) PCB Artwork.

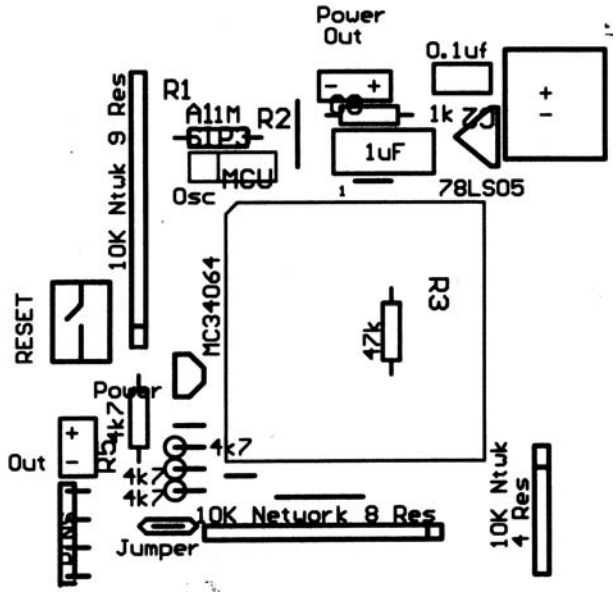

(b) Component locations.

Figure A.11: Main microcontroller PCB (Originally design by Terry Byrne, Faculty of Engineering & Surveying, University of Southern Queensland, Toowoomba, Queensland, 4350, Australia).

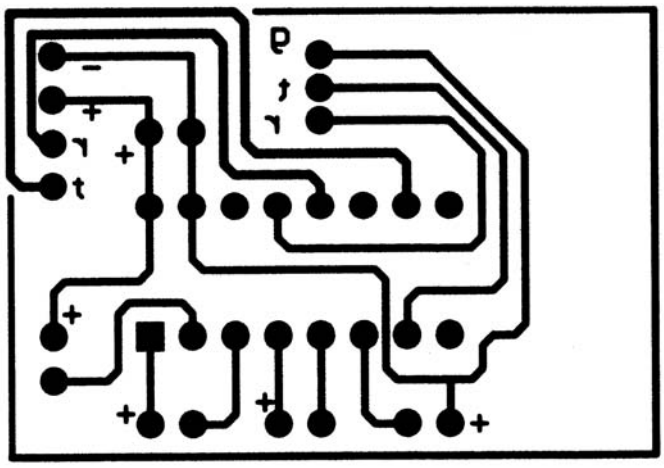

(a) PCB Artwork.

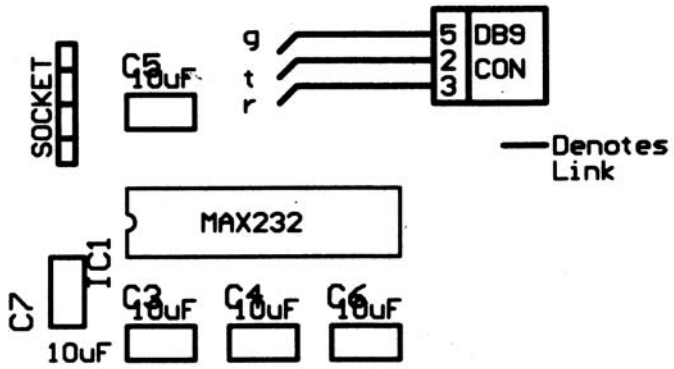

(b) Component locations.

Figure A.12: Serial interface PCB (Originally design by Terry Byrne, Faculty of Engineering & Surveying, University of Southern Queensland, Toowoomba, Queensland, 4350, Australia).

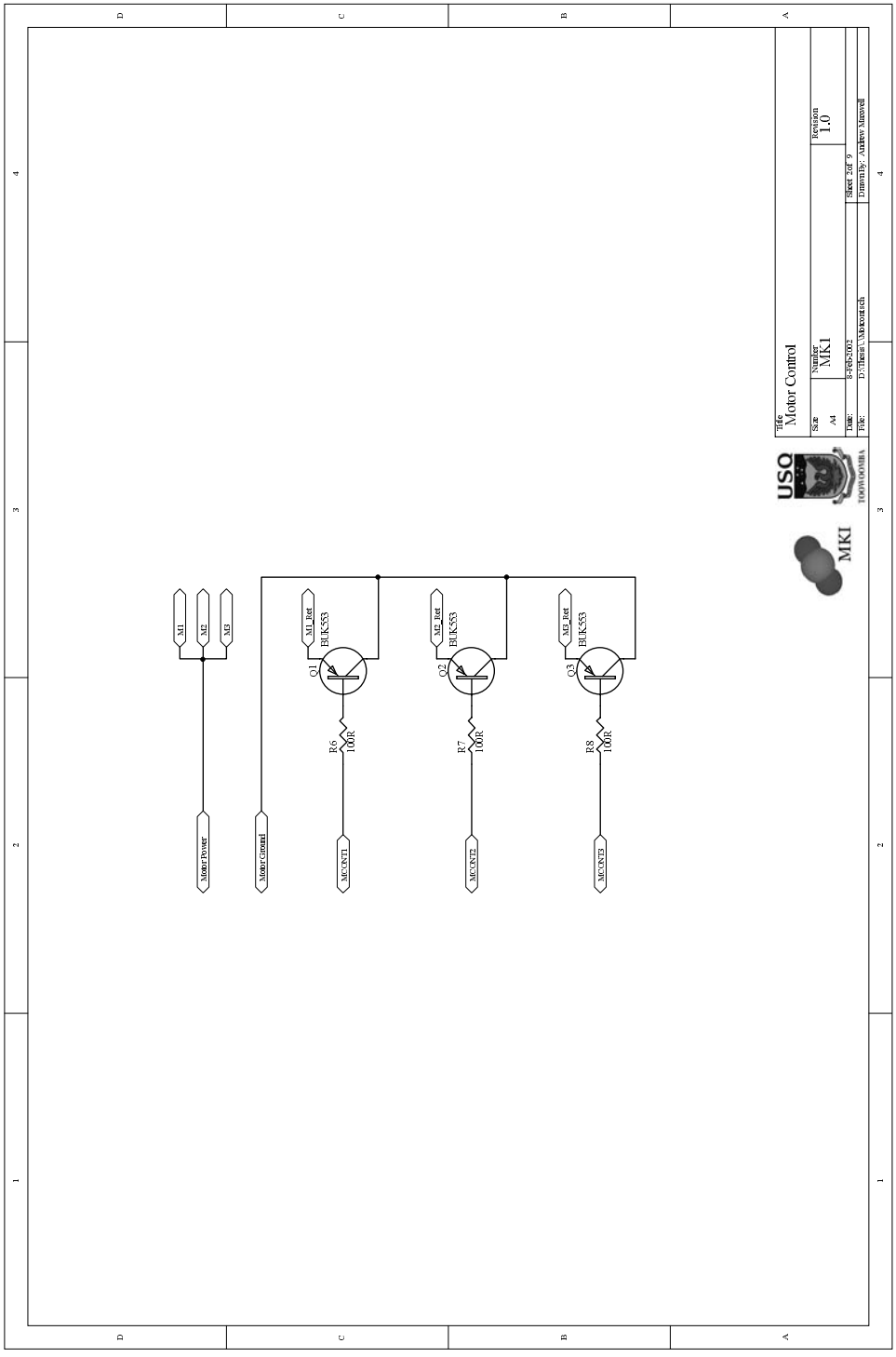

Figure A.13: Motor control sub-system schematic (v1.0).

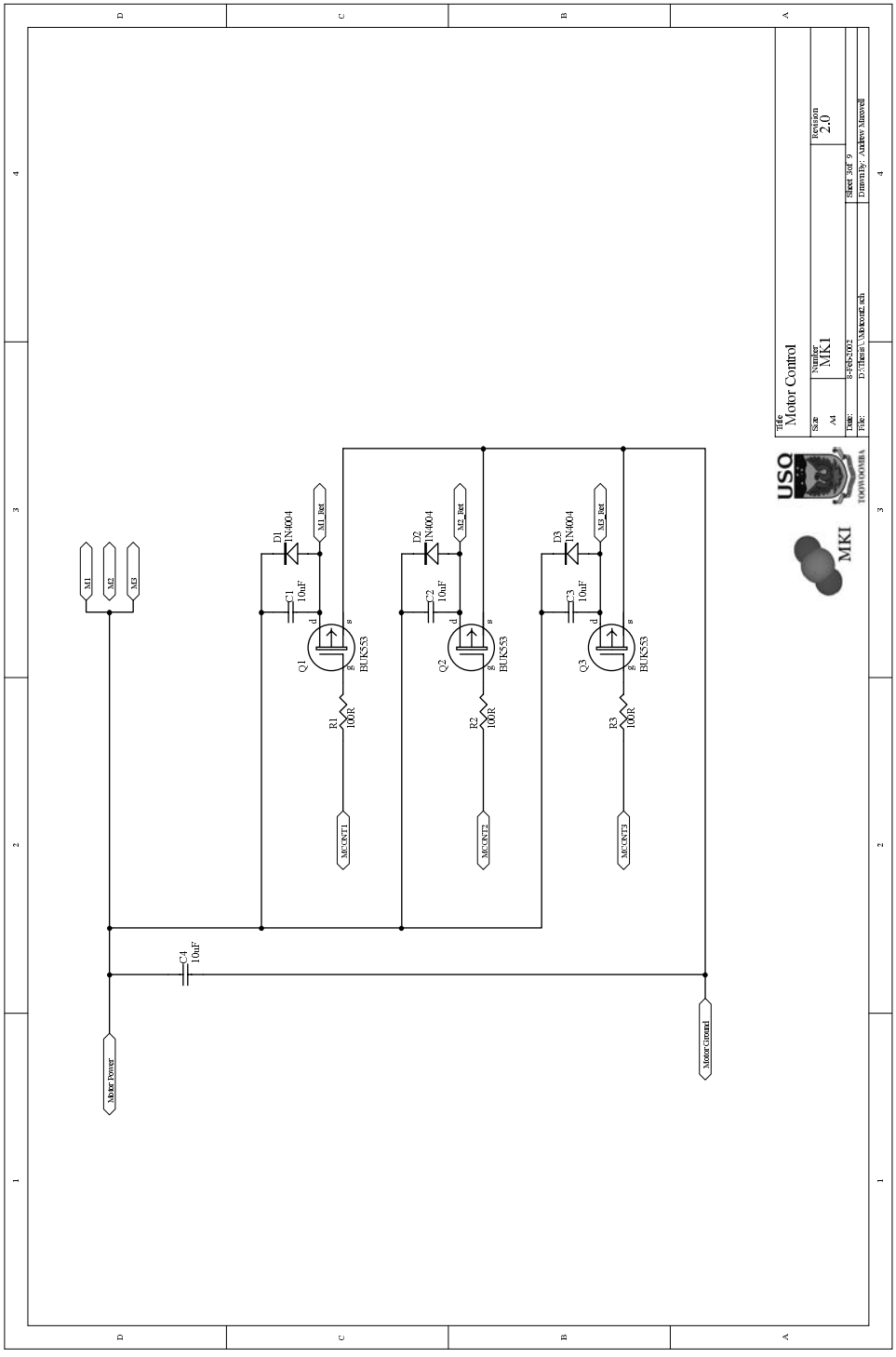

Figure A.14: Motor control sub-system schematic (v2.0).

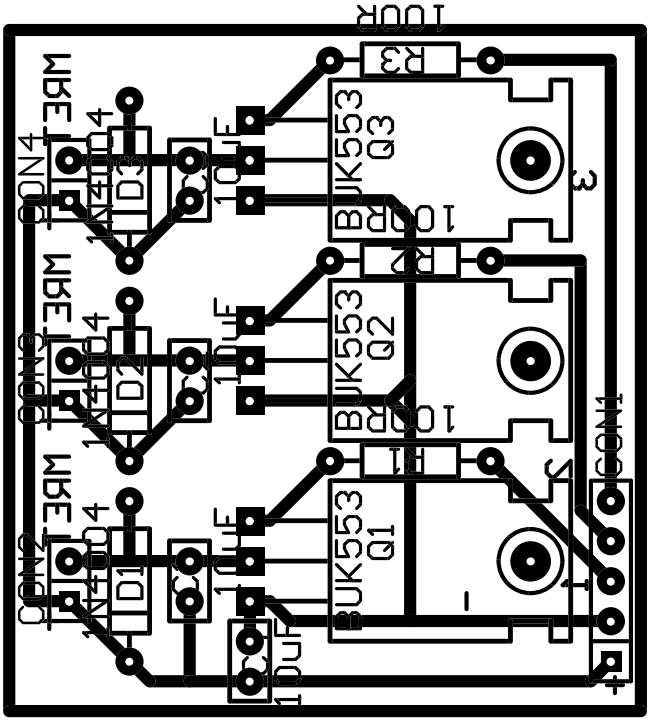

Figure A.15: Motor control sub-system PCB (v2.0).

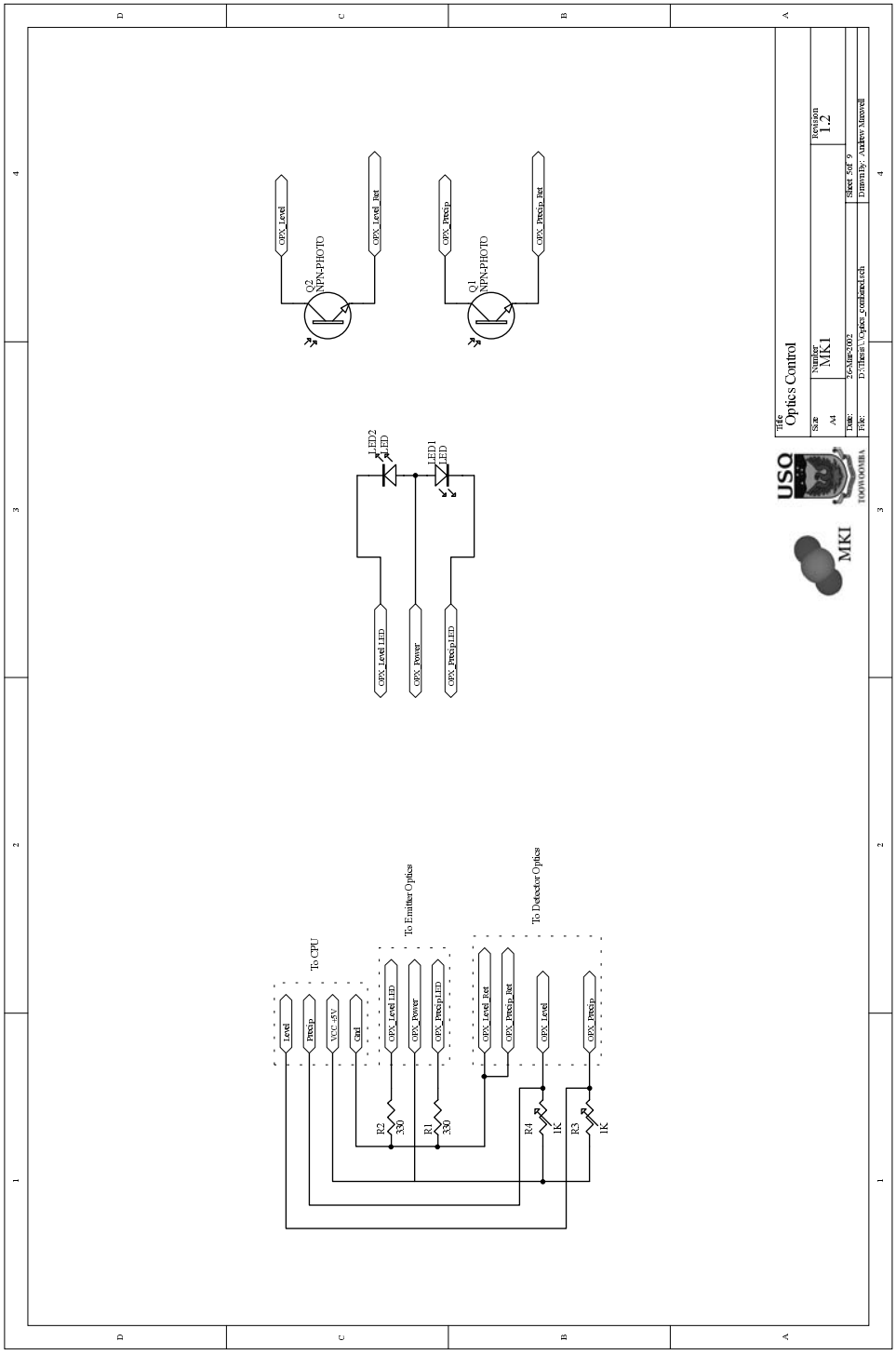

Figure A.16: Optics control sub-system schematic (v1.2).

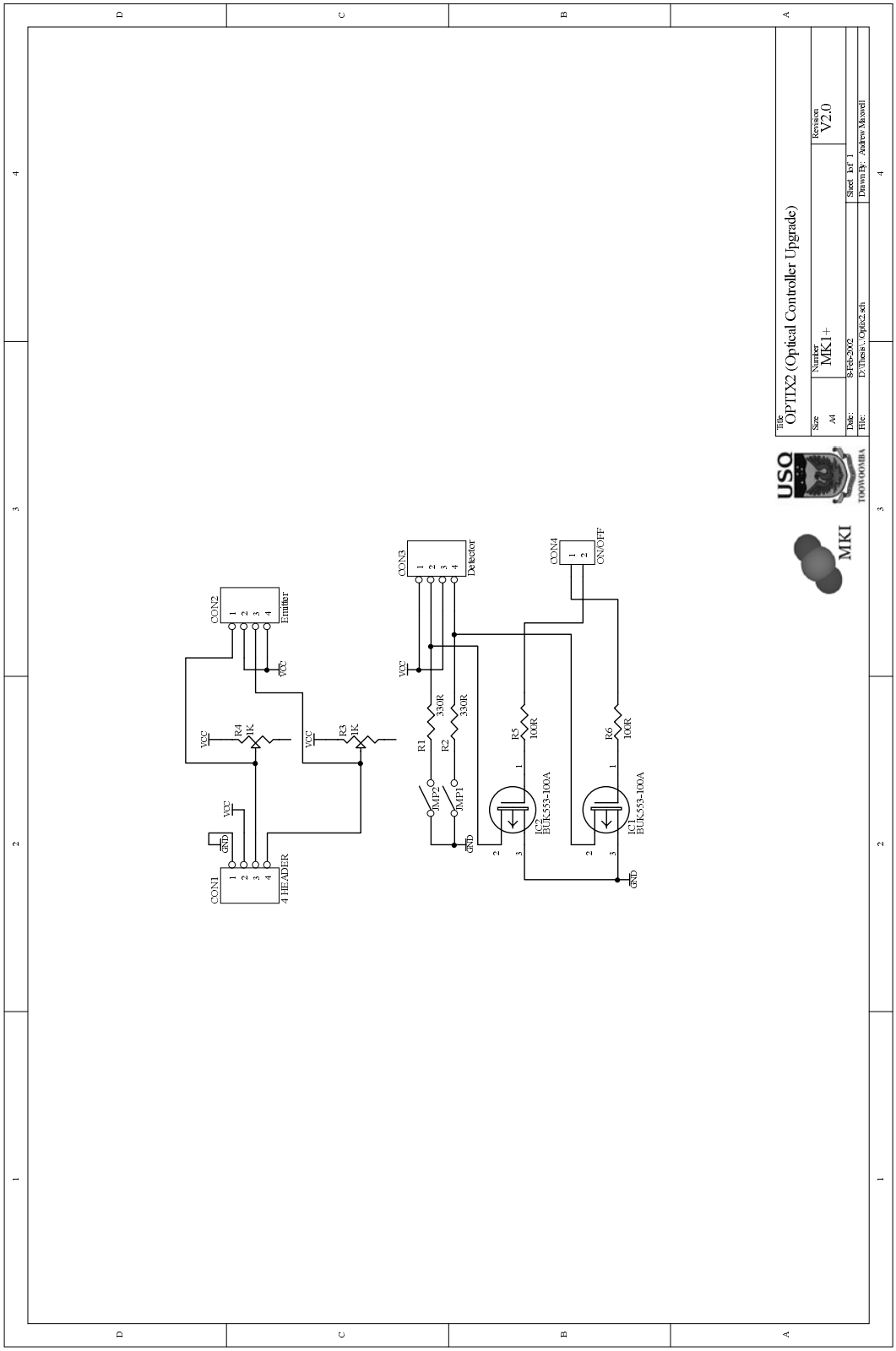

Figure A.17: Optics control sub-system schematic (v2.0).

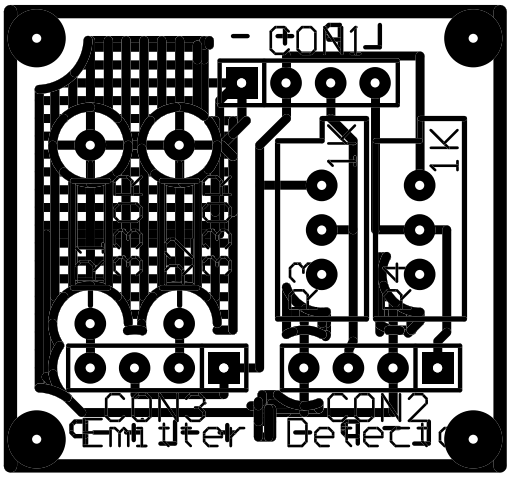

Figure A.18: Optics control sub-system PCB (v1.2).

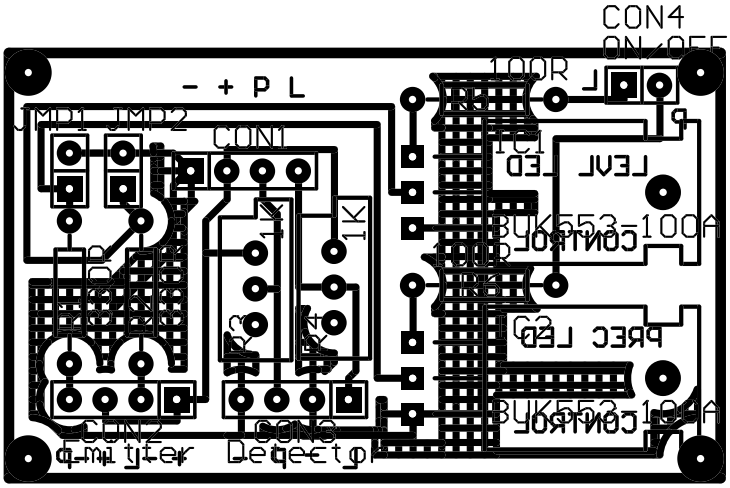

Figure A.19: Optics control sub-system PCB (v2.0).

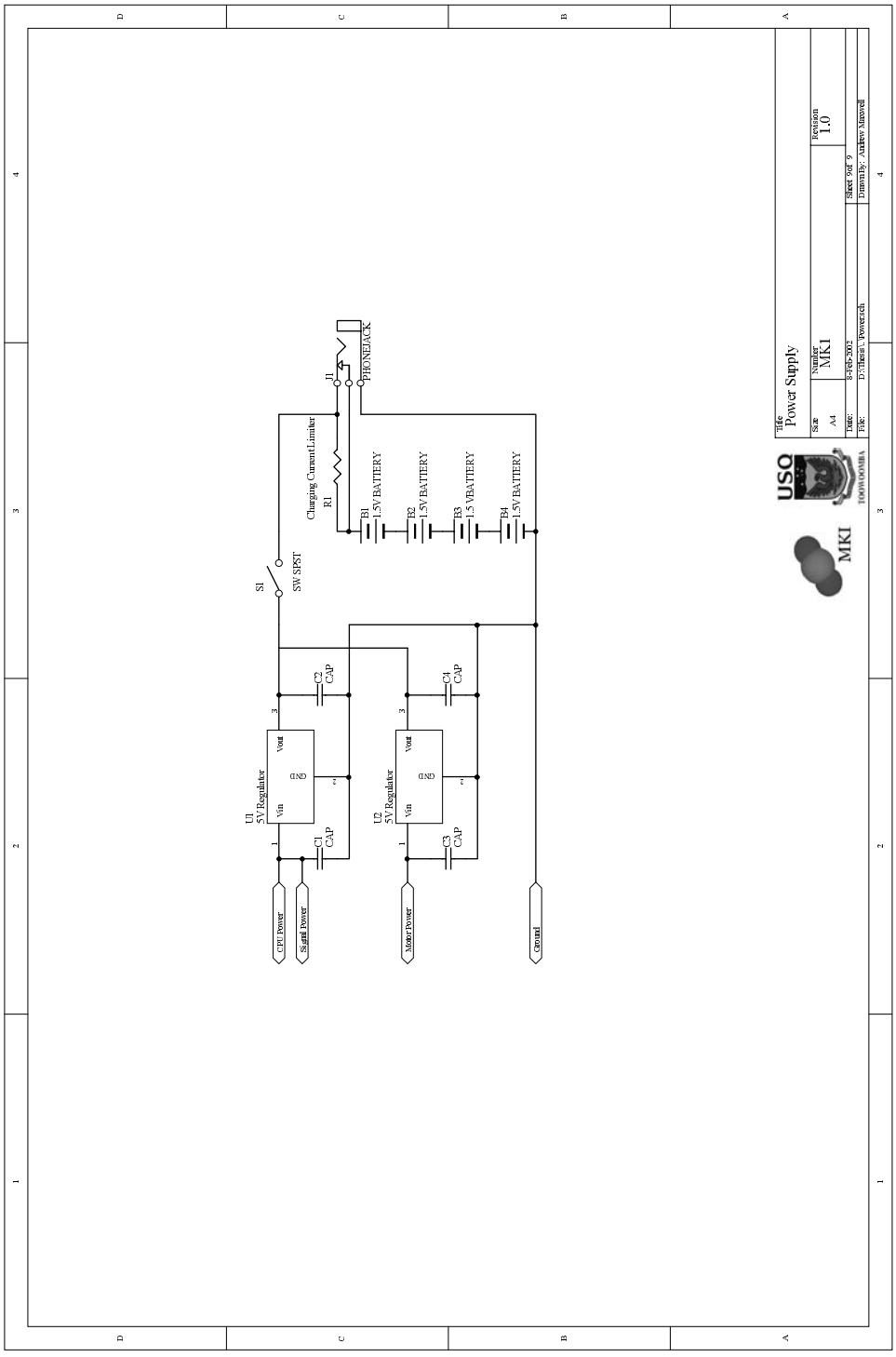

Figure A.20: Power supply sub-system schematic.

A.2.1 Additional Schematic and PCB Artwork

- External A/D converter and MUX testing board schematic.
- External analog interfacing sub-system (v1) schematic.
- External analog interfacing sub-system (v2) schematic.
- External analog interfacing sub-system (v3) schematic.

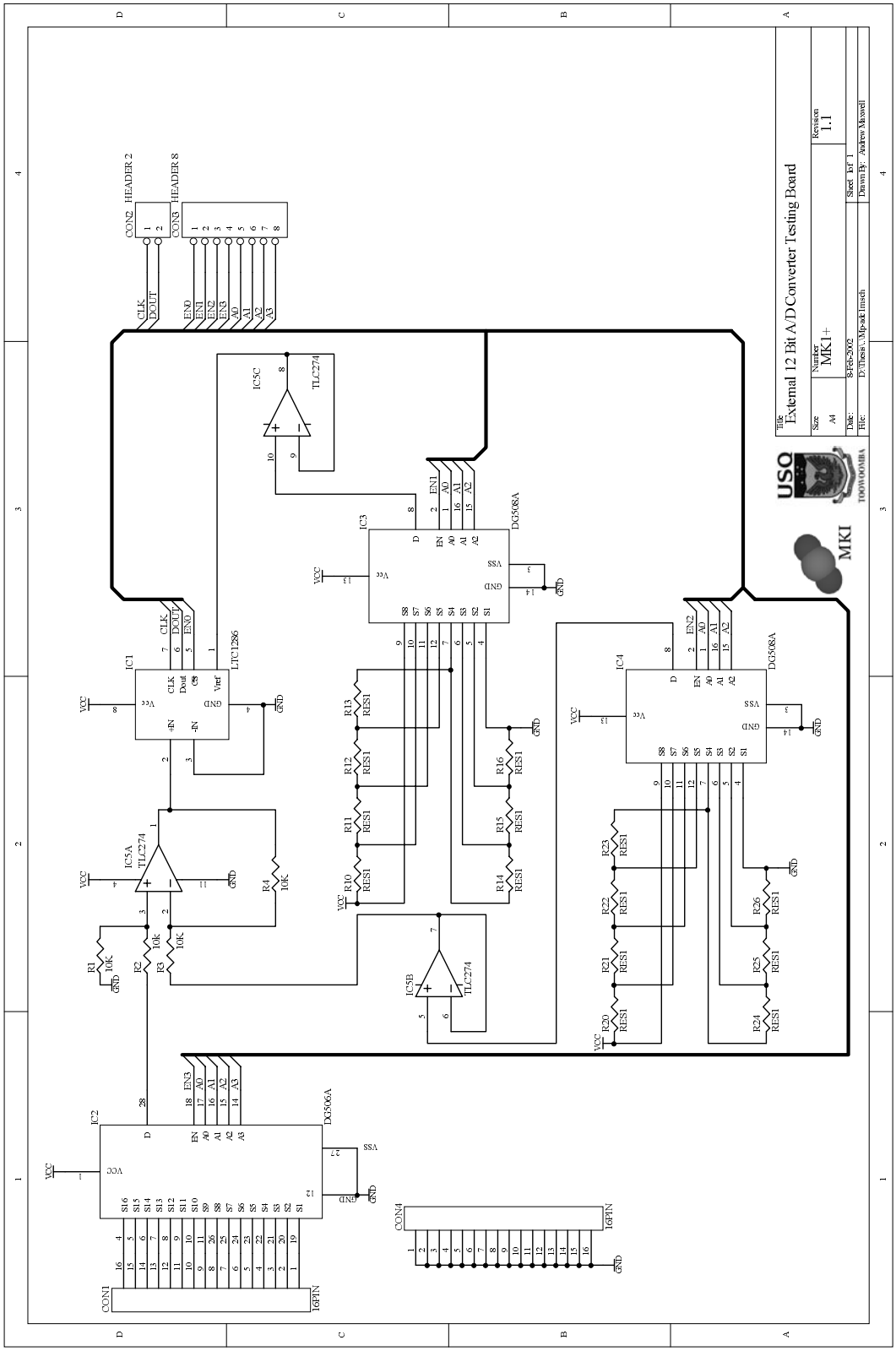

Figure A.21: External 12 bit A/D Converter and multiplexer testing board schematic. This was used as an external expansion board to the main Mk.I microcontroller board (Figure A.10) to test the 12 bit A/D, 16 channel multiplexer, and offset differential amplifier before implementing in the Mk.II prototype instrument.

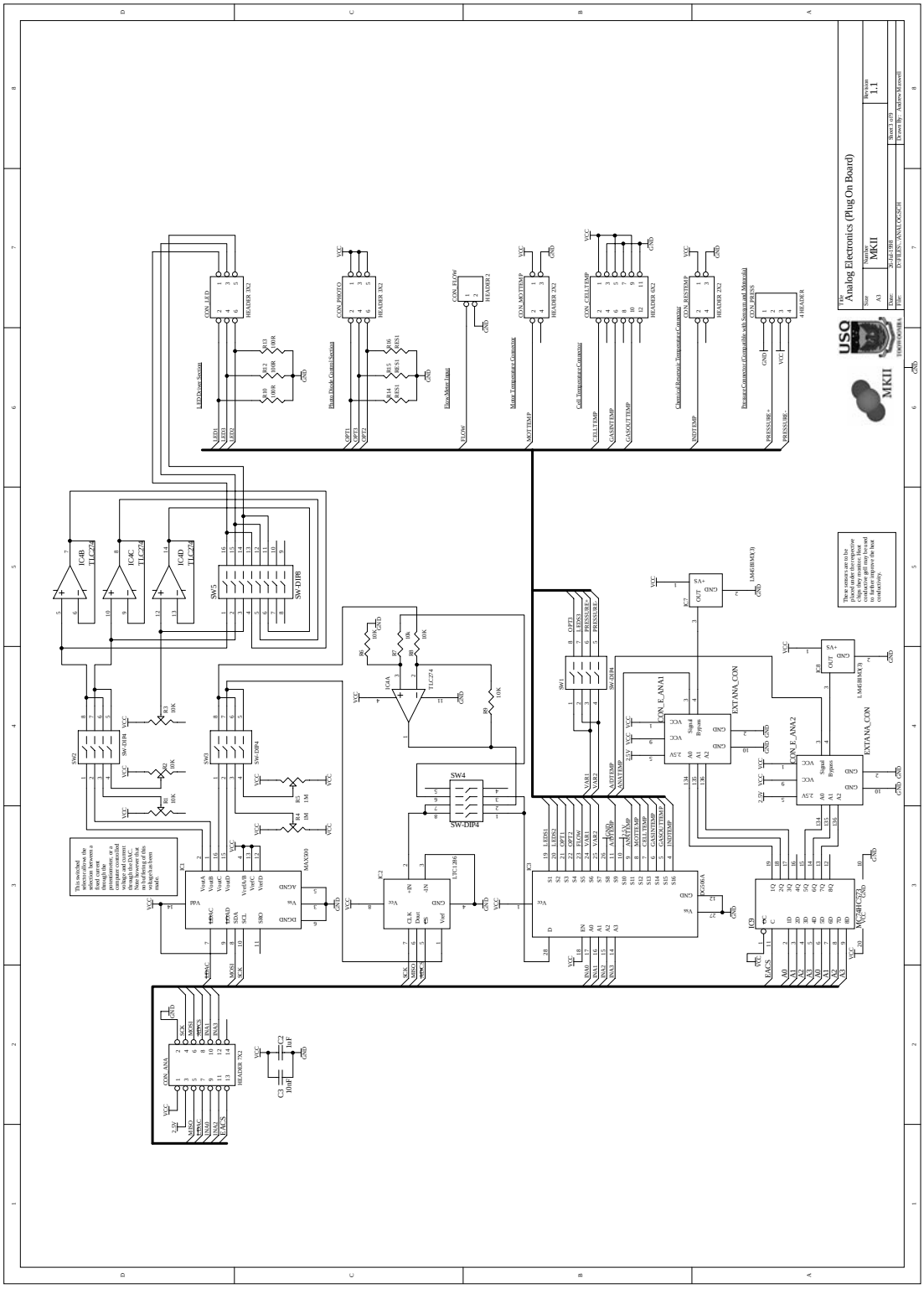

Figure A.22: External analog interfacing sub-system schematic (v1). This was used as an external expansion board to the main Mk.I microcontroller board (Figure A.10) to test the 12 bit A/D, 16 channel multiplexer, and offset differential amplifier before implementing in the Mk.II prototype instrument.

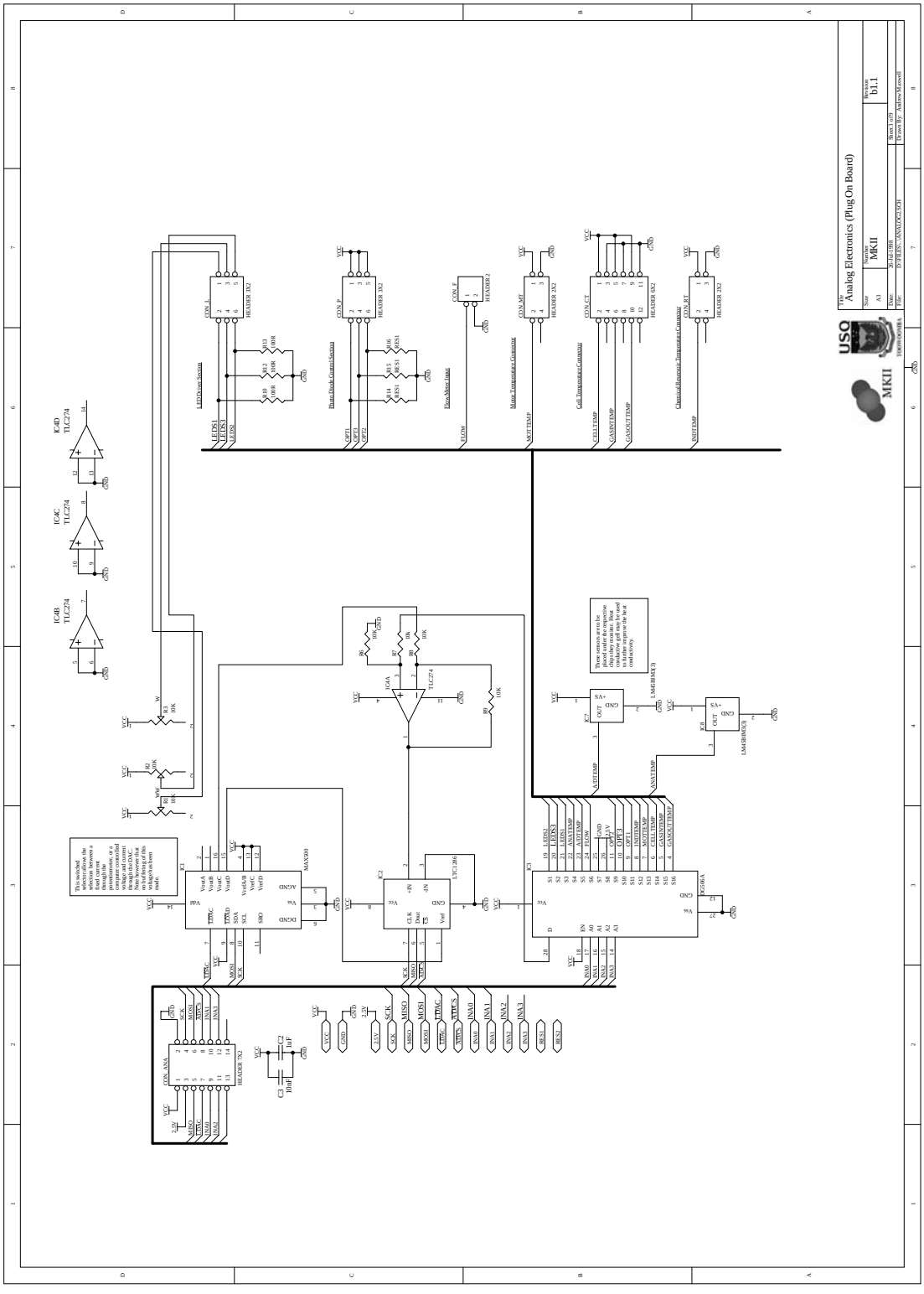

Figure A.23: External analog interfacing sub-system schematic (v2). This was used as an external expansion board to the main Mk.I microcontroller board (Figure A.10) to test the 12 bit A/D, 16 channel multiplexer, and offset differential amplifier before implementing in the Mk.II prototype instrument.

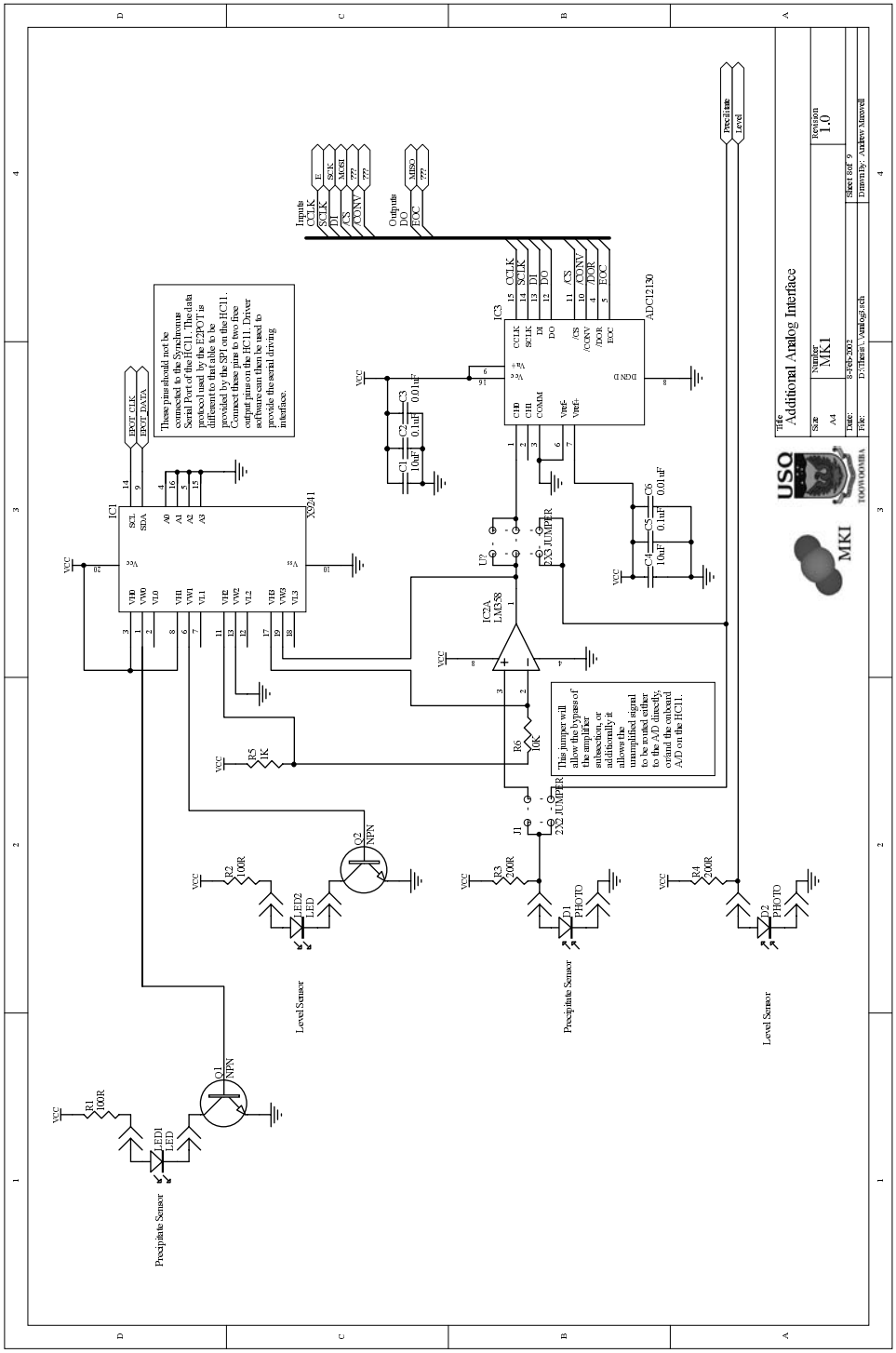

Figure A.24: External analog interfacing sub-system schematic (v3). This was used as an external expansion board to the main Mk.I microcontroller board (Figure A.10) to test the 12 bit A/D, 16 channel multiplexer, and offset differential amplifier before implementing in the Mk.II prototype instrument.

A.3 Mk.II - Schematic and PCB Artwork

- Main Mk.II microcontroller board schematic and PCB.
- Keyboard and LCD display board schematic and PCB.
- External optical cable schematic.
- External temperature cable schematic.

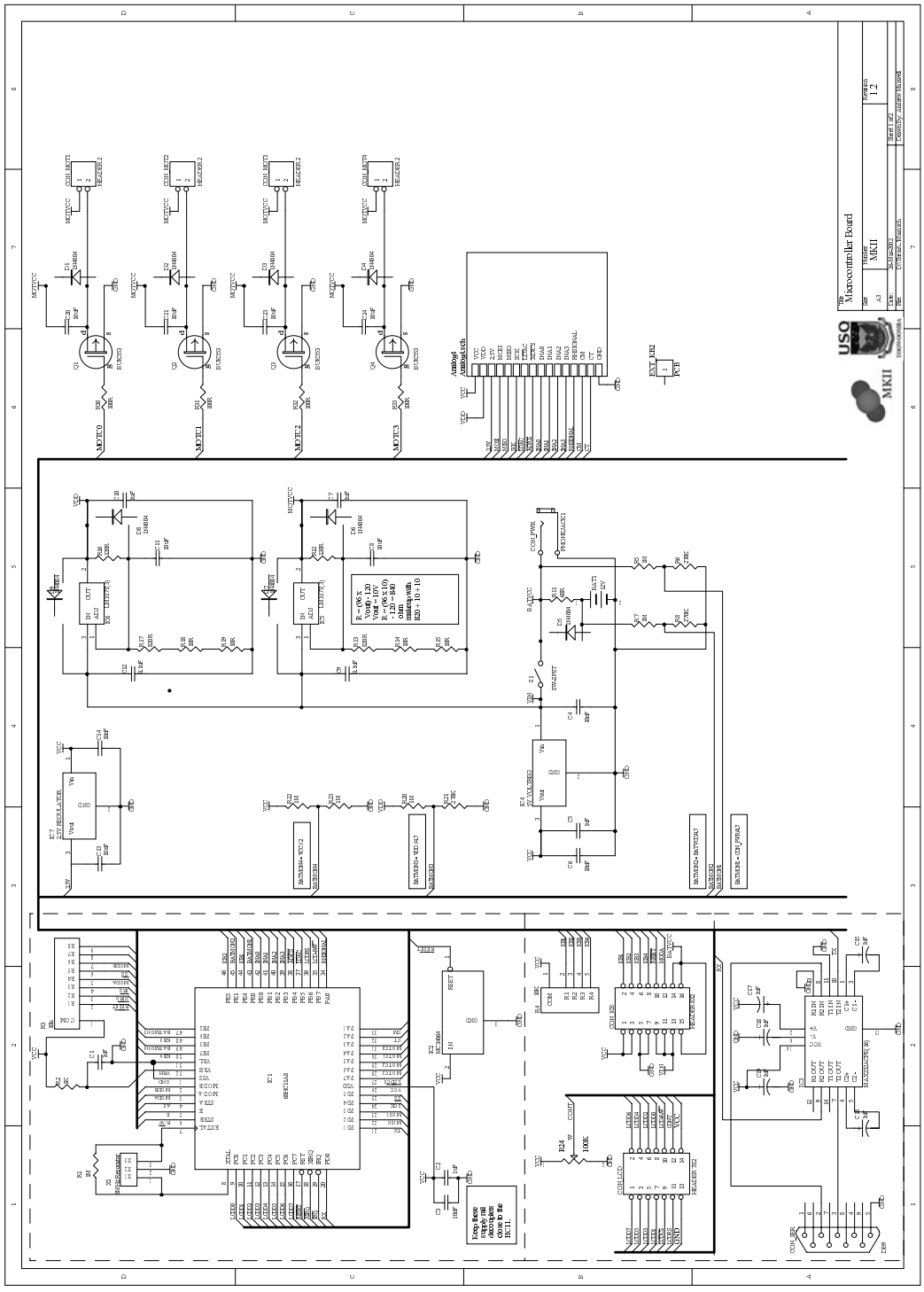

Figure A.25: Main Mk.II microcontroller board schematic.

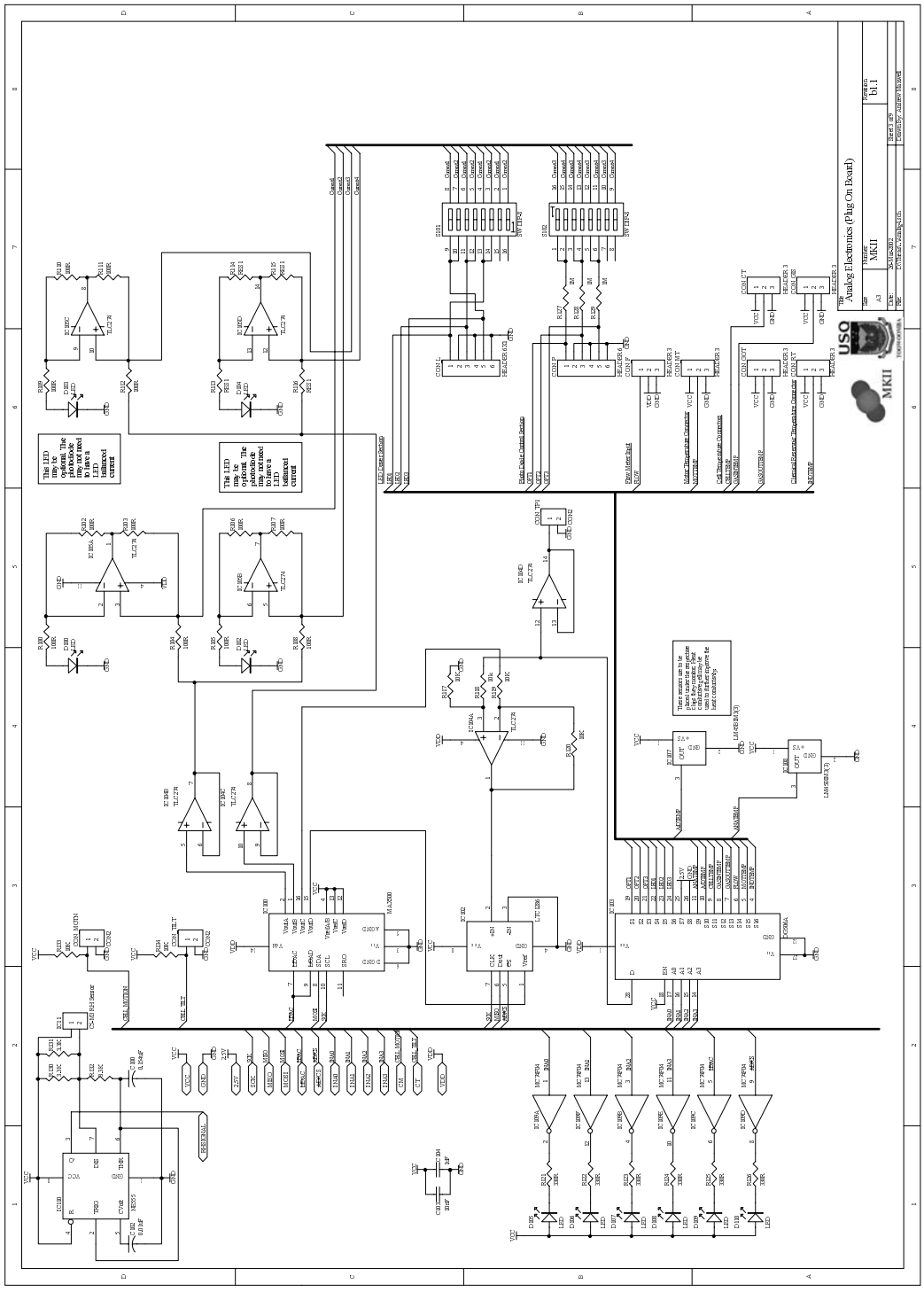

Figure A.26: Analogue electronics schematic.

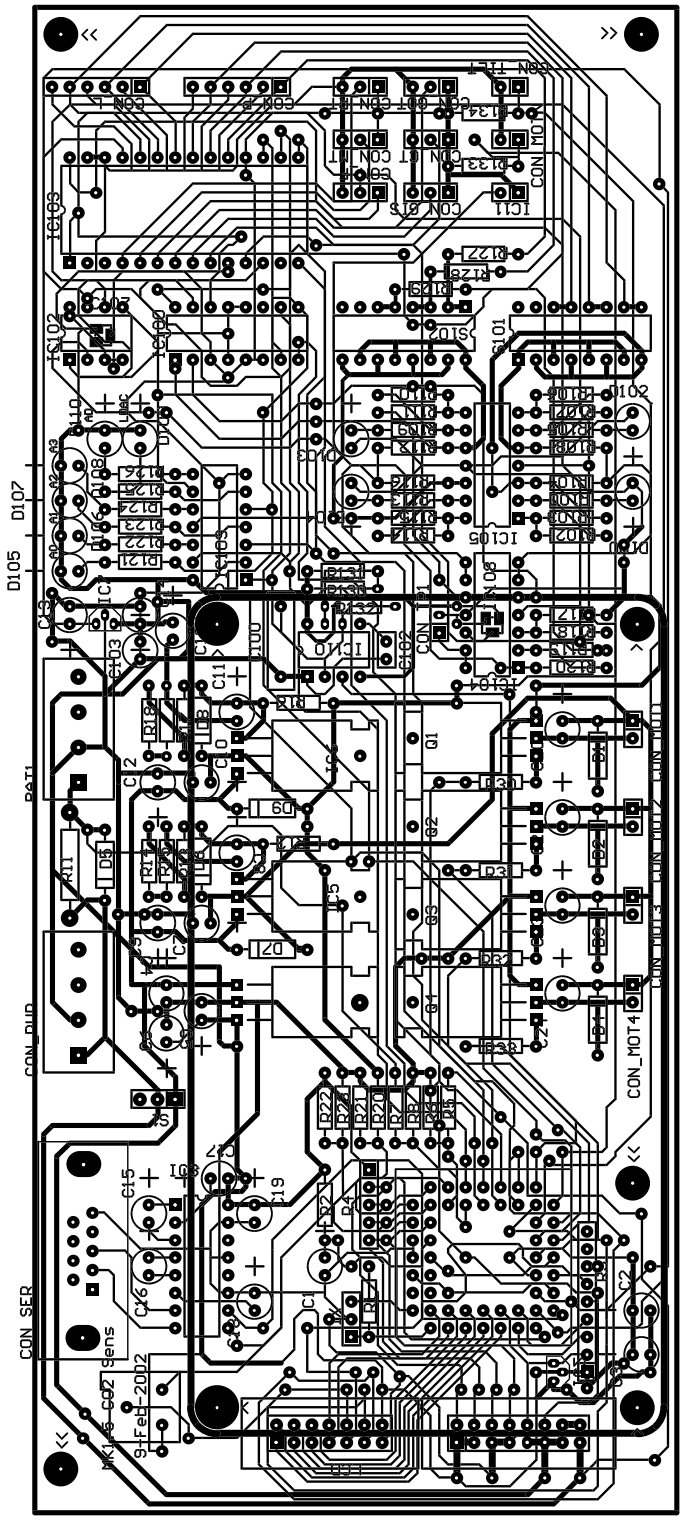

Figure A.27: Mk.II microcontroller board PCB.

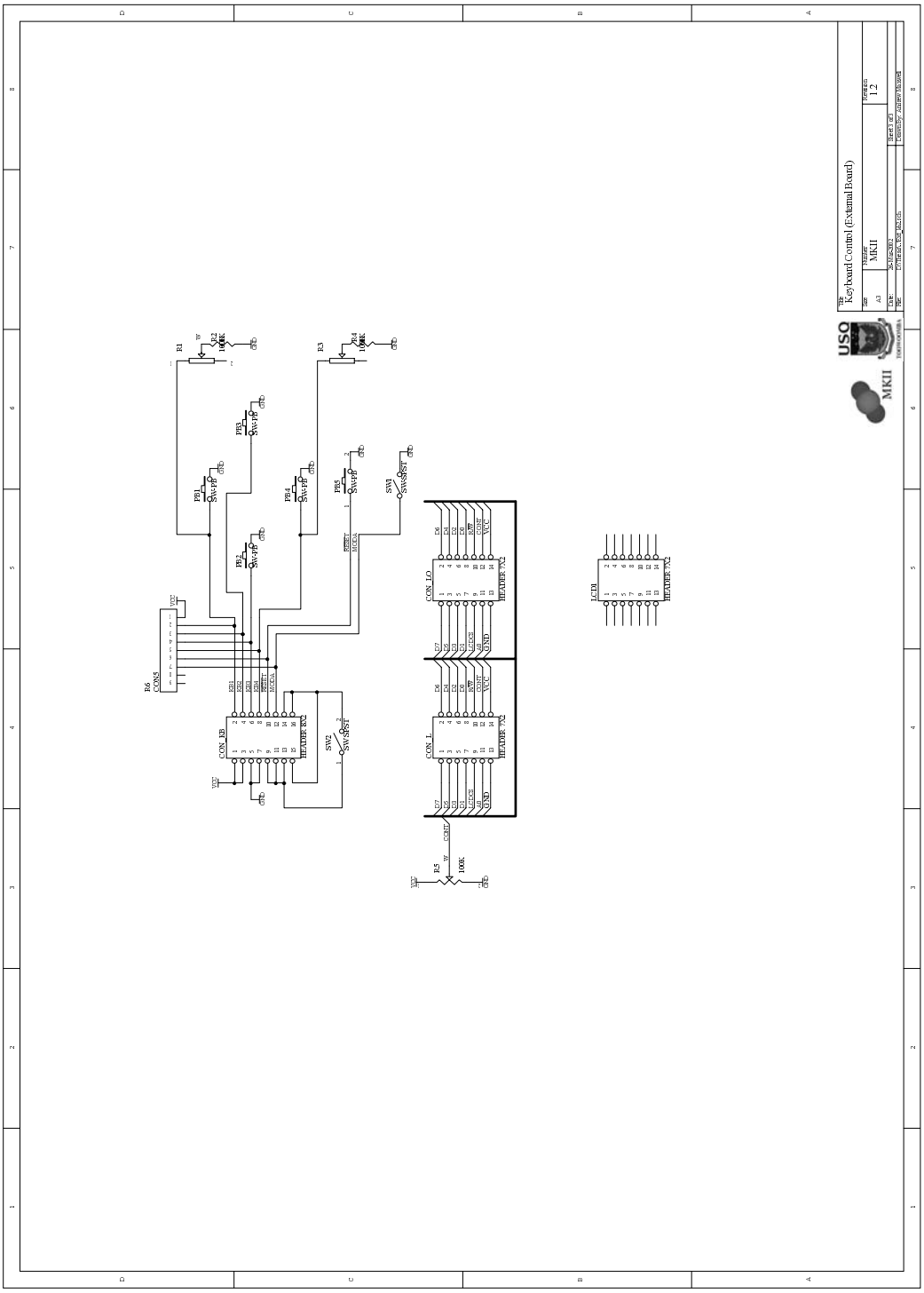

Figure A.28: Keyboard and display board schematic.

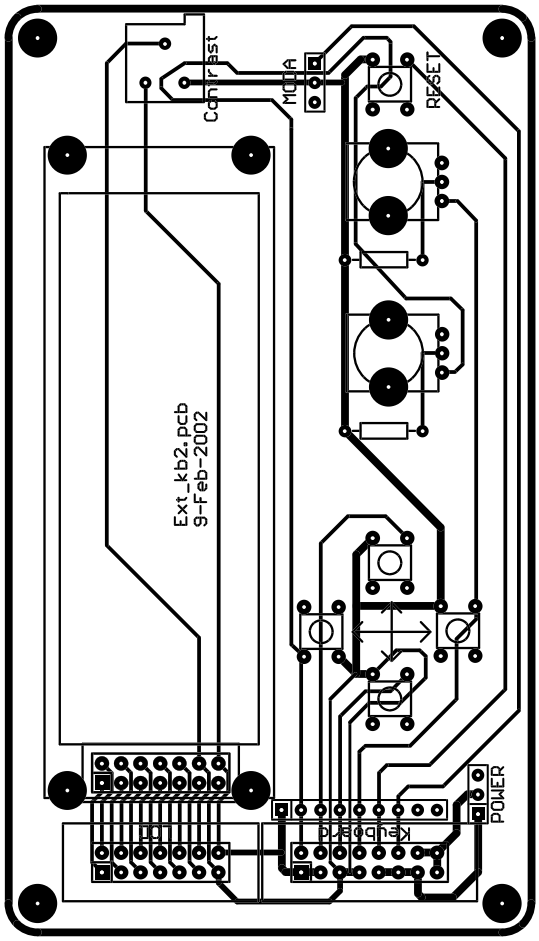

Figure A.29: Keyboard and display board PCB.

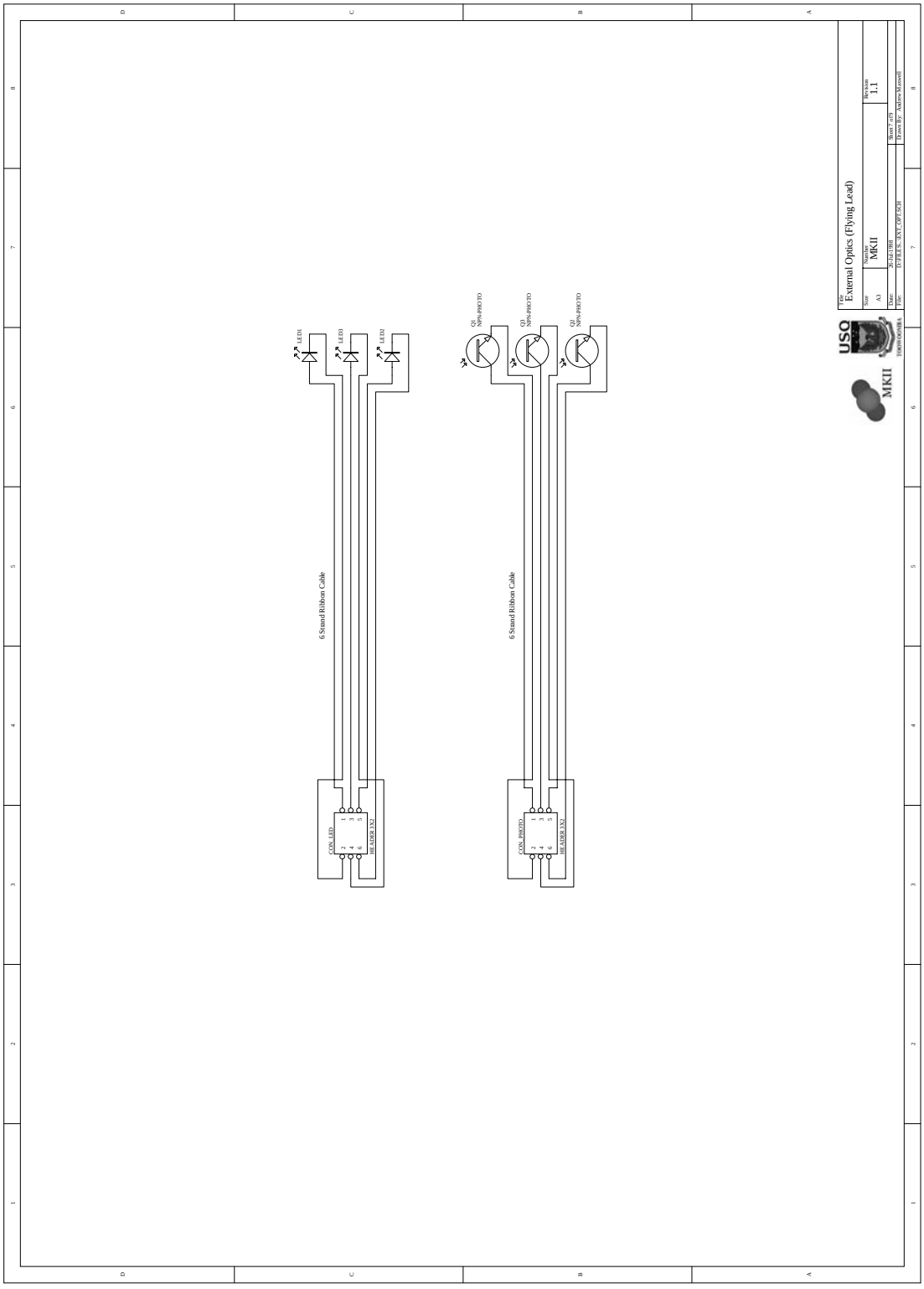

Figure A.30: External cell optics cable schematic.

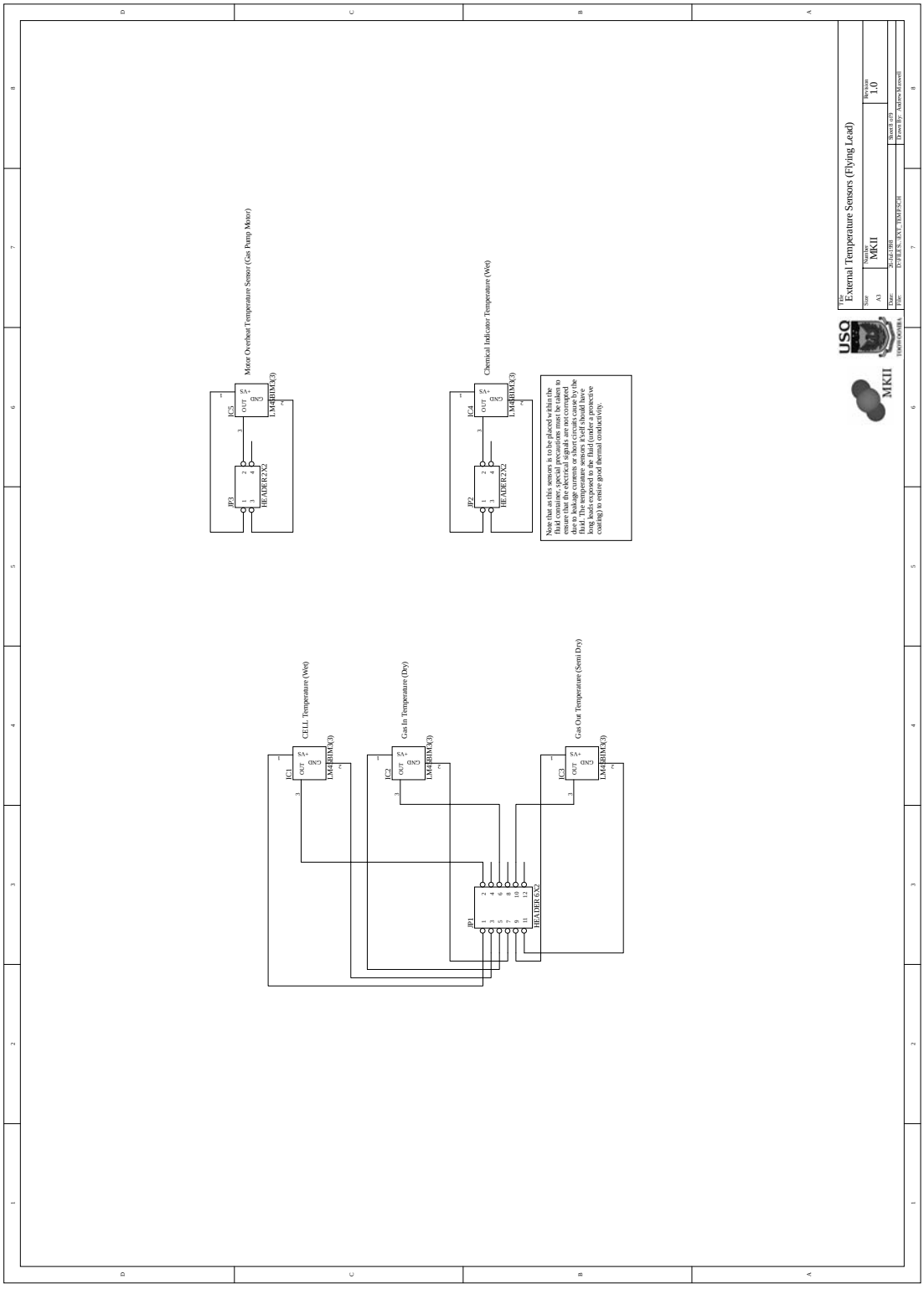

Figure A.31: External temperature sensors cable schematic.

A.3.1 Additional Schematic and PCB Artwork

- External precision flowmeter schematic and PCB.
- External 240v 'bellows' pump control schematic.

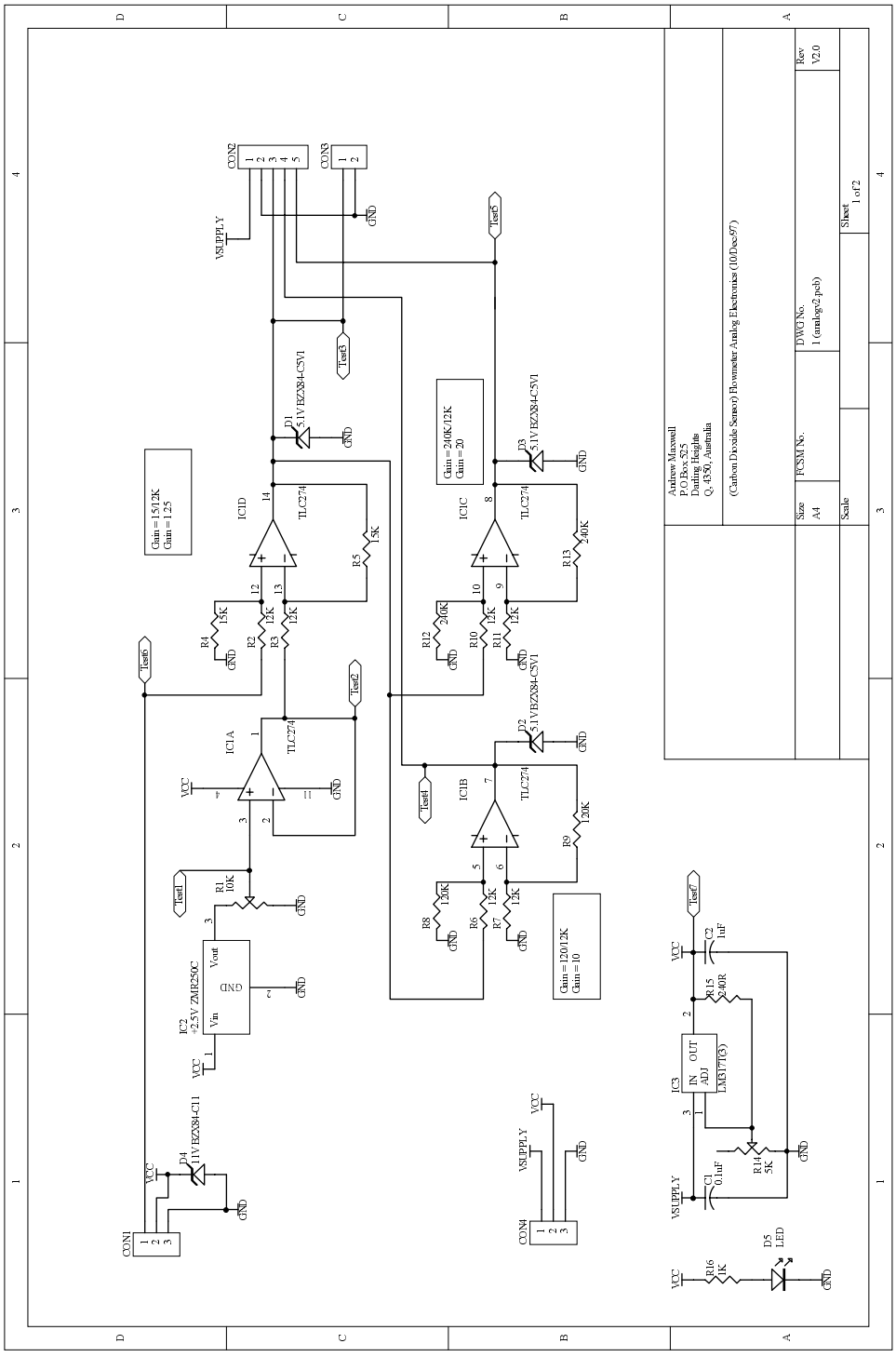

Figure A.32: External flowmeter analog electronics schematic.

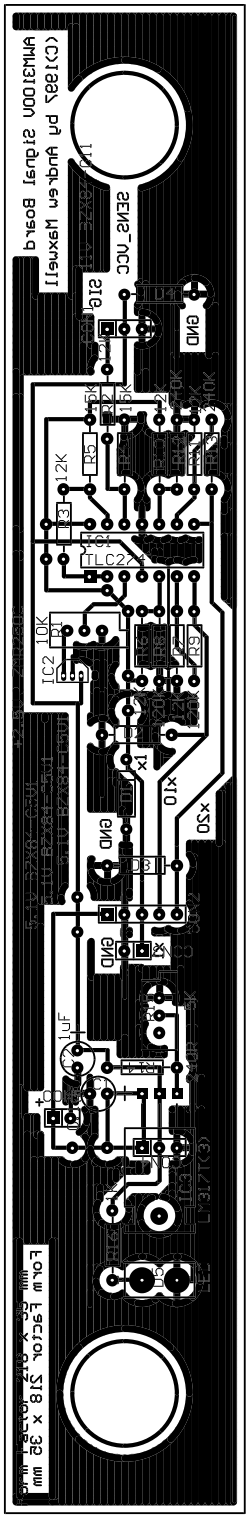

Figure A.33: External flowmeter analog electronics PCB.

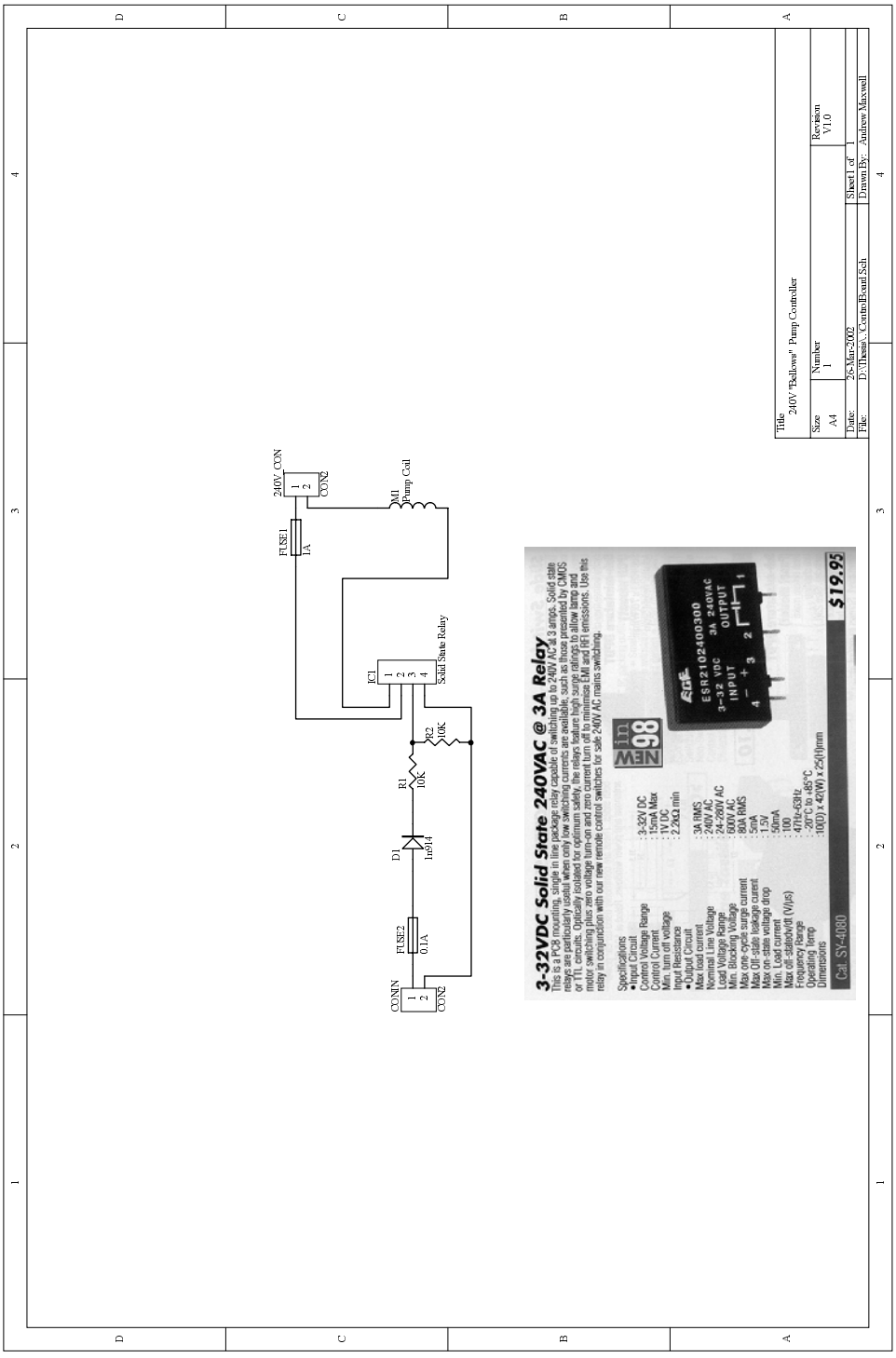

Figure A.34: External 'bellows' pump controller schematic.

A.4 Specifications for Specialist Components

This section contains manufacturer supplied information and specifications for the less commonly available components employed in the hardware prototypes. In some cases only the first few relevant pages are presented. Full specifications can be found on the supplied CDROM. See Appendix G for details.

MAX500ACPE Quad Serial-Interface 8-Bit DAC

LM50C Single - Supply Centigrade Temperature Sensor

AWM3100V Microbridge Mass Airflow Sensor

BUK553 PowerMOS Logic Level FET

LTC1286 Micropower 12-Bit ADC

OP165A GaAs Plastic Infrared Emitting Diode

TDET500C Phototransistor

C3M3 Resistive Humidity Sensor

240VAC @ 3A Solid State Relay

19-1016; Rev 2; 2/96

MAXIM

CMOS, Quad, Serial-Interface 8-Bit DAC

General Description

The MAX500 is a quad, 8-bit, voltage-output digital-to-analog converter (DAC) with a cascadable serial interface. The IC includes four output buffer amplifiers and input logic for an easy-to-use, two- or three-wire serial interface. In a system with several MAX500s, only one serial data line is required to load all the DACs by cascading them. The MAX500 contains double-buffered logic and a 10-bit shift register that allows all four DACs to be updated simultaneously using one control signal. There are three reference inputs so the range of two of the DACs can be independently set while the other two DACs track each other.

The MAX500 achieves 8-bit performance over the full operating temperature range without external trimming.

Applications

Minimum Component Count Analog Systems
Digital Offset/Gain Adjustment
Industrial Process Control
Arbitrary Function Generators
Automatic Test Equipment

Functional Diagram

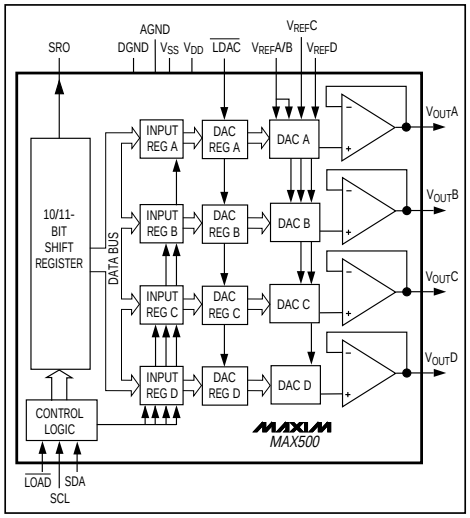

Features

- ♦ **Buffered Voltage Outputs**
- ♦ **Double-Buffered Digital Inputs**
- ♦ **Microprocessor and TTL/CMOS Compatible**
- ♦ **Requires No External Adjustments**
- ♦ **Two- or Three-Wire Cascadable Serial Interface**
- ♦ **16-Pin DIP/SO Package and 20-Pin LCC**
- ♦ **Operates from Single or Dual Supplies**

Ordering Information

PART	TEMP. RANGE	PIN-PACKAGE	ERROR (LSB)
MAX500ACPE	0°C to +70°C	16 Plastic DIP	±1
MAX500BCPE	0°C to +70°C	16 Plastic DIP	±2
MAX500ACWE	0°C to +70°C	16 Wide SO	±1
MAX500BCWE	0°C to +70°C	16 Wide SO	±2
MAX500BC/D	0°C to +70°C	Dice*	±2
MAX500AEPE	-40°C to +85°C	16 Plastic DIP	±1
MAX500BEPE	-40°C to +85°C	16 Plastic DIP	±2
MAX500AEWE	-40°C to +85°C	16 Wide SO	±1
MAX500BEWE	-40°C to +85°C	16 Wide SO	±2
MAX500AEJE	-40°C to +85°C	16 CERDIP	±1
MAX500BEJE	-40°C to +85°C	16 CERDIP	±2
MAX500AMJE	-55°C to +125°C	16 CERDIP	±1
MAX500BMJE	-55°C to +125°C	16 CERDIP	±2
MAX500AMLP	-55°C to +125°C	20 LCC	±1
MAX500BMLP	-55°C to +125°C	20 LCC	±2

Contact factory for dice specifications.

Pin Configurations

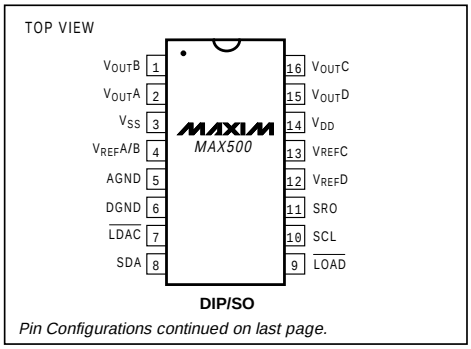

Pin Configurations continued on last page.

Figure A.35: MAX500 Specification (First 4 pages of 12)

CMOS, Quad, Serial-Interface 8-Bit DAC

ABSOLUTE MAXIMUM RATINGS

Power Requirements
- V_{DD} to AGND .....-0.3V, +17V
- V_{DD} to DGND .....-0.3V, +17V
- V_{SS} to DGND .....-7V, (V_{DD} + 0.3V)
- V_{DD} to V_{SS} .....-0.3V, +24V
- Digital Input Voltage to DGND .....-0.3V, (V_{DD} + 0.3V)
- V_{REF} to AGND .....-0.3V, (V_{DD} + 0.3V)
- V_{OUT} to AGND (Note 1).....-0.3V, (V_{DD} + 0.3V)

Power Dissipation (T_A= +70°C)
- Plastic DIP (derate 10.53mW/°C above +70°C).....842mW
- Wide SO (derate 9.52mW/°C above +70°C).....762mW
- CERDIP (derate 10.00mW/°C above +70°C).....800mW
- LCC (derate 9.09mW/°C above +70°C).....727mW

Operating Temperature Ranges
- MAX500_C_ _ .....0°C to + 70°C
- MAX500_E_ _.....-40°C to +85°C
- MAX500_M_ _.....-55°C to +125°C

Storage Temperature Range .....-65°C to +150°C

Lead Temperature (soldering, 10sec) .....+300°C

Note 1: The outputs may be shorted to AGND, provided that the power dissipation of the package is not exceeded. Typical short-circuit current to AGND is 25mA

Stresses beyond those listed under "Absolute Maximum Ratings" may cause permanent damage to the device. These are stress ratings only, and functional operation of the device at these or any other conditions beyond those indicated in the operational sections of the specifications is not implied. Exposure to absolute maximum rating conditions for extended periods may affect device reliability.

ELECTRICAL CHARACTERISTICS—Dual Supplies

(V_{DD} = +11.4V to +16.5V, V_{SS} = -5V ±10%, AGND = DGND = 0V, V_{REF} = +2V to (V_{DD} - 4V), T_A = T_{MIN} to T_{MAX}, unless otherwise noted.)

PARAMETER	SYMBOL	CONDITIONS		MIN	TYP	MAX	UNITS
STATIC PERFORMANCE							
Resolution				8			Bits
Total Unadjusted Error		V_{DD} = 15V ±5%, V_{REF} = 10V	MAX500A			±1	LSB
			MAX500B			±2	
Relative Accuracy		MAX500A				±1/2	LSB
		MAX500B				±1	
Differential Nonlinearity		Guaranteed monotonic				±1	LSB
Full-Scale Error		MAX500A				±1/2	LSB
		MAX500B				±1	
Full-Scale Tempco		V_{REF} = 10V			±5		ppm/°C
Zero-Code Error		T_A = +25°C	MAX500A			±15	mV
			MAX500B			±20	
		T_A = T_{MIN} to T_{MAX}	MAX500A			±20	
			MAX500B			±30	
Zero-Code Tempco					±30		µV/°C
REFERENCE INPUT							
Reference Input Range				2		V_{DD} - 4	V
Reference Input Resistance		V_{REF}C, V_{REF}D		11			kΩ
		V_{REF}A/B		5.5			
Reference Input Capacitance		T_A = +25°C, code dependent (Note 2)				100	pF
Channel-to-Channel Isolation		T_A = +25°C (Notes 2, 3)		-60			dB
AC Feedthrough		T_A = +25°C (Notes 2, 3)		-70			dB
DIGITAL INPUTS							
Digital Input High Voltage	V_{IH}			2.4		5.5	V
Digital Input Low Voltage	V_{IL}					0.8	V
Digital Output High Voltage	V_{OH}	I_{OUT} = -1mA, SRO only		V_{DD} - 1			V
Digital Output Low Voltage	V_{OL}	I_{OUT} = 1mA, SRO only		0.4			V
Digital Input Leakage Current		(Note 4)	Excluding $\overline{LOAD}$			±1	µA
			$\overline{LOAD}$ = 0V			30	
Digital Input Capacitance		T_A = +25°C (Note 2)				8	pF

ELECTRICAL CHARACTERISTICS—Dual Supplies (continued)

(V_{DD} = +11.4V to +16.5V, V_{SS} = -5V ±10%, AGND = DGND = 0V, V_{REF} = +2V to (V_{DD} - 4V), T_A = T_{MIN} to T_{MAX}, unless otherwise noted.)

PARAMETER	SYMBOL	CONDITIONS		MIN	TYP	MAX	UNITS
DYNAMIC PERFORMANCE							
Voltage Output Slew Rate		TA = +25°C (Note 2)		3	8		V/µs
V_{OUT} Settling Time		To ±1/2LSB, V_{REF} = 10V, V_{DD} = +15V, 2kΩ in parallel with 100pF load (Note 2)			2.5	4.5	µs
Digital Feedthrough		(Note 5)			50		nV-s
Digital Crosstalk		(Note 5)			50		nV-s
Output Load Resistance		V_{OUT} = 10V		2			kΩ
POWER SUPPLIES							
Positive Supply Voltage	V_{DD}	For specified performance		11.4		16.5	V
Positive Supply Current	I_{DD}	Outputs unloaded	T_A = +25°C			10	mA
			T_A = T_{MIN} to T_{MAX}			12	
Negative Supply Current	I_{SS}	Outputs unloaded	T_A = +25°C			-9	mA
			T_A = T_{MIN} to T_{MAX}			-10	
SWITCHING CHARACTERISTICS (T_A = +25°C, Note 6)							
3-Wire Mode							
SDA Valid to SCL Setup	t_{S1}			150			ns
SDA Valid to SCL Hold	t_H			0			ns
SCL High Time	t_1			350			ns
SCL Low Time	t_2			350			ns
SCL Rise Time		(Note 7)				50	µs
SCL Fall Time		(Note 7)				50	µs
$\overline{LOAD}$ Pulse Width	t_{LDW}			150			ns
$\overline{LOAD}$ Delay from SCL	t_{LDS}			150			ns
$\overline{LDAC}$ Pulse Width	t_{LDAC}			150			ns
SRO Output Delay	t_{D1}	C_{LOAD} = 50pF				150	ns
2-Wire Mode							
SDA Valid to SCL Hold	t_H			0			ns
SCL High Time	t_1			350			ns
SCL Low Time	t_2			350			ns
SCL Rise Time		(Note 7)				50	µs
SCL Fall Time		(Note 7)				50	µs
$\overline{LDAC}$ Pulse Width	t_{LDAC}			150			ns
SCL Valid to SDA Setup	t_{S1}	Start condition		150			ns
SDA Valid to SCL Setup	t_{S2}	Stop condition		100			ns
SDA Valid to Rising SCL	t_{S3}			125			ns
SRO Output Delay	t_{D1}	C_{LOAD} = 50pF				150	ns

CMOS, Quad, Serial-Interface 8-Bit DAC

ELECTRICAL CHARACTERISTICS—Single Supply

(V_{DD} = +15V ±5%, V_{SS} = AGND = DGND = 0V, V_{REF} = 10V, T_A = T_{MIN} to T_{MAX}, unless otherwise noted.)

PARAMETER	SYMBOL	CONDITIONS		MIN	TYP	MAX	UNITS
STATIC PERFORMANCE							
Resolution				8			Bits
Total Unadjusted Error		V_{DD} = 15V ±5%, V_{REF} = 10V	MAX500A			±1	LSB
			MAX500B			±2	
Relative Accuracy			MAX500A			±1/2	LSB
			MAX500B			±1	
Differential Nonlinearity		Guaranteed monotonic				±1	LSB
Full-Scale Error			MAX500A			±1/2	LSB
			MAX500B			±1	
Full-Scale Tempco		V_{REF} = 10V			±5		ppm/°C
Zero-Code Error		T_A = +25°C	MAX500A			±15	mV
			MAX500B			±20	
		T_A = T_{MIN} to T_{MAX}	MAX500A			±20	
			MAX500B			±30	
Zero-Code Tempco					±30		µV/°C
REFERENCE INPUT—All specifications are the same as for dual supplies.							
DIGITAL INPUTS—All specifications are the same as for dual supplies.							
DYNAMIC PERFORMANCE—All specifications are the same as for dual supplies.							
POWER SUPPLIES							
Positive Supply Voltage	V_{DD}	For specified performance		14.25		15.75	V
Positive Supply Current	I_{DD}	Outputs unloaded	T_A = +25°C			10	mA
			T_A = T_{MIN} to T_{MAX}			12	
SWITCHING CHARACTERISTICS—All specifications are the same as for dual supplies.							

Note 2: Guaranteed by design. Not production tested.
Note 3: T_A = +25°C, V_{REF} = 10kHz, 10V peak-to-peak sine wave.
Note 4: $\overline{LOAD}$ has a weak internal pull-up resistor to V_{DD}.
Note 5: DAC switched from all 1s to all 0s, and all 0s to all 1s code.
Note 6: Sample tested at +25°C to ensure compliance.
Note 7: Slow rise and fall times are allowed on the digital inputs to facilitate the use of opto-couplers. Only timing for SCL is given because the other digital inputs should be stable when SCL transitions.

Typical Operating Characteristics

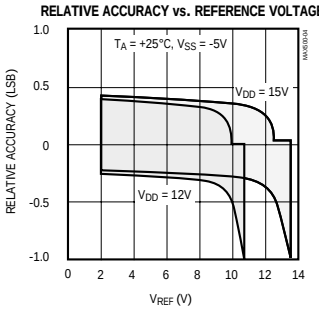

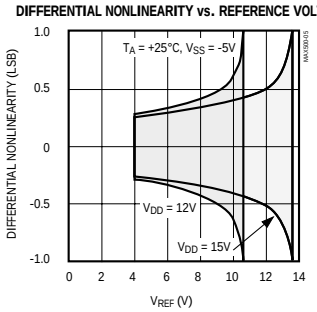

National Semiconductor

ADVANCE INFORMATION
April 1995

LM50B/LM50C
Single-Supply Centigrade Temperature Sensor

General Description

The LM50 is a precision integrated-circuit temperature sensor that can sense a −40°C to +125°C temperature range using a single positive supply. The LM50's output voltage is linearly proportional to Celsius (Centigrade) temperature (+10 mV/°C) and has a DC offset of +500 mV. The offset allows reading negative temperatures without the need for a negative supply. The ideal output voltage of the LM50 ranges from +100 mV to +1.75V for a −40°C to +125°C temperature range. The LM50 does not require any external calibration or trimming to provide accuracies of ±3°C at room temperature and ±4°C over the full −40°C to +125°C temperature range. Trimming and calibration of the LM50 at the wafer level assure low cost and high accuracy. The LM50's linear output, +500 mV offset, and factory calibration simplify circuitry required in a single supply environment where reading negative temperatures is required. Because the LM50's quiescent current is less than 130 μA, self-heating is limited to a very low 0.2°C in still air.

Applications

- Computers
- Disk Drives
- Battery Management
- Automotive
- FAX Machines
- Printers
- Portable Medical Instruments
- HVAC
- Power Supply Modules

Features

- Calibrated directly in ° Celsius (Centigrade)
- Linear + 10.0 mV/°C scale factor
- ±2°C accuracy guaranteed at +25°C
- Specified for full −40° to +125°C range
- Suitable for remote applications
- Low cost due to wafer-level trimming
- Operates from 4.5V to 10V
- Less than 130 μA current drain
- Low self-heating, less than 0.2°C in still air
- Nonlinearity less than 0.8°C over temp

Connection Diagrams

SOT-23

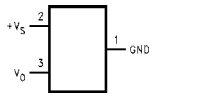

TL/H/12370–1

Top View

See NS Package Number M03B
(JEDEC Registration TO-236AB)

Order Number	SOT-23 Device Marking	Supplied As
LM50BIM3	T5B	250 Units on Tape and Reel
LM50CIM3	T5C	250 Units on Tape and Reel
LM50BIM3X	T5B	3000 Units on Tape and Reel
LM50CIM3X	T5C	3000 Units on Tape and Reel

TO-92
Plastic Package

TL/H/12370–2

Order Number LM50BIZ
or LM50CIZ
See NS Package Number Z03A

Typical Applications

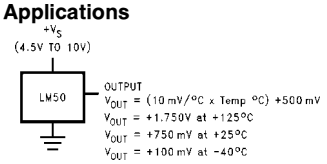

TL/H/12370–3

FIGURE 1. Full-Range Centigrade Temperature Sensor (−40°C to +125°C)

Figure A.36: LM50C Specification

Physical Dimensions inches (millimeters)

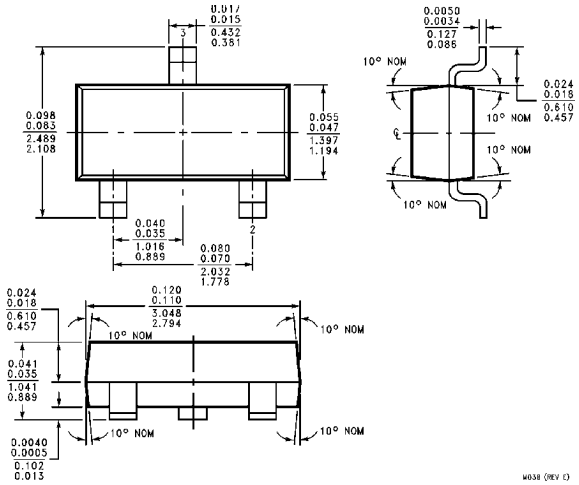

SOT-23 Molded Small Outline Transistor Package (M3)
Order Number LM50BIM3 or LM50CIM3
NS Package Number M03B
(JEDEC Registration TO-236AB)

Physical Dimensions inches (millimeters) (Continued)

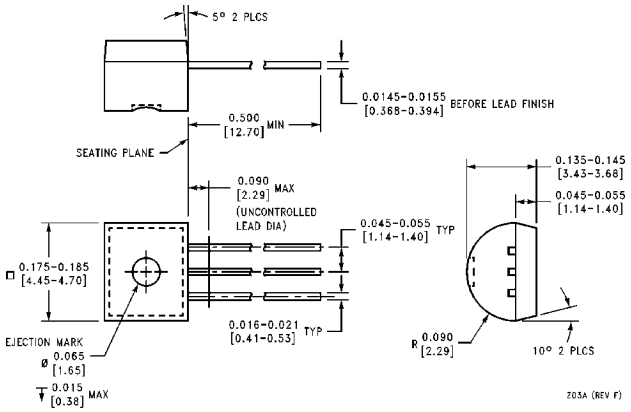

TO-92 Plastic Package (Z)
Order Number LM50AIZ, LM50BIZ or LM50CIZ
NS Package Number Z03A

LIFE SUPPORT POLICY

NATIONAL'S PRODUCTS ARE NOT AUTHORIZED FOR USE AS CRITICAL COMPONENTS IN LIFE SUPPORT DEVICES OR SYSTEMS WITHOUT THE EXPRESS WRITTEN APPROVAL OF THE PRESIDENT OF NATIONAL SEMICONDUCTOR CORPORATION. As used herein:

1. Life support devices or systems are devices or systems which, (a) are intended for surgical implant into the body, or (b) support or sustain life, and whose failure to perform, when properly used in accordance with instructions for use provided in the labeling, can be reasonably expected to result in a significant injury to the user.
2. A critical component is any component of a life support device or system whose failure to perform can be reasonably expected to cause the failure of the life support device or system, or to affect its safety or effectiveness.

National Semiconductor Corporation
1111 West Bardin Road
Arlington, TX 76017
Tel: 1(800) 272-9959
Fax: 1(800) 737-7018

National Semiconductor Europe
Fax: (+49) 0-180-530 85 86
Email: cnjwge@tevm2.nsc.com
Deutsch Tel: (+49) 0-180-530 85 85
English Tel: (+49) 0-180-532 78 32
Français Tel: (+49) 0-180-532 93 58
Italiano Tel: (+49) 0-180-534 16 80

National Semiconductor Hong Kong Ltd.
13th Floor, Straight Block,
Ocean Centre, 5 Canton Rd.
Tsimshatsui, Kowloon
Hong Kong
Tel: (852) 2737-1600
Fax: (852) 2736-9960

National Semiconductor Japan Ltd.
Tel: 81-043-299-2309
Fax: 81-043-299-2408

Airflow Sensors
Microbridge Mass Airflow/Amplified

AWM3000 Series

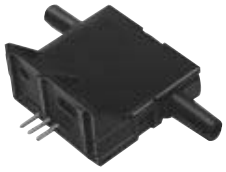

FEATURES
- Laser trimmed for interchangeability
- Flow sensing up to 1.0 LPM

Two Wheatstone bridges control airflow measurement – one provides closed loop heater control, the other contains the twin sensing elements. Figure 1 depicts the heater control circuitry. It minimizes errors due to ambient temperature changes by providing an output proportional to mass flow. The circuit keeps the heater temperature at a constant differential above ambient air temperature, despite variations in airflow and temperature.

The heater circuitry, operational amplifier, and precision thick-film resistors are located on the ceramic substrate. Ambient temperature is sensed by a similar heat-sunk resistor on the chip.

This mode of heater operation also reduces, but does not eliminate, the effects of changes in air density or gas composition. These changes could alter thermal conductance and otherwise change operating characteristics of the heater and sensing resistances.

The sensing bridge supply circuit in Figure 2 is a conventional Wheatstone bridge circuit where dual sensing resistors make up the two active arms of the circuit. The ratiometric voltage output of the device corresponds to the amplified differential voltage across the Wheatstone bridge circuit.

The supply circuit, along with the differential instrumentation amplifier shown in Figure 2 are designed into the sensor package and are precision laser adjusted during manufacture. Active laser trimming, combined with short signal paths, results in excellent noise resistance, repeatability, and sensor interchangeability.

Dust contamination is possible in some airflow applications, but can be minimized. Dust particles in the airstream flow past the chip parallel to its surface. In addition, the microstructure is kept clean by a thermophoretic effect, which impels the micrometer-sized dust particles away from the structure. In an accelerated operating life test, with less than 50 sccm flow, a lifetime equivalent to over 20 years in a typical industrial air environment was achieved with no degradation of sensor response.

Clogging due to dust adherence to chip edges and channel surfaces can be substantially eliminated through the use of a simple filter. The optimum filtering action is obtained with a low impedance filter in series with the small cross-section and high flow impedance of the channel. This permits a large accumulation of dust in the filter without significant change in the combined impedance. Where filtering is desired, a disposable five-micron filter may be used upstream of the flow sensor.

Figure 1
Heater control circuit

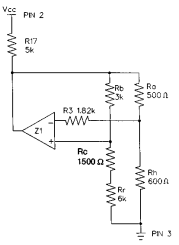

Figure 2
Sensing bridge supply circuit and differential instrumentation amplifier

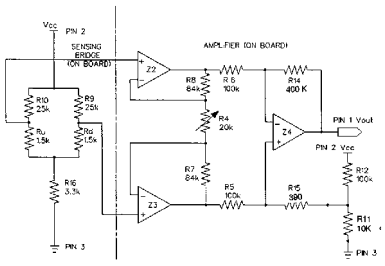

Figure A.37: AWM3100V Specification

Airflow Sensors — AWM3000 Series
Microbridge Mass Airflow/Amplified

AWM3000 ORDER GUIDE

Catalog Listings		AWM3100V	AWM3150V	AWM3200V	AWM3300V
ACCURACY SPECIFICATIONS at 10.0± 0.01 VDC	Flow Range (Full Scale)/ Pressure Range (psi)	+200 sccm/+.2″ H_2O (.5mBar)	30 sccm/+1″ H_2O (.12mBar)	+2.0″ H_2O (5mBar)	+1000 sccm/+1.3 ±.1″ H_2O (3.2mBar)
	Output Voltage @ Laser Trim Point	5 VDC @ 200 sccm	1.5 VDC @ 5 sccm	5 VDC @ 2″ H_2O	5 VDC @ 1000 sccm
	Null Voltage	1.00±.05 VDC	1.00±.10 VDC	1.00±.08 VDC	1.00±.10 VDC
	Null Voltage Shift +25 to +85°C +25 to –25°C	 ±25mV ±25 mV	 ±100mV ±100 mV	 ±25mV ±25 mV	 ±25mV ±25 mV
	Output Voltage Shift 25 to –25°C 25 to 85°C	 –4.0% Reading +4.0% Reading	 ±5% Reading ±5% Reading	 +24.0% Reading –24.0% Reading	 –5.0% Reading (Note 4) +5.0% Reading (Note 4)
	Repeatability & Hysteresis	±0.50% Reading max.	±1% Reading	±0.50% Reading max.	±1% Reading max.
		Min.	Typ.	Max.	
	Excitation (VDC)	8.0	10±.01	15 (Note 2)	
	Power Consumption (mW)	—	30	50	
	Response Time (msec)	—	1.0	3.0 (Note 1)	
	Max. Common Mode Pressure (psi)	—	—	25	
	Temperature Range Operating Storage	 –25 to +85°C (–13 to +185°F) –40 to +90°C (–40 to +194°F)			
	Termination (.100″ centers)	0.025″ square			
	Weight (grams)	10.8			
	Shock Rating (5 drops, 6 axes)	100 g peak			

Notes:
1. Initial warmup time for signal conditioned circuitry is 1 minute max.
2. Output Voltage is ratiometric to supply voltage.
3. Repeatability and Hysteresis tolerances reflect inherent inaccuracies of the measurement equipment.
4. Temperature shifts in differential pressure devices are mostly due to the density change of the gas over temperature. Temperature shifts in the massflow devices are due to the change of the second order TCR coefficient of thin-film and thick-film resistors over temperature, plus shifts in Op Amp.

OUTPUT FLOW VS. INTERCHANGEABILITY

AWM3100V			AWM3150V * *			AWM3200V			AWM3300V		
Flow sccm	Nominal VDC	Tol.(5) ±VDC	Flow sccm	Nominal VDC	Tol.(5) ±VDC	Press in. H_2O	Nominal VDC	Tol.(5) ±VDC	Flow sccm	Nominal VDC	Tol.(5) ±VDC
200	5.00	0.15	30	3.75	.70	2.00	5.00	0.15	1000	5.00	0.15
175	4.80	0.16	20	2.90	.45	1.75	4.59	0.15	900	4.90	0.16
150	4.50	0.17	10	1.95	.20	1.50	4.16	0.16	800	4.80	0.17
125	4.17	0.18	5	1.50	.10	1.25	3.70	0.20	700	4.66	0.18
100	3.75	0.19	4	1.40	.08	1.00	3.25	0.22	600	4.42	0.19
75	3.27	0.19	3	1.30	.08	0.75	2.65	0.22	500	4.18	0.20
50	2.67	0.17	2	1.20	.07	0.50	2.15	0.19	400	3.82	0.21
25	1.90	0.13	1	1.10	.06	0.25	1.55	0.11	300	3.41	0.19
0	1.00	0.05	0	1.00	.05	0.00	1.00	0.08	200	2.96	0.17
									100	2.30	0.14
									0	1.00	0.10

5. The unique design of the microbridge mass airflow sensor accommodates your special requirements. Custom laser-trimming and flow channel dimensioning can conform performance characteristics to specific applications.

Airflow Sensors
Microbridge Mass Airflow/Amplified

AWM3000 Series

OUTPUT CURVES

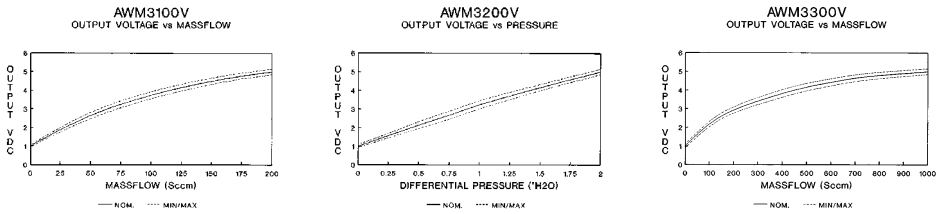

MOUNTING DIMENSIONS (For reference only)

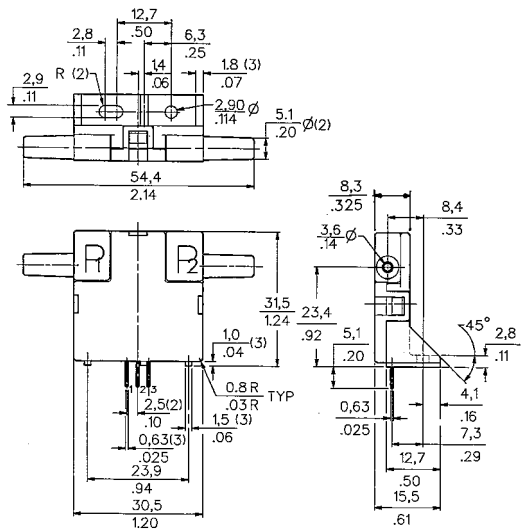

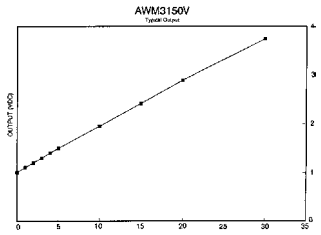

OUTPUT CONNECTIONS

Pin 1	Output Voltage
Pin 2	+ Supply Voltage
Pin 3	Ground

NOTE: Positive flow direction is defined as proceeding into Port 1 (P1) and out of Port 2 (P2), and results in positive output.

PHILIPS INTERNATIONAL 65E D 7110826 0064231 313 PHIN
Philips Semiconductors Product Specification

PowerMOS transistor Logic level FET

BUK553-100A/B

GENERAL DESCRIPTION

N-channel enhancement mode logic level field-effect power transistor in a plastic envelope. The device is intended for use in Switched Mode Power Supplies (SMPS), motor control, welding, DC/DC and AC/DC converters, and in automotive and general purpose switching applications.

QUICK REFERENCE DATA

SYMBOL	PARAMETER	MAX.	MAX.	UNIT
	BUK553	-100A	-100B	
V_{DS}	Drain-source voltage	100	100	V
I_D	Drain current (DC)	13	12	A
P_{tot}	Total power dissipation	75	75	W
T_j	Junction temperature	175	175	°C
$R_{DS(ON)}$	Drain-source on-state resistance; V_{GS} = 5 V	0.18	0.22	Ω

PINNING - TO220AB

PIN	DESCRIPTION
1	gate
2	drain
3	source
tab	drain

PIN CONFIGURATION

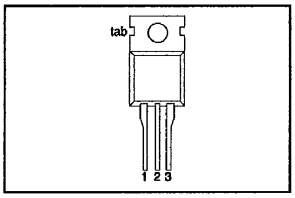

SYMBOL

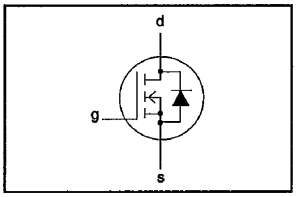

LIMITING VALUES

Limiting values in accordance with the Absolute Maximum System (IEC 134)

SYMBOL	PARAMETER	CONDITIONS	MIN.	MAX.		UNIT
V_{DS}	Drain-source voltage	-	-	100		V
V_{DGR}	Drain-gate voltage	R_{GS} = 20 kΩ	-	100		V
$\pm V_{GS}$	Gate-source voltage	-	-	15		V
$\pm V_{GSM}$	Non-repetitive gate-source voltage	$t_p \leq 50$ µs	-	20		V
				-100A	-100B	
I_D	Drain current (DC)	T_{mb} = 25 °C	-	13	12	A
I_D	Drain current (DC)	T_{mb} = 100 °C	-	9	8.5	A
I_{DM}	Drain current (pulse peak value)	T_{mb} = 25 °C	-	52	48	A
P_{tot}	Total power dissipation	T_{mb} = 25 °C	-	75		W
T_{stg}	Storage temperature	-	- 55	175		°C
T_j	Junction Temperature	-	-	175		°C

THERMAL RESISTANCES

SYMBOL	PARAMETER	CONDITIONS	MIN.	TYP.	MAX.	UNIT
$R_{th\,j\text{-}mb}$	Thermal resistance junction to mounting base		-	-	2.0	K/W
$R_{th\,j\text{-}a}$	Thermal resistance junction to ambient		-	60	-	K/W

Figure A.38: BUK553 Specification (First 2 pages of 5)

STATIC CHARACTERISTICS

T_{mb} = 25 °C unless otherwise specified

SYMBOL	PARAMETER	CONDITIONS	MIN.	TYP.	MAX.	UNIT
$V_{(BR)DSS}$	Drain-source breakdown voltage	V_{GS} = 0 V; I_D = 0.25 mA	100	-	-	V
$V_{GS(TO)}$	Gate threshold voltage	V_{DS} = V_{GS}; I_D = 1 mA	1.0	1.5	2.0	V
I_{DSS}	Zero gate voltage drain current	V_{DS} = 100 V; V_{GS} = 0 V; T_j = 25 °C	-	1	10	µA
I_{DSS}	Zero gate voltage drain current	V_{DS} = 100 V; V_{GS} = 0 V; T_j =125 °C	-	0.1	1.0	mA
I_{GSS}	Gate source leakage current	V_{GS} = ±15 V; V_{DS} = 0 V	-	10	100	nA
$R_{DS(ON)}$	Drain-source on-state resistance	V_{GS} = 5 V; **BUK553-100A**	-	0.17	0.18	Ω
		I_D = 6.5 A **BUK553-100B**	-	0.20	0.22	Ω

DYNAMIC CHARACTERISTICS

T_{mb} = 25 °C unless otherwise specified

SYMBOL	PARAMETER	CONDITIONS	MIN.	TYP.	MAX.	UNIT
g_{fs}	Forward transconductance	V_{DS} = 25 V; I_D = 6.5 A	6.0	8.0	-	S
C_{iss}	Input capacitance	V_{GS} = 0 V; V_{DS} = 25 V; f = 1 MHz	-	620	825	pF
C_{oss}	Output capacitance		-	180	250	pF
C_{rss}	Feedback capacitance		-	90	120	pF
$t_{d\,on}$	Turn-on delay time	V_{DD} = 30 V; I_D = 3 A;	-	10	20	ns
t_r	Turn-on rise time	V_{GS} = 5 V; R_{GS} = 50 Ω;	-	45	60	ns
$t_{d\,off}$	Turn-off delay time	R_{gen} = 50 Ω	-	90	115	ns
t_f	Turn-off fall time		-	40	55	ns
L_d	Internal drain inductance	Measured from contact screw on tab to centre of die	-	3.5	-	nH
L_d	Internal drain inductance	Measured from drain lead 6 mm from package to centre of die	-	4.5	-	nH
L_s	Internal source inductance	Measured from source lead 6 mm from package to source bond pad	-	7.5	-	nH

REVERSE DIODE LIMITING VALUES AND CHARACTERISTICS

T_{mb} = 25 °C unless otherwise specified

SYMBOL	PARAMETER	CONDITIONS	MIN.	TYP.	MAX.	UNIT
I_{DR}	Continuous reverse drain current	-	-	-	13	A
I_{DRM}	Pulsed reverse drain current	-	-	-	52	A
V_{SD}	Diode forward voltage	I_F = 13 A ; V_{GS} = 0 V	-	1.2	1.5	V
t_{rr}	Reverse recovery time	I_F = 13 A; -dI_F/dt = 100 A/µs;	-	90	-	ns
Q_{rr}	Reverse recovery charge	V_{GS} = 0 V; V_R = 30 V	-	0.6	-	µC

AVALANCHE LIMITING VALUE

T_{mb} = 25 °C unless otherwise specified

SYMBOL	PARAMETER	CONDITIONS	MIN.	TYP.	MAX.	UNIT
W_{DSS}	Drain-source non-repetitive unclamped inductive turn-off energy	I_D = 13 A ; V_{DD} ≤ 50 V ; V_{GS} = 5 V ; R_{GS} = 50 Ω	-	-	70	mJ

LINEAR TECHNOLOGY

LTC1286/LTC1298

Micropower Sampling 12-Bit A/D Converters In S0-8 Packages

FEATURES

- **12-Bit Resolution**
- **8-Pin SOIC Plastic Package**
- **Low Cost**
- **Low Supply Current: 250μA Typ.**
- Auto Shutdown to 1nA Typ.
- Guaranteed ±3/4LSB Max DNL
- Single Supply 5V to 9V Operation
- On-Chip Sample-and-Hold
- 60μs Conversion Time
- Sampling Rates:
  - 12.5 ksps (LTC1286)
  - 11.1 ksps (LTC1298)
- I/O Compatible with SPI, Microwire, etc.
- Differential Inputs (LTC1286)
- 2-Channel MUX (LTC1298)
- 3V Versions Available: LTC1285/LTC1288

APPLICATIONS

- Battery-Operated Systems
- Remote Data Acquisition
- Battery Monitoring
- Handheld Terminal Interface
- Temperature Measurement
- Isolated Data Acquisition

DESCRIPTION

The LTC1286/LTC1298 are micropower, 12-bit, successive approximation sampling A/D converters. They typically draw only 250μA of supply current when converting and automatically power down to a typical supply current of 1nA whenever they are not performing conversions. They are packaged in 8-pin SO packages and operate on 5V to 9V supplies. These 12-bit, switched-capacitor, successive approximation ADCs include sample-and-holds. The LTC1286 has a single differential analog input. The LTC1298 offers a software selectable 2-channel MUX.

On-chip serial ports allow efficient data transfer to a wide range of microprocessors and microcontrollers over three wires. This, coupled with micropower consumption, makes remote location possible and facilitates transmitting data through isolation barriers.

These circuits can be used in ratiometric applications or with an external reference. The high impedance analog inputs and the ability to operate with reduced spans (to 1.5V full scale) allow direct connection to sensors and transducers in many applications, eliminating the need for gain stages.

TYPICAL APPLICATIONS

25μW, S0-8 Package, 12-Bit ADC
Samples at 200Hz and Runs Off a 5V Supply

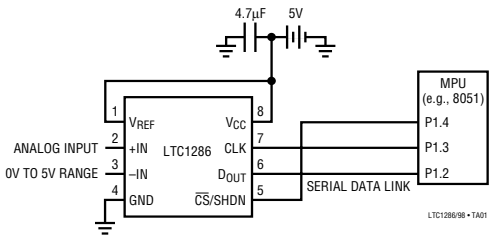

Supply Current vs Sample Rate

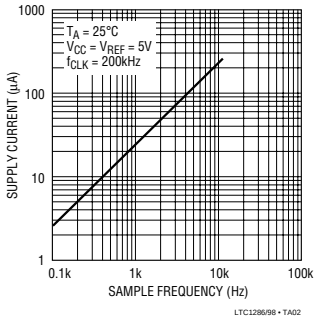

Figure A.39: LTC1286 Specification (First 4 pages of 24)

ABSOLUTE MAXIMUM RATINGS (Notes 1 and 2)

Supply Voltage (V_{CC}) to GND 12V
Voltage
  Analog and Reference ..... –0.3V to V_{CC} + 0.3V
  Digital Inputs ..... –0.3V to 12V
  Digital Output ..... –0.3V to V_{CC} + 0.3V

Power Dissipation 500mW
Operating Temperature Range
  LTC1286C/LTC1298C ..... 0°C to 70°C
  LTC1286I/LTC1298I ..... –40°C to 85°C
Storage Temperature Range ..... –65°C to 150°C
Lead Temperature (Soldering, 10 sec.) ..... 300°C

PACKAGE/ORDER INFORMATION

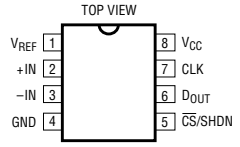

N8 PACKAGE
8-LEAD PLASTIC DIP

T_{JMAX} = 150°C, θ_{JA} = 130°C/W

ORDER PART NUMBER
LTC1286CN8 LTC1286IN8

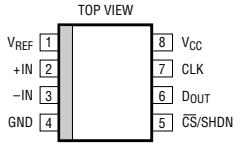

S8 PACKAGE
8-LEAD PLASTIC SOIC

T_{JMAX} = 150°C, θ_{JA} = 175°C/W

ORDER PART NUMBER
LTC1286CS8 LTC1286IS8
PART MARKING
1286C 1286I

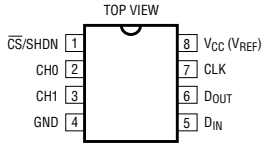

N8 PACKAGE
8-LEAD PLASTIC DIP

T_{JMAX} = 150°C, θ_{JA} = 130°C/W

ORDER PART NUMBER
LTC1298CN8 LTC1298IN8

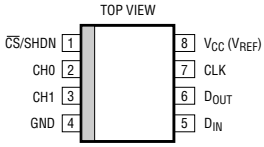

S8 PACKAGE
8-LEAD PLASTIC SOIC

T_{JMAX} = 150°C, θ_{JA} = 175°C/W

ORDER PART NUMBER
LTC1298CS8 LTC1298IS8
PART MARKING
1298C 1298I

Consult factory for military grade parts.

RECOMMENDED OPERATING CONDITIONS

SYMBOL	PARAMETER	CONDITIONS	MIN	TYP	MAX	UNITS
V_{CC}	Supply Voltage (Note 3)	LTC1286 LTC1298	4.5 4.5		9.0 5.5	V V
f_{CLK}	Clock Frequency	V_{CC} = 5V	(Note 4)		200	kHz
t_{CYC}	Total Cycle Time	LTC1286, f_{CLK} = 200kHz LTC1298, f_{CLK} = 200kHz	80 90			µs µs
t_{hDI}	Hold Time, D_{IN} After CLK↑	V_{CC} = 5V	150			ns
$t_{su\overline{CS}}$	Setup Time $\overline{CS}$↓ Before First CLK↑ (See Operating Sequence)	LTC1286, V_{CC} = 5V LTC1298, V_{CC} = 5V	2 2			µs µs
t_{suDI}	Setup Time, D_{IN} Stable Before CLK↑	V_{CC} = 5V	400			ns
t_{WHCLK}	CLK High Time	V_{CC} = 5V	2			µs
t_{WLCLK}	CLK Low Time	V_{CC} = 5V	2			µs
$t_{WH\overline{CS}}$	$\overline{CS}$ High Time Between Data Transfer Cycles	V_{CC} = 5V	2			µs
$t_{WL\overline{CS}}$	$\overline{CS}$ Low Time During Data Transfer	LTC1286, f_{CLK} = 200kHz LTC1298, f_{CLK} = 200kHz	75 85			µs µs

CONVERTER AND MULTIPLEXER CHARACTERISTICS (Note 5)

PARAMETER	CONDITIONS		LTC1286 MIN	LTC1286 TYP	LTC1286 MAX	LTC1298 MIN	LTC1298 TYP	LTC1298 MAX	UNITS
Resolution (No Missing Codes)		●	12			12			Bits
Integral Linearity Error	(Note 6)	●		±3/4	±2		±3/4	±2	LSB
Differential Linearity Error		●		±1/4	±3/4		±1/4	±3/4	LSB
Offset Error		●		3/4	±3		3/4	±3	LSB
Gain Error		●		±2	±8		±2	±8	LSB
Analog Input Range	(Note 7 and 8)	●		–0.05V to V_{CC} + 0.05V					V
REF Input Range (LTC1286) (Notes 7, 8, and 9)	$4.5 \le V_{CC} \le 5.5V$ $5.5V < V_{CC} \le 9V$			1.5V to V_{CC} + 0.05V 1.5V to 5.55V					V V
Analog Input Leakage Current (Note 10)		●		±1				±1	µA

DIGITAL AND DC ELECTRICAL CHARACTERISTICS (Note 5)

SYMBOL	PARAMETER	CONDITIONS		MIN	TYP	MAX	UNITS
V_{IH}	High Level Input Voltage	V_{CC} = 5.25V	●	2			V
V_{IL}	Low Level Input Voltage	V_{CC} = 4.75V	●			0.8	V
I_{IH}	High Level Input Current	$V_{IN} = V_{CC}$	●			2.5	µA
I_{IL}	Low Level Input Current	V_{IN} = 0V	●			–2.5	µA
V_{OH}	High Level Output Voltage	V_{CC} = 4.75V, I_O = 10µA V_{CC} = 4.75V, I_O = 360µA	● ●	4.0 2.4	4.64 4.62		V V
V_{OL}	Low Level Output Voltage	V_{CC} = 4.75V, I_O = 1.6mA	●			0.4	V
I_{OZ}	Hi-Z Output Leakage	$\overline{CS}$ = High	●			±3	µA
I_{SOURCE}	Output Source Current	V_{OUT} = 0V			–25		mA
I_{SINK}	Output Sink Current	$V_{OUT} = V_{CC}$			45		mA
R_{REF}	Reference Input Resistance (LTC1286)	$\overline{CS} = V_{CC}$ $\overline{CS}$ = GND			5000 55		MΩ kΩ
I_{REF}	Reference Current (LTC1286)	$\overline{CS} = V_{CC}$ $t_{CYC} \ge 640\mu s$, $f_{CLK} \le 25kHz$ $t_{CYC} = 80\mu s$, $f_{CLK} = 200kHz$	● ● ●		0.001 90 90	2.5 140 140	µA µA µA
I_{CC}	Supply Current	$\overline{CS} = V_{CC}$	●		0.001	±3.0	µA
		LTC1286, $t_{CYC} \ge 640\mu s$, $f_{CLK} \le 25kHz$ LTC1286, $t_{CYC} = 80\mu s$, $f_{CLK} = 200kHz$	● ●		200 250	400 500	µA µA
		LTC1298, $t_{CYC} \ge 720\mu s$, $f_{CLK} \le 25kHz$ LTC1298, $t_{CYC} = 90\mu s$, $f_{CLK} = 200kHz$	● ●		290 340	490 640	µA µA

DYNAMIC ACCURACY f_{SMPL} = 12.5kHz (LTC1286), f_{SMPL} = 11.1kHz (LTC1298) (Note 5)

SYMBOL	PARAMETER	CONDITIONS	MIN	TYP	MAX	UNITS
S/(N +D)	Signal-to-Noise Plus Distortion Ratio	1kHz/7kHz Input Signal		71/68		dB
THD	Total Harmonic Distortion (Up to 5th Harmonic)	1kHz/7kHz Input Signal		–84/–80		dB
SFDR	Spurious-Free Dynamic Range	1kHz/7kHz Input Signal		90/86		dB
	Peak Harmonic or Spurious Noise	1kHz/7kHz Input Signal		–90/–86		dB

AC CHARACTERISTICS (Note 5)

SYMBOL	PARAMETER	CONDITIONS		MIN	TYP	MAX	UNITS
t_{SMPL}	Analog Input Sample Time	See Operating Sequence			1.5		CLK Cycles
$f_{SMPL(MAX)}$	Maximum Sampling Frequency	LTC1286 LTC1298	● ●	12.5 11.1			kHz kHz
t_{CONV}	Conversion Time	See Operating Sequence			12		CLK Cycles
t_{dDO}	Delay Time, CLK↓ to D_{OUT} Data Valid	See Test Circuits	●		250	600	ns
t_{dis}	Delay Time, $\overline{CS}$↑ to D_{OUT} Hi-Z	See Test Circuits	●		135	300	ns
t_{en}	Delay Time, CLK↓ to D_{OUT} Enable	See Test Circuits	●		75	200	ns
t_{hDO}	Time Output Data Remains Valid After CLK↓	C_{LOAD} = 100pF			230		ns
t_f	D_{OUT} Fall Time	See Test Circuits	●		20	75	ns
t_r	D_{OUT} Rise Time	See Test Circuits	●		20	75	ns
C_{IN}	Input Capacitance	Analog Inputs, On Channel Analog Inputs, Off Channel Digital Input			20 5 5		pF pF pF

The ● denotes specifications which apply over the full operating temperature range.

Note 1: Absolute maximum ratings are those values beyond which the life of a device may be impaired.

Note 2: All voltage values are with respect to GND.

Note 3: These devices are specified at 5V. For 3V specified devices, see LTC1285 and LTC1288.

Note 4: Increased leakage currents at elevated temperatures cause the S/H to droop, therefore it is recommended that $f_{CLK} \geq 120kHz$ at 85°C, $f_{CLK} \geq 75kHz$ at 70° and $f_{CLK} \geq 1kHz$ at 25°C.

Note 5: V_{CC} = 5V, V_{REF} = 5V and CLK = 200kHz unless otherwise specified.

Note 6: Linearity error is specified between the actual end points of the A/D transfer curve.

Note 7: Two on-chip diodes are tied to each reference and analog input which will conduct for reference or analog input voltages one diode drop below GND or one diode drop above V_{CC}. This spec allows 50mV forward bias of either diode for $4.5V \leq V_{CC} \leq 5.5V$. This means that as long as the reference or analog input does not exceed the supply voltage by more than 50mV the output code will be correct. To achieve an absolute 0V to 5V input voltage range will therefore require a minimum supply voltage of 4.950V over initial tolerance, temperature variations and loading. For $5.5V < V_{CC} \leq 9V$, reference and analog input range cannot exceed 5.55V. If reference and analog input range are greater than 5.55V, the output code will not be guaranteed to be correct.

Note 8: The supply voltage range for the LTC1286 is from 4.5V to 9V, but the supply voltage range for the LTC1298 is only from 4.5V to 5.5V.

Note 9: Recommended operating conditions

Note 10: Channel leakage current is measured after the channel selection.

TYPICAL PERFORMANCE CHARACTERISTICS

Supply Current vs Sample Rate

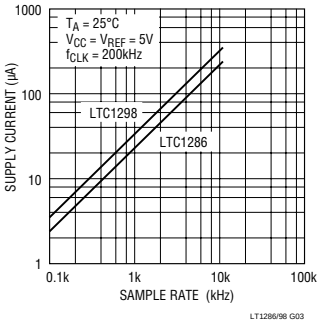

Supply Current vs Temperature

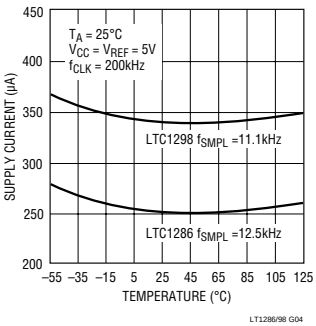

Shutdown Supply Current vs Clock Rate with $\overline{CS}$ High and $\overline{CS}$ Low

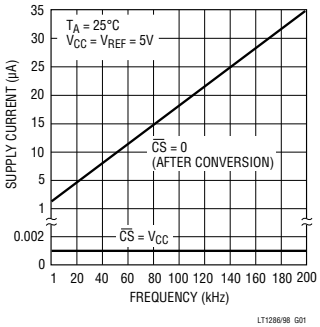

OPTEK

Product Bulletin OP165A
April 1993

GaAs Plastic Infrared Emitting Diodes
Types OP165A, OP165D

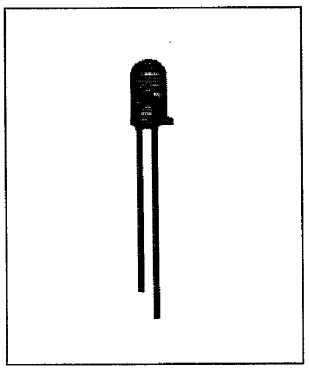

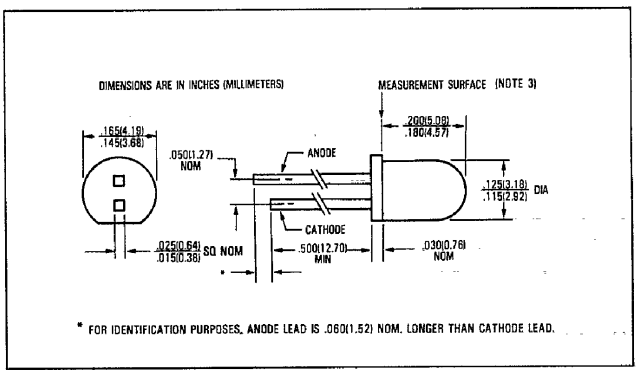

Features

- Narrow irradiance pattern
- Mechanically and spectrally matched to the OP505 and OP535 series devices
- Two power ranges
- Small package size for space limited applications
- T-1 package style

Description

The OP165 series devices are 935nm gallium arsenide infrared emitting diodes molded in IR transmissive amber tinted plastic packages. The narrow irradiance pattern provides high on-axis intensity for excellent coupling efficiency.

Replaces

K6500 series

Note

OP165B, C are replaced by OP163B, C which are equivalent except for the color of the package.

Absolute Maximum Ratings (T_A = 25°C unless otherwise noted)

Reverse Voltage	2.0V
Continuous Forward Current	50mA
Peak Forward Current (1 µs pulse width, 300 pps)	3.0A
Storage and Operating Temperature Range	-40°C to +100°C
Lead Soldering Temperature [1/16 inch (1.6mm) from case for 5 sec. with soldering iron]	260°C(1)
Power Dissipation	100mW(2)

Notes:
(1) RMA flux is recommended. Duration can be extended to 10 sec. max. when flow soldering. A max. of 20 grams force may be applied to the leads when soldering.
(2) Derate linearly 1.33mW/°C above 25°C.
(3) $E_{e(APT)}$ is a measurement of the average apertured radiant incidence upon a sensing area 0.081" (2.06mm) in diameter, perpendicular to and centered on the mechanical axis of the lens, and 0.590" (14.99mm) from the measurement surface. $E_{e(APT)}$ is not necessarily uniform within the measured area.

Typical Performance Curves

Percent Changes in Radiant Intensity vs Time

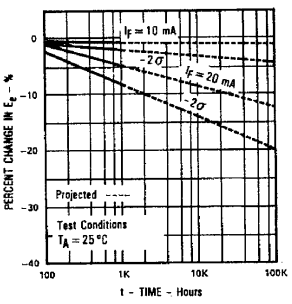

Coupling Characteristics OP165 and OP505

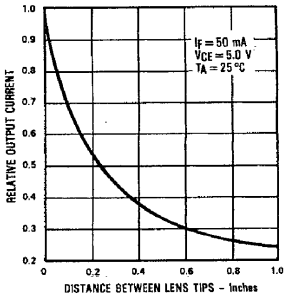

Figure A.40: OP165A Specification

Types OP165A, OP165D

Electrical Characteristics ($T_A = 25°C$ unless otherwise noted)

SYMBOL	PARAMETER		MIN	TYP	MAX	UNITS	TEST CONDITIONS
$E_{e(APT)}$	Apertured Radiant Incidence	OP165D OP165A	1.40 1.95		 3.70	mW/cm^2 mW/cm^2	$I_F = 20$ mA(3) $I_F = 20$ mA(3)
V_F	Forward Voltage				1.60	V	$I_F = 20$ mA
I_R	Reverse Current				100	µA	$V_R = 2.0$ V
λp	Wavelength at Peak Emission			935		nm	$I_F = 10$ mA
B	Spectral Bandwidth Between Half Power Points			50		nm	$I_F = 10$ mA
$\Delta\lambda p/\Delta T$	Spectral Shift with Temperature			+0.30		nm/°C	I_F = Constant
θ_{HP}	Emission Angle at Half Power Points			18		Deg.	$I_F = 20$ mA
t_r	Output Rise Time			1000		ns	$I_{F(PK)} = 100$ mA, PW = 10 µs, D.C. = 10%
t_f	Output Fall Time			500		ns	

Typical Performance Curves

Forward Voltage vs Forward Current

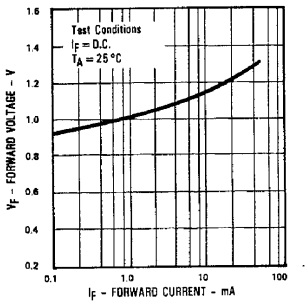

Forward Voltage and Relative Radiant Incidence vs. Forward Current

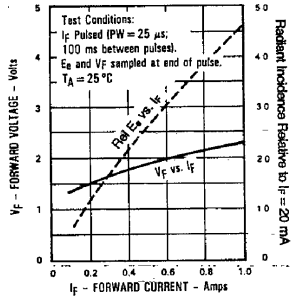

Forward Voltage vs Ambient Temperature

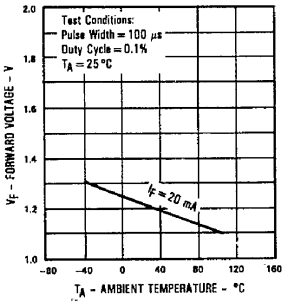

Rise Time and Fall Time vs Forward Current

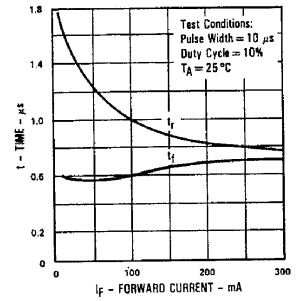

Relative Radiant Intensity and Wavelength at Peak Emission vs Ambient Temperature

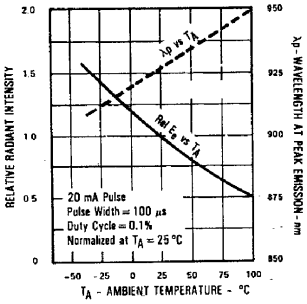

Relative Radiant Intensity vs Angular Displacement

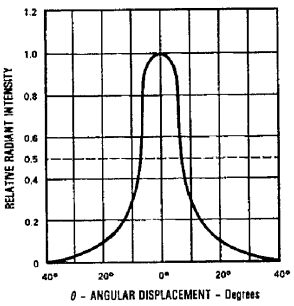

Optek Technology, Inc. 1215 W. Crosby Road Carrollton, Texas 75006 (214)323-2200 Fax (214)323-2396

NPN Silicon Photo-Transistor T1 plastic package

TDET500 Series

THREE-FIVE SYSTEMS

PACKAGE OUTLINE

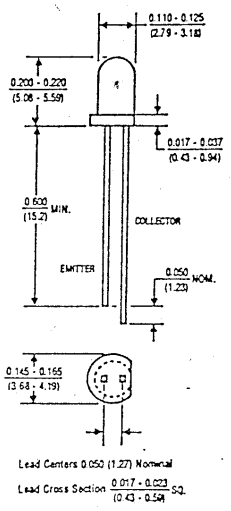

DIMENSIONS:
INCHES
(Millimeters)

FEATURES

- Excellent Spectral Match to Three-Five Systems' 940nm and 880nm Emitters
- Standard T1 (3mm) Plastic Package for Cost Effective, Commercial Use
- Custom Sorting, Grading and Environmental Stress Testing Is Available

APPLICATIONS

- Disk Drives
- Tape Drives
- Printers
- Optical Encoders
- Solid State Relays
- Photoelectric Controls
- Slotted Switches
- Reflective Switches
- Intrusion Alarms

DESCRIPTION

The TDET500 is an NPN silicon phototransistor in a standard T1 plastic package. The device combines high light sensitivity with cost effective packaging.

ABSOLUTE MAXIMUM RATINGS

Average Power Dissipation: 80mW
Derate Linearly from 25°C: 1.33mW/°C
Collector-Emitter Voltage: 30V
Operating & Storage Temp.: -40°C to +85°C
Soldering Time @ 260°C
1/16" From Case: 5 seconds

ELECTRO-OPTICAL CHARACTERISTICS

Symbol	Parameter		Conditions (T_A = 25°C)	Min.	Typ.	Max.	Units
I_L	Light Current	TDET500A	V_{CE} = 5.0V, H = 20mW/cm²	40			mA
		TDET500B	V_{CE} = 5.0V, H = 20mW/cm²	25			mA
		TDET500C	V_{CE} = 5.0V, H = 20mW/cm²	17			mA
		TDET500D	V_{CE} = 5.0V, H = 20mW/cm²	10			mA
		TDET500E	V_{CE} = 5.0V, H = 20mW/cm²	4.0			mA
I_D	Dark Current		V_{CE} = 10V, H = 0mW/cm²			100	nA
$V_{(BR)CEO}$	Collector-Breakdown Voltage		I_C = 100μA	30			V
$V_{(BR)ECO}$	Emitter-Breakdown Voltage		I_C = 100μA	5.0			V
$V_{CE(SAT)}$	Collector-Emitter Saturation Voltage		I_C = 0.5mA, H = 20mW/cm²		0.4		V
	H Source		Unfiltered Tungsten Color Temperature 2870°K				

THREE-FIVE SYSTEMS, Inc.
Phoenix, Arizona
TEL: 602-389-8600; FAX: 602-389-8801

THREE-FIVE SYSTEMS, Ltd.
Swindon, U.K.
TEL: 01793 618835; FAX: 01793 614127

Form DS (S) 001 9501

Figure A.41: TDET500C Specification

NPN Silicon Photo-Transistor, T1 plastic package
TDET500 Series

TYPICAL CHARACTERISTICS

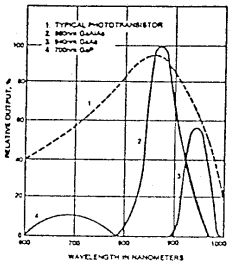

The 880nm wavelength significantly improves the coupling efficiency to typical phototransistors.

FIGURE 1
Spectral Matching Comparison

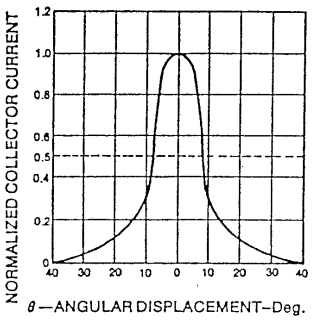

FIGURE 2—Normalized Collector Current vs Angular Displacement

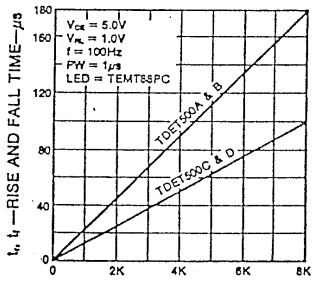

FIGURE 3—Rise and Fall Times vs Load Resistance

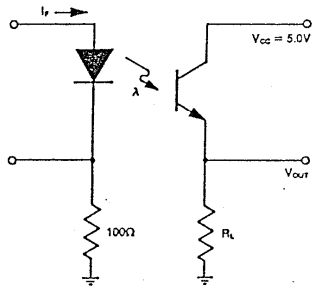

TEST CONDITIONS:
Light source is a pulsed LED with t_r and $t_f \leq 500$ns.
I_F is adjusted for V_{OUT} = 1.0 Volt.

FIGURE 4
Switching Time Test Circuit

THREE-FIVE SYSTEMS, Inc.
Phoenix, Arizona
TEL: 602-389-8600; FAX: 602-389-8801

THREE-FIVE SYSTEMS, Ltd.
Swindon, U.K.
TEL: 01793 618835; FAX: 01793 614127

HUMIDITY SENSORS

C□-M3

CONSTRUCTION

This miniature Humidity Sensor utilises a humidity sensitiive material screened onto a ceramic substrate. The resistance of the device varies exponentially with variation in relative Humidity. It has rapid response with outstanding reproductibility.

FEATURES

Wide humidity detecting range
Outstanding reproducibility
Rapid response
Low hysteresis
Small and Light-weight

APPLICATIONS

Air conditioners, Humidifiers, dehumidifiers
Controller
Copying machines
Clock, Weathermeter
Hydrometer, Hydrorecorder

SPECIFICATION

	C3-M3	C5-M3
RATED VOLTAGE	AC 1V RMS	
RATED POWER	AC 0.2mW	
OPERATING TEMPERATURE RANGE	0 - 60°C	
OPERATING HUMIDITY RANGE	90% RH (MAX)	
RECOMMENDED STORAGE CONDITION	10 - 40°C, 0 - 60% RH	
RECOMMENDED DRIVING FREQUENCY	500Hz TO 2khz	
STANDARD HUMIDITY RESISTANCE	31KΩ (25°C, 60% RH)	
HUMIDITY DETECTING ACCURACY	+/- 5% RH (25°C, 60% RH)	
TEMPERATURE DEPENDENCE	0.5% RH/°C	
MATERIAL OF FILTER CASE	ABS	
COLOUR OF FILTER CASE	DARK GREY	OFF-WHITE
DIMENSIONS	11x27.5x6mm	6.8x24.8x3mm

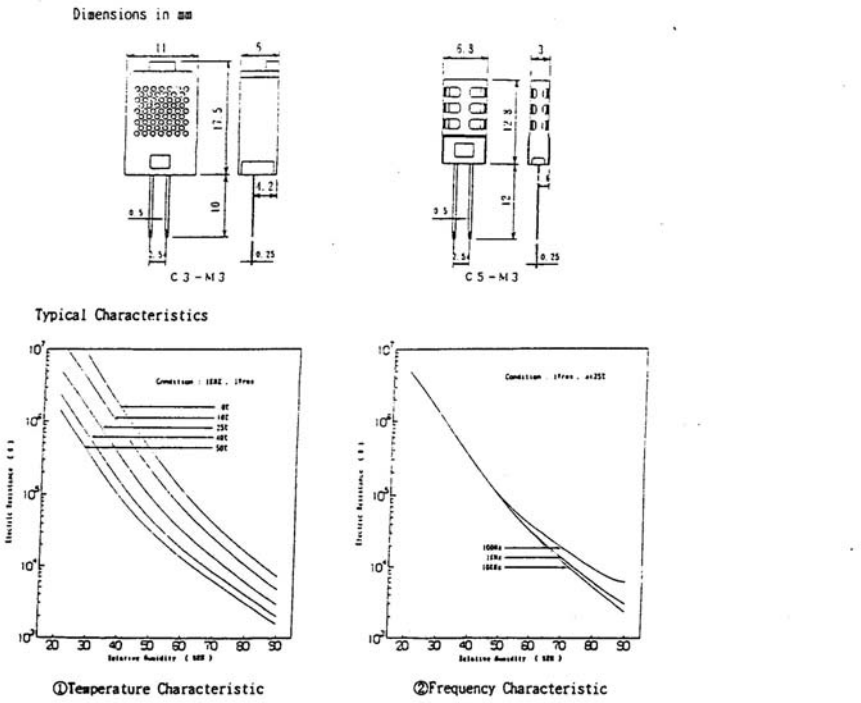

Figure A.42: C3M3 Humidity Sensor Specification

- 3-32VDC Solid State 240VAC @ 3A Relay
- PCB mounting (single in line package)
- Capable of switching up to 240V AC at 3 amps
- Optically Isolated
- Input Circuit
  - Control Voltage Range : 3-32V
  - DC Control Current : 15mA Max
  - Min. turn off voltage : 1V DC
  - Input Resistance : 2.2k min
- Output Circuit
  - Max. load current : 3A RMS
  - Nominal Line Voltage : 240V
  - AC Load Voltage Range : 24-280V AC
  - Min. Blocking Voltage : 600V AC
  - Max. one-cycle surge current : 80A RMS
  - Max. off-state leakage current : 5mA
  - Max. on-state voltage drop : 1.5V
  - Min. Load current : 50mA
  - Max. off-state dv/dt (V/s) : 100
  - Frequency Range : 47Hz-63Hz
- Operating Temp : -20C to +85C
- Dimensions :10(D) x 42(W) x 25(H)mm

Table A.1: Specifications for the Solid State 240VAC @ 3A Relay.

Appendix B

Modelling of the Time-to-Threshold Calibration Data

B.1 The Mk.I Prototype

Following is a detailed exploration of models to represent the calibration data for the 'Mk.I' prototype (from Section 7.3.1). The models examined were:

- an exponential function;
- a polynomial function;
- a power function;
- a cubic spline interpolation; and
- an interpolated (table-lookup) cubic spline.

The details of each of the above five possibilities and the results obtained are set out in the following subsections.

B.1.1 Exponential Function

By inspection of the threshold times (Figure 7.4), an exponential model was seen as possibly suitable to represent this data. A three-parameter exponential equation:

$$f = e^{a+b\cdot t+c\cdot t^2} \tag{B.1}$$

was examined. The exponential equation was then converted to a more suitable notation for the general purpose mathematical software package "MathCad™", namely:

$$f_{CO_2}(z,\hat{u}) = e^{u_0+u_1\cdot z+u_2\cdot z^2} \tag{B.2}$$

where:

$f_{CO_2}(z,\hat{u})$ represents the concentration of CO_2 as a function of the current sample time (z), and the model coefficients vector ($\hat{u}$).

The `genfit()` function within MathCad was then used to resolve the three coefficients (u_0, u_1, and u_2) to provide a fit to the calibration data. The format of the `genfit()` function is:

$$\texttt{result} := \texttt{genfit}(\texttt{xarray}, \texttt{yarray}, \texttt{guessarray}, \texttt{functionarray}) \tag{B.3}$$

where:

$xarray$	=	x coordinates for the data to optimise to;
$yarray$	=	y coordinates for the data to optimise to;
$guessarray$	=	a guess or start point array; and
$functionarray$	=	an array of the function to fit and it's partial derivative equations.

The partial differentials of Equation B.2 with respect to all free variables was then determined, i.e.

$$\frac{\delta f}{\delta u_0} = e^{u_0+u_1\cdot z+u_2\cdot z^2} \tag{B.4}$$

$$\frac{\delta f}{\delta u_1} = e^{u_0+u_1\cdot z+u_2\cdot z^2}\cdot z \tag{B.5}$$

$$\frac{\delta f}{\delta u_2} = e^{u_0+u_1\cdot z+u_2\cdot z^2}\cdot z^2 \tag{B.6}$$

The x-y coordinate data set as well as the start point or guess array were then provided. The values used for the 'baseline + 50' calculations are:

$$vx = \begin{bmatrix} Time\ at\ High\ Cal\% \\ \vdots \\ Time\ at\ LowCal\% \end{bmatrix} = \begin{bmatrix} 21.4 \\ 46.0 \\ 75.1 \\ 158.4 \\ 180.6 \\ 200.0 \end{bmatrix} \tag{B.7}$$

$$vy = \begin{bmatrix} High\ Cal\% \\ \vdots \\ Low\ Cal\% \end{bmatrix} = \begin{bmatrix} 10 \\ 5 \\ 2 \\ 1 \\ .5 \\ .4 \end{bmatrix} \tag{B.8}$$

$$vg = \begin{bmatrix} Parameter\ 1\ Guess \\ Parameter\ 2\ Guess \\ Parameter\ 3\ Guess \end{bmatrix} = \begin{bmatrix} 1 \\ 1 \\ 0 \end{bmatrix} \tag{B.9}$$

where:

vx = the Time-to-Threshold vector;

vy = the CO_2 % concentration at each Time-to-Threshold;

vg = a guess or starting vector;

Due to problems with overflows within MathCad, some of the values were scaled down by a factor of 10, 100, or 1000. These data sets were then configured within the MathCad workbook and the exponential coefficients calculated as set out in Figure B.1. From these results, the concentration of CO_2 for a measured '$baseline + 50$' threshold, the fitted exponential equation is:

$$f_{CO_2}(t) = e^{3.032 - 3.597 \cdot t + 0.871 \cdot t^2} \tag{B.10}$$

The full set of model coefficients for the different baseline calibrations appears in Table B.1. The fit of exponential equations to the calibration data is illustrated in Figure B.2, and B.3. The fit for these curves, whilst reasonable for short threshold times, did not adequately describe longer times (beyond approximately 70 seconds). Also, since this model did not actual pass through the measured calibration data and did not hold true for long threshold times, its overall accuracy and validity was highly questionable. However, this exponential model was used for the Mk.I system as other models were not available at that time. Further exploration has yielded more suitable models as shown in the next subsections.

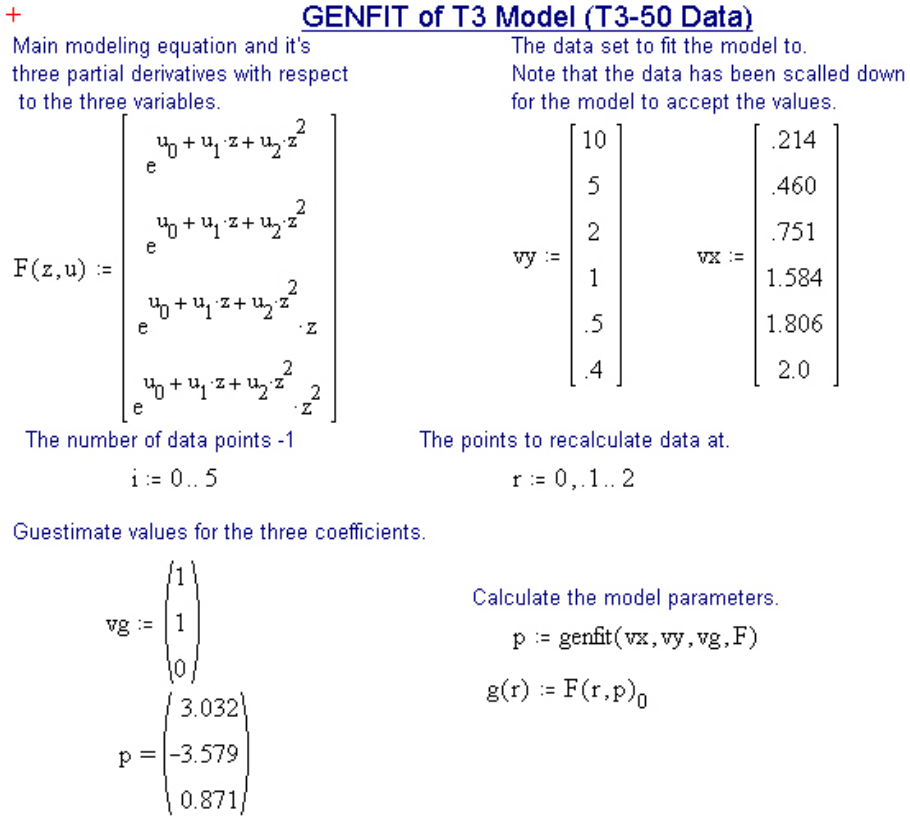

Figure B.1: Example model calculation within the MathCad simulation package.

Table B.1: Coefficients for the exponential model used to describe the threshold times for the Mk.I calibration data.

Model	u_0	u_1	u_2
baseline + 10	2.786	-5.678	1.905
baseline + 20	2.803	-4.481	1.326
baseline + 30	2.841	-3.919	0.996
baseline + 40	2.889	-3.445	0.671
baseline + 50	3.032	-3.597	0.871

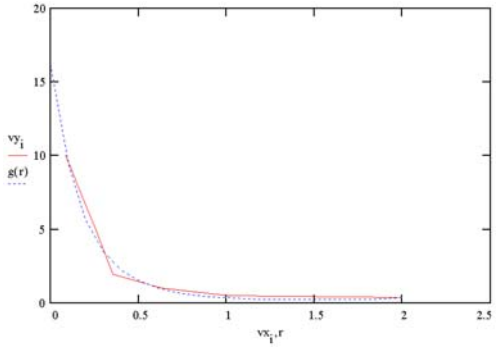

(a) Fit curve for the baseline+10 `genfit()` model.

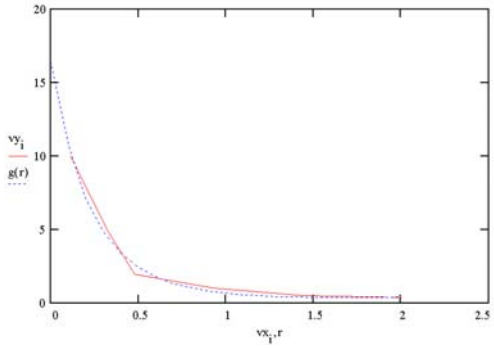

(b) Fit curve for the baseline+20 `genfit()` model.

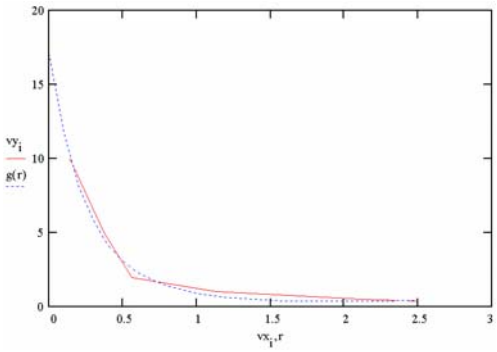

(c) Fit curve for the baseline+30 `genfit()` model.

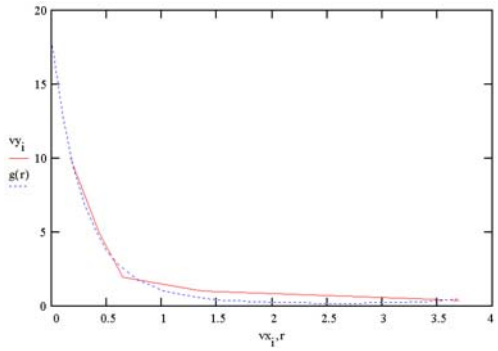

(d) Fit curve for the baseline+40 `genfit()` model.

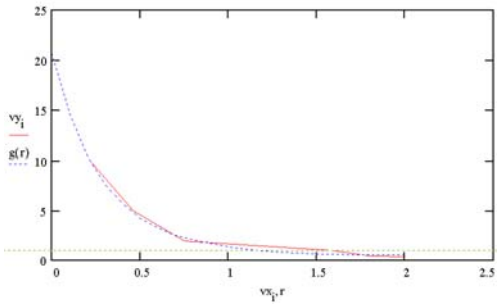

(e) Fit curve for the baseline+50 `genfit()` model.

Figure B.2: Exponential model curves for the `genfit()` model as provided by MathCad.

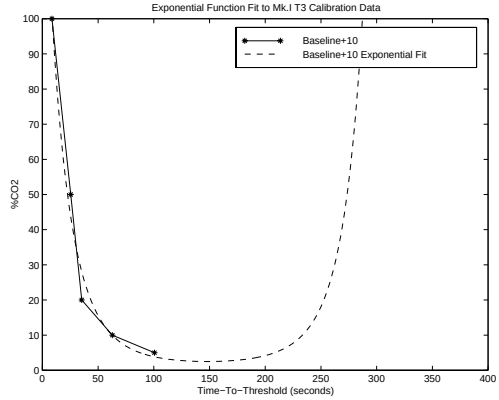

(a) Fit curve for the baseline+10 `genfit()` model.

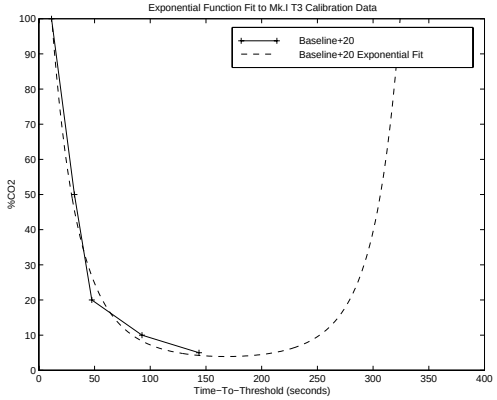

(b) Fit curve for the baseline+20 `genfit()` model.

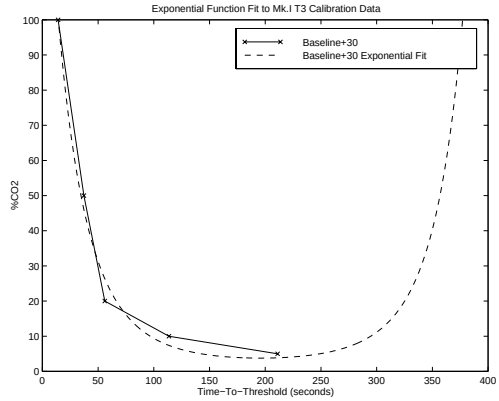

(c) Fit curve for the baseline+30 `genfit()` model.

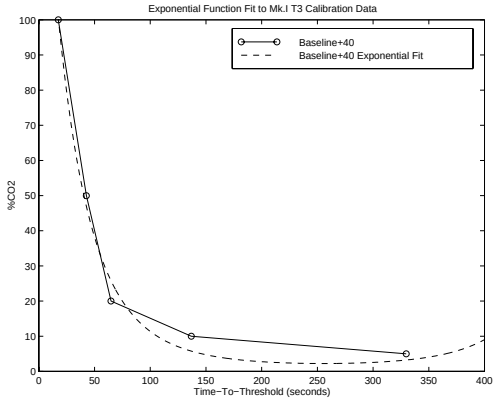

(d) Fit curve for the baseline+40 `genfit()` model.

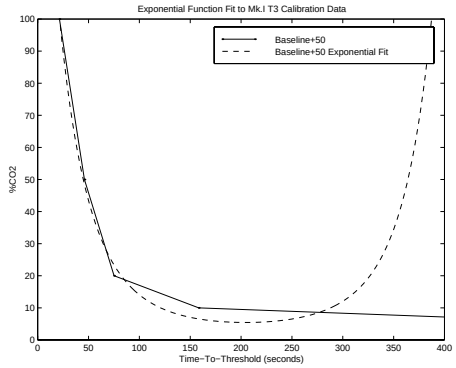

(e) Fit curve for the baseline+50 `genfit()` model.

Figure B.3: Exponential model curves reproduced from the generated model parameters.

B.1.2 Polynomial Function

An nth order polynomial was explored to describe the calibration values, being:

$$y = p_1.x^2 + p_2.x + p_3 \tag{B.11}$$

These polynomials were generated using the `polyfit()` function as part of the "MATLAB™" package. Three polynomials orders were examined to fit all threshold calibration values, being:

$$y_{(2nd)} = p_1.x^2 + p_2.x + p_3 \tag{B.12}$$

$$y_{(3rd)} = p_1.x^3 + p_2.x^2 + p_3.x + p_4 \tag{B.13}$$

$$y_{(4th)} = p_1.x^4 + p_2.x^3 + p_3.x^2 + p_4.x + p_5 \tag{B.14}$$

The result of the fit is illustrated in Figure B.1.2, with coefficients appearing in Tables B.2, B.3, and B.4. As shown in each of these figures, the fit to the desired data was very loose and deemed unsuitable for implementation, with higher order functions resulting in a worse fit.

This was due to the inability of MATLAB to correctly fit this very 'exponential-shaped' data with the given endpoint boundaries as provided by the calibration data. To check this, the end points of the 'baseline+10' data were linearly extended beyond physically permissible ranges (i.e. time less than zero, concentration less than 0%) and several polynomials fit to this extended data. Figure B.5 shows that even with the end point boundaries extended beyond the region of interest, the `polyfit()` function was still unable to adequately model the calibration data.

Whilst it is still possible that a series of polynomials suitable to model this data for use within the model do exist, they were unable to be found using the MATLAB package.

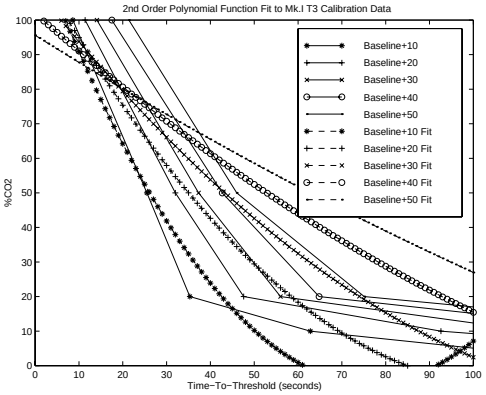

(a) Example 2nd order polynomial fit.

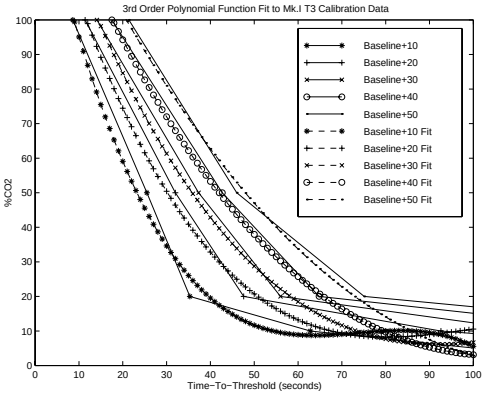

(b) Example 3rd order polynomial fit.

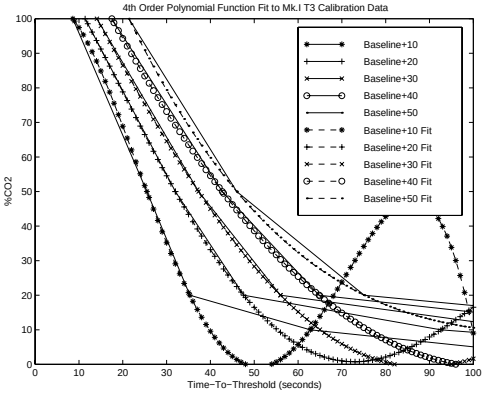

(c) Example 4th order polynomial fit.

Figure B.4: Example polynomial fit to measured "T3" threshold times.

Table B.2: Coefficients for the 2nd order polynomial fit to the threshold times for the Mk.I calibration data.

Model	p_1	p_2	p_3
baseline + 10	0.0217	-3.3191	121.9090
baseline + 20	0.0106	-2.2717	116.5576
baseline + 30	0.0053	-1.5959	109.2147
baseline + 40	0.0025	-1.1152	101.9491
baseline + 50	0.0011	-0.7969	95.6057

Table B.3: Coefficients for the 3rd order polynomial fit to the threshold times for the Mk.I calibration data.

Model	p_1	p_2	p_3	p_4
baseline + 10	-0.0004	0.0792	-5.7251	144.7738
baseline + 20	-0.0002	0.0459	-4.4082	145.4803
baseline + 30	-0.0001	0.0312	-3.7389	147.5231
baseline + 40	0.0000	0.0215	-3.2242	150.4600
baseline + 50	0.0000	0.0149	-2.8002	152.0197

Table B.4: Coefficients for the 4th order polynomial fit to the threshold times for the Mk.I calibration data.

Model	p_1	p_2	p_3	p_4	p_5
baseline + 10	0.0000	0.0047	-0.2472	1.6222	101.4568
baseline + 20	0.0000	0.0007	-0.0358	-1.8509	124.7026
baseline + 30	0.0000	0.0002	-0.0055	-2.3020	132.9328
baseline + 40	0.0000	0.0000	0.0107	-2.7039	143.8777
baseline + 50	0.0000	-0.0001	0.0328	-3.8699	168.8516

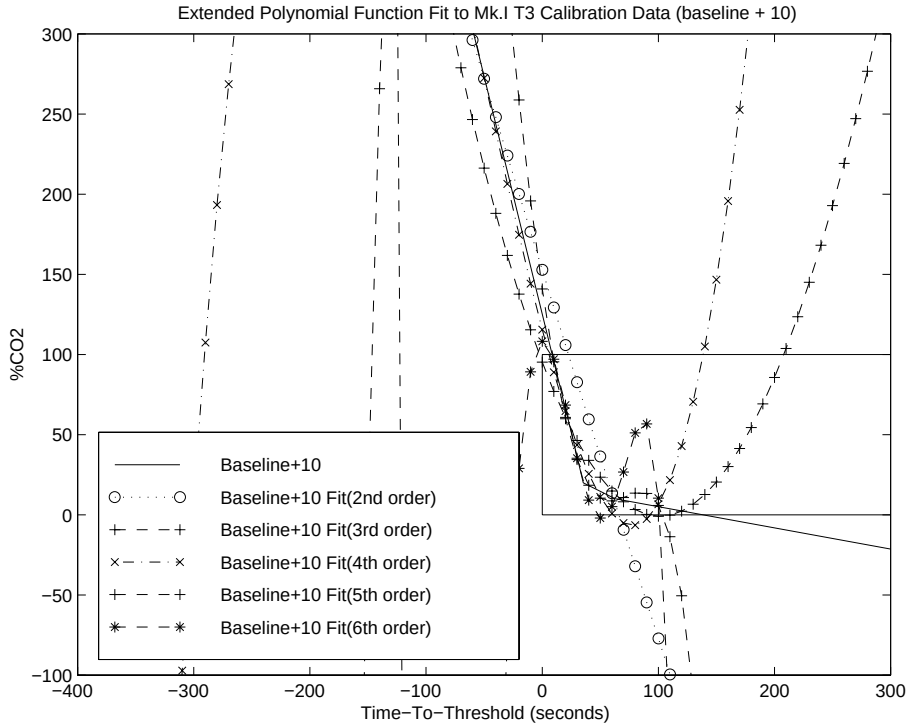

Figure B.5: Example polynomial fit using extended data for the 'baseline + 10' data using the MATLAB simulation package. The region of interest constrained by 0 to 100% CO_2 is contained within the box.

B.1.3 Power Function

This model was developed using the "Microsoft Excel™" trendline package to fit a power series:

$$y = a \times x^b \tag{B.15}$$

to the calibration data. The resulting model is shown in Table B.5 and Figure B.6.

Table B.5: Power fit parameters to measured 'T3' threshold times.

Model	Model Parameters	R^2
baseline + 10	$y = 1768.1 \times x^{-1.2495}$	0.9739
baseline + 20	$y = 2258.1 \times x^{-1.2059}$	0.9671
baseline + 30	$y = 2328.7 \times x^{-1.1455}$	0.9778
baseline + 40	$y = 2107.1 \times x^{-1.0621}$	0.9756
baseline + 50	$y = 1497.5 \times x^{-0.9334}$	0.9533

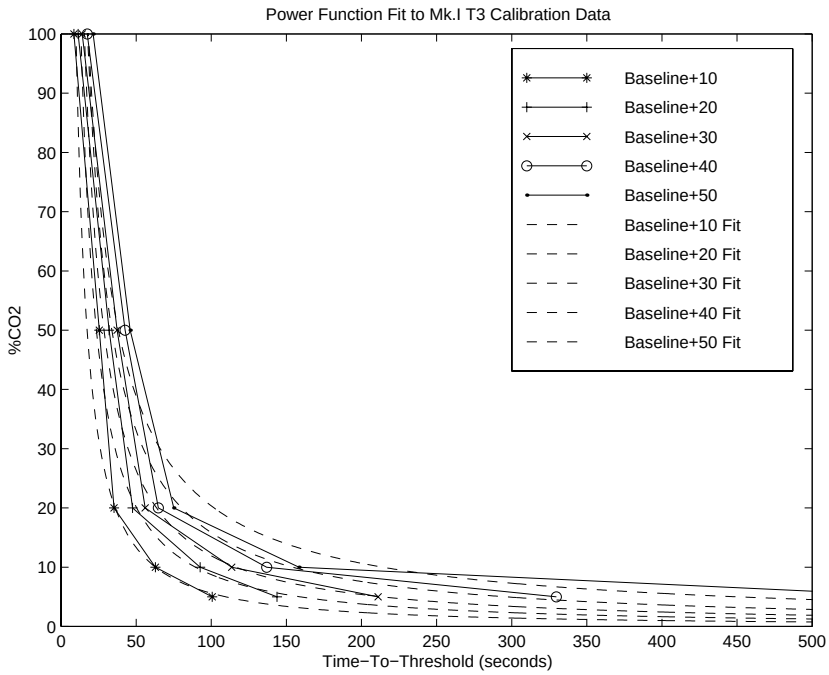

Figure B.6: Power fit curves to measured "T3" threshold times.

This model did show merit, however significant errors are evident when compared to

the calibration set. Also, as the order of this model could not be modified within 'Excel', exploration into improvements of this model could not be performed. This model however could perhaps have been optimised using the MathCad tool, however was unable to be performed due to singularity errors within MathCad. Given the superior results of the interpolated cubic spline fit (Section B.1.4) this was not pursued further.

B.1.4 Cubic Spline Function

The `spline()` function within MATLAB was also explored as a possible model alternative as shown in Figure B.7. As shown the spline function was also unable to cope with the end points in each data set hence was investigated no further.

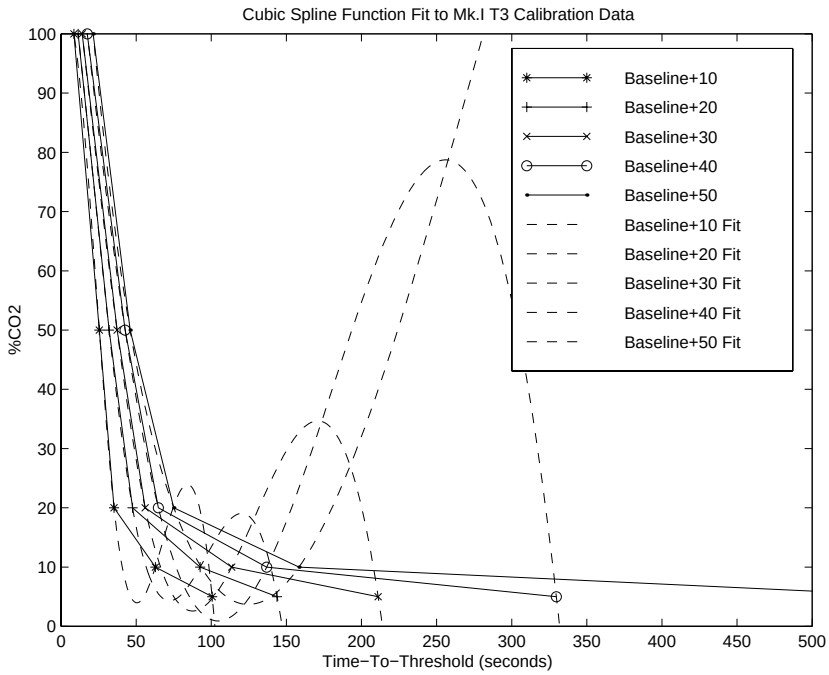

Figure B.7: Spline fit curves to measured 'T3' threshold times.

B.1.5 Interpolated (Table-Lookup) Cubic Spline

The cubic interpolation function `interp1()` within MATLAB was also examined and met with great success. This function was able to interpret between each data point using a separate cubic spline for each interval, resulting in the fit shown in Figure B.8.

However, this function however could only produce a lookup table rather than specific model parameters, and because this required considerable memory (minimum of 3kbytes for $\pm 1\%$ accuracy, more memory for greater accuracy), it was too large to implement in the Mk.I hardware system. However it was used to examine the system's performance at a later date. The other disadvantage of this model was that it could not extrapolate data beyond the values given to the function. This meant that the model could not cope with measurement times beyond the span of the calibration data and therefore would set a lower limit for the CO_2 concentration values measurable by the instrument.

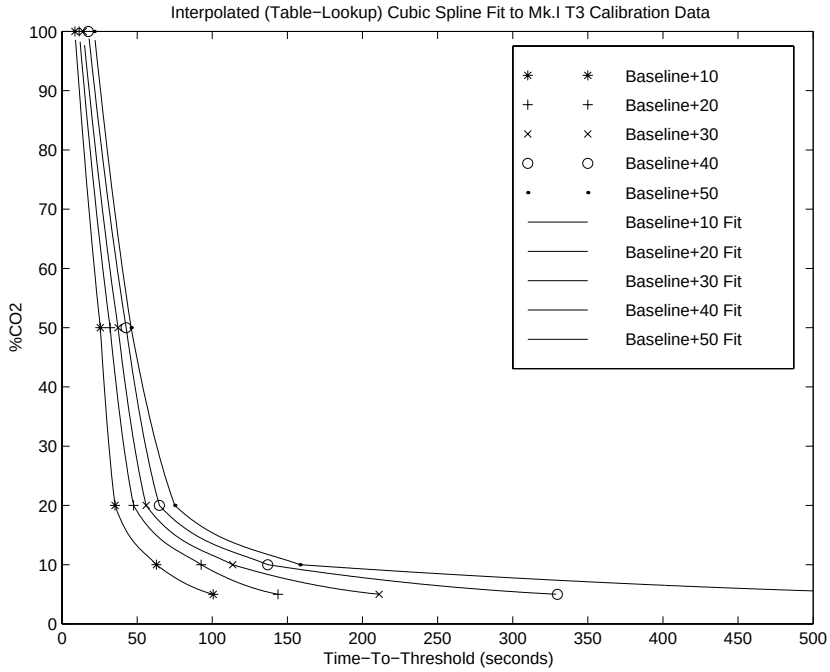

Figure B.8: Interpolated cubic spline fit curves to measured "T3" threshold times.

B.2 The Mk.II Prototype

Following is a detailed exploration of models to represent the calibration data for the 'Mk.II' prototype (from Section 7.4). The models examined were:

- an exponential function;
- a cubic spline interpolation; and
- an interpolated (table-lookup) cubic spline.

The details of each of the above three possibilities and the results obtained are set out in the following subsections.

B.2.1 Exponential Function

This used the same modelling mechanism to that shown in Section B.1.1. The results are seen in Figure B.2.1.

Table B.6: Coefficients for the exponential model used to describe the threshold times for the Mk.II calibration data.

Model	u_0	u_1	u_2
baseline + 10	3.85	-19.258	19.025
baseline + 20	4.022	-12.98	8.853
baseline + 30	4.195	-10.757	5.668
baseline + 40	4.835	-11.881	5.371
baseline + 50	4.609	-9.73	3.789

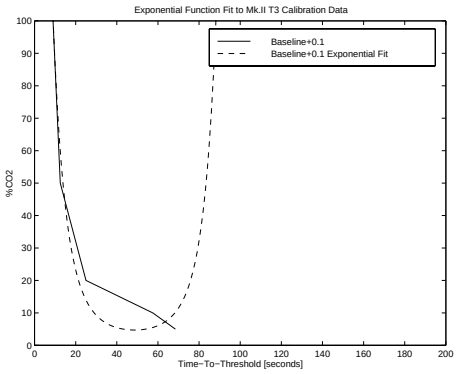

(a) Fit curve for the baseline+0.1V `genfit()` model.

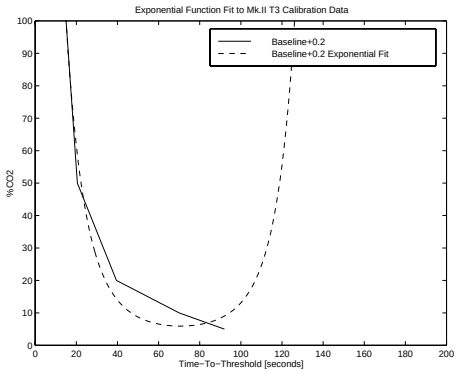

(b) Fit curve for the baseline+0.2V `genfit()` model.

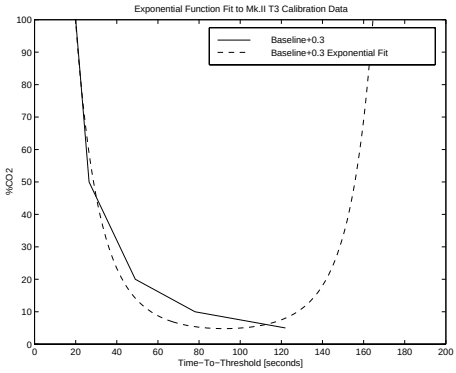

(c) Fit curve for the baseline+0.3V `genfit()` model.

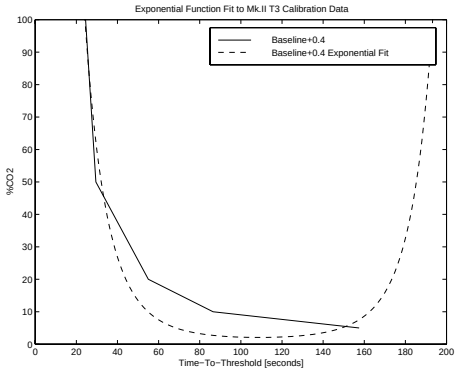

(d) Fit curve for the baseline+0.4V `genfit()` model.

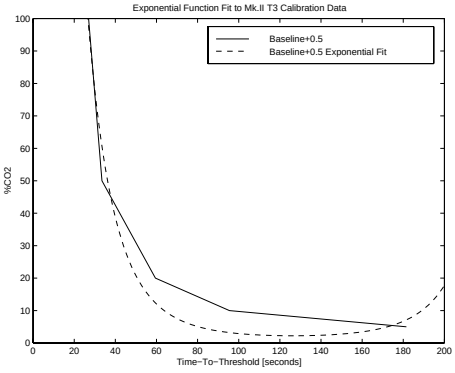

(e) Fit curve for the baseline+0.5V `genfit()` model.

Figure B.9: Mk.II exponential model curves reproduced from the generated model parameters.

B.2.2 Power Function

The 'Power' function was examined in a similar manner to Section B.1.3. The results are shown in Figure B.10) with the calculated coefficients shown in Table B.7.

Table B.7: Mk.II power fit parameters to measured "T3" threshold times.

Model	Model Parameters	R^2
baseline + 10	$y = 1584.3 \times x^{-1.3202}$	0.9722
baseline + 20	$y = 6004.1 \times x^{-1.5448}$	0.9893
baseline + 30	$y = 10972 \times x^{-1.6088}$	0.9944
baseline + 40	$y = 11231 \times x^{-1.5518}$	0.9782
baseline + 50	$y = 12186 \times x^{-1.5307}$	0.9757

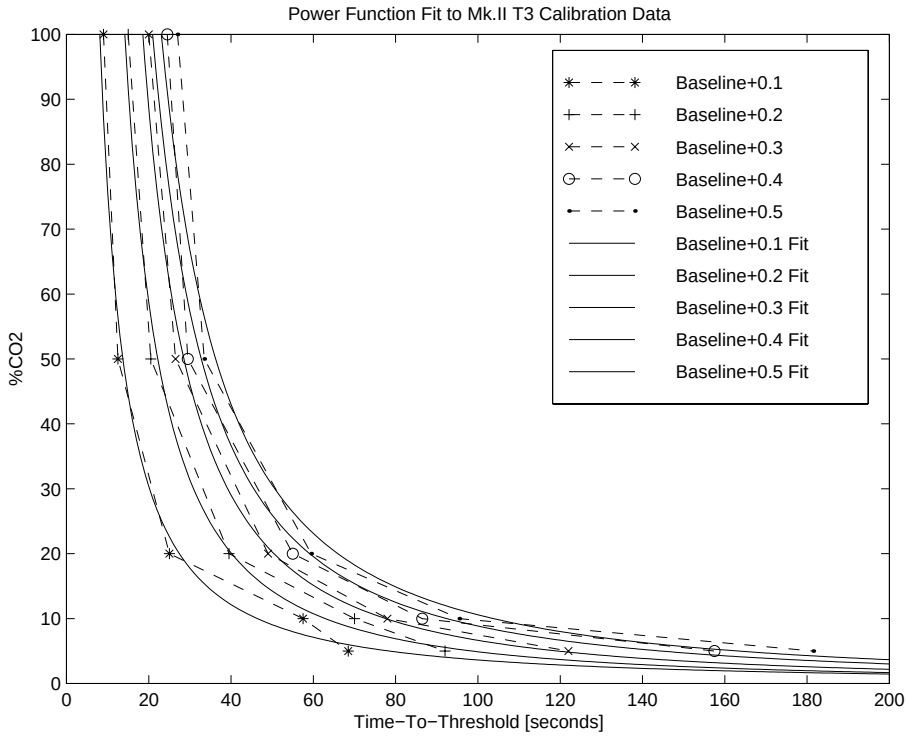

Figure B.10: Power fit curves to measured "T3" threshold times.

B.2.3 Interpolated (Table-Lookup) Cubic Spline

The interpolated function was modelled similar to that shown in Section B.1.5

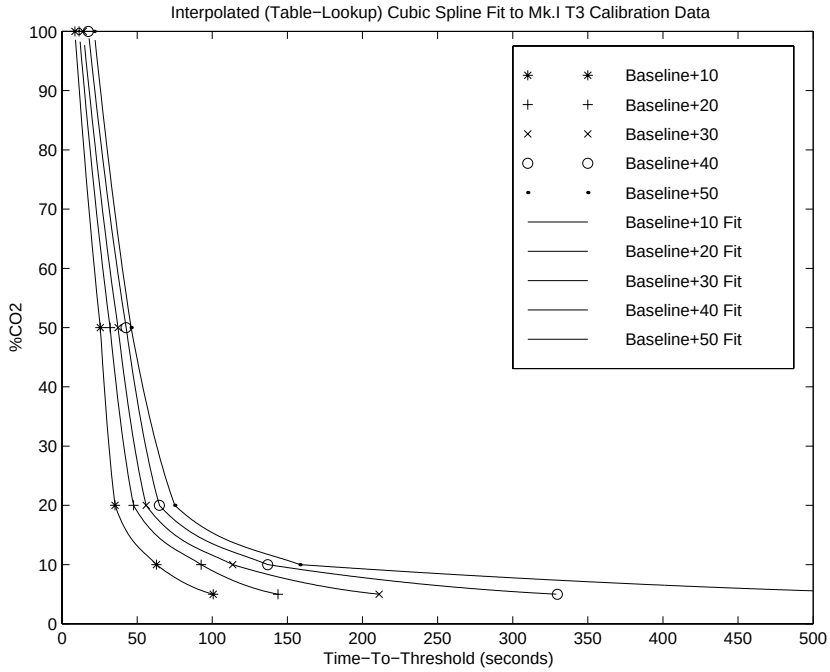

Figure B.11: Interpolated cubic spline fit curves to measured 'T3' threshold times.

Appendix C

Software

All software code including microprocessor/target system software, controlling PC software, analysis software and scripts can be found on the accompanying CDROM. (Chapter 9 contains an overview of this software with further information about the accompanying CDROM in Appendix G)

Assembly language, C, and QuickBasic code is supplied for the various prototypes, as well as extra miscellaneous software components.

Table C.1: Directory structure of the SOFTWARE folder.

SOFTWARE	
└ MKI	Software for the Mk.I prototype
└ MKII	Software for the Mk.II prototype
└ MODEL	Modelling Software
└ MISC	Miscellaneous Software

Appendix D

CO_2 Properties & Measurable Effects

D.1 Carbon Dioxide Fundamental Properties

Table D.1: Fundamental Properties of CO_2. Table 1.

Molecule	Carbon Dioxide, CO_2
Description	Colourless, odourless gas
Lewis Structure	Carbon has four valence electrons Oxygen has six valence electrons Linear, Non-polar 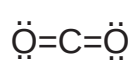 (= is a double bond)
Molecular Weight	44.01 (44 approx)
Bond Lengths	1.1600 Angstrom (Determined by IR techniques)
Freezing Point	-56.6°C @ 5.2 atm
Melting Point	-56.6°C @ 5.2 atm
Triple Point	-56.6°C @ 5.2 atm (1kg per cm^2)
Boiling Point	-78.5°C
Sublimation point	-78.5°C @ 1 atm
Heat of Formation	94.05kg cal per gram mole (169.450 Btu per lb mole)

Table D.2: Fundamental Properties of CO_2. Table 2.

Critical Temperature Critical Pressure	31.0°C 72.80 atm
Density Gas Liquid Density Solid Density	1.98 g/L @ 0°C 0.914 kg/L@ 0°C and 34.4 atm 1.512 kg/L @ -56.6°C
Thermal Conductivity	41.7 10^{-6} cal/sec-cm^2/(°C/cm) @ 37.8°C
Velocity of sound	259 m/sec @ 0°C (Air 331 m/sec @ 0°C)
Latent heat of vaporisation	83.12 gm cal per gm at the triple point, and 101.03 Btu/lb at 0°C
Solubility in Cold Water (temperature as superscript)	171.3^0cm^3 0.348^0g 0.145^{25}g
Solubility in Hot Water (temperature as superscript)	90.1^{20}cm^3 0.097^{40}g 0.058^{60}g
Solubility in other temp waters	0.1 g/100cc H_2O @ 1 atm @ 23°C
Fundamental Vibrational Frequency Symmetrical Stretch Bend Anti symmetrical Stretch	 1333cm^{-1} 667cm^{-1} 2349cm^{-1}
IR Absorption Bands	2349.3 cm^{-1}, 4.256μm 2350 cm^{-1}, 4.26μm 2330 cm^{-1}, 4.3μm 667 cm^{-1}, 14.98μm

(for example Hampel & Hawley, 1973; Gordon & Ford, 1972; Kennedy & Holser, 1966; Barnes et al., 1966; Straughan, 1976; Robinson, 1980)

D.2 Chemical Reactions Involving CO_2

D.2.1 Chemical Reactions

$$CO_{2(aq)} + H_2O_{(l)} \quad \rightleftharpoons \quad H_2CO_{3(aq)} \tag{D.1}$$

$$CaCO_{3(s)} + 2HCl_{(aq)} \quad \rightharpoonup \quad CaCl^{2+}_{2\,(aq)} + H_2O_{(l)} + CO_{2(aq)} \tag{D.2}$$

$$CaCO_{3(s)} \rightharpoonup CaO_{(s)} + CO_{2(aq)} \quad \text{(D.3)}$$

$$CaCO_{3(s)} \overset{heat 900^oC}{\rightleftharpoons} CaO_{(s)} + CO_{2(g)} \quad \text{(D.4)}$$

$$CO_{(g)} + H_2O_{(g)} \rightleftharpoons CO_{2(g)} + H_{2(g)} \quad \text{(D.5)}$$

$$Ca(HCO_3)_{2(aq)} \rightleftharpoons CaCO_{3(s)} + H_2O_{(l)} + CO_{2(g)} \quad \text{(D.6)}$$

$$5CO_{(g)} + I_2O_{5(s)} \rightleftharpoons I_{2(g)} + 5CO_{2(g)} \quad \text{(D.7)}$$

$$2NaHCO_{3(s)} \rightleftharpoons Na_2CO_{3(s)} + CO_{2(g)} + H_2O_{(g)} \quad \text{(D.8)}$$

$$2LiOH_{(aq)} + CO_{2(g)} \rightharpoonup Li_2CO_{3(aq)} + H_2O_{(l)} \quad \text{(D.9)}$$

$$CH_{4(g)} + 2O_{2(g)} \rightharpoonup CO_{2(g)} + 2H_2O_{(l)} \quad \text{(D.10)}$$

D.2.2 Ionic Compositions

$$Ca(OH)_{2(s)} \rightleftharpoons {Ca^{2+}}_{(aq)} + 2{OH^-}_{(aq)} \quad \text{(D.11)}$$

$$CaCO_{3(s)} \rightleftharpoons {Ca^{2+}}_{(aq)} + {CO_3^{2-}}_{(aq)} \quad \text{(D.12)}$$

$$CO_{2(aq)} + H_2O_{(l)} \rightleftharpoons {H^+}_{(aq)} + {HCO_3^-}_{(aq)} \quad \text{(D.13)}$$

$$Ca(OH)_2 + CO_2 \rightleftharpoons {Ca^{2+}}_{(aq)} + 2OH^- + CO_2 \quad \text{(D.14)}$$

$$\rightleftharpoons {Ca^{2+}}_{(aq)} + H_2O + {CO_3}^{2-}{}_{(aq)}$$

D.2.3 Solubility Constants, K_{sp}

Solution	*Solubility*$[g^{-g}]$
$CaCO_3$	5×10^{-9}
$Ca(OH)_2$	1.3×10^{-6}

D.3 Electrochemical Properties of Calcium Hydroxide

Initial investigations into the electrochemical properties of calcium hydroxide ($Ca(OH)_2$) were performed to determine if conductivity (or other electrical method) could be used to identify the CO_2 concentration using this indicator chemical.

D.3.1 Theoretical Basis

During any turbidity measurement (wet chemical analysis method) using $Ca(OH)_2$ as the chemical indicator, there would be several distinctly different chemicals present, namely:

- water ($H_2O_{(aq)}$);
- carbon dioxide ($CO_{2(g)}$);
- calcium hydroxide ($Ca(OH)_{2(aq)}$);
- calcium carbonate ($CaCO_{3(s)}$); and
- $Ca(HCO_3)_{2(aq)}$.

Each of these substances was assumed to have slightly different dielectric properties. The only reported permittivities were that of CO_2 ($\epsilon_r = 1.4492$ (Lide, 2001, p.6–153)) and water (distilled, $\epsilon_r = 81$ (Kraus, 1991, p134)).

It was hypothesised that it was possible to measure an arbitrary ratio of these combined constituents within the reaction cell during a turbidity measurement. Any variation in the ratio would result in a variation of the combined permittivity, which could then be measured as either a conductance, or capacitance measurement.

It is known (Kraus, 1991, p96) that for a parallel plate capacitor, the voltage across the plates is a function of the plate separation and the electric field present.

$$V = Ed \tag{D.15}$$

where:

V is the voltage across the capacitor plates [Volts];
E is the electric field; and
d is the capacitor plate separation [m].

It is also known that the charge across the plates is a function of the flux density and the plate area.

$$Q = DA \tag{D.16}$$

where:

- Q is the charge on one plate;
- D is the flux density between the plates; and
- A is the plate area [m^2].

The flux density magnitude between the parallel plates, is then a function of the permittivity and the electric field.

$$D = \epsilon E \tag{D.17}$$

where:

- ϵ is the permittivity of the dielectric between the plates [Fm^{-1}].

By combining equation D.16 and D.17.

$$Q = \epsilon EA \tag{D.18}$$

The capacitance between the plates is equal to the charge on one plate divided by the voltage across them.

$$\begin{aligned} C &= \frac{Q}{V} \\ &= \frac{\epsilon EA}{Ed} \\ &= \frac{\epsilon A}{d} \end{aligned} \tag{D.19}$$

where:

- C is the capacitance; and
- ϵ is the permittivity of the dielectric between the plates [Fm^{-1}].

By differentiating equation D.19 with respect to time (Equation D.20), it is seen that any variation of the combined permittivity of the solution will vary the capacitance as

measured by a parallel plate capacitor provided both the surface area and separation distance remain constant.

$$\frac{\delta C}{\delta t} = \frac{A}{d}\frac{\delta \epsilon}{\delta t} \tag{D.20}$$

D.3.2 Methodology and Equipment

A small parallel plate capacitor was constructed using PCB material which was then mounted onto an acrylic plastic bracket with 1cm separation. Electrical leads were then soldered onto these plates and connected to the multimeter capable of measuring capacitance (Figure D.1). A bubbling port was added to the assembly to inject the sample gas into the test tube. This port was located on the outer side of one of the capacitor plates to minimise bubbles appearing between the plates and interfering with the capacitance measurements. The test tube was then filled with the $Ca(OH)_2$ indicator solution and gases of different CO_2 concentrations were injected into the test tube. Capacitance measurements were then taken at 5 second increments.

D.3.3 Results

Several sets of capacitance measurements were taken over time with varying concentrations of carbon dioxide in the sample gas. These results are reported in Figure D.2.

It can be seen that there is a clear causal relationship between the concentration of carbon dioxide in the sample gas and the capacitance waveform over time. The trough point in the middle of each waveform was found to correspond with the point of maximum precipitate production. This then showed that capacitance measurements would directly relate to any optical measurement of the precipitate through the cell and could be used as the basis for a non optical turbidity sensor.

(a) Photograph of the capacitor sensor head comprising of the parallel plate capacitor, acrylic seperator/handle and electrical wires.

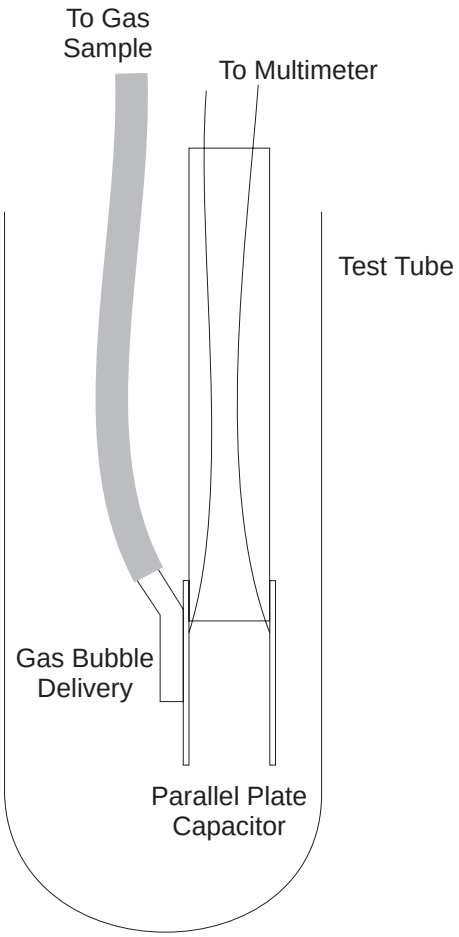

(b) Layout of the capacitor sensor within the test tube.

Figure D.1: Photograph and layout diagram of the capacitive sensor used to examine the electrochemical properties of $Ca(OH)_2$.

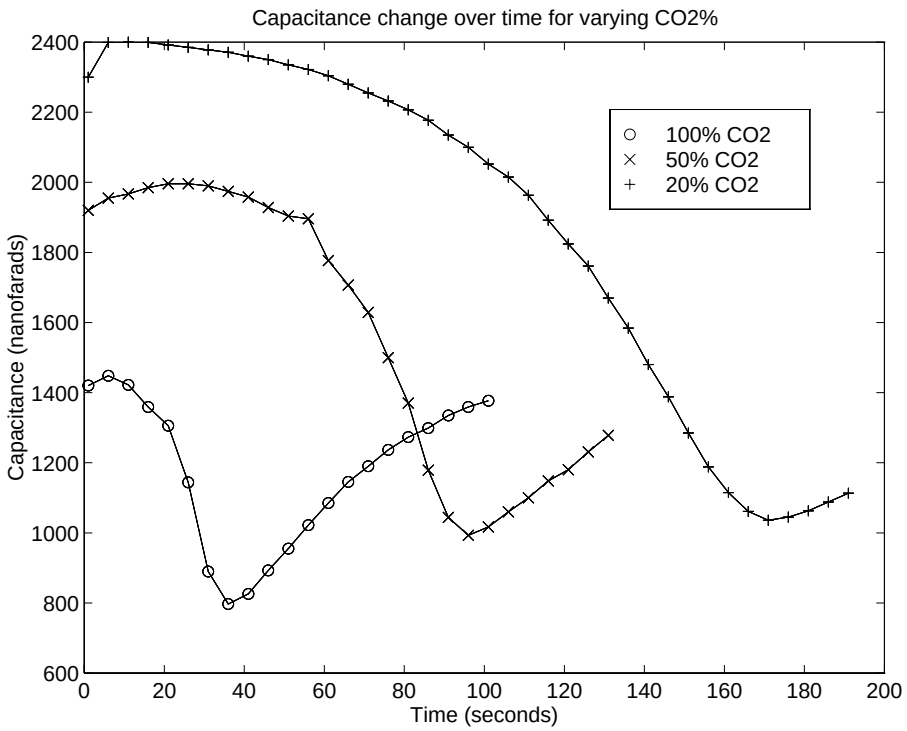

Figure D.2: Causal effect between carbon dioxide concentration and capacitance over time.

D.4 Chemical Resistance Charts

Table D.3: Chemical compatibility of all fabrication materials to the chemicals used (Reproduced from Cole-Parmer catalog, 1997, Page 1364-1372).

Chemical	Polycarbonate	PVDF (Kynar)	Tygon	304 Stainless Steel	316 Stainless Steel	Aluminium	Brass	Neoprene	Natural Rubber
Calcium Hydroxide	D	A[2]	B[2]	B[1]	B	C[1]	–	A	A
Calcium Oxide	–	A	C	A	A	C	–	A	B
Carbon Dioxide (Dry)	–	A	–	A	A[1]	C[1]	B	B	B
Carbon Dioxide (Wet)	–	A	–	A	A[1]	A[1]	–	B	B
Water (Deionised)	–	A[2]	A[2]	A[1]	A[2]	A[2]	A	A	A
Water (Acid, Mine)	B[2]	A	–	B	B	D	D	C	B
Water (Distilled)	A[2]	A	B	A	A	A	A	A	A
Water (Fresh)	A[2]	A	B	A	A	B	D	A	A
Water (Salt)	A[2]	A	B	B	B	B	D	A	A

A - No Effect
B - Minor Effect
C - Moderate Effect
D - Severe Effect
– - No Data
Explanation of Footnotes:
1. Satisfactory to 22^{o}C
2. Satisfactory to 48^{o}C

Appendix E

Other Cell Designs

E.1 Alternative Cell and Fluid Management Designs

Several additional cell geometries were explored as well as controllable fluid valves to potentially overcome deficiencies of the fluid transport design used in the instrument prototypes. These alternative designs are presented below.

E.1.1 Constant Volume Cell

The conceptual "constant volume" cell (Figure E.1), would use a constant closed volume space for both the chemical indicator reagent, and the sample gas, such that a repeatable volume of gas and indicator reagent would be used for each turbidity measurement.

The principle of operation is as follows. The cell would be completely filled with indicator reagent and any gas within the cell void would be expelled through the exhaust valve (Figure E.1(a)-top). Once the cell was full, the exhaust valve would be closed, and the indicator reagent transport pump stopped (Figure E.1(a)). The sample gas would then be pumped into the cell with the displaced indicator solution being forced

out the fluid transport valve (left most - Figure E.1(b)). Once the fluid level in the cell had reduced to a pre-determined volume, the measurement would stop, thereby using a known volume of indicator solution and sample gas per measurement. This cell could overcome the cell and variable flowrate difficulties presented in Chapter 11.

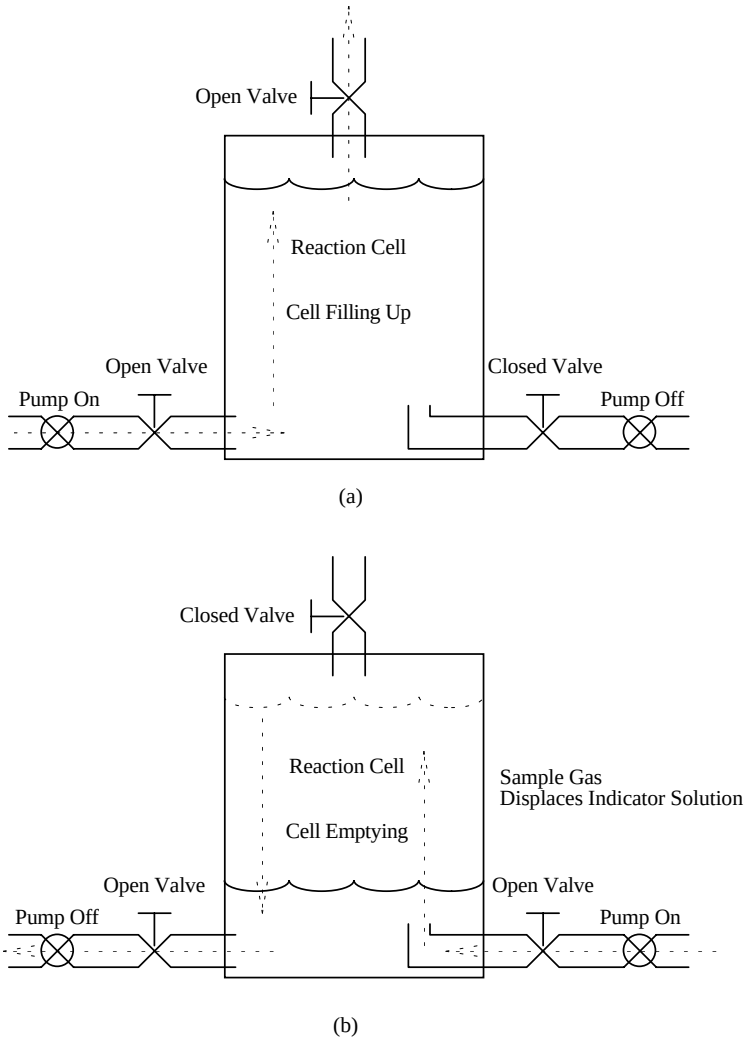

Figure E.1: The conceptual "constant volume" cell showing the cell void, the three ports, and valve/pump assemblies. (a) shows the cell during the filling operation, and (b) shows the cell during a measurement operation.

E.1.2 Additional Valve Designs

To overcome the leakage deficiently of the gear pumps chosen for the measurement instrument prototypes (Section 11.3.6), microcontroller-selectable check valves were investigated. These valves (Figure E.2) were designed such that in the rest position magnets would hold a small ball bearing either remote from an "O" ring seal, or firmly against it, depending on the valve's current state. Two coils allowed the ball bearing to be moved between the two positions. In the closed position, fluid flow from the input port (top) would force more pressure on the ball bearing thereby ensuring a continuous seal. Should fluid flow occur in the opposite direction, the ball bearing could become dislodged and allow fluid flow, hence this valve would operate as a selectable check valve.

Several valves were constructed and tested, however the significant energy levels required to engage or disengage the ball bearing would not be available from the prototype instruments. It was also observed that the energy level required would deform the plastic due to heating of the coils.

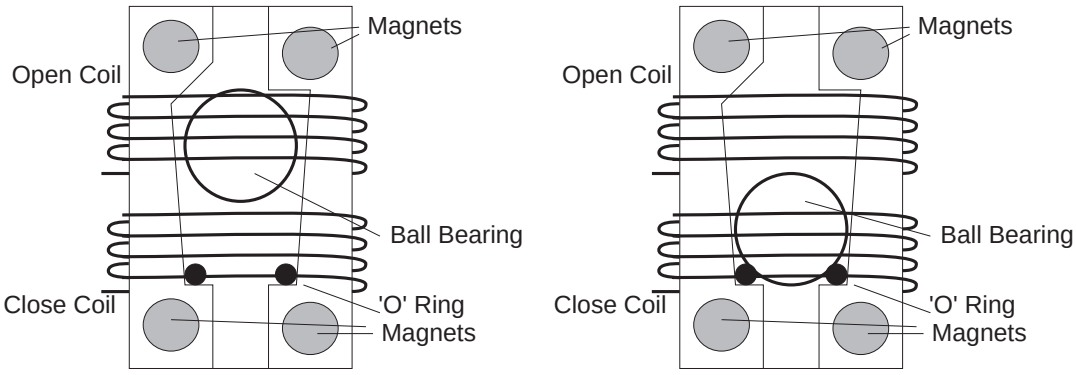

(a) Valve in the open position.

(b) Valve in the closed position.

Figure E.2: Microcontroller selectable fluid check valves. Shown are the magnet and coil assemblies as well as the ball bearing and 'O' ring seal.

E.2 Possible Reaction Cell Port Configurations

Several reaction cell port configurations were considered before settling on the final 3-port system as presented in Chapter 4. The number of possible fluid and gas transport ports and the location of the pumps with respect to these ports allow many possible configurations. Following are some of the more useful combinations of port and pump locations.

E.2.1 Pump Location

The pump location for the gas supply could be considered critical. It it is considered that the pump may contaminate a gas sample through leakage, or leeching of additional gaseous vapours from the pump materials. If the pump is placed upstream, it may contaminate the gas flow before reaching the cell. If the pump is placed downstream of the cell (at the exhaust port), no contamination from the pump would be possible. These two configurations are illustrated in Figure E.3. However contamination of the sample gas by the pump was not considered critical during the development of the instrument prototypes.

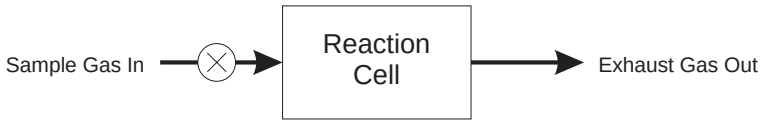

(a) Pump is upstream of the cell. Possible contamination could occur.

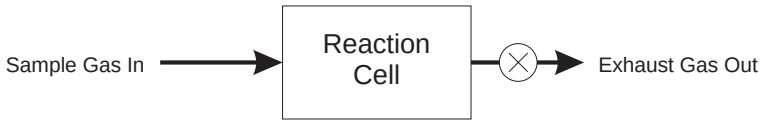

(b) Pump is downstream of the cell. Possible contamination will not occur.

Figure E.3: Example of pump location and possible contamination of the sample gas supply.

E.2.2 Single Port Configurations

Example single port cell configurations are illustrated in Figure E.4. In order for this type of cell to operate, the volume of chemical indicator within the chamber needs to be removed from the cell whilst the sample gas is being injected into the cell. This would be difficult to perform through the single port. Therefore these designs were not pursued.

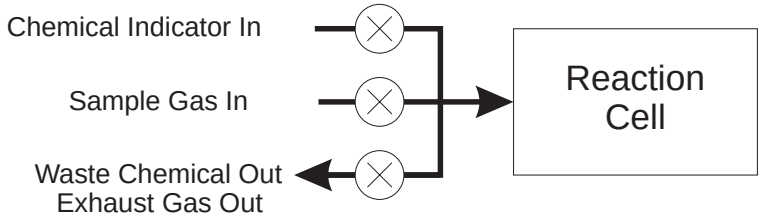

(a) Single port configuration with three separate pumps.

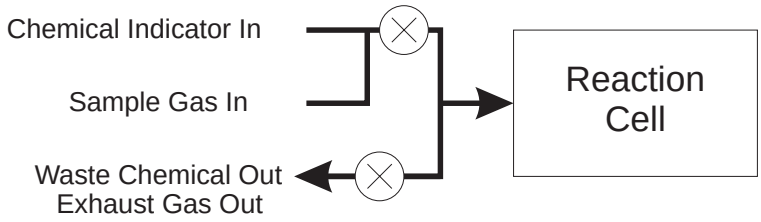

(b) Single port configuration with combined chemical indicator and sample gas input functions through a single pump.

Figure E.4: Two examples of a single port cell configurations (valves would also be required to prevent unwanted flow where combined functions existed).

E.2.3 Dual Port Configurations

Dual port configurations are illustrated in Figure E.5. These configurations allow for escaping sample gas from the cell, where either the waste materials are removed via the same port as the exhaust gas (which would prove difficult to implement) or through the first port (left most in Figure E.5(a) and E.5(c)). By splitting the input functions, a more useful configuration can be obtained (e.g. Figure E.5(c)).

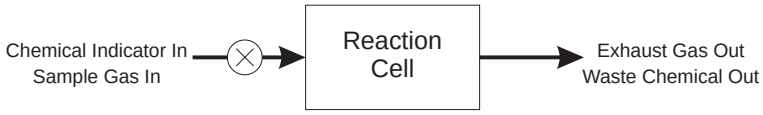

(a) Single up-stream pump.

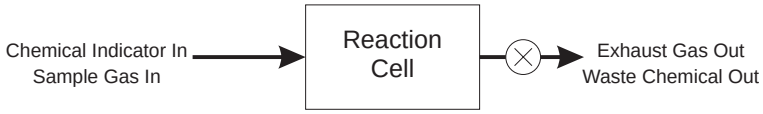

(b) Single down-stream pump (No sample gas contamination).

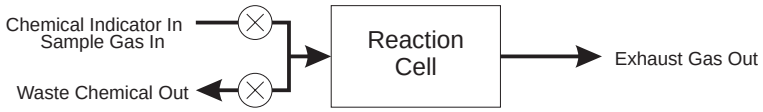

(c) Split input functions with two upstream pumps.

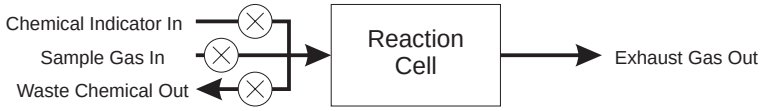

(d) Split input functions with three upstream pumps.

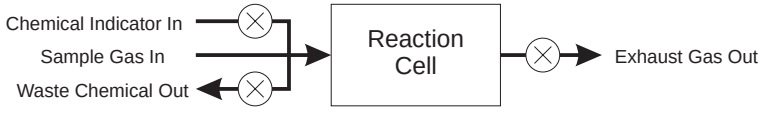

(e) Split input functions with two upstream, and one downstream pump.

Figure E.5: Five examples of dual port cell configurations (valves would also be required to prevent unwanted flow where combined functions existed).

E.2.4 Three-Port Configuration

Alternative three-port configurations are illustrated in Figure E.6. These configurations would allow the sample gas to have its own port suitably located to maximise mixing within the cell. This then typically left one port for reagent control, and one exhaust port. The configuration used for the Mk.I measurement instrument is illustrated in Figure E.6(a), with the configuration for the Mk.II instrument shown in Figure E.6(c).

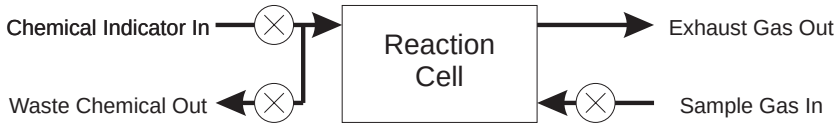

(a) Split input functions on one port with three upstream pumps. This was the configuration used for the Mk.I measurement instrument prototypes.

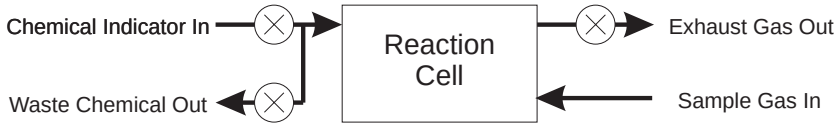

(b) Split input functions on one port with the upstream and one downstream pump (No sample gas contamination).

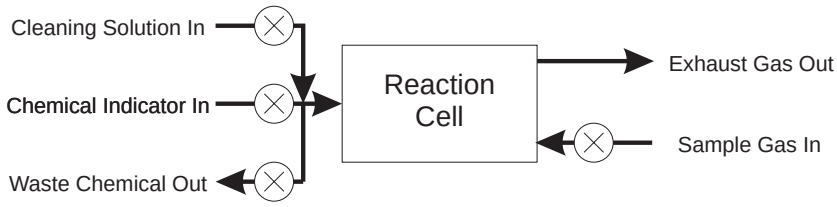

(c) Split input functions on one port with four upstream pumps. This was the configuration used for the Mk.II measurement instrument prototypes.

Figure E.6: Three examples of three-port cell configurations.

E.2.5 Four-Port Configurations

Alternative four-port configurations are illustrated in Figure E.7, where a port could be reserved for almost each fluid transport function. Again a variation can be made as to the location of the sample gas pump (to potentially remain contaminant free). Where a cleaning solution was used, the configuration shown in Figure E.7(c) could be implemented.

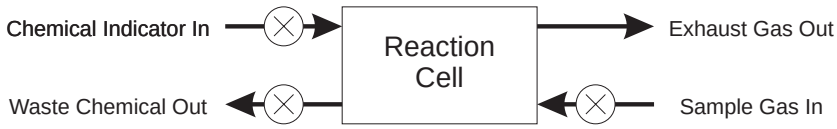

(a) Separate input functions for each port.

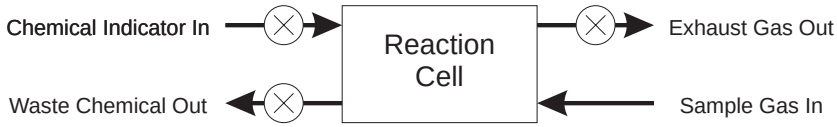

(b) Separate input functions for each port (No sample gas contamination).

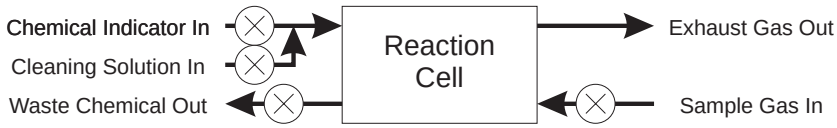

(c) Split input functions on one port should the use of a cleaning reagent be required.

Figure E.7: Three examples of four-port cell configurations.

Appendix F

Gas Laboratory

F.1 Introduction

During this research into carbon dioxide gas sensing systems, it became necessary to configure a gas laboratory suitable for supplying quantities of carbon dioxide gas diluted with known proportions of dry nitrogen, to a device under test with acceptable accuracy and repeatability. Due to a lack of accurate gas calibration equipment available for this work, it also became necessary to develop a simple but effective calibration scheme whereby gas of a known flowrate and composition could be supplied. Least square error minimisation techniques were used to model unlabelled flowmeter's behavior to determine flow settings for each flowmeter to produce a specific gas composition and flowrate.

F.2 Experimental Configuration

The gas laboratory configuration consisted of three main systems being:

1. Precision gas supply via compressed gas cylinders. Two 'E' size cylinders were

used, one for nitrogen and one for carbon dioxide mounted onto a movable trolley to allow easy relocation. Tank specifications were as shown in Table F.1 [1]. Hence the gas cylinders plus tank carrier occupied approximately 120cm(H) × 60cm(W) × 50cm(D).

Table F.1: Nominal dimensions of gas supply cylinders without valve.

Size Code	Tare Weight [kg]	Height [mm]	Outside Diameter [mm]	Min. Water Capacity [kg or L]
Aluminium Cylinders E	22.0	955	215	15.3
Steel Cylinders E	28.0	910	200	23.0

2. Regulators, flow meters, and gas analyser. Appropriate regulators were obtained, matching the gas type and application of the cylinders. To further aid the gas flow rate selection, precision flow meters were also incorporated. An existing carbon dioxide gas analyser was used where possible to check the concentration of the mixed gas.

3. Various miscellaneous components such as valves, connectors, gas tubing, and small consumables were also used.

The experimental configuration (illustrated in Figure F.1) consisted of the two gas cylinders filled with CO_2 and N_2 respectively. Both cylinders had suitable valves and dual stage regulators to provide control over the intermediate gas flow rates from each cylinder. Downstream of these regulators were the metered flowmeters (manufactured by Cole Parmer, sourced from Extech) used to further control the flowrates. Both flowmeters were supplied with basic calibration information for a variety of gases including CO_2 and N_2.

The CO_2 flowmeter[2] was a 155mm stainless steel metered flowmeter fitting with glass float and precision valve with a maximum flow rate of 355mL/min for CO_2. The N_2

[1] http://www.world.net/intelifest/boc/sec2-8.html
[2] Order code `3229-13` from Extech Equipment Pty. Ltd.

flowmeter[3] was the same size but of aluminium construction, with a standard valve capable of metering a maximum flow rate of 2395mL/min for N_2. These flowmeters were unmarked on the reading scale except for a grading from 0 to 150 (full scale). Calibration information was provided by the supplier matching flowrates of various gases to the grading scale on the flowmeters. This calibration information in conjunction with the flowmeters provided some control over the flow rate but for the purpose of the experimentation performed, was insufficient. As the control of the gas rate was poor for low flowrates (as required by the prototype measurement instruments) direct connection of the gas supply to the prototype instrument was not possible. Small sample gas bags were used instead to provide the sample gases to the measurement instruments. A photograph of the gas lab configuration and the sample bags (modified "AromaScan™" gas sample bags) used is shown in Figure F.2.

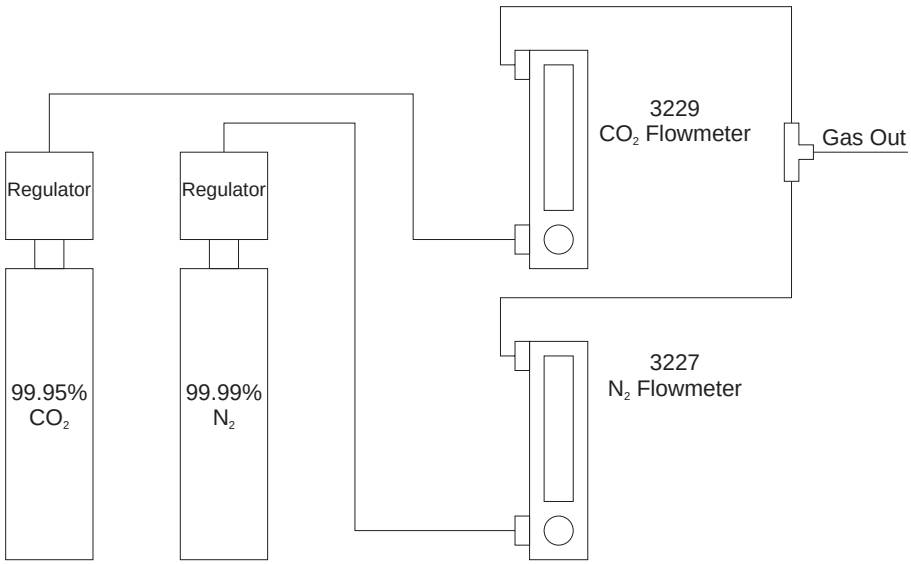

Figure F.1: Connection diagram for the constructed gas laboratory.

[3]Order code 3227-20 from Extech Equipment Pty. Ltd.

(a) Gas cylinders and flowmeters. The CO_2 gas cylinder is on the left with the N_2 gas cylinder on the right.

(b) The two flowmeters. The CO_2 flowmeter is on the left with the N_2 flowmeter on the right.

(c) Sample gas bag.

(d) Valve assembly on the sample gas bag.

Figure F.2: Photographs of the gas laboratory equipment.

The calibration information provided for these flowmeters (for their respective gases) can be seen in Table F.2. This table is expressed graphically in Figures F.3 and F.4. Note that these graphs indicate the calibration curves for CO_2, N_2 and dry air for both flowmeters.

Table F.2: Calibration data for the glass ball flowmeters used within the gas laboratory.

Flowmeter Setting	Flow Rate mL/min N_2 [3227-20]	mL/min CO_2 [3229-13]
10	186	23
20	385	40
30	575	57
40	750	78
50	930	102
60	1103	127
70	1265	154
80	1424	181
90	1562	208
100	1695	235
110	1827	260
120	1951	284
130	2085	306
140	2230	332
150	2395	355

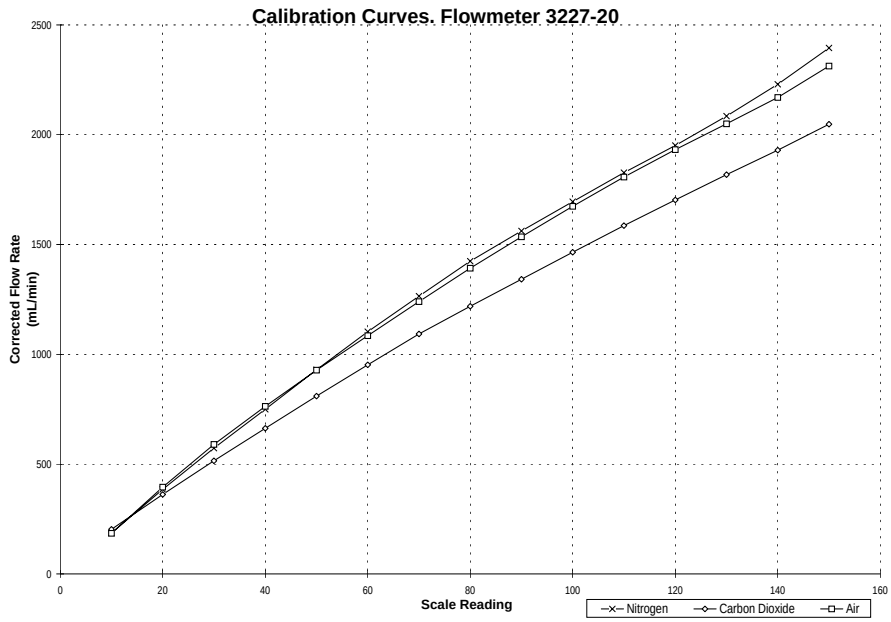

Figure F.3: 3227-20 flowmeter calibration curves for N_2, CO_2 and dry air.

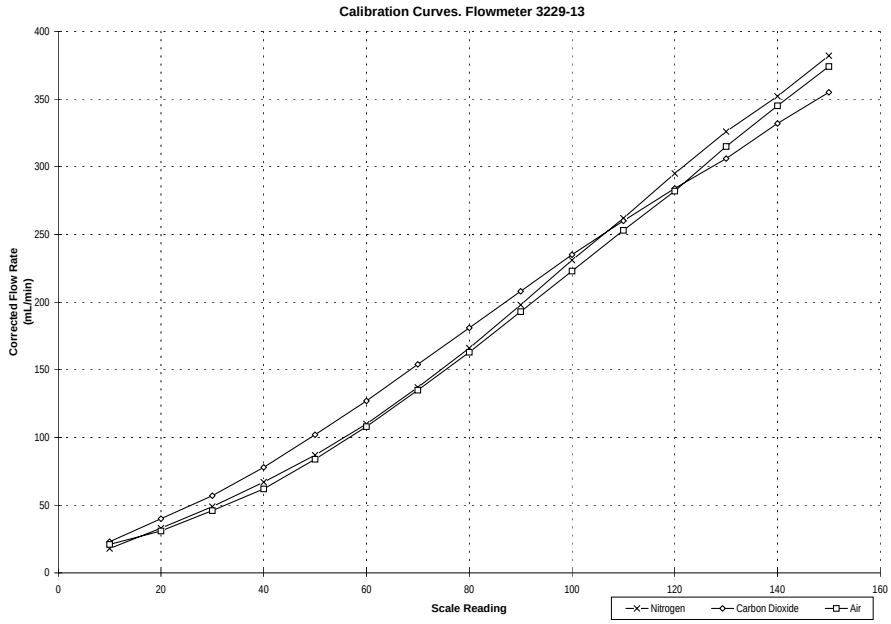

Figure F.4: 3229-13 flowmeter calibration curves for N_2, CO_2 and dry air.

F.3 Gas Flow Calibration Method

When using the gas supply equipment, the two variables were required, the total flow rate of the gas supply (f_{total}), and the desired CO_2 concentration (C_{CO_2}). Because both gas species were combined (Figure F.1) to a single flow (ignoring flowrate loading), the total flowrate would be:

$$f_{total} = f_{CO_2} + f_{N_2} \tag{F.1}$$

where:

f_{total} = the total flow rate of the gas supply [mL/min];
f_{CO_2} = flowrate from the CO_2 flowmeter [mL/min]; and
f_{N_2} = flowrate from the N_2 flowmeter [mL/min].

hence by rearranging:

$$f_{N_2} = f_{total} - f_{CO_2} \tag{F.2}$$

In this particular case, the amount of CO_2 present was of interest and by considering a simple ratio mix, it can be stated that:

$$f_{CO_2} = f_{total} \times C_{CO_2} \tag{F.3}$$

where:

C_{CO_2} = the desired CO_2 concentration [$\%CO_2/100$];

As an extension to this, the actual concentration of gases available within the cylinders required consideration, as neither the CO_2 or N_2 concentration were exactly 100% pure.

Hence to further increase the accuracy, the CO_2 gas supply stream was assumed to contain an impurity, hence:

$$f_{(CO_2)pure} = M_{CO_2} \times f_{CO_2} \tag{F.4}$$

where:

$f_{(CO_2)pure}$	=	the component of the gas flow attributed to %100 pure CO_2;
M_{CO_2}	=	the fractional amount of CO_2 within the cylinder; and with the rest of the flow component being from impurities.

Hence, for a non pure CO_2 source:

$$f_{CO_2} = \frac{f_{total} \times C_{CO_2}}{M_{CO_2}} \tag{F.5}$$

$$f_{N_2} = f_{total} - f_{CO_2} \tag{F.6}$$

where:

f_{CO_2}	=	the calculated flowrate component from the CO_2 flowmeter [mL/min];
f_{total}	=	the required flowrate of the gas supply [mL/min];
C_{CO_2}	=	the required CO_2 concentration [$\%CO_2/100$]; and
f_{N_2}	=	the calculated flowrate component from the N_2 flowmeter [mL/min];

These two equations allowed each flowrate from the two flowmeters to be determined. However, each flowmeter also required a model to properly represent its calibration data.

F.3.1 Flowmeter Modelling

An order adjustable, least square error minimisation routine was written to provide necessary modelling of the flowmeter calibration data as provided for the two flowmeters (at the time "MATLAB™" was unavailable). This software took the calibration information and created a 5th order polynomial model to relate the required flowrate from each flowmeter to a grating value, and likewise a reverse model relating the grating value to an actual flowrate was created. Figure F.5 shows the calibration data and

the fit curve for the N_2 flowmeter calibration data. The error between these two curves is presented in Figure F.6. Likewise the calibration data and fit curve for the CO_2 flowmeter is shown in Figure F.7 with the error shown in Figure F.8.

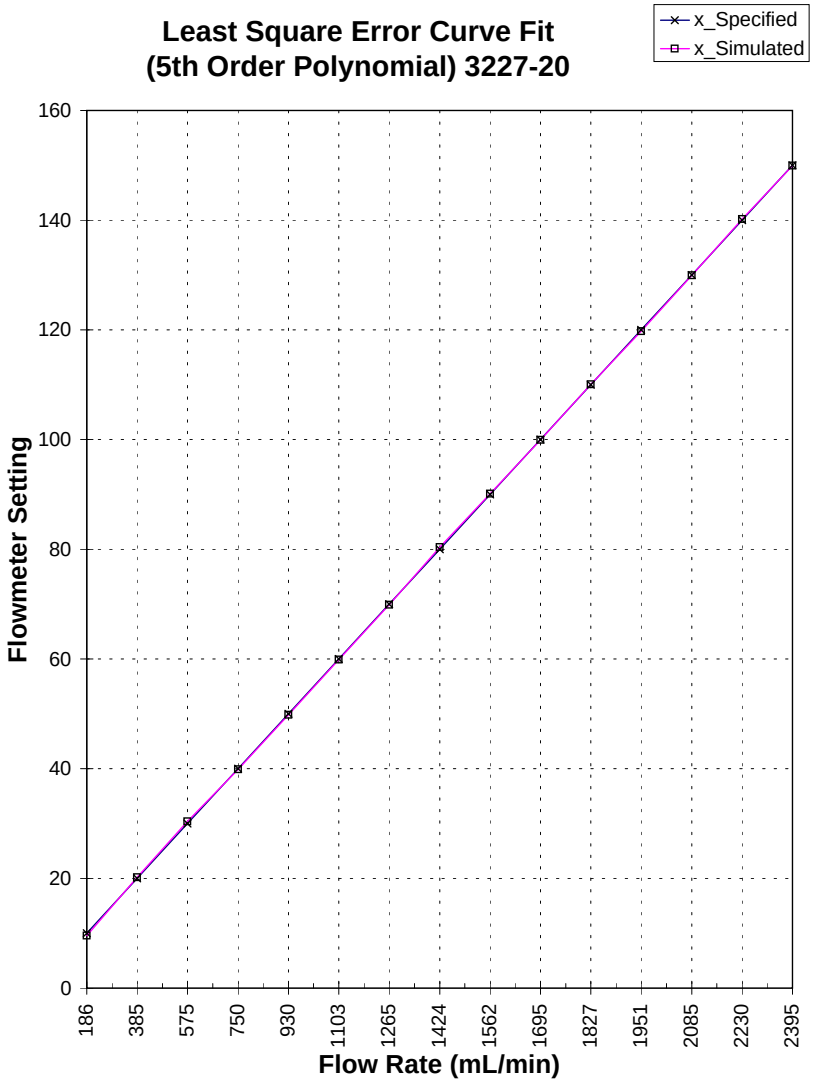

Figure F.5: 3227-20 flowmeter calibration comparison between supplied calibration information and the theoretical calibration model.

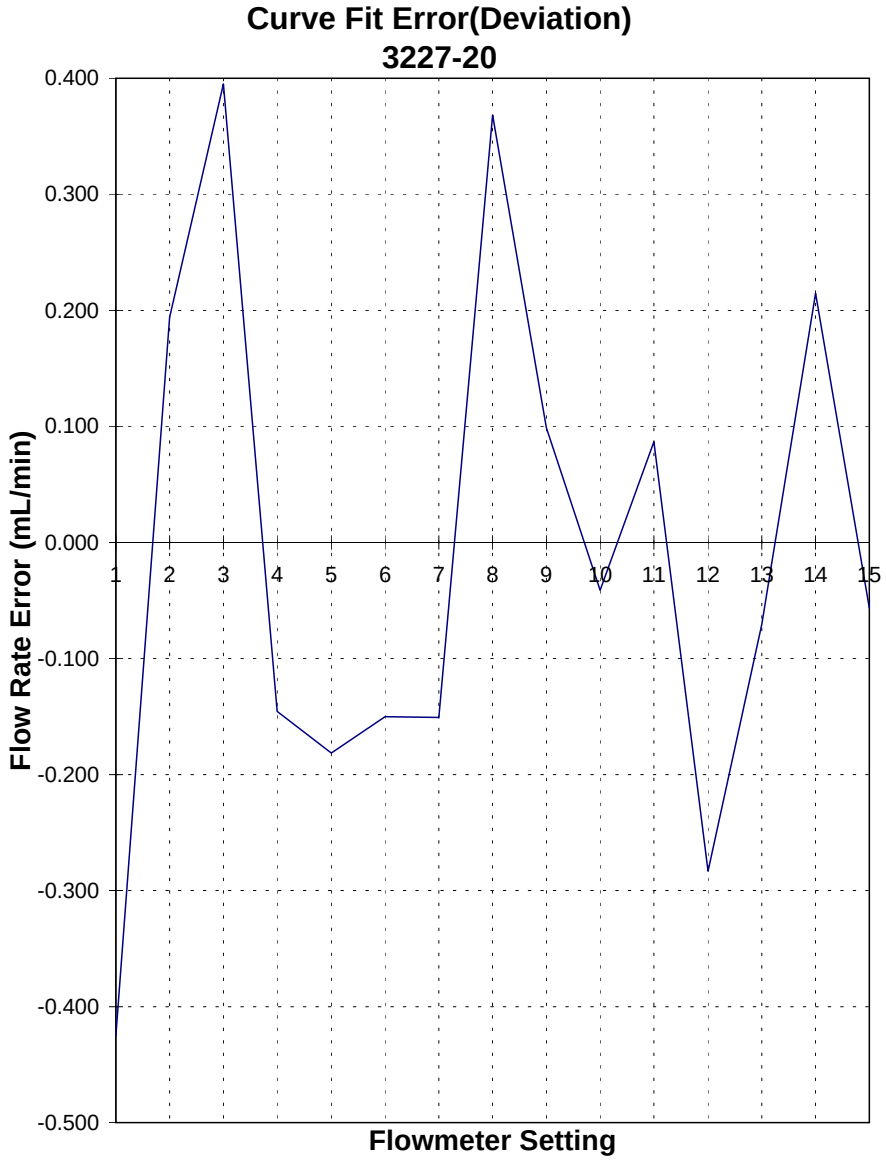

Figure F.6: 3227-20 flowmeter error between supplied calibration information and the theoretical calibration model.

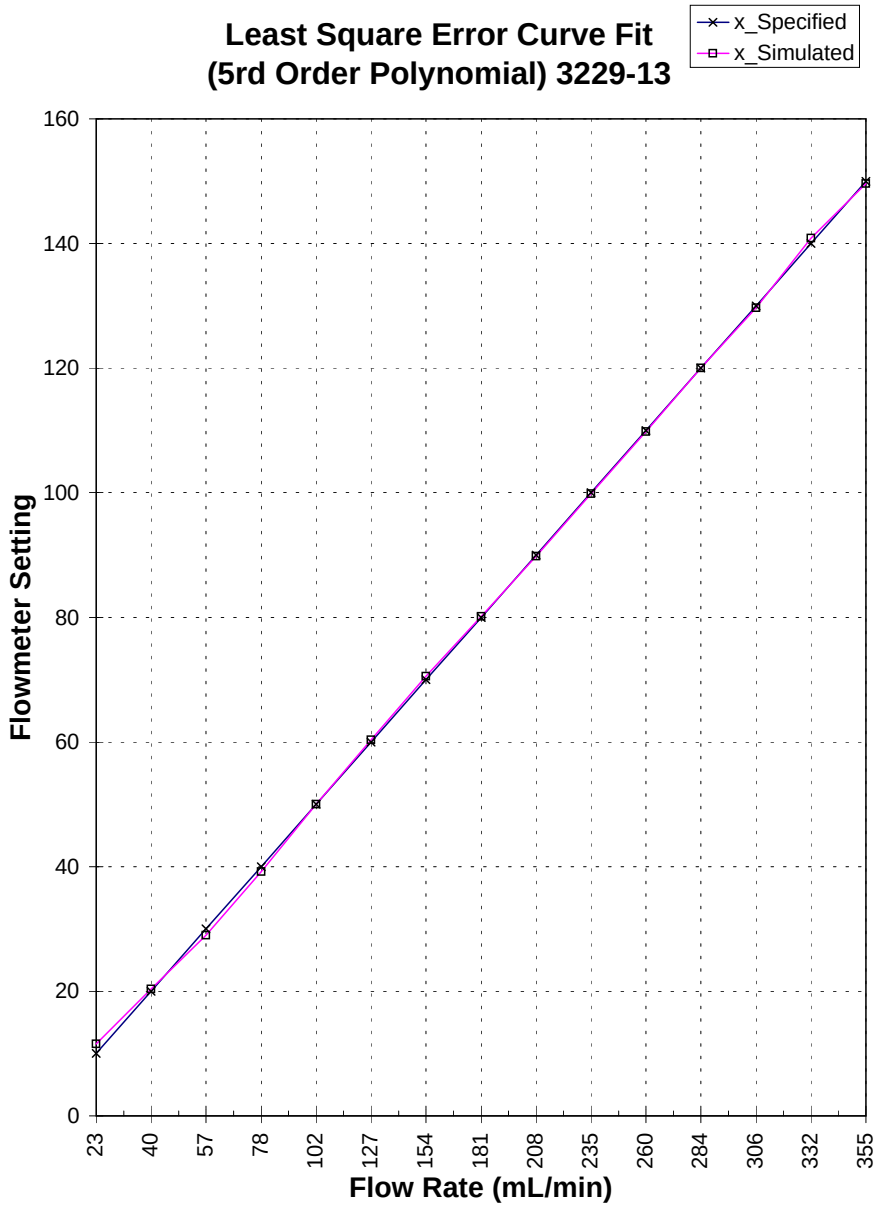

Figure F.7: 3229-13 flowmeter calibration comparison between supplied calibration information and the theoretical calibration model.

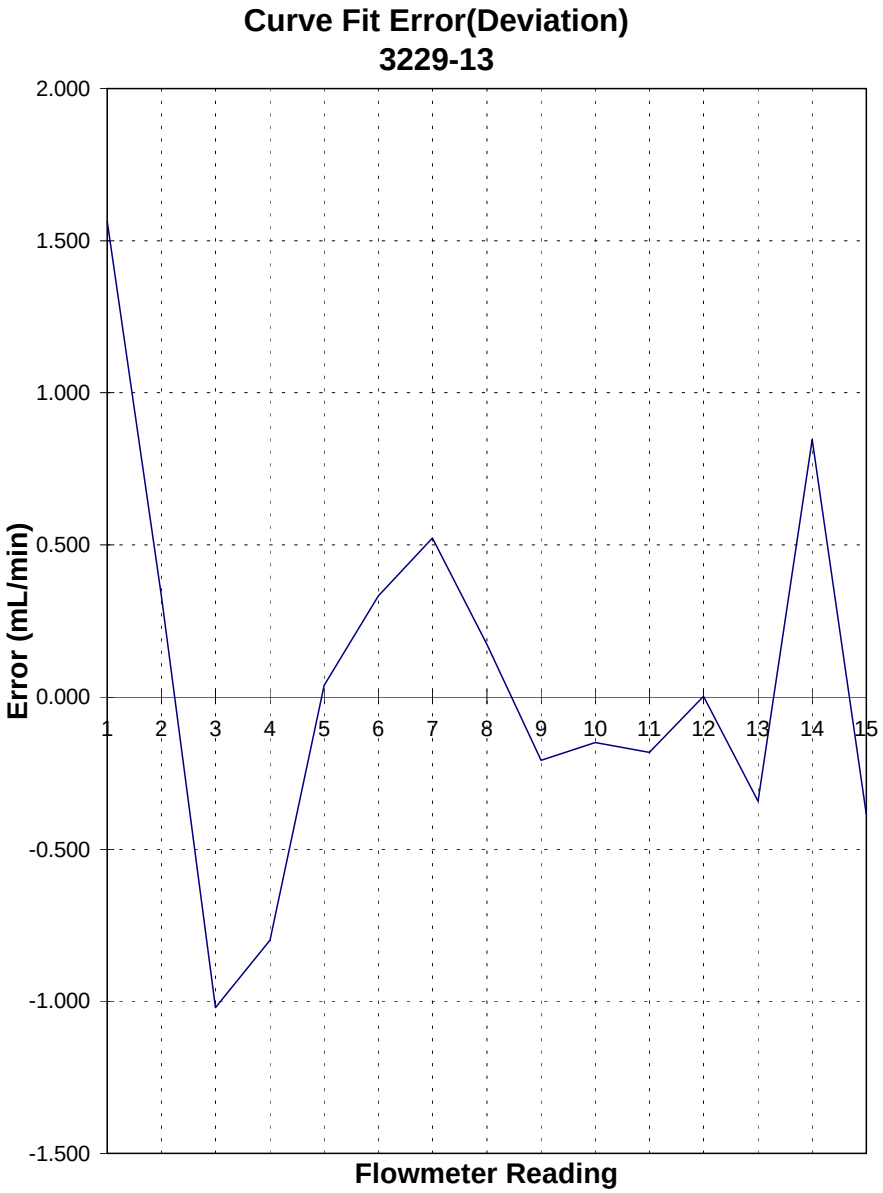

Figure F.8: 3229-13 flowmeter error between supplied calibration information and the theoretical calibration model.

F.3.2 Experimental Validation

To validate the calibration method shown previously, the gas laboratory was configured as shown in Figure F.1, with the gas supply systems, flowmeters, a flowmeter previously calibrated to measure the combined flow rate from the two adjustable flowmeters, and a low range CO_2 gas analyser.

Figure F.9 shows the linear trend of increasing measured CO_2 concentration for an increasing CO_2 gas flow setting (whilst the N_2 flowrate was held fixed at 15), with two sets of results presented. The deviation from the linear trend shown below the 6% measured CO_2 concentration is attributed to the inability to precisely set the flowmeters towards the low end of their flow scale.

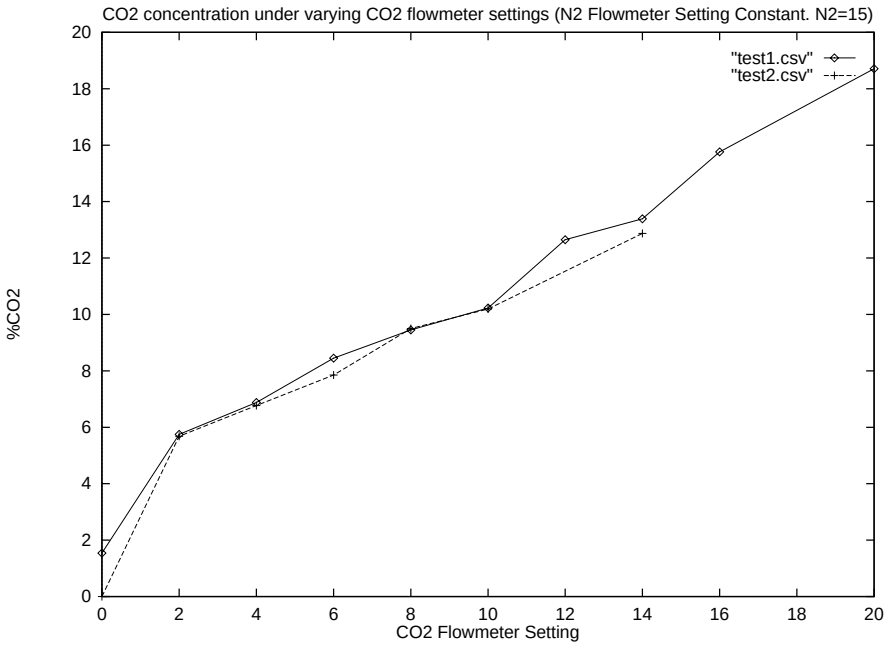

Figure F.9: Measured CO_2 concentration in the supply gas stream while varying CO_2 flowrate and holding N_2 flowrate constant at setting 15.

Figure F.10 shows the linearity for the entire calibration scheme compared to a 1:1 line. Clearly seen is a offset concentration of 5%. This is attributed to loading of the flowmeters due to their being connected in parallel, as well as the inability to precisely

set the flowmeters at these low values. The performance beyond 14% could not be established due to upper limit restriction of the gas analyser being used.

Any errors in this variable CO_2 concentration gas supply system would not directly affect testing of the measurement instruments as both sample gases and test gases were obtained using the same method, hence providing a cancellation of the error.

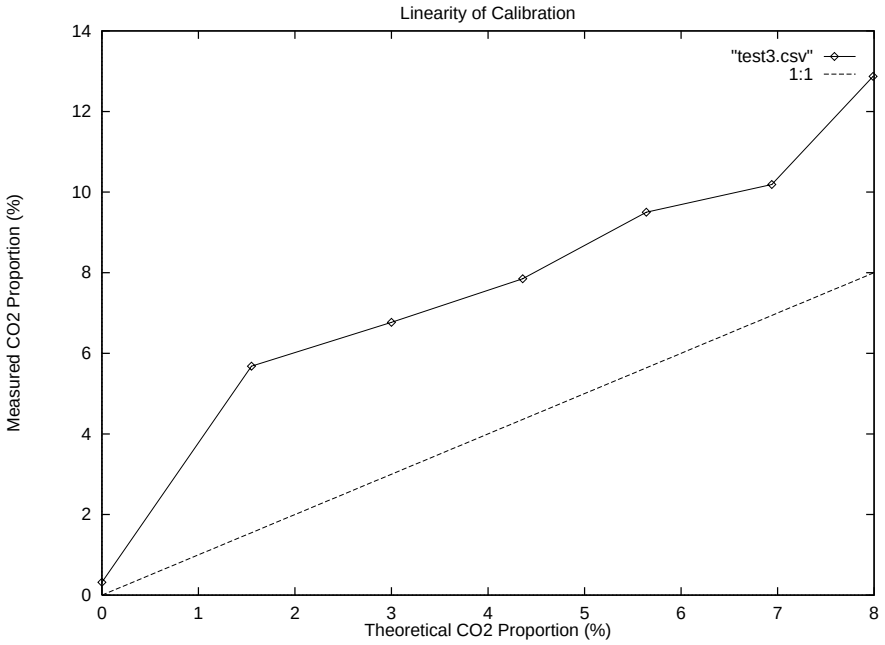

Figure F.10: Linearity of calibration scheme at low CO_2 concentrations.

F.3.3 Produced Calibration Tables

The following tables (presented on the following pages) were generated using the shown calibration method and show the CO_2 and N_2 flowmeter set points for various CO_2 concentrations at various flowrates. A subset of these tables is shown in Table F.3 for demonstration purposes. For example, to obtain 15% CO_2 at a flowrate of 400mL/min, this table shows; $\frac{CO_2 31.34}{N_2 17.69}$, where the CO_2 flowmeter is set to 31.34, and the N_2 flowmeter set to 17.69 on their grating scales respectively.

Table F.3: A subset of the flowmeter set-point tables.

CO_2%	200mL/min	400mL/min	600mL/min
0.00	$\frac{CO_2 0.01}{N_2 10.71}$	$\frac{CO_2 0.01}{N_2 20.74}$	$\frac{CO_2 0.01}{N_2 31.46}$
5.00	$\frac{CO_2 2.94}{N_2 10.21}$	$\frac{CO_2 8.15}{N_2 19.72}$	$\frac{CO_2 14.17}{N_2 29.80}$
10.00	$\frac{CO_2 8.15}{N_2 9.70}$	$\frac{CO_2 20.23}{N_2 18.70}$	$\frac{CO_2 31.34}{N_2 28.16}$
15.00	$\frac{CO_2 14.17}{N_2 9.19}$	$\frac{CO_2 31.34}{N_2 17.69}$	$\frac{CO_2 45.23}{N_2 26.53}$
20.00	$\frac{CO_2 20.23}{N_2 8.68}$	$\frac{CO_2 40.90}{N_2 16.69}$	$\frac{CO_2 57.20}{N_2 24.93}$

The first two tables (on the next page) allow for CO_2 concentrations from 0 to 100% (in steps of 5%) and for flow rates from 100mL/min to 2000mL/min (in steps of 100mL/min). The next two allow for CO_2 concentrations from 0 to 20% (in steps of 1%).

F.3.4 Conclusion

The gas lab operated as required and was able to produce variable concentrations of known CO_2 composition, within limitations of the equipment used, for calibration and testing of the prototype instruments. However, there was a significant problem obtaining reliable CO_2 concentrations below 5%, due to the inability of the flowmeters to be accurately set at these low flowrate levels. For continued exploration of the prototype instrument's performance, a more reliable means of obtaining these gas samples would be required. This could possibly be achieved through the use of double dilution of a calibration gas sample to achieve reliable CO_2 sample gas concentrations below 1%.

CO_2%	100mL/min	300mL/min	500mL/min	700mL/min	900mL/min	1100mL/min	1300mL/min	1500mL/min	1700mL/min	1900mL/min
0.00	$CO_2$0.01 $N_2$5.54	$CO_2$0.01 $N_2$15.69	$CO_2$0.01 $N_2$26.00	$CO_2$0.01 $N_2$37.06	$CO_2$0.01 $N_2$48.38	$CO_2$0.01 $N_2$59.86	$CO_2$0.01 $N_2$72.03	$CO_2$0.01 $N_2$85.48	$CO_2$0.01 $N_2$100.28	$CO_2$0.01 $N_2$115.90
5.00	$CO_2$1.06 $N_2$5.28	$CO_2$5.37 $N_2$14.95	$CO_2$11.12 $N_2$24.66	$CO_2$17.22 $N_2$35.09	$CO_2$28.16 $N_2$45.83	$CO_2$28.72 $N_2$56.67	$CO_2$33.87 $N_2$67.96	$CO_2$38.64 $N_2$80.27	$CO_2$43.10 $N_2$93.84	$CO_2$47.32 $N_2$108.44
10.00	$CO_2$2.94 $N_2$5.01	$CO_2$14.17 $N_2$14.20	$CO_2$25.99 $N_2$23.34	$CO_2$36.29 $N_2$33.13	$CO_2$45.23 $N_2$43.28	$CO_2$53.33 $N_2$53.51	$CO_2$61.01 $N_2$64.01	$CO_2$68.51 $N_2$75.26	$CO_2$75.95 $N_2$87.62	$CO_2$83.36 $N_2$101.05
15.00	$CO_2$5.37 $N_2$4.74	$CO_2$23.16 $N_2$13.46	$CO_2$51.36 $N_2$22.03	$CO_2$62.89 $N_2$31.18	$CO_2$74.10 $N_2$40.73	$CO_2$85.21 $N_2$50.37	$CO_2$96.28 $N_2$60.15	$CO_2$107.83 $N_2$70.45	$CO_2$120.62 $N_2$81.64	$CO_2$133.84 $N_2$93.84
20.00	$CO_2$8.15 $N_2$4.47	$CO_2$31.34 $N_2$12.71	$CO_2$49.36 $N_2$20.74	$CO_2$64.77 $N_2$29.25	$CO_2$79.66 $N_2$38.19	$CO_2$94.43 $N_2$47.25	$CO_2$109.86 $N_2$56.38	$CO_2$127.29 $N_2$65.82	$CO_2$142.92 $N_2$75.92	$CO_2$150.00 $N_2$86.90
25.00	$CO_2$11.12 $N_2$4.19	$CO_2$38.64 $N_2$11.96	$CO_2$59.11 $N_2$19.46	$CO_2$77.81 $N_2$27.34	$CO_2$96.28 $N_2$35.65	$CO_2$116.21 $N_2$44.13	$CO_2$137.50 $N_2$52.65	$CO_2$150.00 $N_2$61.33	$CO_2$150.00 $N_2$70.45	$CO_2$150.00 $N_2$80.27
30.00	$CO_2$14.17 $N_2$3.92	$CO_2$45.23 $N_2$11.21	$CO_2$68.51 $N_2$18.20	$CO_2$90.74 $N_2$25.46	$CO_2$114.06 $N_2$33.13	$CO_2$139.31 $N_2$41.01	$CO_2$150.00 $N_2$48.95	$CO_2$150.00 $N_2$56.96	$CO_2$150.00 $N_2$65.21	$CO_2$150.00 $N_2$73.98
35.00	$CO_2$17.22 $N_2$3.65	$CO_2$51.36 $N_2$10.46	$CO_2$77.81 $N_2$16.94	$CO_2$103.87 $N_2$23.60	$CO_2$133.64 $N_2$30.63	$CO_2$150.00 $N_2$37.90	$CO_2$150.00 $N_2$45.26	$CO_2$150.00 $N_2$52.65	$CO_2$150.00 $N_2$60.15	$CO_2$150.00 $N_2$67.96
40.00	$CO_2$20.23 $N_2$3.37	$CO_2$57.20 $N_2$9.70	$CO_2$87.05 $N_2$15.69	$CO_2$118.40 $N_2$21.78	$CO_2$150.00 $N_2$28.16	$CO_2$150.00 $N_2$34.81	$CO_2$150.00 $N_2$41.58	$CO_2$150.00 $N_2$48.38	$CO_2$150.00 $N_2$55.23	$CO_2$150.00 $N_2$62.22
45.00	$CO_2$23.16 $N_2$3.09	$CO_2$62.89 $N_2$8.94	$CO_2$96.28 $N_2$14.45	$CO_2$133.64 $N_2$19.97	$CO_2$150.00 $N_2$25.73	$CO_2$150.00 $N_2$31.73	$CO_2$150.00 $N_2$37.90	$CO_2$150.00 $N_2$44.13	$CO_2$150.00 $N_2$50.37	$CO_2$150.00 $N_2$56.67
50.00	$CO_2$25.99 $N_2$2.82	$CO_2$68.51 $N_2$8.17	$CO_2$105.83 $N_2$13.21	$CO_2$147.16 $N_2$18.20	$CO_2$150.00 $N_2$23.34	$CO_2$150.00 $N_2$28.70	$CO_2$150.00 $N_2$34.24	$CO_2$150.00 $N_2$39.88	$CO_2$150.00 $N_2$45.55	$CO_2$150.00 $N_2$51.23
55.00	$CO_2$28.72 $N_2$2.54	$CO_2$74.10 $N_2$7.39	$CO_2$116.21 $N_2$11.96	$CO_2$150.00 $N_2$16.44	$CO_2$150.00 $N_2$21.00	$CO_2$150.00 $N_2$25.73	$CO_2$150.00 $N_2$30.63	$CO_2$150.00 $N_2$35.65	$CO_2$150.00 $N_2$40.73	$CO_2$150.00 $N_2$45.83
60.00	$CO_2$31.34 $N_2$2.26	$CO_2$79.66 $N_2$6.60	$CO_2$127.29 $N_2$10.71	$CO_2$150.00 $N_2$14.70	$CO_2$150.00 $N_2$18.70	$CO_2$150.00 $N_2$22.82	$CO_2$150.00 $N_2$27.07	$CO_2$150.00 $N_2$31.46	$CO_2$150.00 $N_2$35.93	$CO_2$150.00 $N_2$40.45
65.00	$CO_2$33.87 $N_2$1.98	$CO_2$86.21 $N_2$5.81	$CO_2$137.50 $N_2$9.45	$CO_2$150.00 $N_2$12.96	$CO_2$150.00 $N_2$16.44	$CO_2$150.00 $N_2$19.97	$CO_2$150.00 $N_2$23.60	$CO_2$150.00 $N_2$27.34	$CO_2$150.00 $N_2$31.18	$CO_2$150.00 $N_2$35.09
70.00	$CO_2$36.29 $N_2$1.70	$CO_2$90.74 $N_2$5.01	$CO_2$147.16 $N_2$8.17	$CO_2$150.00 $N_2$11.21	$CO_2$150.00 $N_2$14.20	$CO_2$150.00 $N_2$17.19	$CO_2$150.00 $N_2$20.23	$CO_2$150.00 $N_2$23.34	$CO_2$150.00 $N_2$26.53	$CO_2$150.00 $N_2$29.80
75.00	$CO_2$38.64 $N_2$1.42	$CO_2$96.28 $N_2$4.19	$CO_2$150.00 $N_2$6.87	$CO_2$150.00 $N_2$9.45	$CO_2$150.00 $N_2$11.96	$CO_2$150.00 $N_2$14.45	$CO_2$150.00 $N_2$16.94	$CO_2$150.00 $N_2$19.46	$CO_2$150.00 $N_2$22.03	$CO_2$150.00 $N_2$24.66
80.00	$CO_2$40.90 $N_2$1.14	$CO_2$101.94 $N_2$3.37	$CO_2$150.00 $N_2$5.54	$CO_2$150.00 $N_2$7.85	$CO_2$150.00 $N_2$9.70	$CO_2$150.00 $N_2$11.71	$CO_2$150.00 $N_2$13.70	$CO_2$150.00 $N_2$15.69	$CO_2$150.00 $N_2$17.69	$CO_2$150.00 $N_2$19.72
85.00	$CO_2$43.10 $N_2$0.85	$CO_2$107.83 $N_2$2.54	$CO_2$150.00 $N_2$4.19	$CO_2$150.00 $N_2$5.81	$CO_2$150.00 $N_2$7.39	$CO_2$150.00 $N_2$8.94	$CO_2$150.00 $N_2$10.46	$CO_2$150.00 $N_2$11.96	$CO_2$150.00 $N_2$13.46	$CO_2$150.00 $N_2$14.95
90.00	$CO_2$45.23 $N_2$0.57	$CO_2$114.06 $N_2$1.70	$CO_2$150.00 $N_2$2.82	$CO_2$150.00 $N_2$3.92	$CO_2$150.00 $N_2$5.01	$CO_2$150.00 $N_2$6.08	$CO_2$150.00 $N_2$7.13	$CO_2$150.00 $N_2$8.17	$CO_2$150.00 $N_2$9.19	$CO_2$150.00 $N_2$10.21
95.00	$CO_2$47.32 $N_2$0.28	$CO_2$120.62 $N_2$0.85	$CO_2$150.00 $N_2$1.42	$CO_2$150.00 $N_2$1.98	$CO_2$150.00 $N_2$2.54	$CO_2$150.00 $N_2$3.09	$CO_2$150.00 $N_2$3.65	$CO_2$150.00 $N_2$4.19	$CO_2$150.00 $N_2$4.74	$CO_2$150.00 $N_2$5.28
100.00	$CO_2$49.36 $N_2$0.00	$CO_2$127.29 $N_2$0.00	$CO_2$150.00 $N_2$0.00	$CO_2$150.00 $N_2$0.00	$CO_2$150.00 $N_2$0.00	$CO_2$150.00 $N_2$0.00	$CO_2$150.00 $N_2$0.00	$CO_2$150.00 $N_2$0.00	$CO_2$150.00 $N_2$0.00	$CO_2$150.00 $N_2$0.00

CO_2%	200mL/min	400mL/min	600mL/min	800mL/min	1000mL/min	1200mL/min	1400mL/min	1600mL/min	1800mL/min	2000mL/min
0.00	$CO_2$0.01 $N_2$10.71	$CO_2$0.01 $N_2$20.74	$CO_2$0.01 $N_2$31.46	$CO_2$0.01 $N_2$42.71	$CO_2$0.01 $N_2$54.08	$CO_2$0.01 $N_2$65.82	$CO_2$0.01 $N_2$78.58	$CO_2$0.01 $N_2$92.73	$CO_2$0.01 $N_2$108.04	$CO_2$0.01 $N_2$123.67
5.00	$CO_2$2.94 $N_2$10.21	$CO_2$8.15 $N_2$19.72	$CO_2$14.17 $N_2$29.80	$CO_2$20.23 $N_2$40.45	$CO_2$26.99 $N_2$51.23	$CO_2$31.34 $N_2$62.22	$CO_2$36.29 $N_2$73.98	$CO_2$40.90 $N_2$86.90	$CO_2$45.23 $N_2$101.05	$CO_2$49.36 $N_2$115.90
10.00	$CO_2$8.15 $N_2$9.70	$CO_2$20.23 $N_2$18.70	$CO_2$31.34 $N_2$28.16	$CO_2$40.90 $N_2$38.19	$CO_2$49.36 $N_2$48.38	$CO_2$57.20 $N_2$58.69	$CO_2$64.77 $N_2$69.51	$CO_2$72.24 $N_2$81.29	$CO_2$79.66 $N_2$94.22	$CO_2$87.05 $N_2$108.04
15.00	$CO_2$14.17 $N_2$9.19	$CO_2$31.34 $N_2$17.69	$CO_2$45.23 $N_2$26.53	$CO_2$57.20 $N_2$35.93	$CO_2$68.51 $N_2$45.55	$CO_2$79.66 $N_2$55.23	$CO_2$90.74 $N_2$65.21	$CO_2$101.94 $N_2$75.92	$CO_2$114.06 $N_2$87.62	$CO_2$127.29 $N_2$100.28
20.00	$CO_2$20.23 $N_2$8.68	$CO_2$40.90 $N_2$16.69	$CO_2$57.20 $N_2$24.93	$CO_2$72.24 $N_2$33.68	$CO_2$87.05 $N_2$42.71	$CO_2$101.94 $N_2$51.80	$CO_2$118.40 $N_2$61.04	$CO_2$135.61 $N_2$70.77	$CO_2$150.00 $N_2$81.29	$CO_2$150.00 $N_2$92.73
25.00	$CO_2$25.99 $N_2$8.17	$CO_2$49.36 $N_2$15.69	$CO_2$68.51 $N_2$23.34	$CO_2$87.05 $N_2$31.46	$CO_2$105.83 $N_2$39.88	$CO_2$127.29 $N_2$48.38	$CO_2$147.16 $N_2$56.96	$CO_2$150.00 $N_2$65.82	$CO_2$150.00 $N_2$75.26	$CO_2$150.00 $N_2$85.48
30.00	$CO_2$31.34 $N_2$7.65	$CO_2$64.77 $N_2$14.70	$CO_2$79.66 $N_2$21.78	$CO_2$101.94 $N_2$29.25	$CO_2$127.29 $N_2$37.06	$CO_2$150.00 $N_2$44.98	$CO_2$150.00 $N_2$52.94	$CO_2$150.00 $N_2$61.04	$CO_2$150.00 $N_2$69.51	$CO_2$150.00 $N_2$78.58
35.00	$CO_2$36.29 $N_2$7.13	$CO_2$64.77 $N_2$13.70	$CO_2$90.74 $N_2$20.23	$CO_2$118.40 $N_2$27.07	$CO_2$147.16 $N_2$34.24	$CO_2$150.00 $N_2$41.58	$CO_2$150.00 $N_2$48.95	$CO_2$150.00 $N_2$56.38	$CO_2$150.00 $N_2$64.01	$CO_2$150.00 $N_2$72.03
40.00	$CO_2$40.90 $N_2$6.60	$CO_2$72.24 $N_2$12.71	$CO_2$101.94 $N_2$18.70	$CO_2$135.61 $N_2$24.93	$CO_2$150.00 $N_2$31.46	$CO_2$150.00 $N_2$38.19	$CO_2$150.00 $N_2$44.98	$CO_2$150.00 $N_2$51.80	$CO_2$150.00 $N_2$58.69	$CO_2$150.00 $N_2$65.82
45.00	$CO_2$45.23 $N_2$6.08	$CO_2$79.66 $N_2$11.71	$CO_2$114.06 $N_2$17.19	$CO_2$150.00 $N_2$22.82	$CO_2$150.00 $N_2$28.70	$CO_2$150.00 $N_2$34.81	$CO_2$150.00 $N_2$41.01	$CO_2$150.00 $N_2$47.25	$CO_2$150.00 $N_2$53.51	$CO_2$150.00 $N_2$59.86
50.00	$CO_2$49.36 $N_2$5.94	$CO_2$87.05 $N_2$10.71	$CO_2$127.29 $N_2$15.89	$CO_2$150.00 $N_2$20.74	$CO_2$150.00 $N_2$26.00	$CO_2$150.00 $N_2$31.46	$CO_2$150.00 $N_2$37.06	$CO_2$150.00 $N_2$42.71	$CO_2$150.00 $N_2$48.38	$CO_2$150.00 $N_2$54.08
55.00	$CO_2$53.33 $N_2$5.01	$CO_2$94.43 $N_2$9.70	$CO_2$139.31 $N_2$14.20	$CO_2$150.00 $N_2$18.70	$CO_2$150.00 $N_2$23.34	$CO_2$150.00 $N_2$28.16	$CO_2$150.00 $N_2$33.13	$CO_2$150.00 $N_2$38.19	$CO_2$150.00 $N_2$43.28	$CO_2$150.00 $N_2$48.38
60.00	$CO_2$57.20 $N_2$4.47	$CO_2$101.94 $N_2$8.68	$CO_2$150.00 $N_2$12.71	$CO_2$150.00 $N_2$16.69	$CO_2$150.00 $N_2$20.74	$CO_2$150.00 $N_2$24.93	$CO_2$150.00 $N_2$29.25	$CO_2$150.00 $N_2$33.68	$CO_2$150.00 $N_2$38.19	$CO_2$150.00 $N_2$42.71
65.00	$CO_2$61.01 $N_2$3.92	$CO_2$109.86 $N_2$7.65	$CO_2$150.00 $N_2$11.21	$CO_2$150.00 $N_2$14.70	$CO_2$150.00 $N_2$18.20	$CO_2$150.00 $N_2$21.78	$CO_2$150.00 $N_2$25.46	$CO_2$150.00 $N_2$29.25	$CO_2$150.00 $N_2$33.13	$CO_2$150.00 $N_2$37.06
70.00	$CO_2$64.77 $N_2$3.37	$CO_2$118.40 $N_2$6.60	$CO_2$150.00 $N_2$9.70	$CO_2$150.00 $N_2$12.71	$CO_2$150.00 $N_2$15.69	$CO_2$150.00 $N_2$18.70	$CO_2$150.00 $N_2$21.78	$CO_2$150.00 $N_2$24.93	$CO_2$150.00 $N_2$28.16	$CO_2$150.00 $N_2$31.46
75.00	$CO_2$68.51 $N_2$2.82	$CO_2$127.29 $N_2$5.54	$CO_2$150.00 $N_2$8.17	$CO_2$150.00 $N_2$10.71	$CO_2$150.00 $N_2$13.21	$CO_2$150.00 $N_2$15.69	$CO_2$150.00 $N_2$18.20	$CO_2$150.00 $N_2$20.74	$CO_2$150.00 $N_2$23.34	$CO_2$150.00 $N_2$26.00
80.00	$CO_2$72.24 $N_2$2.26	$CO_2$135.61 $N_2$4.47	$CO_2$150.00 $N_2$6.60	$CO_2$150.00 $N_2$8.68	$CO_2$150.00 $N_2$10.71	$CO_2$150.00 $N_2$12.71	$CO_2$150.00 $N_2$14.70	$CO_2$150.00 $N_2$16.69	$CO_2$150.00 $N_2$18.70	$CO_2$150.00 $N_2$20.74
85.00	$CO_2$75.95 $N_2$1.70	$CO_2$142.92 $N_2$3.37	$CO_2$150.00 $N_2$5.01	$CO_2$150.00 $N_2$6.60	$CO_2$150.00 $N_2$8.17	$CO_2$150.00 $N_2$9.70	$CO_2$150.00 $N_2$11.21	$CO_2$150.00 $N_2$12.71	$CO_2$150.00 $N_2$14.20	$CO_2$150.00 $N_2$15.69
90.00	$CO_2$79.66 $N_2$1.14	$CO_2$150.00 $N_2$2.26	$CO_2$150.00 $N_2$3.37	$CO_2$150.00 $N_2$4.47	$CO_2$150.00 $N_2$5.54	$CO_2$150.00 $N_2$6.60	$CO_2$150.00 $N_2$7.65	$CO_2$150.00 $N_2$8.68	$CO_2$150.00 $N_2$9.70	$CO_2$150.00 $N_2$10.71
95.00	$CO_2$83.36 $N_2$0.57	$CO_2$150.00 $N_2$1.14	$CO_2$150.00 $N_2$1.70	$CO_2$150.00 $N_2$2.26	$CO_2$150.00 $N_2$2.82	$CO_2$150.00 $N_2$3.37	$CO_2$150.00 $N_2$3.92	$CO_2$150.00 $N_2$4.47	$CO_2$150.00 $N_2$5.01	$CO_2$150.00 $N_2$5.54
100.00	$CO_2$87.05 $N_2$0.00	$CO_2$150.00 $N_2$0.00	$CO_2$150.00 $N_2$0.00	$CO_2$150.00 $N_2$0.00	$CO_2$150.00 $N_2$0.00	$CO_2$150.00 $N_2$0.00	$CO_2$150.00 $N_2$0.00	$CO_2$150.00 $N_2$0.00	$CO_2$150.00 $N_2$0.00	$CO_2$150.00 $N_2$0.00

CO_2%	100mL/min	300mL/min	500mL/min	700mL/min	900mL/min	1100mL/min	1300mL/min	1500mL/min	1700mL/min	1900mL/min
0.00	CO0.01 $N_2$5.54	CO0.01 $N_2$15.69	CO0.01 $N_2$26.00	CO0.01 $N_2$37.06	CO0.01 $N_2$48.38	CO0.01 $N_2$59.86	CO0.01 $N_2$72.03	CO0.01 $N_2$85.48	CO0.01 $N_2$100.28	CO0.01 $N_2$115.90
1.00	$CO_2$0.14 $N_2$5.49	$CO_2$0.52 $N_2$15.54	$CO_2$1.06 $N_2$25.73	$CO_2$1.73 $N_2$36.66	$CO_2$2.51 $N_2$47.87	$CO_2$3.39 $N_2$59.22	$CO_2$4.35 $N_2$71.21	$CO_2$5.37 $N_2$84.42	$CO_2$6.45 $N_2$98.98	$CO_2$7.57 $N_2$114.41
2.00	$CO_2$0.31 $N_2$5.44	$CO_2$1.38 $N_2$15.39	$CO_2$2.94 $N_2$25.46	$CO_2$4.85 $N_2$36.27	$CO_2$7.01 $N_2$47.36	$CO_2$9.32 $N_2$58.58	$CO_2$11.72 $N_2$70.39	$CO_2$14.17 $N_2$83.37	$CO_2$16.61 $N_2$97.68	$CO_2$19.03 $N_2$112.92
3.00	$CO_2$0.52 $N_2$5.38	$CO_2$2.51 $N_2$15.25	$CO_2$5.37 $N_2$25.19	$CO_2$8.73 $N_2$35.87	$CO_2$12.33 $N_2$46.85	$CO_2$16.00 $N_2$57.94	$CO_2$19.63 $N_2$69.57	$CO_2$23.16 $N_2$82.33	$CO_2$26.55 $N_2$96.39	$CO_2$29.78 $N_2$111.42
4.00	$CO_2$0.77 $N_2$5.33	$CO_2$3.86 $N_2$15.10	$CO_2$8.15 $N_2$24.93	$CO_2$12.94 $N_2$35.48	$CO_2$17.83 $N_2$46.34	$CO_2$22.58 $N_2$57.30	$CO_2$27.10 $N_2$68.76	$CO_2$31.34 $N_2$81.29	$CO_2$35.33 $N_2$95.12	$CO_2$39.10 $N_2$109.93
5.00	$CO_2$1.06 $N_2$5.28	$CO_2$3.37 $N_2$14.95	$CO_2$11.12 $N_2$24.66	$CO_2$17.22 $N_2$35.09	$CO_2$23.16 $N_2$45.83	$CO_2$28.72 $N_2$56.67	$CO_2$33.87 $N_2$67.96	$CO_2$38.64 $N_2$80.27	$CO_2$43.10 $N_2$93.84	$CO_2$47.32 $N_2$108.44
6.00	$CO_2$1.38 $N_2$5.22	$CO_2$3.51 $N_2$14.80	$CO_2$14.17 $N_2$24.40	$CO_2$21.41 $N_2$34.69	$CO_2$28.18 $N_2$45.32	$CO_2$34.36 $N_2$56.03	$CO_2$40.00 $N_2$67.16	$CO_2$45.23 $N_2$79.25	$CO_2$50.16 $N_2$92.58	$CO_2$54.89 $N_2$106.95
7.00	$CO_2$1.73 $N_2$5.17	$CO_2$3.64 $N_2$14.65	$CO_2$8.73 $N_2$24.13	$CO_2$25.43 $N_2$34.30	$CO_2$32.87 $N_2$44.81	$CO_2$39.55 $N_2$55.40	$CO_2$45.85 $N_2$66.36	$CO_2$51.86 $N_2$78.24	$CO_2$56.82 $N_2$91.33	$CO_2$62.14 $N_2$105.47
8.00	$CO_2$2.11 $N_2$5.11	$CO_2$10.51 $N_2$14.50	$CO_2$20.23 $N_2$23.87	$CO_2$29.25 $N_2$33.91	$CO_2$37.24 $N_2$44.30	$CO_2$44.38 $N_2$54.77	$CO_2$50.96 $N_2$65.57	$CO_2$57.20 $N_2$77.24	$CO_2$63.27 $N_2$90.08	$CO_2$69.26 $N_2$103.99
9.00	$CO_2$2.51 $N_2$5.06	$CO_2$12.33 $N_2$14.35	$CO_2$23.16 $N_2$23.60	$CO_2$32.87 $N_2$33.52	$CO_2$41.34 $N_2$43.79	$CO_2$48.95 $N_2$54.14	$CO_2$56.05 $N_2$64.79	$CO_2$62.89 $N_2$76.25	$CO_2$69.63 $N_2$88.84	$CO_2$76.32 $N_2$102.51
10.00	$CO_2$2.94 $N_2$5.01	$CO_2$14.17 $N_2$14.20	$CO_2$25.99 $N_2$23.34	$CO_2$36.29 $N_2$33.13	$CO_2$45.23 $N_2$43.28	$CO_2$53.33 $N_2$53.51	$CO_2$61.01 $N_2$64.01	$CO_2$68.51 $N_2$75.26	$CO_2$75.95 $N_2$87.62	$CO_2$83.36 $N_2$101.05
11.00	$CO_2$3.30 $N_2$4.95	$CO_2$16.00 $N_2$14.05	$CO_2$28.72 $N_2$23.08	$CO_2$39.55 $N_2$32.74	$CO_2$48.95 $N_2$42.77	$CO_2$57.89 $N_2$52.88	$CO_2$65.89 $N_2$63.23	$CO_2$74.10 $N_2$74.28	$CO_2$82.25 $N_2$86.40	$CO_2$90.37 $N_2$99.59
12.00	$CO_2$3.86 $N_2$4.90	$CO_2$17.83 $N_2$13.90	$CO_2$31.34 $N_2$22.82	$CO_2$42.66 $N_2$32.35	$CO_2$52.55 $N_2$42.26	$CO_2$61.76 $N_2$52.25	$CO_2$70.75 $N_2$62.46	$CO_2$79.66 $N_2$73.31	$CO_2$88.53 $N_2$85.20	$CO_2$97.40 $N_2$98.14
13.00	$CO_2$4.35 $N_2$4.84	$CO_2$19.63 $N_2$13.75	$CO_2$33.87 $N_2$22.66	$CO_2$45.65 $N_2$31.96	$CO_2$56.06 $N_2$41.75	$CO_2$65.89 $N_2$51.63	$CO_2$75.38 $N_2$61.69	$CO_2$85.21 $N_2$72.35	$CO_2$94.80 $N_2$84.00	$CO_2$104.65 $N_2$96.70
14.00	$CO_2$4.85 $N_2$4.79	$CO_2$21.41 $N_2$13.61	$CO_2$36.29 $N_2$22.29	$CO_2$48.55 $N_2$31.57	$CO_2$59.49 $N_2$41.24	$CO_2$70.00 $N_2$51.00	$CO_2$80.40 $N_2$60.92	$CO_2$90.74 $N_2$71.40	$CO_2$101.17 $N_2$82.81	$CO_2$112.36 $N_2$95.27
15.00	$CO_2$5.37 $N_2$4.74	$CO_2$23.16 $N_2$13.46	$CO_2$38.64 $N_2$22.03	$CO_2$51.36 $N_2$31.18	$CO_2$62.89 $N_2$40.73	$CO_2$74.10 $N_2$50.37	$CO_2$85.21 $N_2$60.15	$CO_2$96.28 $N_2$70.45	$CO_2$107.83 $N_2$81.64	$CO_2$120.62 $N_2$93.84
16.00	$CO_2$5.91 $N_2$4.68	$CO_2$24.87 $N_2$13.31	$CO_2$40.90 $N_2$21.78	$CO_2$54.11 $N_2$30.79	$CO_2$66.27 $N_2$40.22	$CO_2$78.18 $N_2$49.75	$CO_2$90.00 $N_2$59.39	$CO_2$101.94 $N_2$69.51	$CO_2$114.92 $N_2$80.47	$CO_2$129.04 $N_2$92.43
17.00	$CO_2$6.45 $N_2$4.63	$CO_2$26.55 $N_2$13.16	$CO_2$43.10 $N_2$21.62	$CO_2$56.82 $N_2$30.41	$CO_2$69.63 $N_2$39.71	$CO_2$82.25 $N_2$49.12	$CO_2$94.80 $N_2$58.64	$CO_2$107.83 $N_2$68.58	$CO_2$122.40 $N_2$79.32	$CO_2$136.75 $N_2$91.03
18.00	$CO_2$7.01 $N_2$4.57	$CO_2$28.18 $N_2$13.01	$CO_2$45.23 $N_2$21.26	$CO_2$59.49 $N_2$30.02	$CO_2$72.98 $N_2$39.20	$CO_2$86.32 $N_2$48.50	$CO_2$99.66 $N_2$57.88	$CO_2$114.06 $N_2$67.65	$CO_2$129.90 $N_2$78.17	$CO_2$143.68 $N_2$89.64
19.00	$CO_2$7.57 $N_2$4.52	$CO_2$29.78 $N_2$12.86	$CO_2$47.32 $N_2$21.00	$CO_2$62.14 $N_2$29.63	$CO_2$76.32 $N_2$38.69	$CO_2$90.37 $N_2$47.87	$CO_2$104.65 $N_2$57.13	$CO_2$120.62 $N_2$66.73	$CO_2$136.75 $N_2$77.04	$CO_2$150.00 $N_2$88.27
20.00	$CO_2$8.15 $N_2$4.47	$CO_2$31.34 $N_2$12.71	$CO_2$49.36 $N_2$20.74	$CO_2$64.77 $N_2$29.25	$CO_2$79.66 $N_2$38.19	$CO_2$94.43 $N_2$47.25	$CO_2$109.86 $N_2$56.38	$CO_2$127.29 $N_2$65.82	$CO_2$142.92 $N_2$76.92	$CO_2$150.00 $N_2$86.90

CO_2%	200mL/min	400mL/min	600mL/min	800mL/min	1000mL/min	1200mL/min	1400mL/min	1600mL/min	1800mL/min	2000mL/min
0.00	$CO_2$0.01 $N_2$10.71	$CO_2$0.01 $N_2$20.74	$CO_2$0.01 $N_2$31.46	$CO_2$0.01 $N_2$42.71	$CO_2$0.01 $N_2$54.08	$CO_2$0.01 $N_2$65.82	$CO_2$0.01 $N_2$78.58	$CO_2$0.01 $N_2$92.73	$CO_2$0.01 $N_2$108.04	$CO_2$0.01 $N_2$123.67
1.00	$CO_2$0.31 $N_2$10.61	$CO_2$0.77 $N_2$20.54	$CO_2$1.38 $N_2$31.12	$CO_2$2.11 $N_2$42.26	$CO_2$2.94 $N_2$53.51	$CO_2$3.86 $N_2$65.09	$CO_2$4.85 $N_2$77.64	$CO_2$5.91 $N_2$91.55	$CO_2$7.01 $N_2$106.64	$CO_2$8.15 $N_2$122.13
2.00	$CO_2$0.77 $N_2$10.51	$CO_2$2.11 $N_2$20.33	$CO_2$3.86 $N_2$30.79	$CO_2$5.91 $N_2$41.81	$CO_2$8.15 $N_2$52.94	$CO_2$10.51 $N_2$64.37	$CO_2$12.94 $N_2$76.71	$CO_2$15.39 $N_2$90.37	$CO_2$17.83 $N_2$105.23	$CO_2$20.23 $N_2$120.59
3.00	$CO_2$1.38 $N_2$10.41	$CO_2$3.86 $N_2$20.13	$CO_2$7.01 $N_2$30.46	$CO_2$10.51 $N_2$41.35	$CO_2$14.17 $N_2$52.37	$CO_2$17.83 $N_2$63.65	$CO_2$21.41 $N_2$75.79	$CO_2$24.87 $N_2$89.21	$CO_2$28.18 $N_2$103.83	$CO_2$31.34 $N_2$119.03
4.00	$CO_2$2.11 $N_2$10.31	$CO_2$5.91 $N_2$19.92	$CO_2$10.51 $N_2$30.13	$CO_2$15.39 $N_2$40.90	$CO_2$20.23 $N_2$51.80	$CO_2$24.87 $N_2$62.93	$CO_2$29.25 $N_2$74.87	$CO_2$33.37 $N_2$88.05	$CO_2$37.24 $N_2$102.44	$CO_2$40.90 $N_2$117.47
5.00	$CO_2$2.94 $N_2$10.21	$CO_2$8.15 $N_2$19.72	$CO_2$14.17 $N_2$29.80	$CO_2$20.23 $N_2$40.45	$CO_2$25.99 $N_2$51.23	$CO_2$31.34 $N_2$62.22	$CO_2$36.29 $N_2$73.96	$CO_2$40.90 $N_2$86.90	$CO_2$45.23 $N_2$101.05	$CO_2$49.36 $N_2$115.90
6.00	$CO_2$3.86 $N_2$10.11	$CO_2$10.51 $N_2$19.52	$CO_2$17.83 $N_2$29.47	$CO_2$24.87 $N_2$39.99	$CO_2$31.34 $N_2$50.66	$CO_2$37.24 $N_2$61.81	$CO_2$42.66 $N_2$73.06	$CO_2$47.73 $N_2$85.76	$CO_2$52.55 $N_2$99.67	$CO_2$57.20 $N_2$114.33
7.00	$CO_2$4.85 $N_2$10.01	$CO_2$12.94 $N_2$19.31	$CO_2$21.41 $N_2$29.14	$CO_2$29.25 $N_2$39.54	$CO_2$36.29 $N_2$50.09	$CO_2$42.66 $N_2$60.80	$CO_2$48.55 $N_2$72.16	$CO_2$54.11 $N_2$84.63	$CO_2$59.49 $N_2$98.29	$CO_2$64.77 $N_2$112.76
8.00	$CO_2$5.91 $N_2$9.90	$CO_2$15.39 $N_2$19.11	$CO_2$24.87 $N_2$28.87	$CO_2$33.37 $N_2$39.09	$CO_2$40.90 $N_2$49.52	$CO_2$47.73 $N_2$60.10	$CO_2$54.11 $N_2$71.27	$CO_2$60.25 $N_2$83.51	$CO_2$66.27 $N_2$96.92	$CO_2$72.24 $N_2$111.19
9.00	$CO_2$7.01 $N_2$9.80	$CO_2$17.83 $N_2$18.91	$CO_2$28.18 $N_2$28.48	$CO_2$37.24 $N_2$38.64	$CO_2$45.23 $N_2$48.95	$CO_2$52.55 $N_2$59.39	$CO_2$59.49 $N_2$70.39	$CO_2$66.27 $N_2$82.40	$CO_2$72.98 $N_2$95.57	$CO_2$79.66 $N_2$109.61
10.00	$CO_2$8.15 $N_2$9.70	$CO_2$20.23 $N_2$18.70	$CO_2$31.34 $N_2$28.16	$CO_2$40.90 $N_2$38.19	$CO_2$49.36 $N_2$48.38	$CO_2$57.20 $N_2$58.69	$CO_2$64.77 $N_2$69.51	$CO_2$72.24 $N_2$81.29	$CO_2$79.66 $N_2$94.22	$CO_2$87.05 $N_2$108.04
11.00	$CO_2$9.32 $N_2$9.60	$CO_2$22.58 $N_2$18.50	$CO_2$34.36 $N_2$27.83	$CO_2$44.38 $N_2$37.73	$CO_2$53.33 $N_2$47.82	$CO_2$61.76 $N_2$58.00	$CO_2$70.00 $N_2$68.64	$CO_2$78.18 $N_2$80.20	$CO_2$86.32 $N_2$92.88	$CO_2$94.43 $N_2$106.48
12.00	$CO_2$10.51 $N_2$9.50	$CO_2$24.87 $N_2$18.30	$CO_2$37.24 $N_2$27.51	$CO_2$47.73 $N_2$37.28	$CO_2$57.20 $N_2$47.25	$CO_2$66.27 $N_2$57.30	$CO_2$75.21 $N_2$67.77	$CO_2$84.10 $N_2$79.12	$CO_2$92.95 $N_2$91.55	$CO_2$101.94 $N_2$104.92
13.00	$CO_2$11.72 $N_2$9.40	$CO_2$27.10 $N_2$18.10	$CO_2$40.00 $N_2$27.18	$CO_2$50.96 $N_2$36.83	$CO_2$61.01 $N_2$46.68	$CO_2$70.75 $N_2$56.61	$CO_2$80.40 $N_2$66.91	$CO_2$90.00 $N_2$78.04	$CO_2$99.06 $N_2$90.23	$CO_2$109.86 $N_2$103.37
14.00	$CO_2$12.94 $N_2$9.29	$CO_2$29.25 $N_2$17.90	$CO_2$42.66 $N_2$26.86	$CO_2$54.11 $N_2$36.38	$CO_2$64.77 $N_2$46.12	$CO_2$75.21 $N_2$55.92	$CO_2$85.58 $N_2$66.06	$CO_2$95.91 $N_2$76.97	$CO_2$106.63 $N_2$88.92	$CO_2$118.40 $N_2$101.82
15.00	$CO_2$14.17 $N_2$9.19	$CO_2$31.34 $N_2$17.69	$CO_2$45.23 $N_2$26.53	$CO_2$57.20 $N_2$35.93	$CO_2$68.51 $N_2$45.55	$CO_2$79.66 $N_2$55.23	$CO_2$90.74 $N_2$65.21	$CO_2$101.94 $N_2$75.92	$CO_2$114.06 $N_2$87.62	$CO_2$127.29 $N_2$100.28
16.00	$CO_2$15.39 $N_2$9.09	$CO_2$33.37 $N_2$17.49	$CO_2$47.73 $N_2$26.21	$CO_2$60.25 $N_2$35.48	$CO_2$72.24 $N_2$44.98	$CO_2$84.10 $N_2$54.54	$CO_2$95.91 $N_2$64.37	$CO_2$108.23 $N_2$74.87	$CO_2$121.96 $N_2$86.33	$CO_2$135.61 $N_2$98.75
17.00	$CO_2$16.61 $N_2$8.99	$CO_2$35.33 $N_2$17.29	$CO_2$50.16 $N_2$25.89	$CO_2$63.27 $N_2$35.03	$CO_2$75.35 $N_2$44.41	$CO_2$88.63 $N_2$53.85	$CO_2$101.17 $N_2$63.53	$CO_2$114.92 $N_2$73.83	$CO_2$129.90 $N_2$85.05	$CO_2$142.92 $N_2$97.23
18.00	$CO_2$17.83 $N_2$8.89	$CO_2$37.24 $N_2$17.09	$CO_2$52.55 $N_2$25.57	$CO_2$66.27 $N_2$34.58	$CO_2$79.66 $N_2$43.85	$CO_2$92.95 $N_2$53.17	$CO_2$106.63 $N_2$62.69	$CO_2$121.96 $N_2$72.80	$CO_2$137.13 $N_2$83.79	$CO_2$150.00 $N_2$95.72
19.00	$CO_2$19.03 $N_2$8.78	$CO_2$39.10 $N_2$16.89	$CO_2$54.89 $N_2$25.25	$CO_2$69.26 $N_2$34.13	$CO_2$83.36 $N_2$43.28	$CO_2$97.40 $N_2$52.48	$CO_2$112.36 $N_2$61.86	$CO_2$129.04 $N_2$71.78	$CO_2$143.68 $N_2$82.54	$CO_2$150.00 $N_2$94.22
20.00	$CO_2$20.23 $N_2$8.68	$CO_2$40.90 $N_2$16.69	$CO_2$57.20 $N_2$24.93	$CO_2$72.24 $N_2$33.68	$CO_2$87.05 $N_2$42.71	$CO_2$101.94 $N_2$51.80	$CO_2$118.40 $N_2$61.04	$CO_2$135.61 $N_2$70.77	$CO_2$150.00 $N_2$81.29	$CO_2$150.00 $N_2$92.73

Appendix G

CDROM Contents

A CDROM disc has been supplied with the original dissertation documentation. This CDROM contains all code listings, applications and documentation associated with the this dissertation[1]. This CDROM is supplied in ISO9660 format with Windows 95 CDROM extensions (Joliet format, with long file names).

The contents are broken into several subgroups.

Table G.1: Root directory structure of the included CDROM disc.

SOFTWARE	Software listings
HARDWARE	Hardware/mechanical drawings and specifications
MISC	Additional documentation

[1] Only those files which can be supplied without contravening copyright legislation have been included.

G.1 Software

This section contains all software listings written for the target hardware prototypes, and for the simulation and control packages. Assembly language, C, and QuickBasic code supplied for the various prototypes is provided.

Table G.2: Directory structure of the SOFTWARE folder.

- SOFTWARE
  - MKI — Software for the Mk.I prototype
  - MKII — Software for the Mk.II prototype
  - MODEL — Modelling Software
  - MISC — Miscellaneous Software

G.2 Hardware

This section contains all hardware designs and schematics of the instrument prototypes, and additional hardware constructed. Schematics, printed circuit board designs, mechanical drawings, and specifications are provided.

Table G.3: Directory structure of the HARDWARE folder.

- HARDWARE
  - MKI — Mk.I drawings and schematics.
  - MKII — Mk.II drawings and schematics.
  - CELLS — Reaction cell drawings and schematics.
  - SPECS — Hardware component specifications.
  - MISC — Miscellaneous drawing and schematics.

G.3 Misc

This section contains miscellaneous documentation, videos, and also includes a copy of this dissertation in Postscript and PDF format.